DEVELOPMENT OF PROGRESSIVE PERFORATION FAILURE MODEL FOR IMPROVING SAND RATE PREDICTION

A Dissertation

by

MOHIT DHOLI

Submitted to the Office of Graduate and Professional Studies of
Texas A&M University
in partial fulfillment of the requirements for the degree of

DOCTOR OF PHILOSOPHY

Chair of Committee,	Nobuo Morita
Committee Members,	Kan Wu
	Jihoon Kim
	Hiroko Kitajima
Head of Department,	Jeff Spath

May 2020

Major Subject: Petroleum Engineering

ABSTRACT

Formation sand production has been a recurring problem for the oil and gas industry since the advent of the hydrocarbon exploration and extraction. The effects of sand production are adverse in nature and are two folds; causing decrease in well productivity (due to sand control measures) and erosion of equipments. High strength rocks rarely disintegrate and produce sand, even if they do it is very late in the life of the well. Soft and weak rocks may produce sand very early in the life of the well and thus will need sand control measures. Intermediate strength rocks need to be evaluated for their sand production potential. As a producer, the endeavor is to extend hydrocarbon production without employing any sand control measures. A robust estimate of onset and the rate of sand production will provide the necessary information to regulate the operation schedule such that no or little sand production occurs throughout the life of the well. The same analysis will also furnish the operator with appropriate information on completions and sand control techniques to employ in case of excessive sand production predictions.

In this study, a coupled finite element numerical sand rate model is developed which is calibrated with poly-axial sand production experiments. The effect of stress anisotropy on the onset of sand production and the rates of sand production is evaluated. Sand production is a moving boundary problem hence adaptive meshing is employed. It is found that increase in axial and lateral anisotropy would make the rock more susceptible to sand production. The onset is found to be earlier in these cases. Also, the sand rates are higher with higher anisotropies. A field study is also presented which reaffirms the need of sand rate calculation. The numerical model is made in such a way that different completion schemes can be tried and tested for sand rate results.

DEDICATION

To the three most important women in my life - my mother, wife and daughter.

ACKNOWLEDGMENTS

I would like to express my sincere gratitude towards Dr. Nobuo Morita for his valuable guidance, teachings, passion and candidness. I feel very fortunate to have worked under his supervision.

I also thank Dr. Kan Wu, Dr. Jihoon Kim and Dr. Hiroko Kitajima for suggesting valuable improvements.

I am also thankful to my family and friends who have supported me in my endeavor with encouragement, advice and love. I always draw inspiration and guidance from my late father who had a kind, forgiving and spiritual heart. I am also indebted to the divine force for showing me the way.

CONTRIBUTORS AND FUNDING SOURCES

Contributors

This work was supported by the dissertation committee consisting of Professor Nobuo Morita (advisor) and Kan Wu, Jihoon Kim of the Department of Petroleum Engineering and Professor Hiroko Kitajima of the Department of Geology & Geophysics.

The experimental data was shared by Dr. Euripides Papamichos from the research project "Increasing profitability of sand producing fields" funded by PETROMAKS 2 program of the Research Council of Norway and Aker BP, DEA Norway, Hess, Occidental Petroleum and Exxon-Mobil (Project number 268159).

The field study data was provided by Japan Oil Engineering Co., Japan.

All other work conducted for the dissertation was completed by the student independently.

Funding Sources

Financial support for this research was provided by Kureha Corporation, Japan and graduate scholarship from Texas A&M University.

TABLE OF CONTENTS

Page

LIST OF FIGURES

FIGURE Page

LIST OF TABLES

TABLE Page

1. INTRODUCTION

Formation sand production has been a recurring problem for the oil and gas industry since the advent of the hydrocarbon exploration and extraction. The effects of sand production are adverse in nature and are two folds; causing decrease in well productivity and erosion of equipment. Sand production especially occurs in shallow, softer, geologically young formations with practically little cementation to hold the sand grains together (Penberthy and Shaughnessy (1992)). Estimates suggest that seventy percent of the total world's oil and gas reserves are found in poorly consolidated reservoirs (Bianco and Halleck (2001)). These are prone to sand production which is always considered an alarming situation due to the potential hazards. The formation sand can erode surface equipment, plug perforations or entire well, settle in surface vessels thus lowering their holding or carrying capacity and significantly lower productivity (Willson et al. (2002)). Operators spend millions of dollars annually trying to avoid sand production related problems since these assets are lucrative due to their high productivity potential and recovery rates. Usually, the remedies include slowing the production rate or using gravel packing (Penberthy and Shaughnessy (1992)).

The research conducted to study sand production phenomena can be broadly divided into four stages. Before 1980s, the risk of a field producing sand was studied using wireline logs. Drawdown control was a major preventive element. From 1980 - 1998, researchers started using finite element method to study onset of sand production by coupling fluid flow with geomechanical model. Studies showed that depletion and drawdown affect sanding risk simultaneously. From 1998 - 2017, many studies were done to improve prediction of sand onset using both experiments and finite element method. Simple analytical models were developed to estimate sand rate. From 2018 onwards, poly-axial volumetric experiments were conducted to assess the effect of stress anisotropy on sand onset and rate. Simultaneously, finite element method is used with adaptive meshing to predict sand rate.

A robust estimate of onset and the rate of sand production will provide the necessary informa-

tion to regulate the production schedule such that no or little sand production occurs throughout the life of the well. The same analysis will also furnish the operator with appropriate information on what sand control techniques to employ in case of excessive sand production predictions.

Sand production is a very complex phenomenon as it includes the dynamic interaction between rock material and fluid flow. During the production of hydrocarbons, rock loses its integrity and may deform excessively resulting in instability. Some of this material may flow along with the fluid and produced at the surface facility. The nature of sand production is as such that it is affected by many factors like in-situ stresses, rock properties, fluid properties, completion design etc.

Common techniques used in sand management related decisions can be broadly classified into experimental, analytical and numerical. Physical model testing in the laboratory is expensive and cumbersome. Furthermore, a large number of tests need to be performed for parametric study. Nevertheless, these results enhance our understanding of the physical phenomenon and the data can be used to derive empirical relationships or calibrate numerical models. Analytical models are fast and much easier to use but they oversimplify the complex real conditions and hence may not be valid in various cases. They are also more suitable for predicting the onset of sand production. Numerical modeling is one of the best techniques to capture multiphysics of sand production. It can also incorporate experimental results and analytical solutions.

1.1 Research Objectives

The main goal is to develop a coupled geomechanical and fluid flow poro-elasto-plastic model for the estimation of onset and rate of sand production. Since sand production is a moving boundary problem, adaptive meshing is utilized to capture this effect. The model will be calibrated with poly-axial volumetric sand production experiments. The model can be used for both experimental analysis as well as field completion schemes.

1.2 Outline of the Dissertation

The dissertation is presented in six chapters. Chapter 1 introduces the topic of research.

Chapter 2 reviews the mechanisms identified in sand production. Additionally, previous exper-

imental and numerical studies are discussed and reviewed.

Chapter 3 discusses the development of a coupled geomechanical and fluid flow poro-elasto-plastic model for sand production. The fundamentals of sand production is discussed and the sand rate model is developed.

Chapter 4 discusses the calibration of the numerical model using the poly-axial volumetric sand production experiments and the effect of axial and lateral stress anisotropy on sand production.

Chapter 5 presents an offshore field case study based in Middle East. The numerical model is deployed to estimate sand production potential of the wells drilled in this field. The results are compared with the field observation.

Finally, chapter 6 summarizes the conclusions of this research and proposes recommendations for future work.

2. BACKGROUND AND LITERATURE REVIEW

2.1 Fundamentals of Sand Production

Forecasting perforation cavity stability in natural completions (i.e. perforated casing) refers to sand production prediction. Material around the perforation cavity is degraded during well operation. If the seepage force is sufficient to remove the sand grains, sand production occurs. The degradation around the perforation and borehole may occur due to drilling activities, reservoir pressure depletion, high drawdown, and strength weakening effect of water. Since many factors affect sand production, a comprehensive study including various disciplines like geology, rock mechanics, petrophyics, completions and reservoir engineering is required.

Perforation cavity failure may occur in tension or shear, depending on the stress state and flow rate (Morita (1994)). Fig. 2.1 shows perforation cavity failure understood from a perspective of a triaxial test. Application of a small in-situ stress on a cavity is equivalent to small applied load (Point A) on a core plug. The material is deformed but is still in elastic state therefore only high flow rate can cause any disintegration. No plastic zone is created in a cavity. This type of failure gives rise to tensile sand production.

If the in-situ stresses on the perforation cavity increase due to subsequent reservoir depletion, sand may be produced with small flow rates only. Yielding occurs before stress state reaches point C and the material shows ductility behavior. A plastic region is created in the cavity; the core starts to show signs of failure at point C. In this way, shear sand production occurs. When a well is shut-in, stresses on the cavity are released (Point B). Only the elastic strains reverse at this point and there is some permanent deformation set in. Opening up the production will lead to hysteresis. A small flow rate now can dislodge sand particles from the cavity. This may also be termed as tensile type sand production.

When a sheared zone is enlarged significantly after the peak stress (Point C) is reached, the residual strength (Point D) may be able to support the post-failure zone. This region is weak and

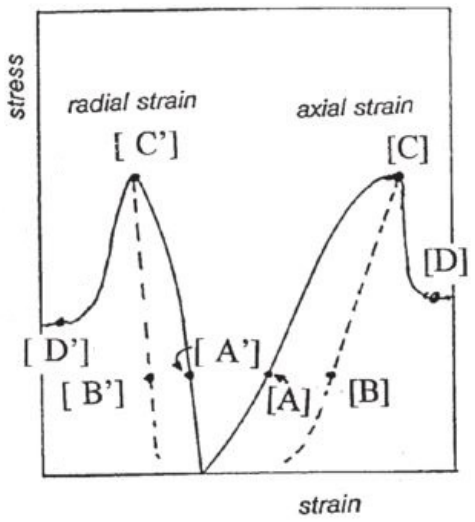

Figure 2.1: Understanding perforation cavity failure mechanics from a triaxial test (after Morita (1994)).

even a small flow rate can erode away this failed part of the cavity. It may be called a tensile type of sand production but to distinguish it from the one occurring at high flow rate, it is called erosion type of failure.

2.2 Challenges due to Sand Production

The production of formation rock material has challenged the oil and gas industry since the drilling of the first well. It is one of the oldest adverse condition affecting well productivity and the operation of surface facilities. Sand production is associated with fluid flow rate and the stress state at the perforation cavity surface. A completion scheme must be designed considering the sand production potential of the formation. The consequences depend much on the severity of the sand rate. With low rates, periodic removal of debris from the surface facilities and subsequent disposal is operable. On the contrary, with high rates, the well may be lost permanently. Penberthy and Shaughnessy (1992) advises to decide on a tolerable limit above which sand control methods would be desirable. The authors observe that usually 0.1% (by volume) of solids production can be termed as excessive. This value depends on many practical factors and therefore should be agreed to during the development of the asset.

Formation solids production can cause operational problems if the quantity is high. Although, periodic removal of sand can ease some of the issues for low rates. Serious damage may occur due to erosion of surface facilities, casing damage and increase in downtime (Penberthy and Shaughnessy (1992)). Erosional effect of sand on surface facilities can turn out to be a major safety hazard if the equipments fail to operate. These events may lead to leakage of hydrocarbon fluids.

On land operations, sand can be easily removed from the surface facilities but special treatment is needed on offshore platforms before disposing off the sand. Produced sand is of no value at all, however it can wreck havoc if produced without anticipation. The erosion of equipments is much more severe in case of high flow rate gas wells. Entire casing string could be subjected to abnormally high loads in case of formation failure and sand production. The well is lost when casing buckles and ultimately fails.

In multi-million dollar wells, operators install downhole sensors and other equipments to collect valuable data. These sensors may malfunction in the presence of fines or simply the solids may hinder the collection of accurate data. Produced fines may be retained in the wellbore due to insufficient drag which, in turn, may cause sand bridging. This process can fill up the tubing and stop the flow altogether. It causes loss of productivity and a wash out must be performed before production can be restored.

2.3 Perforation Cavity Failure Mechanisms

Study of perforation cavity stability requires a mathematical formulation of sand failure mechanism. The mechanisms may act alone or in conjunction for failure to take place. Compressive (shear), tensile or erosion type of failures are regarded as major ones (Veeken et al. (1991)).

2.3.1 Compressive Failure

When the tangential stress (σ_θ) at the cavity wall is high due to reservoir depletion (increase in effective in-situ stresses) or drawdown, compressive failure may occur. Compressive and shear failure terms will be used in this text interchangeably. Due to this failure, sand may be produced at a small flow rate (Morita (1994)). On a stress-strain plot (Fig. 2.1) obtained from a triaxial

test, point C depicts this failure state. An elastic-brittle or an elasto-plastic failure model can be adopted. The elastic-brittle model is easier to implement but is unrealistic (Rahmati et al. (2013)). Furthermore, there are various choices for yield envelopes (e.g. Drucker-Prager, Mohr-Coulomb) and failure criterion (stress or strain based) to choose from (Veeken et al. (1991)). The constitutive models significantly alter the results and hence need to be carefully verified with experimental data.

Shear type of failure is usually seen in the later life of the reservoir (Morita et al. (1998)). Due to reservoir depletion, the effective stresses on the sand particles increase causing crushing of grains. This crushed material can be easily carried away, even by a low fluid flow. Thus, pressure maintenance of the field becomes important to keep shear failure in check.

2.3.2 Tensile Failure

This type of failure occurs when the drag forces due to fluid flow become high, such that the tensile radial stress at the cavity wall exceeds the tensile failure envelope (Veeken et al. (1991)). Application of small stress on a cavity is equivalent to small applied load (Point A in Fig. 2.1) in a triaxial test. The rock deforms but is still in elastic state therefore a high flow rate is required to cause disintegration (Morita (1994)). The stability criterion can be related in terms of normalized pressure gradient at the cavity wall (Morita et al. (1989b)).

$$g_{pn}^{c} = r_c \left(\frac{\partial p}{\partial r} \right)_{r_c} \tag{2.1}$$

The critical drawdown pressure gradient (Eq. 2.1), is the largest possible normalized drawdown pressure gradient without cavity failure; where r and r_c are the radius of investigation and cavity radius respectively. A critical value of g_{pn} was first derived by Bratli and Risnes (1981) for a spherical cavity geometry. Damaged permeability around the cavity greatly affects normalized pressure gradient by increasing it. During shut-in, the plastically deformed material near the cavity wall may develop tensile damage due to unloading of stresses. During start-up of the production the well pressure is lowered, thus the pore pressure gradient at the cavity wall will be significantly

larger until stable conditions prevail (Tronvoll et al. (1992)). The stability criterion is shown in Fig. 2.2 which was first introduced by Morita et al. (1989a). The horizontal axis is normalized pressure gradient at the cavity surface, while the vertical axis is the drop in well pressure. It signifies that at low effective stress state, high flow rate is necessary to begin tensile cavity failure. As reservoir depletes, a low flow rate can dislodge the sand particles from the plasticized region of cavity. Thus shear failure is dominant. These stability envelopes alter after water breakthrough as well

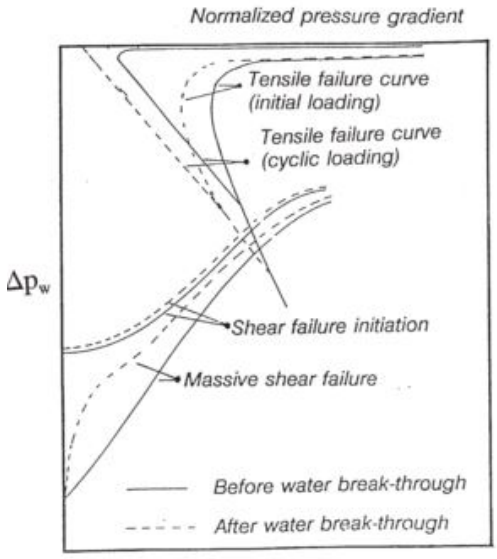

Figure 2.2: Perforation cavity stability envelope (after Morita et al. (1989a)).

after effective stress state change. Therefore these failure envelopes are constructed for various expected reservoir depletion scenarios.

2.3.3 Volumetric Failure

Haimson and Kovacich (2003); Papamichos et al. (2008) observed a slit-like failure zone associated with compaction bands. This type of failure is different than shear or tensile and has been observed in laboratory tests on sandstones with porosity greater than 20 percent (Fjaer et al. (2008)). The failure zone grows from the tip of the initial sheared zone, with failed material taking up less space than before. This failed material may then be washed away with fluid flow and the

slit-like failure zone grows rapidly. Haimson and Kovacich (2003) proposed that the slit length is dependent on the stress contrast. This results in significant sand production in the laboratory. However, field validation of this type of failure is still unclear.

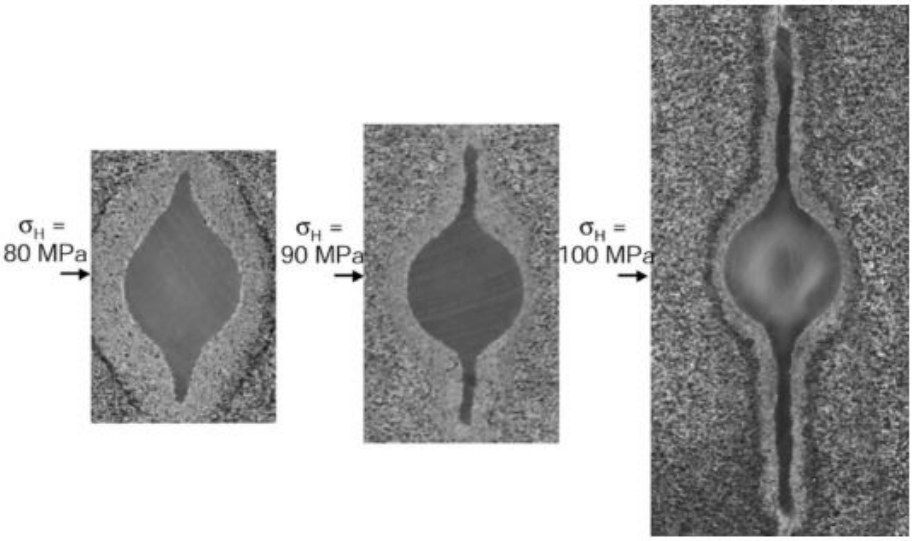

Figure 2.3: Slit-like failure observed by Haimson and Kovacich (2003). Showing dependence on stress contrast

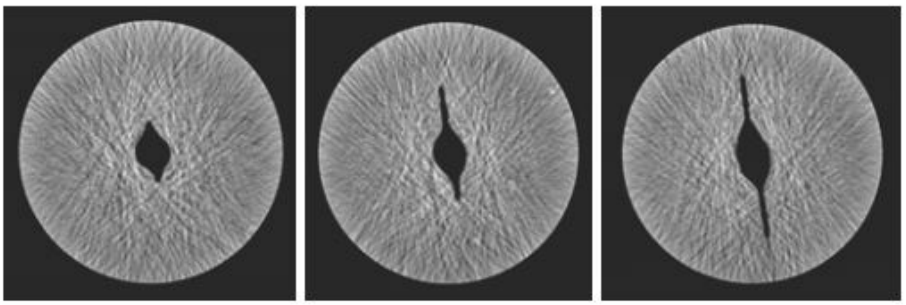

Figure 2.4: Slit-like failure observed by Papamichos et al. (2008).

2.3.4 Erosion Failure

If the fluid flow velocity is high enough to detach sand grains from the cavity surface exceeding the cohesion holding them together, erosion failure occurs. It behaves somewhat like tensile failure but there is a distinction between the two mechanisms; the erosion failure is induced only when a sheared zone has enlarged significantly (Morita (1994)).

2.4 Sand Production Prediction Review

When developing a weak or intermediate strength sandstone oil or gas reservoir, sand production is anticipated. It is required to evaluate the necessity of sand control measures by employing sand production prediction. Research studies have been going on for more than half a century now. Existing prediction techniques can be broadly distinguished into experimental, analytical and numerical. Significant advances have been made in understanding, employing and interpreting their results. A review of experimental and numerical work is presented here.

2.4.1 Experimental Work

Laboratory experiments are generally conducted to study the behavior of sand production in wide-ranging conditions. The physical models are tested by varying one parameter at a time and evaluating its effect.

2.4.1.1 Sand Arching

The first few studies were done to understand the mechanism of failure of rock causing sand production from perforation collapse. During this early period, scientists observed that sand arching was the most important mechanism to explain the strength of perforation cavity. The first of these studies was done by Terzaghi (1936) using a trap door experiment. A box is filled with unconsolidated sand where the bottom consisted of a hole through which sand could drop out. The experiment conducted by Terzaghi (1936) concluded that arching in sand is a stable phenomenon where the loads on sand are transferred to the surroundings.

Hall and Harrisberger (1970) called attention to the trap door experiment (Fig. 2.5) again when they studied the stability of sand arches. In the experiment, a steel cylinder with a central hole is filled with sand and a piston is used to simulate overburden loads. Fluid flow is introduced uniformly below the piston. The flow rate is steadily increased until a small amount of sand is produced suddenly. Further increase in flow rate does not produce sand due to a stable arch formation. It failed at a higher flow rate. An arch is a self-supporting structure spanning an opening. It resolves the vertical stress into horizontal stresses. By this effect, loads on the cavity structure can be transferred partly or wholly beside it. Hall and Harrisberger (1970) investigated the conditions required to form a stable arch over an opening at high stresses. They observed that densely packed sand and cohesiveness are conditions that must be met for arch formation. A critical flow rate is necessary to destabilize the sand arch which may form back at relieved stresses (Fig. 2.6). Since the arch would fail in a step fashion, sand is produced in bursts. Hall and Harrisberger (1970) did not quantify the critical flow rate.

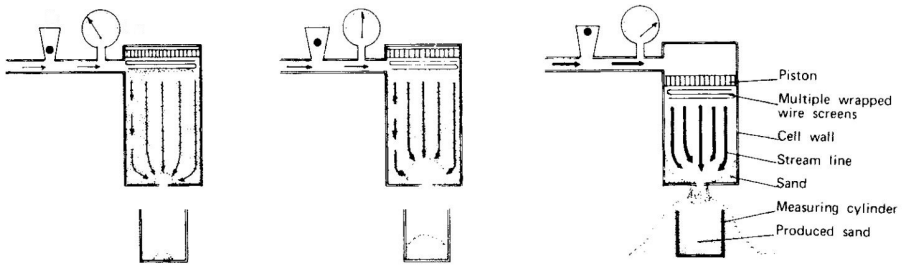

Figure 2.5: Schematic of a trap door experiment (after Bratli and Risnes (1981)).

Bratli and Risnes (1981) developed a theoretical model for the stability of sand arches. The effect of fluid flow was studied along with the criteria describing the stability and failure of sand arches. For the model, they assumed a spherical arch with radial pressures acting on inner and outer faces. Experiments similar to that of trap door were conducted (Fig. 2.5). It was found that the theoretical model is able to explain experimental results qualitatively. A critical flow rate was determined at which the sand arch collapses.

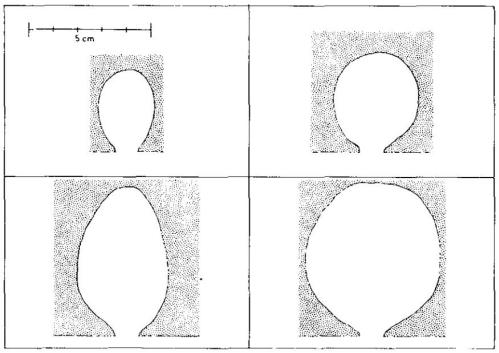

Figure 2.6: Profiles of sand cavity with increasing failure (after Bratli and Risnes (1981)).

Perkins and Weingarten (1988) studied the stability conditions of a spherical cavity in unconsolidated sand and synthetic weakly-cemented rocks. Through experiments, they found that a region of disaggregated material is formed on the cavity surface when confining pressure was applied. Fluid flow seemed to aggravate the shear failure zone. The disaggregated material is at the limit of tensile stability (Fig. 2.7). As the flow rate increases, drag forces on the cavity surface increase. To stabilize, permeability of the failed zone increases by dilation. When porosity reaches a critical value, where the interlocking forces holding sand grains together is insufficient, total collapse occurs.

Bianco and Halleck (2001) conducted experiments to study the effect of wetting phase saturation on the stability of sand arches in weakly consolidated sandstones. They found that within a critical wetting phase saturation solids production is minimal due to stabilization effect of sand arches. Also, no wetting phase presence showed little arch stability and massive sand was produced. Hence, cohesion plays an important role in sand arch stability. On failure, the cavity was filled with dilated, wetting-phase saturated, agglomerated blocks of sand. In field, water cut destroys the cohesion holding the arch stable inducing massive collapse and sand production.

Yim et al. (1994) conducted experiments and developed semi-analytical flow model to analyze the results. The experimental setup was similar to that of a trap door experiment conducted by Hall and Harrisberger (1970). Factors affecting sand arch stability were studied, such as ratio of sand grain size and outlet hole size, grain size distribution and angularity of sand grains. Conceptually,

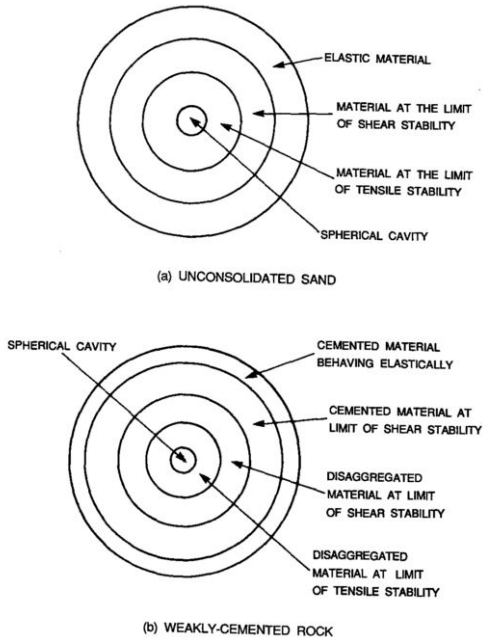

Figure 2.7: Schematic showing various theoretical zones surrounding a spherical cavity in (a) unconsolidated sand, and (b) weakly-cemented rock (after Perkins and Weingarten (1988)).

cavity growth must stop when seepage force drop below arch destabilizing force. Yim et al. (1994) argue that contrary to belief, there are other factors which make arch stability drop as the cavity grows. They observed that mode of pressure application can also trigger sanding. Random large pressure fluctuations near wellbore create an environment for sanding.

Such studies, as mentioned above, prove that sand arching is a real phenomenon which may contribute to perforation cavity stability. Thus, arch stability must be taken into account while estimating sand production.

2.4.1.2 Experiments to Predict Onset of Sand Production

During 1980s, production engineers realized that if rock had a certain minimum strength, perforations were stable and did not produce any sand. Laboratory experiments were conducted at TerraTek, Sintef, Waseda University etc. to clarify the mechanism of small cavity failure. The objective of these experiments were to relate the initiation of perforation failure to the strength of the rock.

Tronvoll (1992) conducted large scale model experiments to investigate the effect of rock stresses and fluid flow on perforation cavity stability. Produced sand was measured at a calibrated sand trap. A cylindrical cavity is used to simulate flow conditions in a perforation (Fig. 2.8). The sample is stressed and fluid is flown. The study observed that disintegrated material was present at the cavity wall beyond failure. When this is spalled off from the cavity wall, the stresses in the vicinity are redistributed as cavity size grows. It was also observed that the outer boundary of the failure zone approaches spherical geometry (Fig. 2.9).

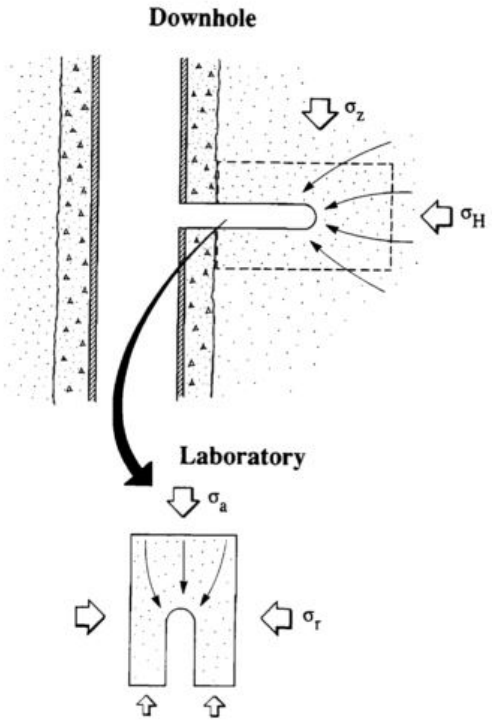

Figure 2.8: Sketch showing simulation of in-situ production condition in a laboratory setting (after Tronvoll (1992)).

Kooijman et al. (1992) conducted large scale laboratory tests to investigate the influence of both effective stress increase and drawdown on sand production. Short bursts of sand occurred (transient) after every drawdown and effective stress increase. Material failure near cavity occurs due to higher stresses and these particles are eroded away with fluid flow. After sometime, the

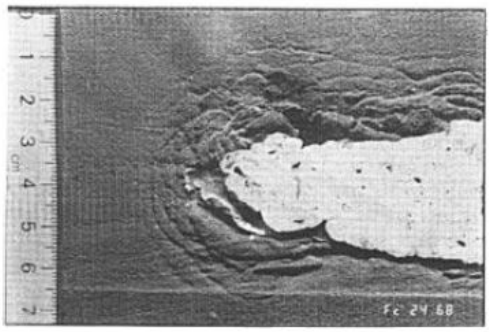

Figure 2.9: Cross-section of cavity showing failure zone approaching spherical geometry (after Tronvoll (1992)).

sand arch becomes stable and further increase in stresses are needed to induce sand production. Kooijman et al. (1992) found massive sand production with water cut. The tests were run on an cylindrical well with multiple perforations on an outcrop rock (Fig. 2.10).

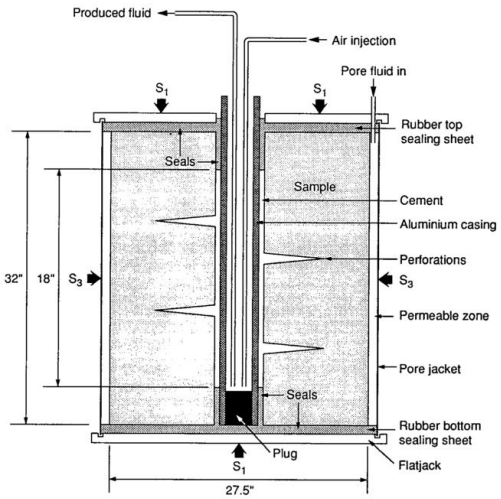

Figure 2.10: Experimental setup for multiple perforation test (after Kooijman et al. (1992)).

Tronvoll et al. (1992) studied sand production from a perforation cavity by conducting laboratory tests and validation using numerical simulations. This was one of the first, in such kind of studies on sand production. It was observed that the perforation cavity was still stable even after

shear failure initiated at the cavity wall. The post failure zone grows with increasing confining stress and is carried away by drag forces due to fluid flow. The outer boundary of the failure zone approached a hemispherical geometry. Thus, the cavity stability was found to be depended on both the initial shear strength of the rock, and on the residual strength and geometry of the failed region.

Thick-walled cylinder test (Antheunis et al. (1976)) has become quite a regular test to evaluate sanding potential of a particular rock material. In these tests, a hollow cylindrical core sample is hydrostatically loaded until collapse. Typical ratio of external to internal cylindrical diameter is 3 with 0.5 in. as internal diameter. The length of the sample is typically 3 in. The sample is loaded in a pressure cell externally and the hollow internal cavity is open to atmospheric pressure. The stress at which the specimen collapses is known as the Thick-Walled Cylinder (TWC) strength. It corresponds to the strength of a perforation cavity.

Several studies (van den Hoek et al. (2000); Willson et al. (2002); Nouri et al. (2006); Papamichos et al. (2000)) have employed TWC in their analyses to measure sand production potential of a formation. Uchida et al. (2014) elaborated on the interpretation of TWC results with respect to perforation stability in the field and introduced an alternative to TWC. Depending on the availability of cores, TWC is estimated for the formation which then helps calculate the onset of sanding. Khaksar et al. (2018) shows a series of new empirical equations to derive TWC from porosity, unconfined compressive strength, log derived properties such as acoustic transit times and dynamic elastic moduli.

2.4.1.3 Cavity Failure Prediction Using Mechanical Logs

It is extremely important to determine accurate strength of rocks for geomechanical application like evaluating sand production potential. Quantitative strength can be determined using core analysis which is subject to the availability of core samples. Coring is expensive and almost always skipped by operators. In this case, porosity-based or sonic log-based rock strength is determined. Many such empirical correlations exist depending on the rock type, depth and field.

The mechanical logs are used to assess the UCS/TWC of the rock material from which onset of sand production is predicted. Khaksar et al. (2009) provides a succinct list of commonly used

correlations to predict UCS and TWC from logs.

2.4.1.4 Volumetric Sand Production Experiments

Conducting volumetric sand production tests for each type of reservoir rock is not only cumbersome but also impractical and expensive. Therefore, numerical sand production prediction models have been developed. However, calibration and validation of these models is dependent on reliable sand production data. The data is made available through either experiments or field measurements. Typical laboratory volumetric sand production tests measure produced sand from loaded hollow cylindrical sample with fluid flow.

Papamichos et al. (2000) conducted volumetric sand production laboratory tests with hollow cylindrical specimens (Fig. 2.12). The purpose of the study was to establish a relation between the sand rate and the applied stresses and fluid flow (Fig. 2.11). The authors observed that sand production is stochastic by nature and thus the sand rate varies a lot with time (also confirmed from the sand arch experiments performed by Hall and Harrisberger (1970); Bratli and Risnes (1981)). Thus, Papamichos et al. (2000) use cumulative produced sand which is simpler to analyze. It was also found that a critical flow rate was necessary to erode away the failed material at the face of the cavity. The failure zone expanded with increased external stress making it easier for fluid flow to erode failed material, thus increasing sand rate. The authors also observe that the sand rate is unaffected by the time period during which no change in stress or flow rate is induced.

van den Hoek et al. (2000) performed an experimental study for the prediction of sand failure around cylindrical and hemispherical cavities in weak sandstones under a variety of stresses and fluid flow conditions. The study used hollow cylindrical samples of friable Castlegate and weakly consolidated Saltwash South outcrop sandstones for conducting tests. The external stresses and fluid flow were varied in such a way that a lot of different loading paths were created. The authors found that cavity failure shows a size effect which decreases with increasing fluid flow. The failure mode: compressive or tensile depends on cavity size and not on near-wellbore stress or drawdown. van den Hoek et al. (2000) observe that failure around cavity will be generally compressive and only for very small cavities tensile failure is induced by fluid flow. In their opinion, the role of fluid

flow is just to remove the failed material debris.

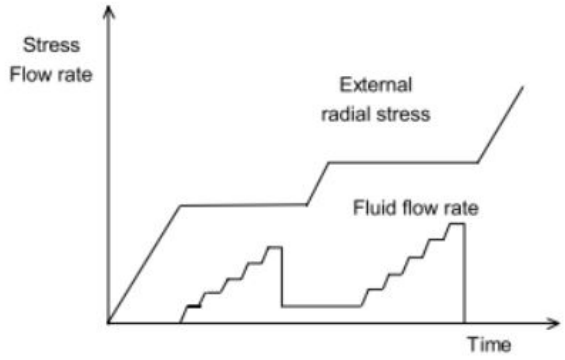

Figure 2.11: Sketch showing variation of external stress and fluid flow to study their effect on sand production (after Papamichos et al. (2010)).

Papamichos et al. (2010) conducted laboratory tests to study the effect of water weakening, capillary cohesion and water breakthrough on sand production. Castlegate, Saltwash South and North outcrop sandstones were used for carrying out the experiments (Fig. 2.12). The result show that volumetric sand production is unaffected by fluid type under one phase flow conditions i.e. it is the same for oil and water. For irreducible water saturation specimens flown with oil, the sand production was found to be much lower. This indicated that capillary cohesion stabilizes failed rock near cavity surface. Water breakthrough instantaneously increase sand production by destroying cohesion. By analyzing the stress at which sand production starts, effect of water on strength of rock was estimated. Presence of water happened to weaken the rock and caused earlier failure.

Rahmati et al. (2012) conducted volumetric physical tests on Saltwash South sandstones. Fluid is flown through the sample exiting from the perforation carrying sand particles with it. Hydrostatic external stress was applied. The produced sand mass is recorded continuously over time. The confining stress and flow rate are varied throughout the experiment. Increased external stress led to higher sand production while decreasing them showed no appreciable sand (Fig. 2.13). The

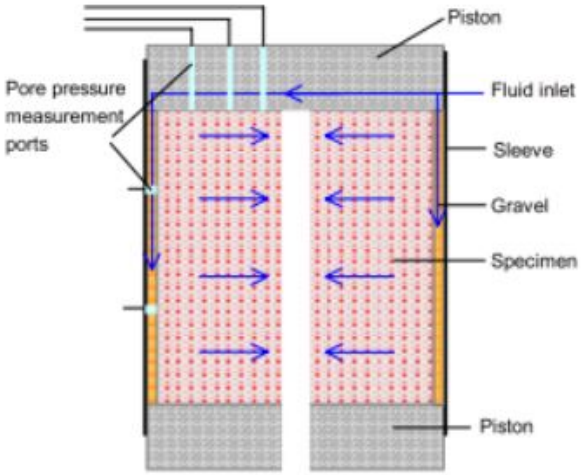

Figure 2.12: Schematic of the laboratory test setup for hollow cylinder specimen (after Papamichos et al. (2010)).

authors compared the laboratory results with numerical simulation.

Fattahpour et al. (2012) studied sand production experimentally by conducting tests on large cylindrical samples. External stresses, fluid flow and produced sand are monitored and recorded continuously. The authors classified sand production as transient, continuous and catastrophic. With change in stress state or flow rate, a transient sand rate is established. When the system stabilizes, continuous sand production is observed. With water cut or with unstable cavity geometry, catastrophic sand production is observed. This is reported in monitored field cases as well. The authors also note that with larger perforations produced sand production increased. Also, higher strength rocks had low failure rates.

Papamichos (2018) argue that extrapolating numerical model calibrated with results of isotropic tests to anisotropic conditions may not be directly valid. The non-uniform failure zones during anisotropic conditions give substantially different sand production. It is theorized that sand onset is lowered due to anisotropy but its effect on sand mass and rate have not been investigated.

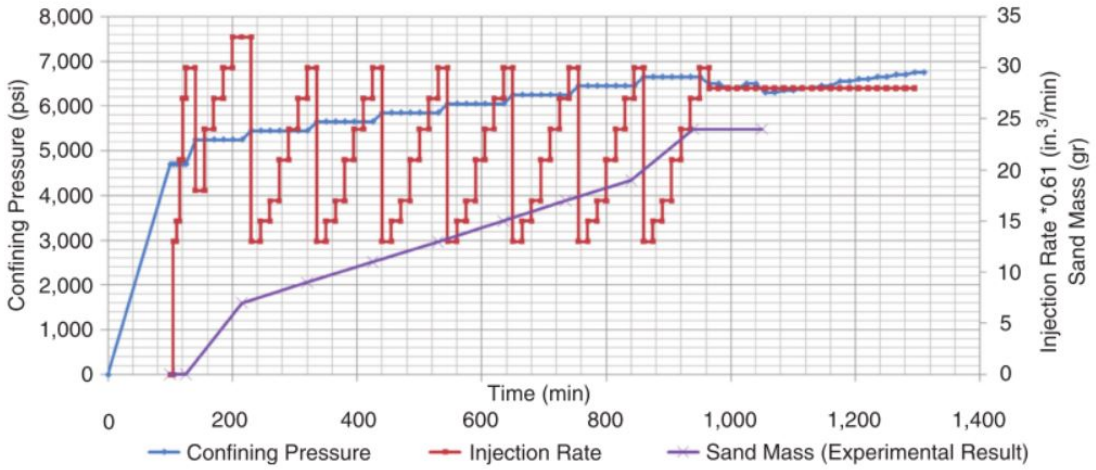

Figure 2.13: Experimental result (after Rahmati et al. (2012)).

2.4.2 Numerical Work

Not all conditions can be simulated in a laboratory. Thus, considerable efforts have been put in to develop numerical models to predict sand production. Routine laboratory tests can only estimate the onset of sand production. To capture the rates and cumulative mass with time, special setups are necessary which are called volumetric sand production prediction experiments. Numerical modeling is the least expensive and most robust method for sand production prediction and hence is the most popular. Sand production is a complex phenomenon which depends on many parameters acting at the same time. Only numerical models have the capability to capture these complex interactions and produce meaningful insights. Furthermore, experimental results can be used to calibrate the model.

The phenomenon of sand production cannot happen in isolation and requires fluid flow to erode perforation cavity surface. Essentially, it requires coupling of geostructural and fluid flow modules. The model can be categorized as using continuum or discontinuum approach.

There can be no crack or discontinuity in the domain when using the continuum approach. Popular methods are finite difference and finite element method. Discontinuous methods like discrete element method require large computational time. The model requires an exact replica of

particle arrangement as in reality. These micro-properties are difficult to estimate. Thus, for sand production prediction, continuum methods are more popular.

Continuum models make various assumptions about constitutive laws, sanding criterion and numerical procedures with different level of complexity to capture the physical behavior of material failure and sand production. Primarily, studies were conducted to estimate the onset of sand production. It allowed the control of operation of a well such that sand production could be delayed. Vardoulakis et al. (1996) proposed hydrodynamic erosion in sandstones causing removal of failed material by applying filtration theory. Later, Papamichos and Stavropoulou (1998) combined the evolution of localized deformation with erosion. The formation of a narrow zone of concentrated plastic deformation (shear bands) is called deformation localization (Sulem et al. (1999)). Since then, many studies used hardening/softening behavior of a sandstone in their models (Papamichos and Malmanger (2001); Vaziri et al. (2002); Nouri et al. (2006, 2007); Vaziri et al. (2008); Detournay (2009); Nouri et al. (2009); Kim et al. (2011)).

Earlier on, an elastic brittle failure was assumed to cause sand production and thus was implemented in models (Nordgren (1977); Coates and Denoo (1981); Risnes et al. (1982); Edwards (1983)). These models underestimate rock's load carrying capacity and caused earlier initiation of sand production. An elasto-plastic material model is more realistic in estimating rock strength and deformation under load (Morita et al. (1989b); Antheunis et al. (1976); Peden and Yassin (1986); Papamichos and Malmanger (2001); Wan and Wang (2004); Servant et al. (2006); Wang et al. (2005, 2006); Detournay (2009); Vaziri et al. (2008); Alireza et al. (2003); Rahmati et al. (2012); Azadbakht et al. (2012)). Mohr-Coulomb yield criterion has been mostly employed by researchers, however some have used Drucker-Prager as well (Chin and Ramos (2002); Wang et al. (2005)). Morita et al. (1989b) used a modified kinematic model with a cap. Vaziri et al. (2002) modified the Mohr-Coulomb model using a bilinear yield envelope to distinguish sand production behavior under low and high confining stresses. Detournay (2009) used compaction mode of failure to account for slit mode of cavity development in high porosity rocks. Haimson (2007) first showed that slit mode of cavity failure is related to localized compressive deformation. It was found that

pore collapse is mostly responsible for slit mode of cavity failure associated with sand production.

There are various choices for using a sanding criterion and they are mainly based on shear and tensile failure, critical pressure gradient, critical drawdown pressure, critical plastic strain or erosion (Rahmati et al. (2013)). Tensile mode of failure is found to be responsible for material removal after degradation of rock. In cemented rocks, shear failure weakens the rock structure. In high porosity sandstone, pore collapse may occur due to reservoir depletion. Weingarten and Perkins (1995) used critical pressure gradient as a sanding criterion. Morita et al. (1989b) proposed a model that can use either shear or tensile failure as onset of sand production. Burton et al. (1998) used critical plastic strain as a failure criterion.

Sand production is a moving boundary problem since produced sand increases the cavity size and alters the cavity shape. Wang et al. (2011); Nouri et al. (2006) used adaptive meshing to capture this phenomenon. Sand particles can coalesce and form a sand bridge in the perforation tunnel. This can considerably lower fluids production from that perforation and also filter out sand production. The current numerical models are incapable of simulating this phenomenon (Rahmati et al. (2013)). Sand production in injector wells may need a different approach and has been studied by Morita et al. (1998); Vaziri et al. (2008). Water cut destroys capillary cohesion between sand particles resulting in massive sand production (Vaziri et al. (2002)). Solution gas flow has been found to destabilize cavity by applying additional seepage forces and increase sand production (Wan and Wang (2004)).

3. DEVELOPMENT OF A PORO-ELASTO-PLASTIC GEOSTRUCTURAL MODEL WITH SINGLE PHASE FLUID FLOW

3.1 Introduction

Sand production is a phenomenon that occurs during hydrocarbon production induced by stress concentration near a wellbore and perforations. If the sand is poorly consolidated, a massive sand production occurs. Even if sandstone is relatively strong, sand production may occur when the effective in-situ stress becomes large due to the reservoir depletion or a high drawdown. For poorly consolidated sand, predictions of on-set of sand production and sand rate are not necessary since these intervals require gravel packing. However, it is essential to predict the onset of sand production and sand rate for medium to hard formation, since unnecessary gravel pack significantly reduce well productivity by fines plugging. Most sandstones are ductile with large plastic deformations if the deviatoric stress becomes high. The effect of hydrocarbon production on the mechanical response of the nearby formation essentially requires coupling of structural deformation and fluid flow models. Most current models assume linear elastic response which overestimates sand onset (earlier onset) and supposedly result in higher sand production. A more realistic approach would be to utilize elasto-plastic material model.

Rocks are generally composite materials, and hence heterogeneous on a microscopic scale. The void space, within rock fabric, which is filled with fluid plays an important role in rock mechanical behavior. The general theory of the mechanics of porous rocks is referred to as "poroelasticity" and was chiefly developed by Biot (1941, 1973). The theory of poroelasticity is fundamentally higher than classical elasticity. Since we are dealing with porous rocks exhibiting plastic behavior, a poro-elasto-plastic model is developed for this study.

For continuum mechanics, a poro-elasto-plastic problem can be solved numerically using the Finite Element Method (FEM). FEM has been widely used in all engineering disciplines with varied problems. FEM is flexible in handling complex material, different geometries and boundary

conditions. Thus, FEM is adopted in this work.

3.2 Mathematical Model

3.2.1 Poro-Elastic Formulation

The behavior of a fluid saturated geological material can be described by the theory and equations of poro-elasto-plasticity. For fluid flow, a transient flow model calculates pore pressure distribution around perforations for a given set of boundary conditions. The processes can be described by these fundamental equations below.

Equation of equilibrium:

$$\sigma_{ij,j} + F_j = 0 \tag{3.1}$$

Strain - displacement equation:

$$\varepsilon_{ij} = \frac{1}{2}\left(\frac{\partial u_i}{\partial x_j} + \frac{\partial u_j}{\partial x_i}\right) \tag{3.2}$$

Stress - strain equation:

$$\varepsilon_{ij} = \frac{1+\nu}{E}\sigma^e_{ij} - \frac{1+\nu}{E}\sigma^e_{kk}\delta_{ij} - \frac{1-2\nu_m}{E_m}p\delta_{ij} + \varepsilon^N_{ij} \tag{3.3}$$

where σ is the stress, ε is the total strain, ε^N_{ij} is the initial non-linear strain, p is pore pressure, δ_{ij} is the Kronecker's delta, ν is the bulk Poisson's ratio, ν_m is the rock matrix Poisson's ratio, E is the Young's modulus and E_m is the Young's modulus for rock matrix.

For fluid flow through porous media, below equations are used.

$$\nabla[\rho u] = -\frac{\partial(\rho\phi)}{\partial t} - q \tag{3.4}$$

$$u = -\frac{k}{\mu}\beta\nabla p \tag{3.5}$$

where ρ is the fluid density, u is the flow velocity, ϕ is the porosity, q is the flow mass rate, k is the

permeablity, μ is the viscosity and β is the non-Darcy coefficient.

Tensile stresses and strains are assumed to be positive while pore pressures are positive in compression. The above two sets of governing equations can be discretized and coupled to solve for fluid pressure and displacement for a single phase poro-elastic formation.

3.2.2 Poro-Elasto-Plastic Formulation

Elasto-plastic behavior is characterized by an initial elastic response on to which plastic deformation is superimposed after a certain level of stress has been reached. Plastic deformatoin is irreversible in nature. The onset of plasticity is governed by a yield criterion which evaluates the stress at which yielding occurs. Post-yield deformation generally occurs at a reduced stiffness.

For one-dimensional problem, Fig. 3.1 shows an ideal stress-strain curve for a material. It shows that the material initially deforms elastically till the yield stress. On loading further, the material assumes linear strain-hardening with a tangent modulus. The total strain on application of further load can be separated into elastic and plastic strains as

$$d\varepsilon = d\varepsilon^e + d\varepsilon^p \tag{3.6}$$

where ε^e is the elastic and ε^p is the plastic strain.

Thus, for a complete elasto-plastic theory we need a stress-strain relation before the onset of plastic deformation, a yield criterion which gives the stress at which plasticity starts and a post-yield stress-strain relationship.

This study uses a linear stress-strain relationship before yielding which includes initial non-linearity. For yielding, Drucker-Prager yield criterion (Drucker and Prager (1952)) is used since it fits well to relatively consolidated sandstones. It is an approximation to the Mohr-Coulomb law as a modification of Von-Mises yield criterion.

$$\alpha J_1 + \sqrt{J_2'} = k' \tag{3.7}$$

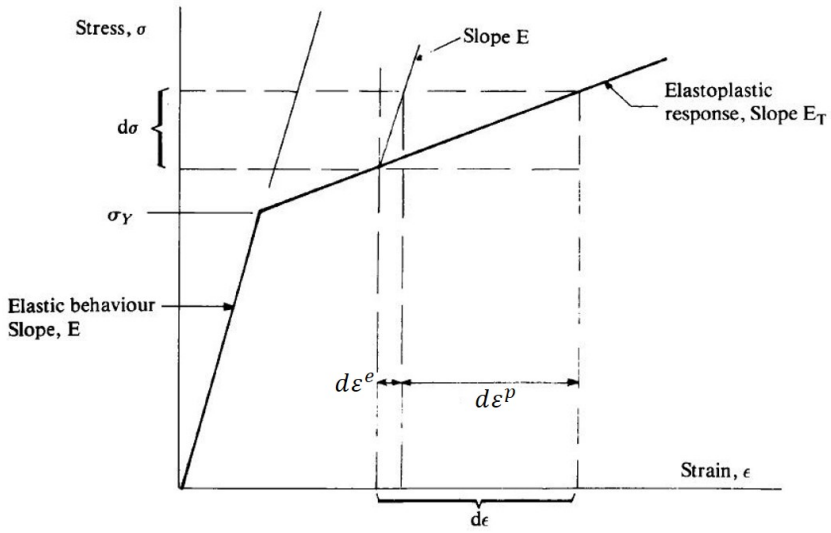

Figure 3.1: Simple elastic, linear strain hardening stress-strain behavior for uniaxial compression case (after Owen and Hinton (1980)).

where $\alpha = \frac{2\sin(\phi)}{\sqrt{3(3-\sin(\phi))}}$, $k' = \frac{6c\cos(\phi)}{\sqrt{3(3-\sin(\phi))}}$, c is cohesion and ϕ is the angle of internal friction.

In the model, Drucker-Prager yield criterion uses the octahedral shear stress and the mean stress (Eq. 3.8). The octahedral shear stress is the deviation from the hydrostatic stress. It is also proportional to the shear strain energy.

$$\tau_{oct} = f(\sigma_m) \tag{3.8}$$

where $\tau_{oct} = \sqrt{(2J_2'/3)}$ is the octahedral shear stress and σ_m is the mean stress, J_2' is the second deviatoric stress invariant.

The yield surface has the form of a circular cone as shown in Fig. 3.2. The yield criterion is expressed in terms of stress invariants as below.

$$J_1 = \sigma_{ii} \tag{3.9}$$

$$J_2 = \frac{1}{2}\sigma_{ij}\sigma_{ij} \tag{3.10}$$

$$J_3 = \frac{1}{3}\sigma_{ij}\sigma_{jk}\sigma_{ki} \tag{3.11}$$

$$J_2' = \frac{1}{2}\left(\sigma_{ij} - \frac{1}{3}\delta_{ij}\sigma_{kk}\right)\left(\sigma_{ij} - \frac{1}{3}\delta_{ij}\sigma_{kk}\right) \tag{3.12}$$

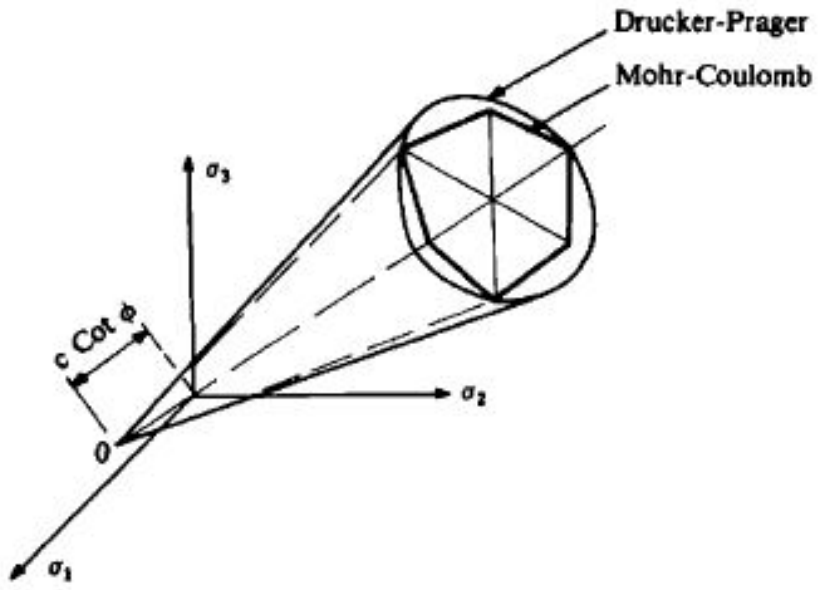

Figure 3.2: Geometrical representation of Drucker-Prager and Mohr-Coulomb yield criterion in principal stress space (after Owen and Hinton (1980)).

After yielding, the relationship between stress and strain is given by strain hardening. The material behavior will be partly elastic and partly plastic. The elastic strain component is related to stress increment using Eq. 3.3.

The yield surface varies at each stage of plastic deformation, with subsequent yield surfaces being dependent on the plastic strains. The stress-strain relationship of elasto-plastic problems are determined by the flow rule which assumes that the direction of total strain increment is proportional to the deviatoric stress. To determine the plastic strain component, it is assumed that the flow direction is perpendicular to the yield surface (f). Hence, the flow direction can be determined if the yield surface is given. This assumption simplifies rock testing procedure to determine the plastic flow direction.

The flow direction is determined by Eq. 3.13.

$$d\varepsilon_{ij}^{p} = d\lambda \frac{\partial f}{\partial \sigma_{ij}^{e}} \tag{3.13}$$

where $d\lambda$ is a proportionality constant termed as plastic multiplier and f is the yield function.

Suppose stresses are incremented along the yield surface, or $f(\sigma_{ij}^{e}) = constant$, then for any $d\sigma_{ij}^{e}$

$$df = \frac{\partial f}{\partial \sigma_{ij}^{e}} d\sigma_{ij}^{e} = 0 \tag{3.14}$$

Eq. 3.14 is termed as a normality condition since it implies that $\partial f / \partial \sigma_{ij}^{e}$ is a vector directed normal to the yield surface at the stress point under consideration. Suppose a yield surface like Eq. 3.15 is selected,

$$f = \sqrt{S_{ij} S_{ij}} - g(J_1) \tag{3.15}$$

where $S_{ij} = \sigma_{ij} - \sigma_m \delta_{ij}$ is the deviatoric stress, then

$$\frac{\partial f}{\partial \sigma_{ij}^{e}} = \frac{S_{ij}}{\sqrt{S_{ij} S_{ij}}} - g' \delta_{ij} \tag{3.16}$$

Hence, if g' = 0

$$d\varepsilon_{ij}^{p} = d\lambda \frac{S_{ij}}{\sqrt{S_{ij} S_{ij}}} \tag{3.17}$$

Eq. 3.17 is known as the Prandtl-Reuss equation which is a general flow rule.

As plastic flow progresses, hardening is induced with the growth of plastic strain. The process is called the strain hardening and the controlling parameter is given by the magnitude of the plastic strain as in Eq. 3.18.

$$\varepsilon^{p} = \int \sqrt{\frac{2}{3} d\varepsilon_{ij}^{p} d\varepsilon_{ij}^{p}} \tag{3.18}$$

In the model, the yield surface for inelastic region is implemented as

$$F(\sigma, \kappa) = \sqrt{J_2} + G(J_1) - \left[S_o^{y} + \int exp(B_1 + B_2 \kappa + B_3 \kappa^2 + ...) d\kappa \right] \tag{3.19}$$

where κ is the hardening parameter ε^p in case of strain hardening, $G(J_1) = A_0 + A_1 J_1 + A_2 J_1^2 + ...$, S_o^y, A_0, A_1, A_2... B_1, B_2, B_3... need to be determined from triaxial test results. S_o^y = 0 for Drucker-Prager yield criterion. From fitting a polynomial function to $\sqrt{J_2}$ vs J_1, A_0, A_1, A_2... are determined. B_1, B_2, B_3... are determined from curve fitting $\sqrt{J_2}$ + $G(J_1)$ vs κ.

When plasticity is taken into account, the constitutive law for stress-strain relation is different but the fluid flow equation is the same. As plastic deformation is dependent on the loading path, it is necessary to take incremental stress-strain relation into account. The incremental form of elasto-plastic stress-strain relation is given by

$$d\sigma = D_{ep} d\varepsilon \tag{3.20}$$

where D_{ep} is the elasto-plastic stress-strain matrix.

Following Owen and Hinton (1980), D_{ep} is given by

$$D_{ep} = D - \frac{D\frac{\partial f}{\partial \sigma}\left(D\frac{\partial f}{\partial \sigma}\right)^T}{H'\sqrt{\frac{2}{3}\left(\frac{\partial f}{\partial \sigma}\right)^T\left(\frac{\partial f}{\partial \sigma}\right)} + \left(\frac{\partial f}{\partial \sigma}\right)^T D\left(\frac{\partial f}{\partial \sigma}\right)} \tag{3.21}$$

where D is the usual matrix of elastic constants considering initial non-linearity,

$f = \sqrt{J_2} + G(J_1)$ and $H(\kappa) = S_o^y + \int exp(B_1 + B_2\kappa + B_3\kappa^2 + ...)d\kappa$.

Eq. 3.3 can be rewritten as

$$\varepsilon_{ij} = \frac{1+\nu}{E}\sigma_{ij}^e - \frac{1+\nu}{E}\sigma_{kk}^e\delta_{ij} - \frac{1-2\nu_m}{E_m}p\delta_{ij} + \varepsilon_{ij}^N + \varepsilon_{ij}^p \tag{3.22}$$

where ε_{ij}^p is the plastic strain.

Thus, fluid flow and geostructural models are sequentially coupled to solve for fluid pressure and nodal displacements.

3.3 Finite Element Implementation

One of the most effective ways to solve a complex problem is to divide it into a number of easily solvable sub-problems and then combine all the solutions. FEM approaches a problem in a similar fashion by dividing the realistic type of continuous problem into finite number of individual components also knows as 'elements'. The discretization method finds an approximate solution which approaches the true solution.

A set of governing mathematical equations and boundary conditions is called a strong form of the problem. These equations relate the various knowns and unknowns in the real problem. To derive finite element equations, the strong form of the problem needs to be converted to the integral form known as the weak form. The principle of virtual work is used to derive the weak form which is extremely convenient and powerful. The weak form is valid for non-linear as well as linear stress-strain relations. For more details, please refer to Zienkiewicz et al. (2013).

In structural analysis, the weak form can be written as:

$$\int_{\Omega} B^T D B d\Omega[u^e] = \int_{\Gamma} N^T t d\Gamma + \int_{\Omega} B^T D \varepsilon^o d\Omega + \int_{\Omega} B^T D \sigma^o d\Omega + \int_{\Omega} B^T D H_p d\Omega \tag{3.23}$$

where the L.H.S term contains the stiffness matrix; and in R.H.S, the first term is the boundary load, the second term is the body force due to residual strain, the third term is the body force due to residual stress and the fourth term is the body force due to pore pressure. D is the elasto-plastic matrix relating stresses and strains.

For fluid flow, the principle of virtual work gives

$$\int_{\Omega} (\nabla N)^T T (\nabla N) d\Omega[P^{n+1}] - \frac{C(P^n)}{\Delta T} \int_{\Omega} N^T N d\Omega[P^{n+1}] = -\frac{C(P^n)}{\Delta T} \int_{\Omega} N^T N d\Omega[P^n] - \int_{\Gamma} N^T q d\Gamma \tag{3.24}$$

where N is the shape function, T is the transmissibility, C is the compressibility, P is the pressure and q is the flow rate.

These weak forms are derived using virtual work principle. It states that for arbitrary virtual

displacement, if the internal and external work becomes stationary, the structure attains equilibrium.

3.4 Sand Rate Model

The mechanism of sand production involves coupling of two phenomenon: (1) the mechanical instability and degradation around the wellbore and perforation and (2) the hydromechanical instability due to flow induced pressure gradient on the decemented material around the cavity. It is a complex phenomenon depending on many parameters related to stress fields, material properties and the completion type. All these parameters interact with each other making the problem highly non-linear. There have been many attempts to solve this problem and these models were discussed in the previous chapter.

Numerical methods so far developed have several limitations. Most of the models assume only one failure mechanism which may not be sufficient and cannot be applied to field cases. The models assume simple geometries and boundary conditions which may be sufficient to investigate the effect of a single parameter. Real well geometries are complex with multiple perforations. Most of the models simply assume elastic brittle failure mechanism which is easy to implement but overestimates sanding onset. Most of the models are made for estimating onset of sand production. In many cases, volumetric sand rates are low enough to not employ any sand control methods. For these cases, estimation of sand production rates are also important. However, sand production is a moving boundary problem and only a couple of studies have tackled this problem using adaptive meshing (Rahmati et al. (2013)). The model created in this study aims to fill all the above gaps.

The numerical model deployed to estimate sand production rates continues the calculations even after failure occurs predicting onset of sand production. With new technologies, the surface facilities are equipped to handle some sand production with regular removal of the debris. This tolerable limit is specific to a project and varies on the composition of fluid produced as well. For example, sand production in gas wells is very harmful to the well and facilities due to excessive erosion and generally has very low tolerable limit as compared to oil wells. Deciding a tolerable limit is a multidisciplinary activity and depends on many factors as discussed. If the sand

production rates are within the tolerable limits for considerable amount of time after onset, the completions team may decide to postpone any sand control activity. This results in operation expenses savings as well as increased productivity. This relationship motivated the study to estimate sand production.

There are various moving parts of this model and they will be explained in the following subsections.

3.4.1 Geomechanical Model

FEM modeling is used to calculate displacements in the domain due to application of various loads. The domain is divided into finite number of elements and nodal displacements are calculated which can be interpolated within the elements using shape functions. The geomechanical simulator is built in-house and is capable of handling a poro-elasto-plastic deformation in 3D. There are four types of loading considered:

- In-situ stresses with drilling overbalance are applied first;
- Release overbalance from perforation surface for oil and gas production;
- Effective stresses are increased due to depletion and;
- Total drawdown loads are applied in the end.

All these loads are applied incrementally. Since the non-linear stress state depends upon loading history, several iterations are required to converge onto a solution for each increment of load. The failure can be triggered by either shear or tensile failure mechanism. Boundary conditions can be prescribed at the borehole as well as far field.

3.4.2 Fluid Flow Model

FEM modeling was done to simulate transient fluid flow conditions for a single phase oil reservoir. FEM divides the domain of interest into finite number of elements in which approximate solution is obtained using governing equations. A set of boundary conditions are prescribed in the

domain along with the fluid and flow properties. The model calculates the pore pressure distribution in the domain as well as flow rate in each element. Non-Darcy flow was assumed to simulate the flow realistically because a high flow are often induces a high pressure gradient around the cavity.

3.4.2.1 Fluid Flow Model Validation

For validation of the numerical flow model, open-hole flow rate is compared with the analytical solution. For radial flow, the steady state solution for a single phase (oil) flow is given by

$$p_e - p_{wf} = \frac{q\mu}{2\pi kh} \ln\left(\frac{r_e}{r_w}\right) \tag{3.25}$$

where p_e and p_{wf} are the pressures at the boundary and bottomhole respectively, q is the flow rate, μ is the viscosity, k is the permeability, h is the net pay, r_e and r_w are the radii of the boundary and well respectively.

The data for analytical solution is listed in the Table 3.1. The well spacing is assumed to be 40 acre.

Steady state radial solution data	
Boundary radius (r_e)	1,320 ft
Well radius (r_w)	4.25 in
Fluid density (ρ_o)	0.75 gm/cc
Viscosity (μ)	1.4 cp
Boundary pressure (p_e)	1,000 psi
Bottomhole pressure (p_{wf})	0 psi
Permeability (k)	0.1 Darcy
Net pay thickness (h)	21 in

Table 3.1: Data used for fluid flow model validation using steady state radial flow analytical solution.

The flow calculations in the numerical model are done in Darcy units hence the sand face flow rate from the analytical solution is calculated as

$$q = \frac{2\pi kh}{\mu}\frac{p_e - p_{wf}}{\ln(r_e/r_w)} = \frac{2\pi(0.1)(53.34)}{(1.4)}\frac{(68.046-0)}{\ln(1320/0.354167)} = 198.087\ cc/sec$$

The numerical flow model for a borehole without any damage, with external radial boundary at 1,320 ft gives sand face rate as 199.46 cc/sec. The error is about 0.7%.

3.4.3 Coupled Model

As has been stated before, sand production phenomenon is a coupled process of deformation occurring around the perforation cavity due to various forces and the change in flow conditions due to formation failure. The setup of the model is such that the fluid flow and mechanical behavior are sequentially coupled. The coupling mechanism is through pore pressure and mechanical effect on porosity and permeability. Sand production is a phenomena which will happen during oil and gas production. Knowing this and that oil and gas compressibility are much higher than that of rock compressibility, fixed strain method is used for coupling fluid flow and mechanical behavior.

The basic structure of the program is similar for geomechanical as well as fluid flow modules. The geomechanical module is capable of handling poro-elasto-plastic deformation of material in 3D. The flow module is a transient fluid flow model which calculates pore pressure distribution in the domain. Both the modules use the same mesh. The fundamental structure is presented in Fig. 3.3. For sequential coupling, transient fluid flow model and geostructural model are controlled from the main body of the program. As the structure of the program shows, all the global variables are defined in the main program as well as the input files are read. The mesh geometry of the domain, element and nodal configuration as well as their sizes and positions are the same for flow and geomechanical modules. It is not essential but certainly makes the data flow easier between the two modules.

In the initial part of the program, in-situ stresses and overbalance stresses are applied in the domain. As sand production problem accompanies fluid flow, these loads are applied before coupling starts. These loads change stress state in the domain and may cause perforation failure if the

material is very weak. Loads are applied incrementally in steps and the solution is converged to by iterating.

Sequential coupling now begins with the start of transient flow model calculating pore pressure distribution in the domain for a set of boundary conditions. A constant pressure or flow boundary can be provided as an input to the flow code. Pore pressures are calculated for pre-determined time of production and then used as an input in geomechanical module. Reservoir depletion and drawdown loads are applied to calculate new stress state and deformation. These loads are also applied in incremental steps with iterations to converge to a solution. Reservoir depletion changes the effective in-situ stresses around the perforations enhancing their instability because of higher stress concentration.

3.4.4 Rock Properties Modeling

A constitutive law describes the deformation of the rock material as a response to the stress applied and is expressed as the stress-strain relationship. Historically, numerous laboratory triaxial test results have established a complex relationship between applied stresses and strains. The relationship often depends on microscopic properties of the material, in-situ depth of the material, confining pressure, pore pressure, temperature, anisotropy and grain size distribution. Rock exhibits volumetric expansion and contraction and also increased rigidity as the hydrostatic pressure increase.

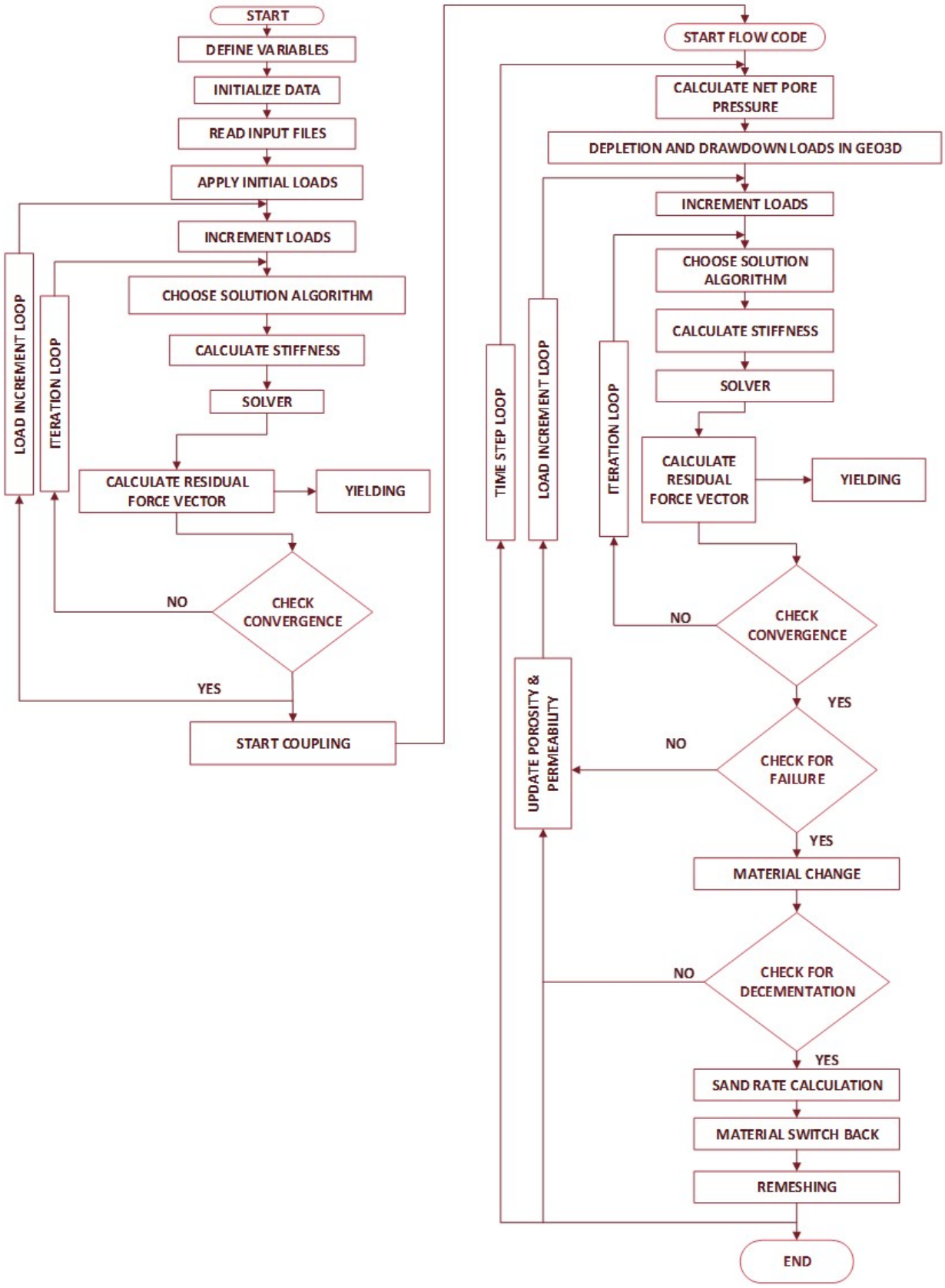

Figure 3.3: Structure of the coupled finite element computer program coded for the calculation of sand rate.

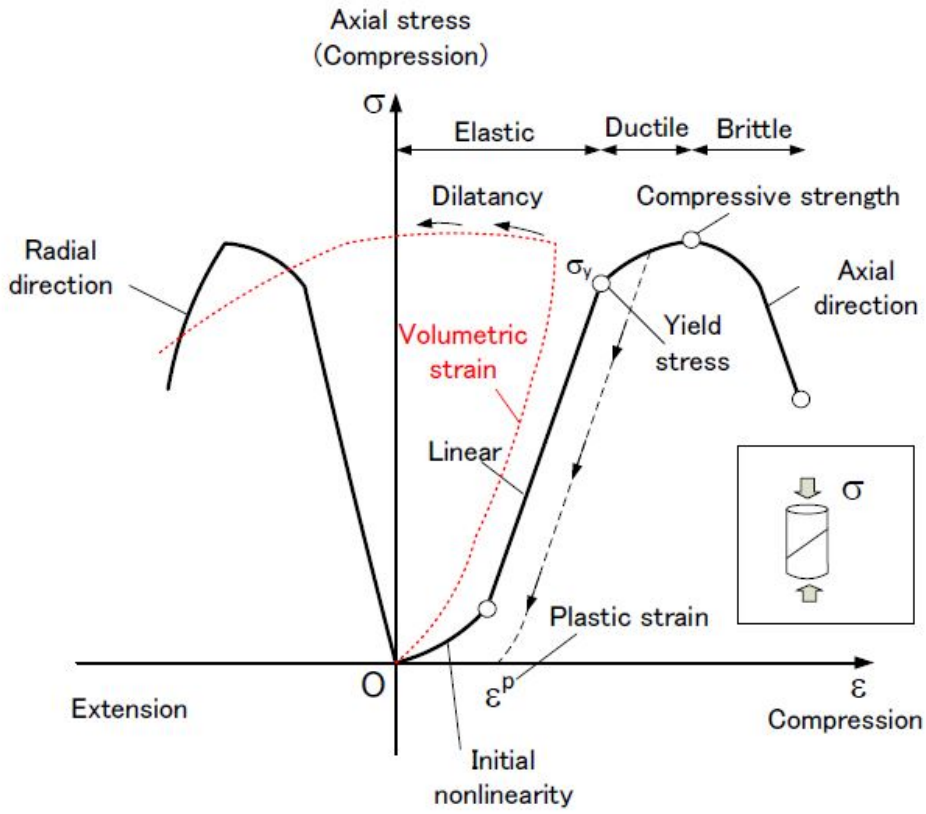

Figure 3.4: Structure of the coupled finite element computer program coded for the calculation of sand rate.

Simple constitutive relations may be useful for analytical studies but for the development of numerical discretization techniques like FEM, a robust equation is necessary. Morita and Gray (1980) developed a non-linear constitutive formulation which closely simulates the behavior of rocks with pore pressure. The technique is used in this study as well. The relationship is composed of four separate parts: an initial non-linear region, an elastic region, a plastic region, and volume change of the rock matrix due to fluid pressure. All these parts are depicted in Fig. 3.4.

The initial non-linear region appears for small loads in both compression and extension tests due to closing and opening of micro-cracks. Fig. 3.5 depicts the initial non-linear strain due to

closing of mode I cracks. The strains are a function of principal stresses as

$$\begin{aligned} \varepsilon_{11}^{N} &= a_1 \left(1 - e^{\beta_1 \sigma'_{11}}\right) \\ \varepsilon_{22}^{N} &= a_2 \left(1 - e^{\beta_2 \sigma'_{22}}\right) \\ \varepsilon_{33}^{N} &= a_3 \left(1 - e^{\beta_3 \sigma'_{33}}\right) \end{aligned} \tag{3.26}$$

where a_1, a_2 and a_3 are determined from stress-strain plots as in Fig. 3.5. The parameter β_i is determined from the slope of the semi-log plot $\frac{a_i - \varepsilon_i}{a_i}$ vs stress.

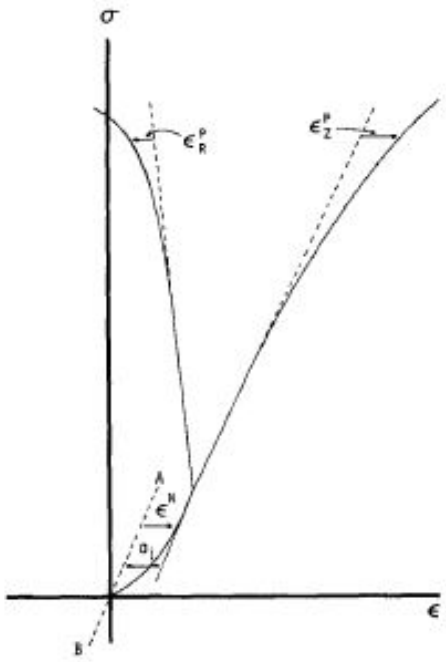

Figure 3.5: Schematic of initial and final non-linearity (after Morita and Gray (1980)).

In the elastic region, rock deforms linearly and on unloading, is assumed to return to its original state. Young's modulus (E) and Poisson's ratio (ν) are determined for each of the triaxial test results and the average value is used for analysis. The yield stress is picked at the end of the elastic region.

At the yield point, rock will start deforming permanently and plasticity kicks in. The rock further deforms in the ductile region without losing its capacity to bear load. Eq. 3.19 is the equation for the yield surface representing volume expansion. Drucker-Prager yield criterion fits intermediate to hard rocks relatively well hence we employ it in our analysis. S_o^y = 0 for Drucker-Prager yield criterion. From fitting a polynomial function to $\sqrt{J_2}$ vs J_1, A_0, A_1, A_2... are determined. B_1, B_2, B_3... are determined from curve fitting $\sqrt{J_2}$ + $G(J_1)$ vs ε^p.

Increasing stresses further will fail the specimen. At this point, equivalent plastic strain (ε^p) is picked for each of the triaxial tests.

With this exercise, mathematical constitutive law relating stresses and strains are determined. The loading path for the triaxial tests that are used to form these relations should be decided bearing in mind existing field conditions.

3.4.5 Failure Criterion

A failure criterion is defined as the relationship defining the stress or strain level at which failure occurs. A failure mechanism is incorporated in a numerical technique so as to inform the modeler of the load capacity of the rock. Without which the rock will have infinite capacity to bear loads. A stress based failure criterion fails the rock material when a predefined stress state is reached for one or more elements. On the other hand, a strain based failure criterion fails the rock when a predefined strain is attained.

Rahmati et al. (2013) lists several failure mechanisms used in different studies such as shear and tensile failure, critical pressure gradient, critical drawdown pressure, critical plastic strain and erosion criteria. Antheunis et al. (1976) discussed that for brittle material elastic limit, in the form of a relationship between principal stresses, can be used as a failure criterion. However, for friable sandstones elastic limit is easily surpassed and the material flows (Fig. 3.6). Sandstones show ductile behavior in which they are able to endure a certain amount of permanent strain without collapsing.

Depending on the initial stress anisotropy, increase in effective stresses due to reservoir depletion and drawdown, plastic zones are created in the perforations. Unlike in brittle rock failure

where the material loses its strength and crumbles at a stress state, plastic rock flows with little changes in stress state. The induction of plastic behavior in the vicinity of perforations makes it difficult to judge failure based on stress level. Antheunis et al. (1976) found that a perforation fails when equivalent plastic strain exceeds a certain critical value. An important conclusion drawn by their study is that critical plastic strain failure criterion is independent of the hardness of the rock material. Thus, a strain-based failure criterion is employed in this work. For weak sandstone, the magnitude of plastic strain has a good correlation with failure occurrence hence, in this study, critical plastic strain failure criterion is used. Fig. 3.7 shows the strains in an elasto-plastic material in one dimension. For a 3D problem, a scalar quantity is calculated known as equivalent plastic strain given by the Eq. 3.27.

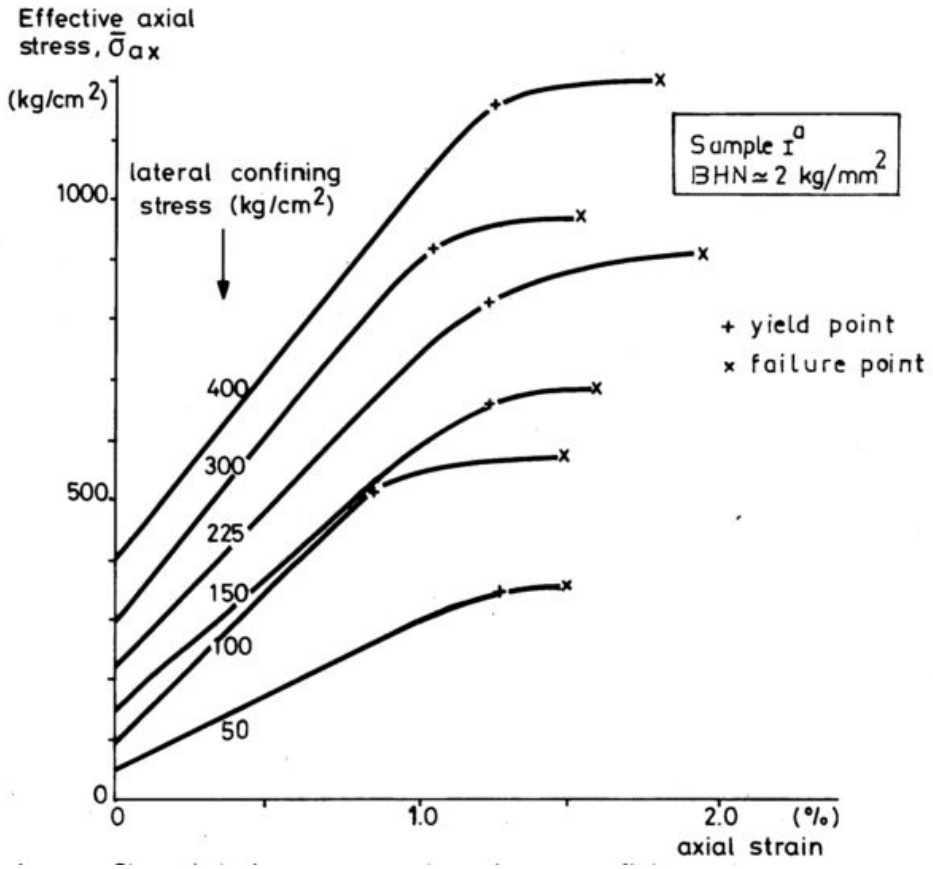

Figure 3.6: Stress-strain relation of a sandstone showing ductile flow after yielding at various confining pressures after initial hydrostatic preloading (after Antheunis et al. (1976)).

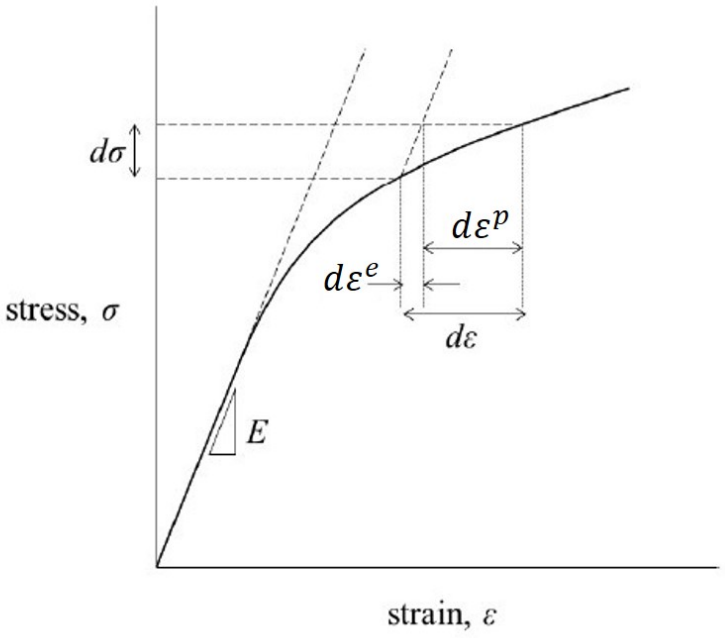

Figure 3.7: Stress-strain curve in one dimension depicting elastic and plastic strains (after Owen and Hinton (1980)).

$$\varepsilon^p = \int \sqrt{\frac{2}{3} d\varepsilon_{ij}^p d\varepsilon_{ij}^p} = \int \sqrt{\frac{2}{3}(d\varepsilon_z^p + 2d\varepsilon_r^p)} \tag{3.27}$$

A value of critical plastic strain is obtained from performing triaxial experiments where it is picked right after the end of ductile region. The failure occurs when equivalent plastic strain exceeds critical plastic strain value.

3.4.6 Material Property Change

Several experimental studies like Hall and Harrisberger (1970) and Bratli and Risnes (1981) have studied stability of sand arches under stresses and fluid flow. These studies report that failed material contains a large proportion of crushed grains which is essentially a different material. In the numerical model, a material change module (Fig. 3.3) is implemented which is triggered due to failure. With each increment in loads, all the failed material achieves its residual strength.

It is assumed that failed zone reduces its strength to that of poorly consolidated sand. Although triaxial experiments show considerable residual strength, this assumption leads to conservative estimates. This residual strength may keep cavity intact in spite of failure initiation depending on the geometry of the failure zone.

3.4.7 Erosion Criterion

At lower stress state, high fluid flow rate is required to disintegrate the formation which is known as tensile type failure. On the contrary, at a high stress state low flow rates can induce shear type of failure. Tensile type of failures are common in short perforation lengths with low perforation density owing to high flow rates. However, with recent advancements of high density perforation guns with effectively longer perforation low flow rates are observed in each perforation providing less chance of tensile type of failure (Morita (1994)). Hence, the main focus of this study is shear type of failure. Plastic strain is used for a shear type of failure condition because it can occur owing to large plastic deformation even if the stress state is not critical.

After plastic failure of material around the cavity there exists residual strength in the failure zone which supports itself. This postfailure zone may form stable cavity arches which may strengthen the formation and lower the sand production rate. Sand arches are able to transfer the axial loads w.r.t the sand arch to horizontal loads. Additional forces are necessary to overcome the arch strength either by increase in fluid flow rate or by increase in effective stresses. Laboratory volumetric sand flow experiments (Papamichos et al. (2000)) have shown the effect of fluid flow rate on sand production. Failed rock material is not instantly produced and requires certain hydrodynamic force to disintegrate the granular material. This force overcomes the sand arch strength and the cohesion due to capillary forces. Thus, a critical flow rate is required to dislodge these grains from the failed part of the cavity.

Combining the sand arch stability theories of Clearly et al. (1979), Bratli and Risnes (1981) and Morita et al. (1989b), Morita et al. (2006) developed a post-failure model applicable to both unconsolidated and intermediate strength formations. Experiments were conducted to measure arch strength under various conditions observed in the field. It was observed that the mechanical

strength of unconsolidated sand arch depends on the ratio of sand grain size and radius of curvature of the arch. The sand arch also has strength contributed by the capillary pressure effect. For low flow rate wells, as long as there is no water cut the capillary pressure effect is sufficient to suppress sand production. As the flow rate increases, hydrodynamic forces on the arch increases turning the effective radial stresses tensile. Thus, at a critical flow rate tensile failure occurs which may also be called erosion failure since the flow at the cavity surface is non-uniform due to heterogeneity of the material.

There are two parts that add up to produce the critical flow rate. First, capillary pressure and second, the dependence on grain size distribution. For the development of an analytical solution matching the experimental results Morita et al. (2006) assumed a hemispherical cavity surface with a linear Mohr-Coulomb yield envelope, a perfectly plastic material in post-failure zone and critical plastic strain failure criterion. The first part is given by Eq. 3.28

$$q_c = \frac{0.59kR}{\mu}\left[\frac{c_{correction}\bar{p_c}\beta_f}{2\pi R^2}\right] \tag{3.28}$$

where q_c is the critical flow rate in bbl/day/sq.in, k is permeability in Darcy, R is the sand arch radius in ft, μ is viscosity in cp, $\bar{p_c}$ is $\phi S_w p_{capillary}$ which comes out to be 0.384, $c_{correction}$ is the correction factor for limited flow area due to heterogeneity and is 0.14, β_f is $2\tan^2(\phi_f + \pi/2)$ with ϕ_f equal to 30°.

Empirical relationship between critical flow rate and the grain size distribution is shown by Fig. 3.8 and given by Eq. 3.29.

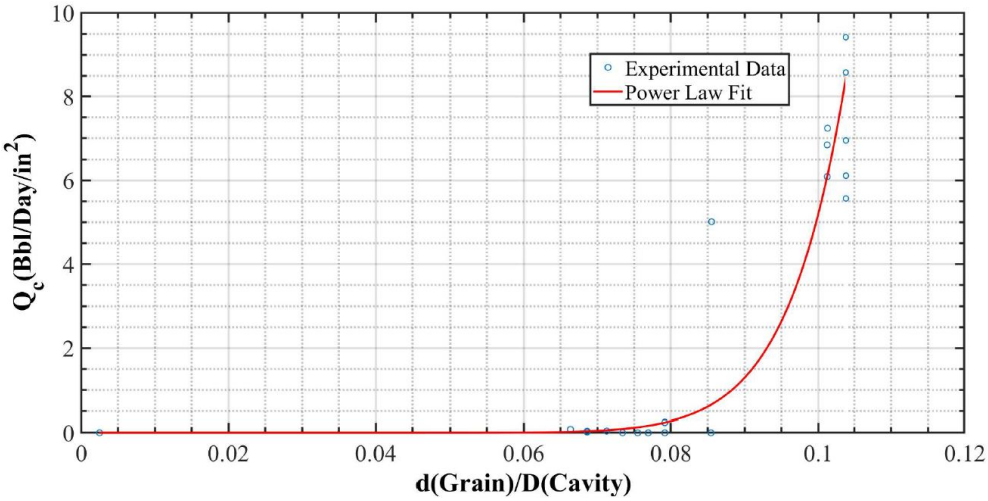

Figure 3.8: Experimental data fitted with an empirical relation between critical flow rate and grain size distribution.

$$q_c = 7.957 \times 10^{13} \left(\frac{D_{50}}{D_{CavitySurface}} \right)^{13.19} \left(0.25 \frac{k}{\mu} \right) \tag{3.29}$$

where D_{50} is the median grain size and $D_{CavitySurface}$ is the sand arch diameter, both in ft.

The total critical flow rate is given by Eq. 3.30 which is the combination of Eq. 3.28 and 3.29.

$$q_c = \frac{0.59kR}{\mu} \left[\frac{c_{correction} \bar{p_c} \beta_f}{2\pi R^2} \right] + 7.957 \times 10^{13} \left(\frac{D_{50}}{D_{CavitySurface}} \right)^{13.19} \left(0.25 \frac{k}{\mu} \right) \tag{3.30}$$

For unconsolidated sand, porosity ϕ = 0.4, water saturation S_w = 0.2, $p_{capillary}$ = 4.8 psi are assumed to give correct result with the experiments.

The turbulent fluid flow around the cavity region required to destabilize cavity is also correlated with Reynold's number (Willson et al. (2002)). Hence, the condition for erosional flow due to sand arch failure is given by the Eq. 3.31

$$u > u_c \tag{3.31}$$

where u is given by the quantity obtained from Eq. 3.32 divided by surface area and u_c is the

critical flow velocity in cm/sec.

$$q = q_f \left(1 + 1.31735 \times 10^{-12} \frac{\beta k \rho u}{\mu} \right) \tag{3.32}$$

where q_f is the fluid flow rate in cc/sec, β is the non-Darcy flow coefficient given by $\frac{2.65 \times 10^{10}}{k^{1.2}}$ /ft, k is permeability in mD, ρ is the fluid density in lb/ft^3, u is fluid velocity in in/sec and μ is viscosity in cp.

3.4.8 Sand Rate Calculation

With plastic failure region developed around the cavity and sufficient fluid flow rate to dislodge the sand grains from this failed surface, sand production rate can be calculated. It is assumed that the rate of flow of solids equals that of fluid flow i.e. there is no slippage between the two phases. Sand is not produced from the entire cavity surface for light oil, gas and water. It is observed to be produced from scattered areas in the cavity unlike with the production of heavy oil where almost all the surface area produces sand. Hence, assuming solids release area and the mobility of multiphase fluid flow are related with a power law, the sand rate is assumed to be given by Eq. 3.33.

$$\frac{dM_s}{dt} = A_1 \rho_s \psi(\varepsilon^p) u_{res} \left[\frac{M_{ref}}{M_w + M_o + M_g} \right]^{A_2} \left(\frac{1 - \phi}{\phi} \right) \varphi_f dS \tag{3.33}$$

where,

$\frac{dM_s}{dt}$: Sand production rate in gm/sec

A_1: Loading factor to be determined using experiments and field data

A_2: Mobility exponent to be determined using experiments and field data

ρ_s: Solid mass density (gm/cc)

u_{res}: Fluid velocity at reservoir conditions (cm/sec)

M_i: In-situ mobility (i = water(w), oil(o), gas(g)) in md/cp

M_{ref}: Reference mobility from experiment/field in md/cp

ϕ: Porosity

φ_f: Fraction of failed surface area

$\psi(\varepsilon^p)$: Linear function of post-failure plastic strain to judge extent of failure

dS: Failed surface area (cm^2)

A_1 & A_2 are parameters which need to be calibrated using experimental and field data. The reference mobility is either from the fluid used in the experiment or from field data, whichever is being used for calibration. The other mobilities in denominator are the in-situ mobilities from the field data. The mobility ratio will take into account multi-phase flow effect. However, in this study only single phase flow is studied.

3.4.9 Adaptive Meshing

Sand production is a moving boundary problem. With increase in effective stresses the plastic failure region moves away from the cavity surface and deep into the reservoir. As discussed, a critical fluid flow rate is required to destabilize the sand arch now by creating tensile stresses in the cavity thus inducing sand flow. As sand is eroded away into the well bore, the cavity enlarges and attains larger surface area and volume. If the same fluid flow rate is maintained, the hydrodynamic forces decrease. Eventually, the flow rate drops below the critical value unable to create enough tensile forces for detachment of sand grains and sand production halts.

Numerical modeling of such a phenomenon requires adaptive meshing algorithm which is also termed as remeshing. The physical process of removal of material is naturally depicted numerically using remeshing. Yet, we were able to find only two such studies in the literature (Wang et al. (2011) and Nouri et al. (2006)). Some of the reasons of such low usage of remeshing are that it requires a larger computational effort and advance computational geometry algorithms. Wang et al. (2006) proposed to remesh the domain when the mesh quality drops below a certain threshold measured by distortion. Nouri et al. (2006) proposed an adaptive mesh for their 2D simulation by moving nodes on the cavity face if the sanding criterion is satisfied.

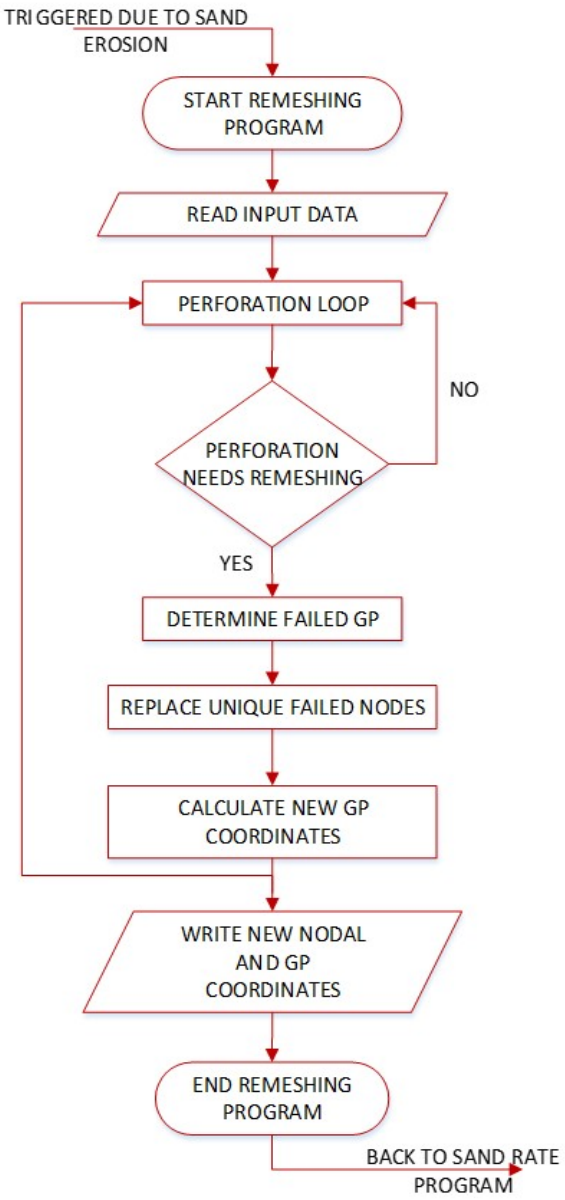

Figure 3.9: Structure of the remshing computer program coded in MathWorks® MATLAB which is called from the sand rate program and outputs new nodal and Gauss point coordinates.

In this study, remeshing is performed on a 3D mesh. Failure and subsequent erosion triggers the remeshing algorithm. For a reliable analysis providing accurate displacements and stress predictions one of the prerequisites is the definition of mesh geometry. Finite number of elements are used to interpolate approximate solutions in the domain. The modeler may use experience and/or

experimental results to create a suitable mesh geometry for a reasonable accuracy. Mesh density, type of elements, number of elements and nodes, element size, analysis type (linear or non-linear), computational time, discontinuities and large distortions are some of the things to think while designing the mesh. The same concerns need to be kept in mind while remeshing. Automatic meshing algorithms may remove an element after the sand is removed from that region. This alteration may produce destabilizing discontinuities. For this reason, in this study, the element and nodal configuration (number, type and geometry) of the domain is kept the same while the total volume of the cavity increases with sand production. A 3D remeshing module is prepared and integrated with the failure and erosion module.

There are two types of cavity geometries studied. In field conditions an ellipsoidal perforation geometry and in laboratory conditions, a cylindrical cavity geometry is considered. Different algorithms are coded for the two geometries and implemented.

After remeshing is performed, new nodal quantities must be evaluated for the same application of loading conditions. The change of locations due to remeshing warrant that all the calculations are performed again for the newly created mesh. Another way to achieve this is by utilizing numerical inverse mapping (Murti et al. (1988)) but it is a highly non-linear problem and hence the computational effort is extensive. In this study, recalculation of displacements and stresses is not done after remeshing. It was found that the new nodal locations are not far from the original and hence the recalculated displacements and stresses would be mostly the same. Ignoring the recalculation aspect saves a lot of computational effort and hence highly desired.

3.4.10 Alteration of Porosity and Permeability

With deformations occurring in the vicinity of wellbore and perforation cavity, the fabric of rock structure alters. Similarly, as pore pressure depletes the void space in the porous rock changes. Thus the porosity and permeability are altered due to fluid flow and sand production.

With each increment of loading condition, stress state changes in the domain leading to displacements. Subsequently, porosity and permeability are altered. Porosity is related to change in

unit pore volume, calculated using Eq. 3.34.

$$d(PV) = \phi(1 + \varepsilon_{kk}^{T}) - \phi_o = \varepsilon_{kk}\phi_o + \left(1 - \frac{c_m}{c_b} - \phi_o\right)(\varepsilon_{kk} + c_m\Delta\bar{p}) + \varepsilon_{ii}^{n} + \varepsilon_{ii}^{p} \tag{3.34}$$

where,

ϕ: Updated porosity

$d(PV)$: Change in pore volume

ε_{kk}: Linear elastic strain

ϕ_o: Initial porosity

c_m: Matrix compressibility (/psi)

c_b: Bulk compressibility (/psi)

$\Delta\bar{p}$: Change in pore pressure (psi)

ε_{ii}^{n}: Initial non-linear strain

ε_{ii}^{p}: Plastic strain

ε_{ii}^{T}: Total strain

Permeability is assumed to be a function of pore geometry and the Kozeny-Carman model is used to relate permeability to porosity. The relation is given by Dullien (1979) as

$$k \propto \frac{\phi^3}{(1-\phi)^2} \tag{3.35}$$

where k is the permeability and ϕ is the porosity.

4. SAND RATE PREDICTION FOR SINGLE-HOLE POLY-AXIAL EXPERIMENTS

4.1 Introduction

For realistic sand rate predictions, qualitative results from experiments are not sufficient as they provide an understanding but no relationship is established. Volumetric sand production experiments need to be performed to quantify anticipated amount of sand over a time period with certain reservoir depletion and drawdown. Papamichos et al. (2000) studied the relationship between sand rate and the applied stresses and fluid flow rates. It was observed that a critical flow rate was necessary to erode the disintegrated material clinging on to the cavity surface. Sand production rate was found to increase with increasing fluid flow rate. Other experimental investigations were carried out by Rahmati et al. (2012) and Fattahpour et al. (2012). Physical models are expensive and time consuming and that is why isotropic external stresses have been the norm. These results are then extrapolated to anisotropic stress conditions using numerical models. The primary differences between the two test conditions is the region of failure around the cavity surface and the shape of cavity after removal of failed material. Stress anisotropy effect has been studied by Papamichos (2018) and preliminary results indicate difference in sand onset stress from isotropic cases. It is theorized that sand production rate is not equally affected due to stress anisotropy. A research project at Sintef (Norway) is undertaken precisely to study the relationship of sand rates and stress anisotropy.

In this chapter, we explain the experimental setup and share the results of the experiments[1]. The objective here is to calibrate the numerical model with the experimental results and derive a sand mass rate equation. The ambient conditions of the experiment, loading path and other factors are discussed in detail. Similarly, the numerical model inputs are introduced thoroughly and the comparison of experimental results and that of the model are presented. Two types of experiments are discussed – isotropic and anisotropic. The analysis from the isotropic test and the corresponding numerical model shows that the model is able to qualitatively predict the sand

[1] Provided by Sintef

production behavior. The effect of external stress and fluid flow rate is studied. Furthermore, the analysis from the anisotropic tests' numerical models demonstrate the quantitative behavior of sand production rate.

4.2 Isotropic Test

Volumetric sand production test was performed on a hollow cylinder specimen with radial fluid flow. The test was performed on the Castlegate outcrop. The main objective of including this experimental analysis is to show that the numerical model is able to assess sand rate prediction qualitatively. Hence, only one relevant test result is used here. Papamichos et al. (2000) contains the results from all the experiments. Later, anisotropic tests are discussed in detail and used to calibrate sand mass rate equation.

4.2.1 Experiment

The test was performed in a pressure vessel with a capacity of 15.6 kpsi. It mainly comprised of the confining cell for the application of confining pressure, the top and bottom loading pistons and the base plate for application of the axial load, and a substructure equipped with a sand trap for monitoring the produced sand during volumetric experiments. Fig. 4.1 shows the interior of the cell with a 100 mm external diameter hollow cylinder specimen mounted in position. The base plate and the bottom piston are specially made to enable specimen failure and debris to pass through center holes.

The specimen is placed on the bottom piston and the cylindrical surface is isolated from the confining fluid with a nitrile sleeve. The sleeve is perforated for radial fluid flow through the specimen (Fig. 2.12). Inside the sleeve there is a lining of steel mesh for proper fluid distribution. In isotropic tests the top piston is pulled back and replaced by a cap at the upper surface such that equal confining pressure is applied to the external boundary of the specimen. The control accuracy of confining pressure is less than 30 psi.

The confining pressure is measured with a pressure transducer with a resolution of 30 psi. The flow rate is measured at the fluid pump by a turbine flow meter with a resolution of 0.04 l/min, and

the pressure at the pump is measured by a pressure transducer with a resolution of 15 psi.

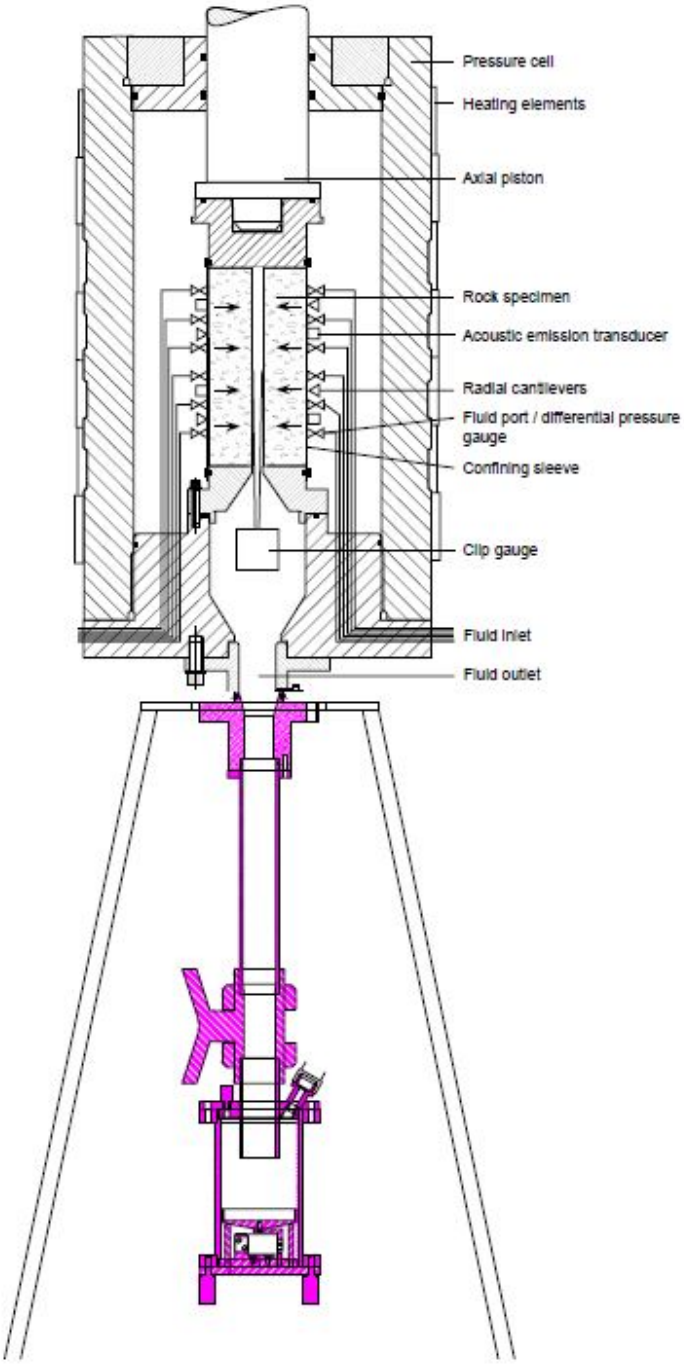

Figure 4.1: Pressure cell for volumetric sand production tests with a hollow cylinder specimen mounted in position. The bottom colored assembly contains a sand trap for continuous measurement of produced sand (Papamichos et al. (2002)).

A sand trap with an integrated load cell was installed for continuous measurements of produced sand (Fig. 4.2). This instrument was calibrated for the weight responses. The following data was recorded during the experiment every 5 secs:

- Confining pressure.
- Axial, internal and external radial deformations.
- Pore pressures at five different radial distances.
- Fluid flow rate.
- Produced sand weight.

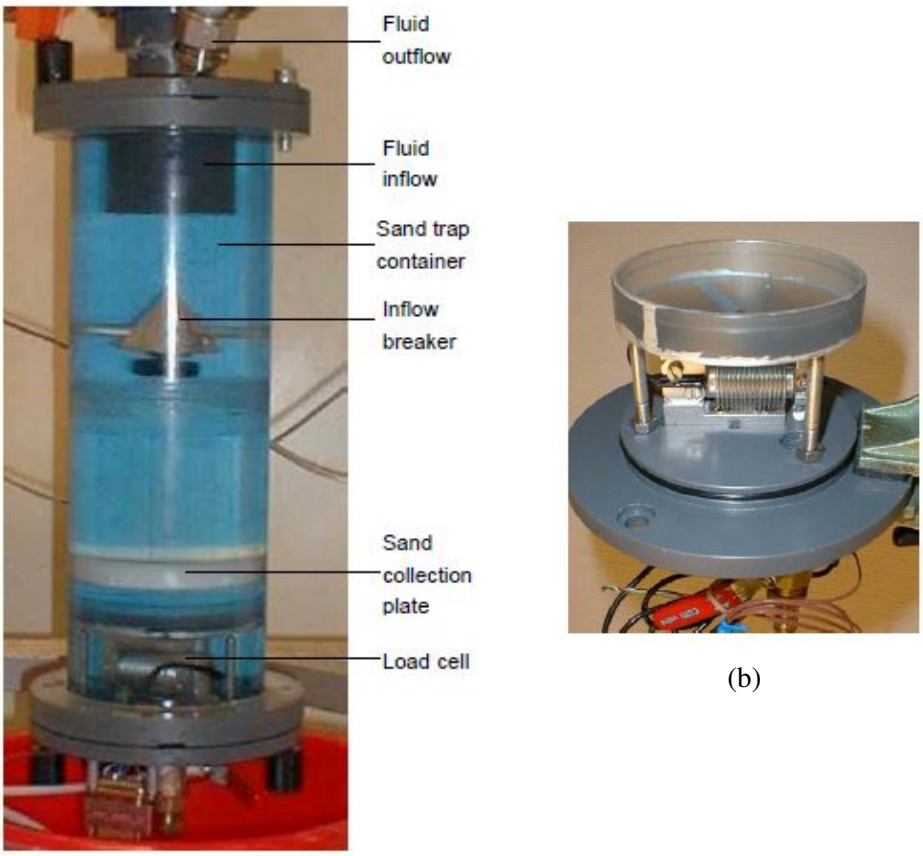

(a)

(b)

Figure 4.2: (a) The sand trap and, (b) load cell in the sand trap (after Papamichos et al. (2002)).

The test was performed with oil saturated specimen (Fig. 4.3). The specimen was saturated prior to mounting in a desiccator filled with pore fluid. The mounting was carried as quickly as safety would permit as the pore fluid may seep out of the specimen which deteriorates the saturation. The saturation oil was a mixture of lamp paraffins and had a viscosity of 3.55 cp. A few pore volumes of fluid were flown through the test sample until no more air is seen coming of the cell to ensure complete saturation prior to testing.

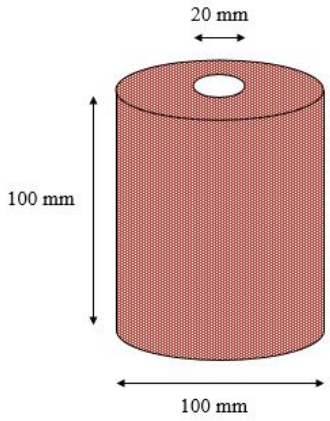

Figure 4.3: Schematic of a hollow cylinder specimen used in the isotropic volumetric sand production experiment.

The test was isotropic meaning that the axial stress equaled the externally applied stress. The external stress was applied with increments of 1.45 psi/sec until a predetermined value is reached. At this stress level, constant fluid flow is achieved by applying an external pore pressure. After certain flow, the fluid flow rate was increased in steps until the 4 liter/min flow rate limit is reached. Then the fluid flow was reduced to 0.25 liter/min and external stress was increased; this procedure was repeated as shown in Fig. 2.11. When sand production was observed the external stress and the fluid flow rate were kept constant until no further sand was produced or after 60 min.

The data from the test result on Castlegate specimen is shown in Fig. 4.4 . Sand production onset external stress is determined to be 5,510 psi. The sand production rate increases rapidly over

a very short span of time and the specimen collapsed suddenly at 5,555 psi. All the failed material had been produced.

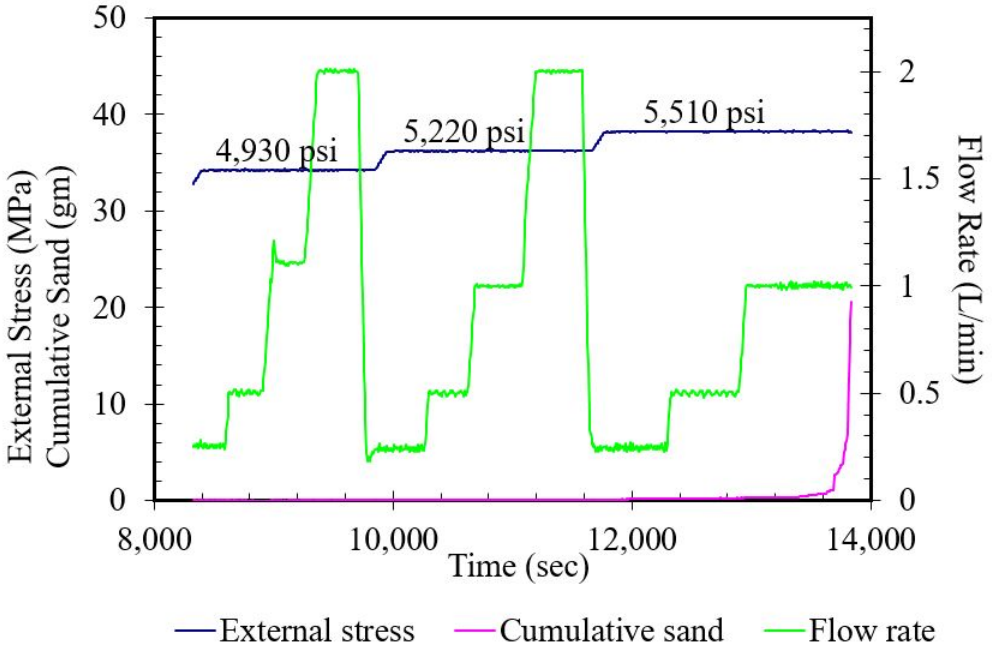

Figure 4.4: External stress, fluid flow rate, and cumulative weight of produced sand is shown with time when isotropic volumetric test is run on Castlegate outcrop specimen (after Papamichos et al. (2002)).

4.2.2 Numerical Model

The sequentially coupled fluid flow and geomechanical model is setup using the data from the experiment. The objective of the numerical modeling is to predict a sand production behavior similar to that observed in the experiment. The poro-elasto-plastic model described in the previous chapter is utilized here. Various input parameters essential for the model to run are listed in Table 4.1 .

The steady state fluid flow rate is maintained by applying pore pressures at the external and internal faces of the specimen. The hollow cavity is at the atmospheric pressure. It is infeasible to replicate the decrement in fluid flow after it achieves its highest value so the fluid flow begins late

in the numerical model.

The material properties of the Castlegate outcrop sandstone are estimated from the triaxial test results data. A schematic of the apparatus is shown in Fig. 4.5. These tests were performed on core plugs of $3''$ length and $1.5''$ diameter. The tests were conducted under fully drained conditions with lamp paraffin oil. The strain rate was kept constant at 5×10^{-6} /sec. The measured data are as follows:

- axial load,
- confining pressure,
- axial and radial deformations,
- cumulative fluid volume pumped and,
- inlet and outlet absolute pore pressures.

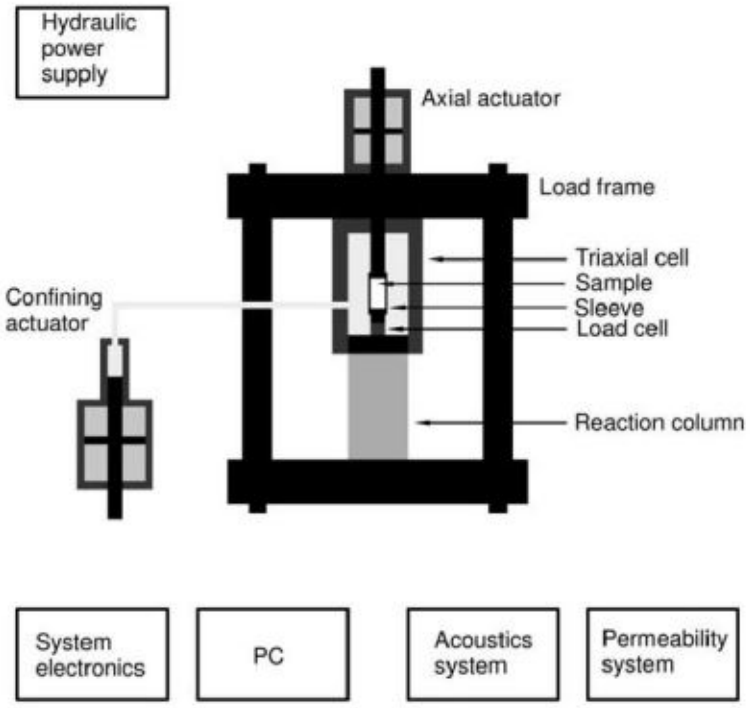

Figure 4.5: Schematic of triaxial test apparatus (after Fjaer et al. (2008)).

Simulation Conditions	
Specimen height	100 mm
Specimen internal diameter	20 mm
Specimen external diameter	100 mm
Initial permeability	1,026 md
Initial Porosity	24.6%
S_{wi}	0%
Fluid density	0.78 gm/cc
Fluid viscosity	3.55 cp
Oil compressibility	1.068×10^{-5} 1/psi
Solid density	2.65 gm/cc
Failure criterion: Critical plastic strain (ε_c^p)	0.003671

Table 4.1: Simulation conditions for isotropic volumetric sand production experiment.

The constitutive relations are derived from the stress-strain curves (Fig. 4.6). There were two tests conducted for confining pressure of 2 MPa but only one set is shown. The unconfined compressive strength (UCS) is determined to be 2,060 psi and the calculated Young's modulus and Poisson's ratio are 1,204 kpsi and 0.4643 respectively. Cohesion and friction angle are calculated to be 539 psi and 46.6° from a plot of peak axial and confining stress (Fig. 4.7).

The theoretical constitutive relations are shown in Fig. 4.8 which are derived using Morita and Gray (1980) and the procedure described in the previous chapter. These mathematical relations take into account the initial non-linearity, linear elasticity, yield criterion and post yield envelope. Critical plastic strain is used as the failure criterion (Fig. 4.9) and ε_c^p is calculated to be 0.003671. The yield envelope is shown in Fig.

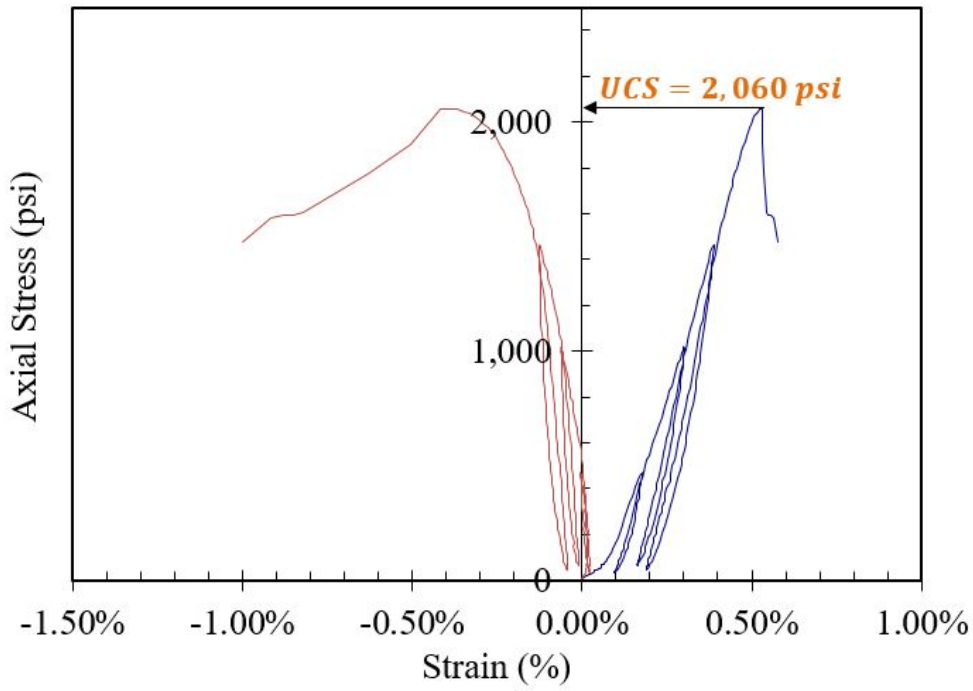

(a) σ_3 = 0 MPa

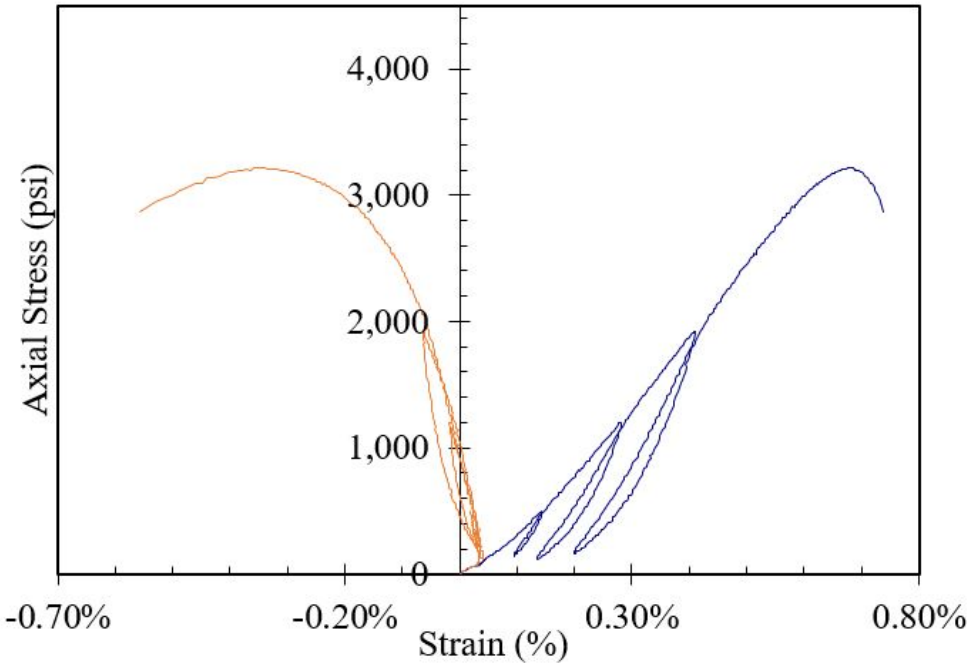

(b) σ_3 = 0.5 MPa

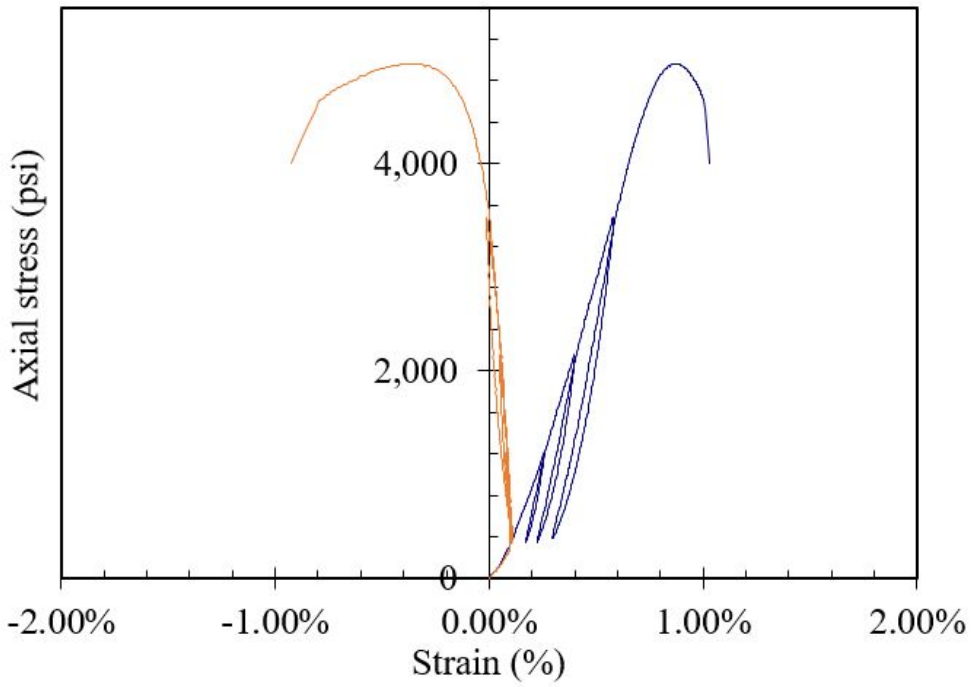

(c) σ_3 = 2 MPa

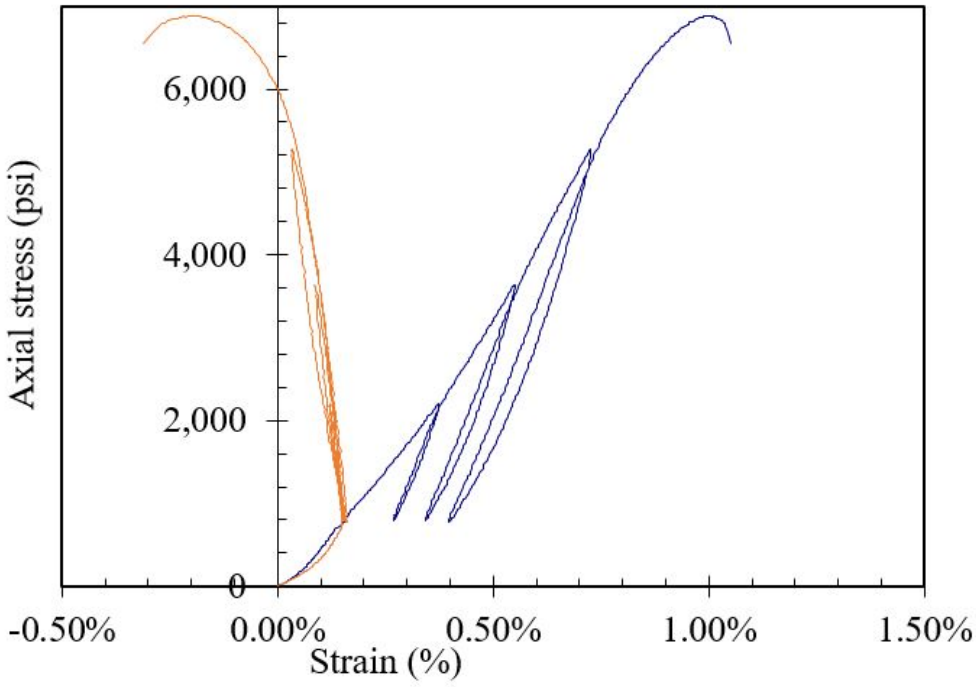

(d) σ_3 = 5 MPa

Figure 4.6: The stress strain curves at different confining pressures for Castlegate sandstone.

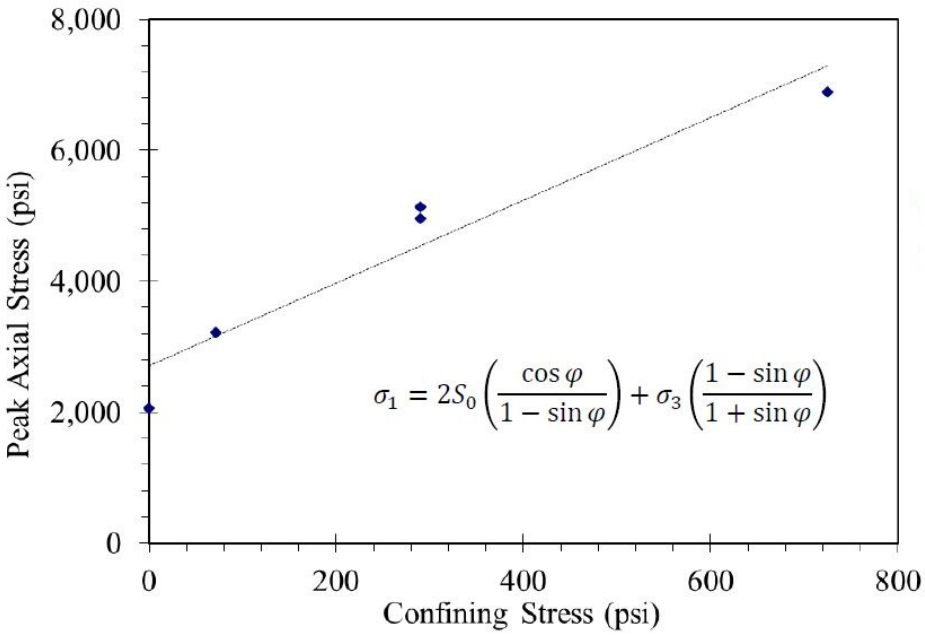

Figure 4.7: Theoretical composite stress strain curves for the Castlegate outcrop sandstone.

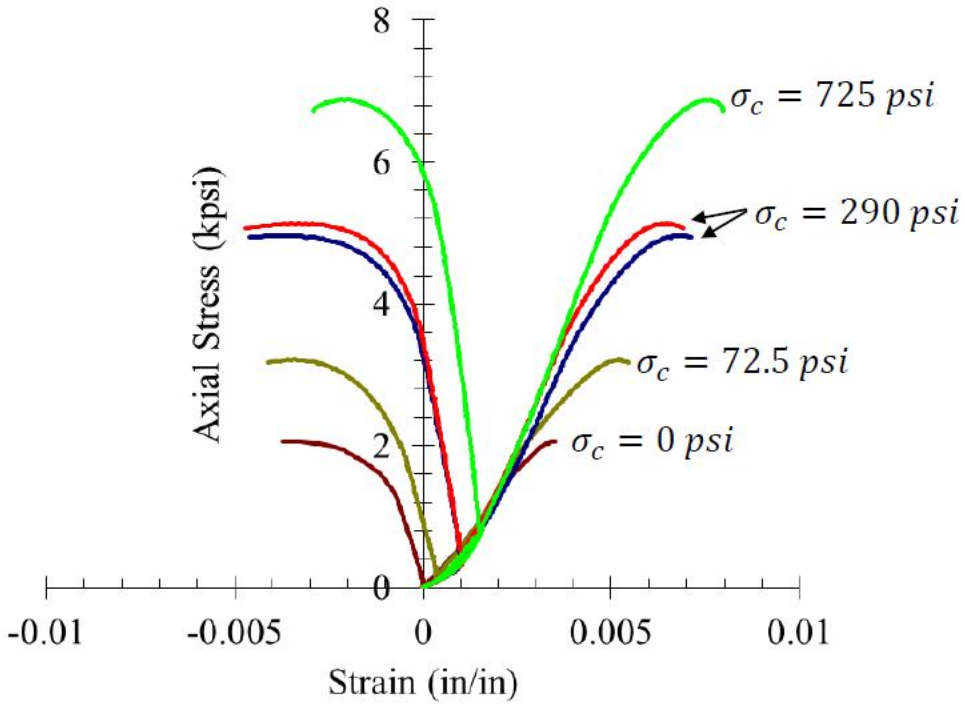

Figure 4.8: Theoretical composite stress strain curves for the Castlegate outcrop sandstone.

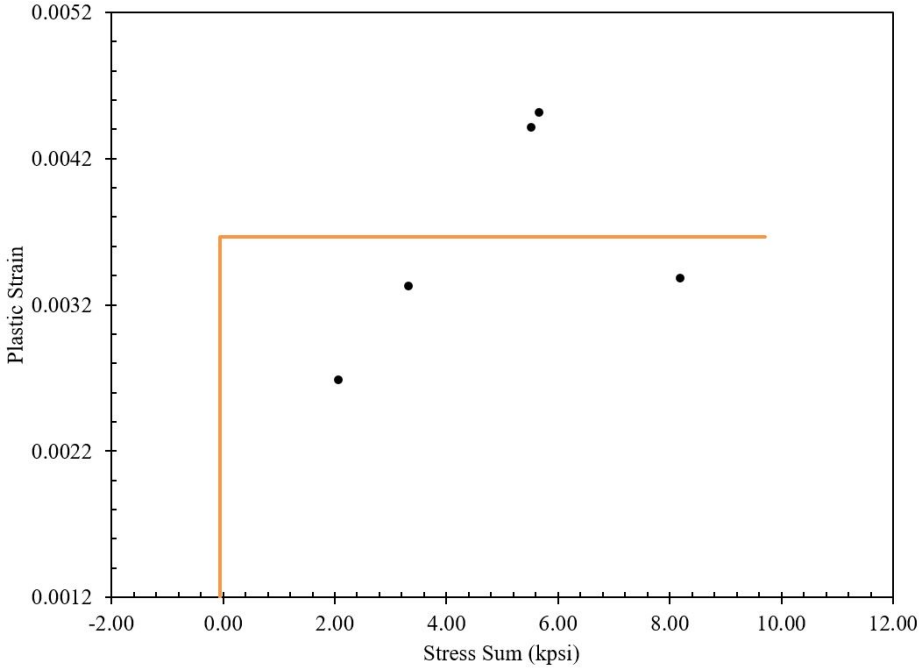

Figure 4.9: Critical plastic strain failure envelope for the Castlegate outcrop sandstone.

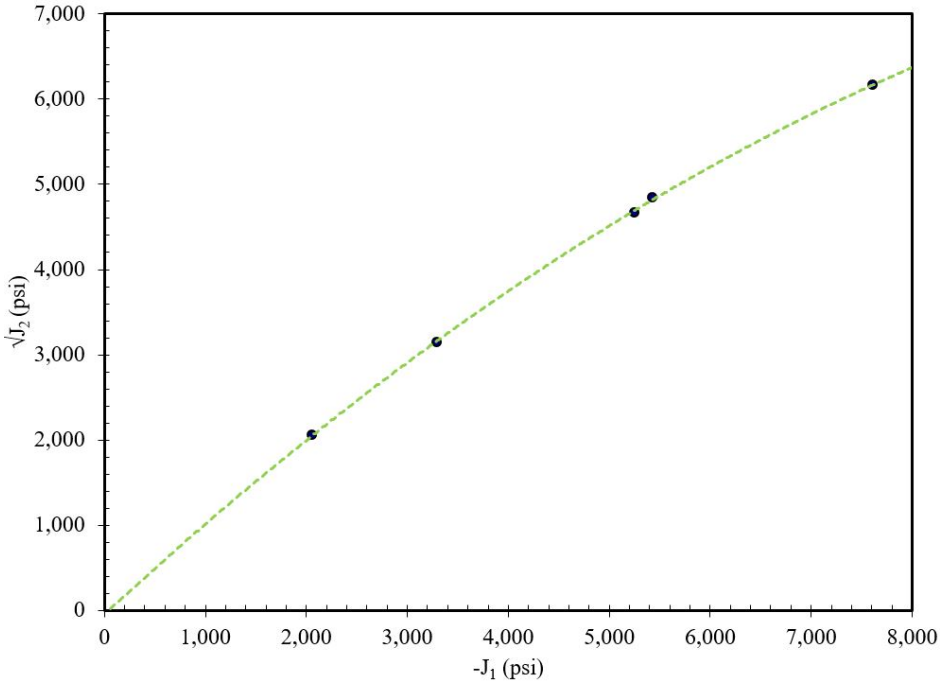

Figure 4.10: Yield envelope for the Castlegate outcrop sandstone.

The mesh used for the simulation is of exactly the same radii as that of the specimen so there is no size effect involved (Fig. 4.11). For saving computational effort and time, vertical symmetry has been taken advantage of and only half of the specimen is simulated. There are 3 number of layers in the vertical direction, 14 radial layers and 16 tangential layers. The total number of elements is 672.

There are four stages of loading that can be applied in the geomechanical simulator however, not all stages are necessary for simulation of controlled experimental conditions. These are namely,

- In-situ stresses plus drilling overbalance,
- removing overbalance before production,
- reservoir depletion and,
- drawdown.

In-situ stresses and application/removal of overbalance is unnecessary in this context. Failure is happening due to only two types of forces, application of external stress and fluid flow through the specimen. The increment in isotropic stresses can be simulated as depletion acting on the external surface of the specimen.

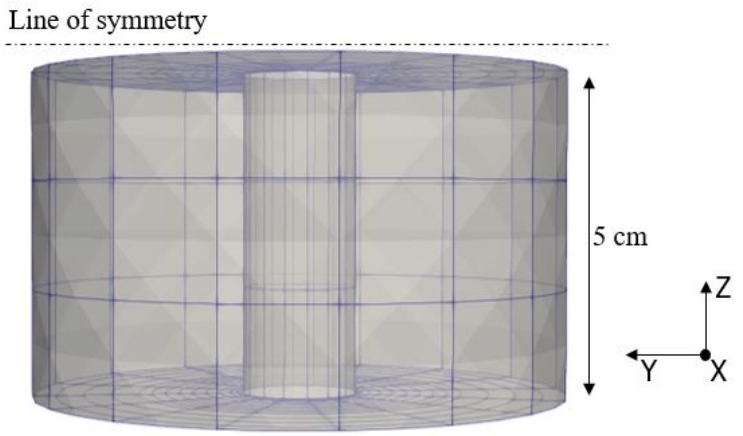

(a) Side view.

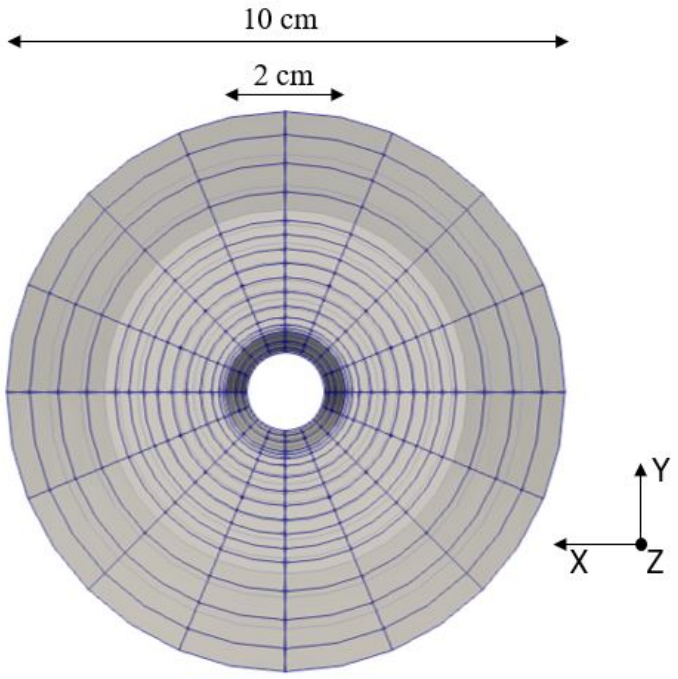

(b) Top view.

Figure 4.11: Numerical mesh for Castlegate sandstone specimen used in the isotropic volumetric sand production test.

The onset of sand production estimated by the numerical simulation is 5,400 psi. It is very close to the onset obtained from the experiment which is 5,510 psi. The failure seems to start from the top of the cavity which in fact, is the center of the specimen due to vertical symmetry (Fig. 4.12).

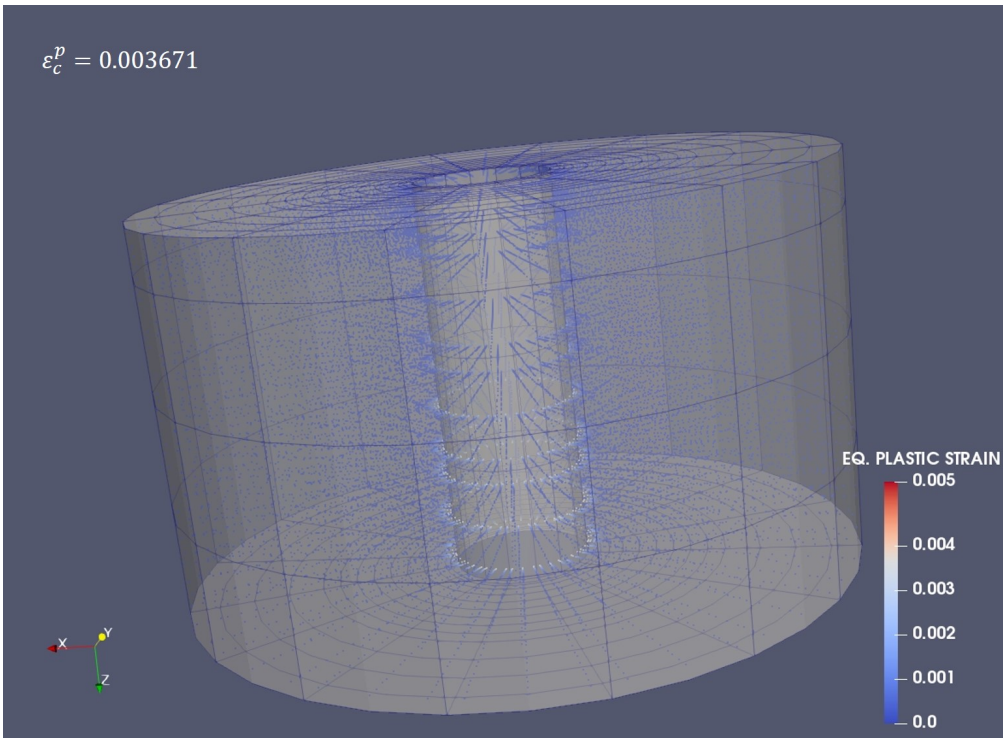

Figure 4.12: Picture at the beginning of failure which seems to be occuring at the bottom of the hollow cylindrical cavity which is actually the center of the specimen. The slight hue shows failure region.

The volumetric sand production result from the numerical analysis is shown in Fig. 4.13. The external stress is continuously increased until 6,000 psi and the fluid flow rate is increased in steps. The cumulative sand production qualitatively matches the results obtained from experiment (Fig. 4.4). This result encourages us to study sand production and estimate sand rate quantitatively.

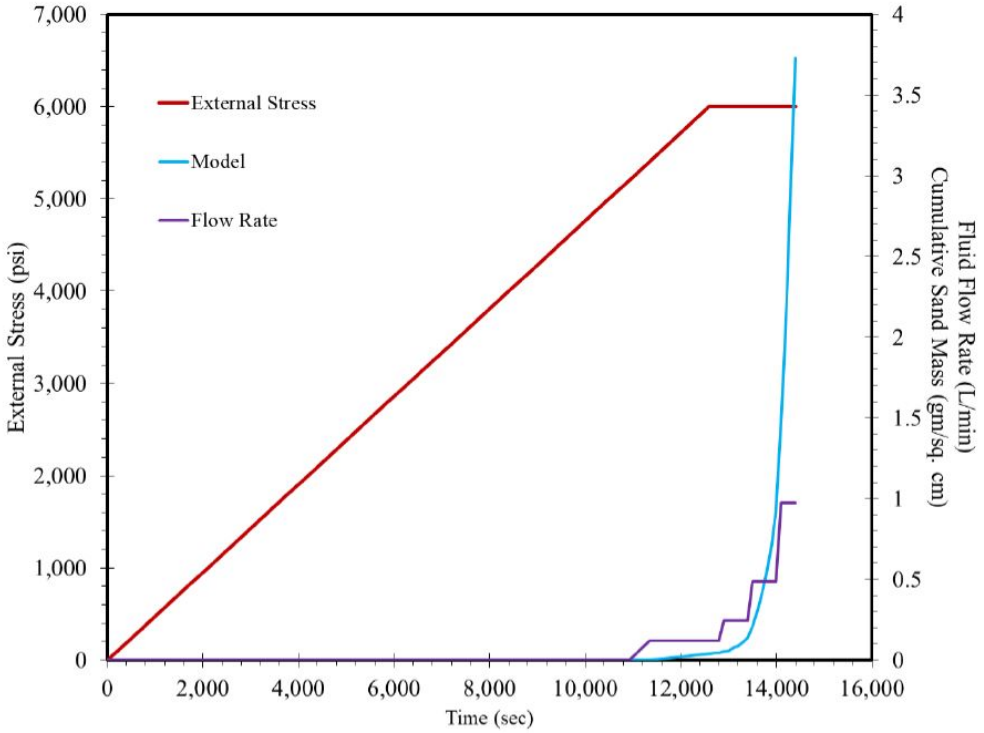

Figure 4.13: External stress, flow rate and cumulative sand mass result from the numerical study with isotropic stress conditions on Castlegate outcrop material.

4.3 Anisotropic Tests

A test program has been running at Sintef in Norway conducting anisotropic volumetric sand production experiments. The tests were performed on Castlegate outcrop sandstone rock material. The main objective of using these test results is to develop a numerical sand mass rate equation, calibrated with these results, which can estimate sand rate and cumulative sand production quantitatively.

A total of six experiments have been conducted and their summary is presented in Table 4.2. σ_z, σ_r and σ_R are the applied stresses in the vertical, minimum and maximum horizontal direction respectively. K_z and K_r are the stress ratios, vertical to maximum horizontal and minimum to maximum horizontal respectively. K_z denotes axial anisotropy and K_r that of lateral. By altering these ratios, anisotropic effect on the onset of sand production and sand rates can be studied.

ID	Material	$\mathbf{K_z}(\frac{\sigma_z}{\sigma_R})$	$\mathbf{K_r}(\frac{\sigma_r}{\sigma_R})$
01	Castlegate	1	1/3
02	Castlegate	1	2/3
03	Castlegate	2/3	2/3
04	Castlegate	4/3	2/3
05	Castlegate	2	2/3
06	Castlegate	1	1

Table 4.2: The test program summary for anisotropic volumetric sand production experiments.

An unconventional semi-circular geometric shape is chosen for the specimen. Fig. 4.14 shows the typical specimen design with the three principal stresses indicated. The maximum horizontal stress is applied on the straight face whereas the minimum horizontal on the curved face.

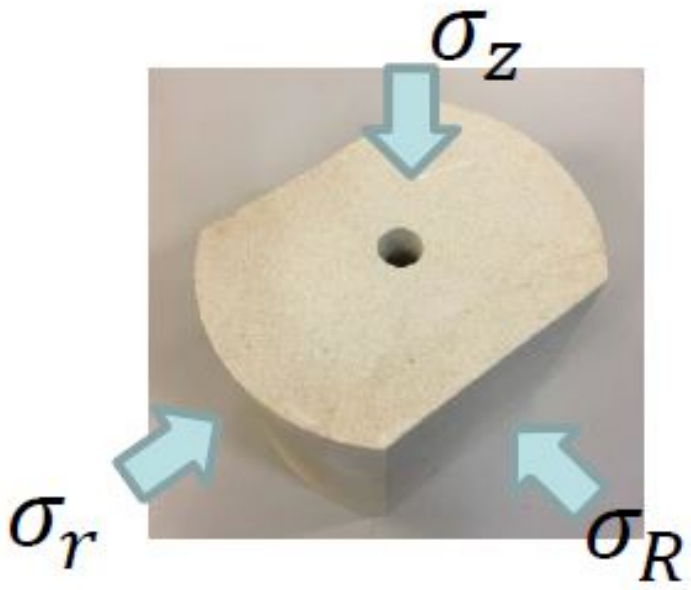

Figure 4.14: Castlegate outcrop specimen used in the anisotropic volumetric sand production experiments.

There are several benefits of using such a geometry. Specimens with this design are easier and faster to mount on the equipment; this design reduces the risks of leakage during fluid flow, radial flow is more uniform and the anisotropic stresses can be well approximated to a rectangular geometry.

The equipment used to carry out the experiments has a capacity to apply up to 14,500 psi of hydrostatic pressure. The vertical and maximum horizontal deviatoric stresses are applied using top and side pistons with additional load of 7,250 psi. All the stresses are applied simultaneously with a preset rate. The semi-circular geometry of the specimen is attached with two steel molds on the straight faces. The specimen is separated from the confining fluid using a nitrile sleeve. Radial fluid flow is established by applying an external pressure. The cylindrical hole is at ambient pressure condition. The sleeve has a steel wired mesh to distribute the fluid flow uniformly along the surface of the specimen. Fig. 4.15 shows dimensions of a typical specimen prepared for experimental setup. The length to external diameter ratio is 1:1. The diameter of the central hollow cylinder is 20 mm typically.

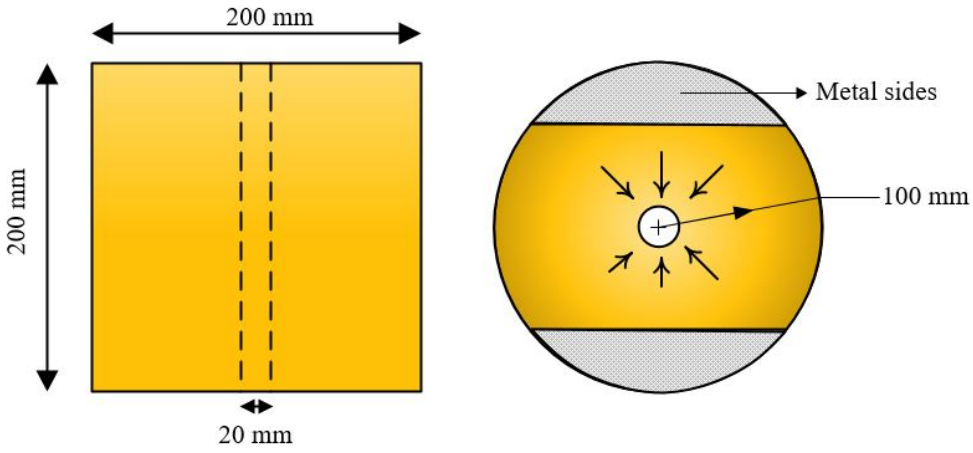

Figure 4.15: Schematic of prepared specimen used before setting up the experiment.

The experiments are carried out with irreducible water saturated samples. To achieve this,

samples are fully saturated with brine solution prior to mounting. Oil is flown through the samples until no more production of water is observed.

The equipment used for the experiment has a sand trap at the bottom of the assembly where all the debris is collected. Weight of produced sand is continuously measured in this sand trap. There are pressure sensors to record all the three principal stresses; sensors are installed to measure internal and external deformations.

Figure 4.16: Equipment used for poly-axial volumetric sand production experiment (Courtesy - Sintef).

The material used in the experiments is Castlegate outcrop sandstone for which the triaxial test results (Fig. 4.6 - 4.7) are used for deriving the constitutive relations (Fig. 4.8). The unconfined compressive strength (UCS) is determined to be 2,060 psi and the calculated Young's modulus and Poisson's ratio are 1,204 kpsi and 0.4643 respectively. The critical plastic strain criterion is used for judging failure (Fig. 4.9). The ε_c^p is calculated to be 0.003671. The grain size distribution of the material is important to judge erosion and thus it was carried out and the results are in Fig. 4.17. The D_{50} is 198.9 μm.

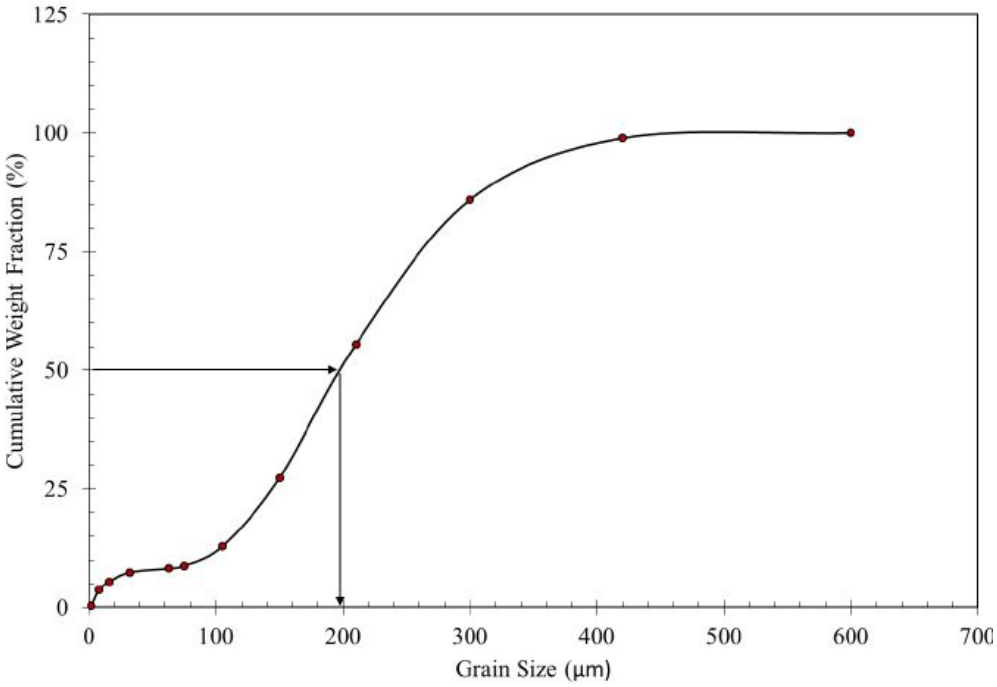

Figure 4.17: Castlegate sandstone grain size distribution (adopted from Papamichos et al. (2002)).

The mesh used for the numerical simulation is of exactly the same external and internal radii as that of the specimen so there is no size effect involved (Fig. 4.18). For saving computational effort and time, vertical symmetry has been taken advantage of and only half of the specimen is simulated. There are 3 number of layers in the vertical direction, 14 radial layers and 16 tangential layers. The total number of elements is 672.

To further save computation effort and time, elasto-plastic material is used only in the inner 8 radial layers. The outer 6 layers have the material with elastic properties only. This is reasonable since failure begins in the central hole and propagates outward. Fig. 4.19 shows the two materials used in the simulation.

There are four stages of loading that can be applied in the geomechanical simulator however, not all stages are necessary for simulation of controlled experimental conditions. These are namely,

- In-situ stresses plus drilling overbalance,
- removing overbalance before production,
- reservoir depletion and,
- drawdown.

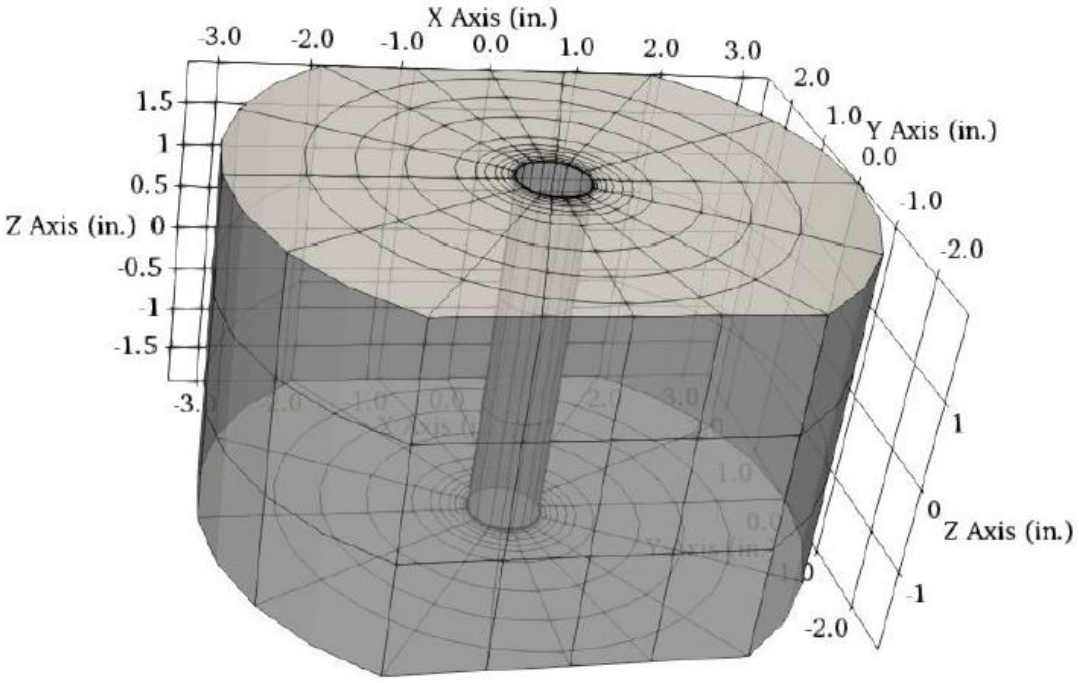

Figure 4.18: Mesh used in numerical simulation for Castlegate sandstone specimen used in the poly-axial volumetric sand production test.

In-situ stresses and application/removal of overbalance is unnecessary in this context. Failure is happening due to only two types of forces, application of external stresses and fluid flow through the specimen. The increment in three principal stresses can be simulated as depletion acting on the external surfaces of the specimen. The σ_z, σ_r and σ_R are applied in the directions of z-, x- and y-axis respectively.

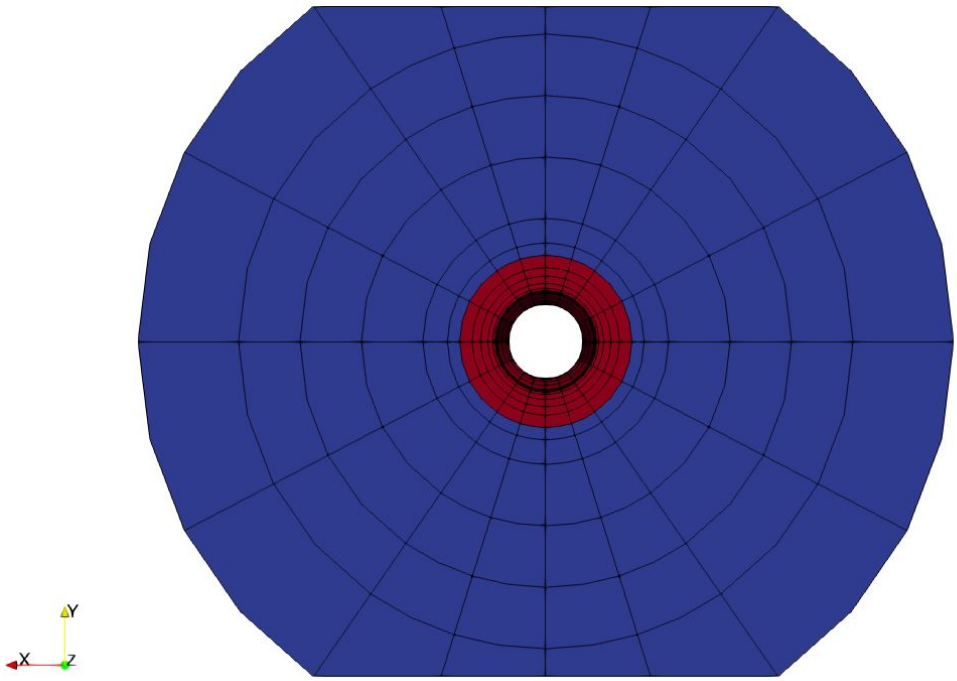

Figure 4.19: Cross-section of the mesh with elastic (blue) and elasto-plastic (red) Castlegate material used in the numerical simulation of poly-axial volumetric sand production tests.

The fluid flow in the experiments is kept constant at 1.6 L/min by applying and adjusting external pore pressure. In the numerical model, only half of the specimen is simulated so an external pore pressure of 0.015 psi would give 0.804 L/min of radial fluid flow. The pressure distribution in the specimen is shown in Fig. 4.20. The pressure contours are overlapped by the specimen mesh. The central hole is exposed to the atmosphere.

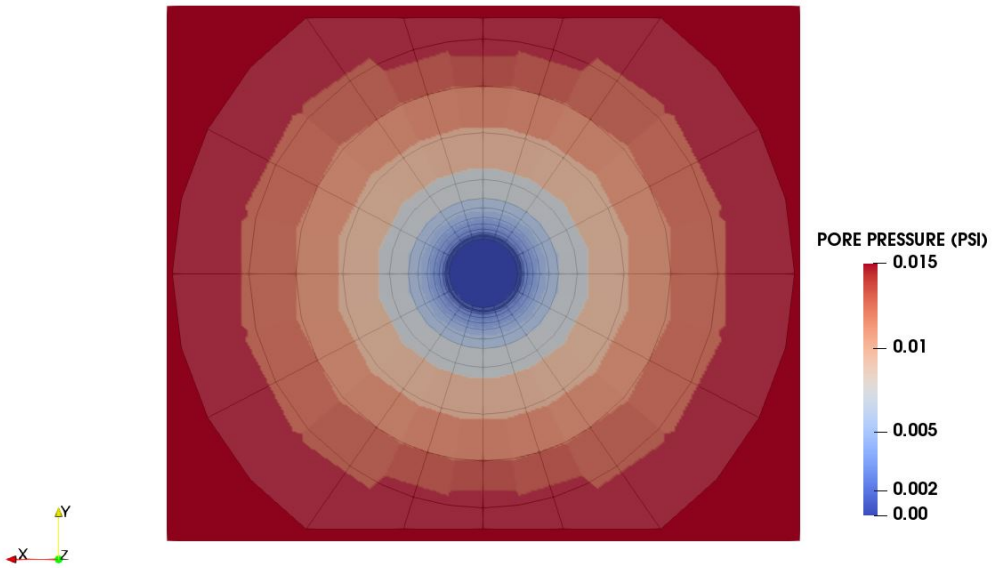

Figure 4.20: Cross-section of the mesh showing pressure distribution causing fluid flow in the specimen during the poly-axial volumetric sand production experiment.

4.3.1 Calibration of Sand Mass Rate Equation

With plastic failure region developed around the cavity and sufficient fluid flow rate to dislodge the sand grains from this failed surface, sand production rate can be calculated. It is assumed that the rate of flow of solids equals that of fluid flow i.e. there is no slippage between the two phases. Sand is not produced from the entire cavity surface for light oil, gas and water. It is observed to be produced from scattered areas in the cavity unlike with the production of heavy oil where almost all the surface area produces sand. Hence, assuming solids release area and the mobility of multiphase fluid flow are related with a power law, the sand rate is assumed to be given by the Eq. 4.1.

$$\frac{dM_s}{dt} = A_1 \rho_s \psi(\varepsilon^p) u_{res} \left[\frac{M_{ref}}{M_w + M_o + M_g} \right]^{A_2} \left(\frac{1-\phi}{\phi} \right) \varphi_f dS \tag{4.1}$$

where,

$\frac{dM_s}{dt}$: Sand production rate in gm/sec

A_1: Loading factor to be determined using experiments and field data

A_2: Mobility exponent to be determined using experiments and field data

ρ_s: Solid mass density (gm/cc)

u_{res}: Fluid velocity at reservoir conditions (cm/sec)

M_i: In-situ mobility (i = water(w), oil(o), gas(g)) in md/cp

M_{ref}: Reference mobility from experiment/field in md/cp

ϕ: Porosity

φ_f: Fraction of failed surface area

$\psi(\varepsilon^p)$: Linear function of post-failure plastic strain

dS: Failed surface area (cm^2)

The mobility ratio is included to take into account the effect of multi-phase flow. In the experiments, only oil is flowing hence, M_{ref} is that of oil. The ratio of mobilities becomes unity with single phase flow and so only one calibration parameter (A_1) can be determined through these anisotropic experiments. The linear function of post-failure plastic strain (Eq. 4.2) is assumed to be the difference between the average plastic strain of the failing gauss points and the critical plastic strain in each of the failing elements. The purpose of this function is to include the extent of post-failure zone in the sand rate calculation.

$$\psi(\varepsilon^p) = \bar{\varepsilon}^p - \varepsilon_c^p \tag{4.2}$$

For one phase flow, Eq. 4.1 is reduced to Eq. 4.3.

$$\frac{dM_s}{dt} = A_1 \rho_s (\bar{\varepsilon}^p - \varepsilon_c^p) u_{res} \left(\frac{1-\phi}{\phi} \right) \varphi_f dS \tag{4.3}$$

The sand rate is calculated for each failing element and then combined to get the total rate. For the time period in which $\bar{\varepsilon}^p$ is smaller than ε_c^p, sand rate is reported as zero. It indicates that the residual strength of the failed rock material will hold the element intact until the average plastic strain exceeds the critical plastic strain. It can be clearly seen that the sand rate is reported in the in-situ conditions as the flow rate is at the perforation surface. The transport phenomena of

sand debris from reservoir to the surface is also very complex. Moreover, coupling it with sand production simulation was not the objective of this study. There is going to be a delay in observing the produced sand at the surface due to a variety of reasons outside the scope of this work.

By performing the simulation for all the six poly-axial experiments, the calibration parameter A_1 is determined. Once the cavity fails, its shape becomes irregular and stress concentration occurs almost everywhere. In these poly-axial experiments, external stresses are monotonically increased, simulating typical field conditions where reservoir depletion significantly increases vertical effective stress whereas increase in lateral stresses are small. As the reader can understand by now that various factors affect failure estimation and subsequent sand rate calculation. However, the most dominant factor is maximum stress increment after perforation failure. Since the rock strength also significantly affects sand rate, we assume, under the monotonically increase in external stresses, the loading factor A_1 be a function of $\Delta\sigma^e_{max}/TWC$. The loading factor is found to be dependent on the ratio of change in maximum principal effective stress (after the onset of sand production) and the Thick-Walled Cylinder strength (TWC). The expression to determine the loading factor is given by Eq. 4.4. This equation may be improved if more experiments are conducted.

$$A_1 = 1.331 \times 10^{-1} e^{-2.541\left[\frac{\Delta\sigma^e_{max}}{TWC}\right]} \tag{4.4}$$

The loading factors determined from all the experiments and the Eq. 4.4 are shown to fit in Fig. 4.21. The 95% confidence interval is also shown on the plot. Eq. 4.5 and Eq. 4.6 provide the lower and upper bound of the loading factor respectively. The relationship is of expected nature. At the onset of sand production, depletion is low but the sand rates are quite high. Later, when sand production has taken place for a while, the depletion is high but the sand rates are low. The TWC strength of Castlegate sandstone is 4,806 psi calculated from the correlation Eq. 4.7 determined from experiments. Fig. 4.22 shows the experimental data points and the curve fit.

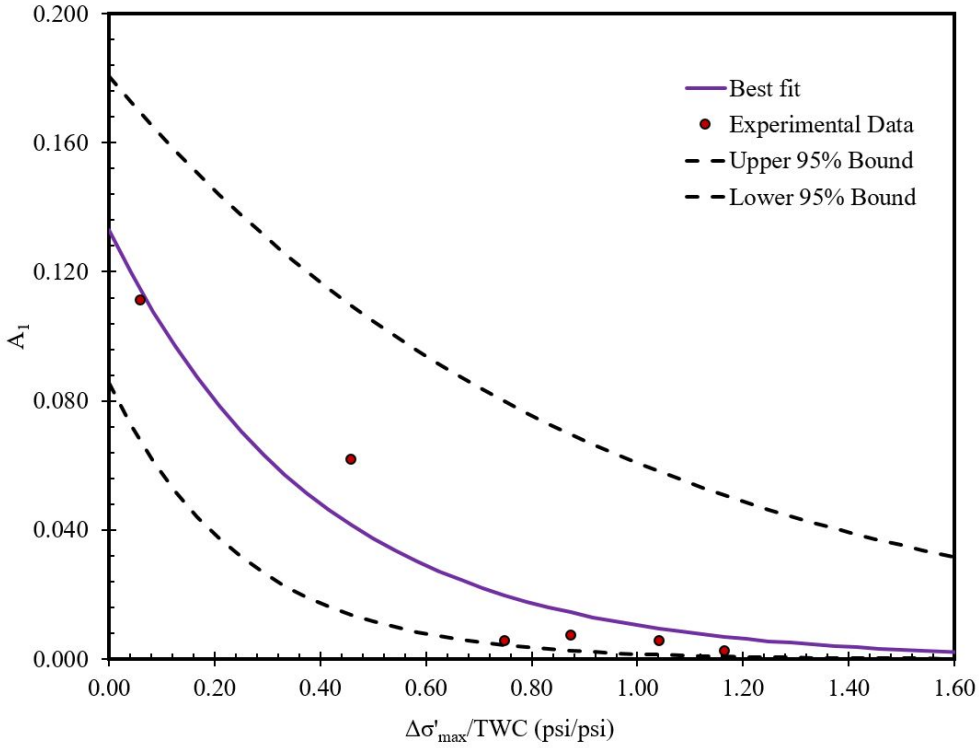

Figure 4.21: Best fit and the 95% confidence intervals of the loading factor A_1 determined from experiments.

$$A_1^{lower} = 0.8556 \times 10^{-1} e^{-3.992\left[\frac{\Delta\sigma^e_{max}}{TWC}\right]} \tag{4.5}$$

$$A_1^{upper} = 1.806 \times 10^{-1} e^{-1.090\left[\frac{\Delta\sigma^e_{max}}{TWC}\right]} \tag{4.6}$$

$$\frac{TWC}{UCS} = -2.0 \times 10^{-4} UCS + 2.7489 \tag{4.7}$$

The Eq. 4.7 is based on the experiments performed on rock material from North sea which resembles Castlegate sandstone in character and properties.

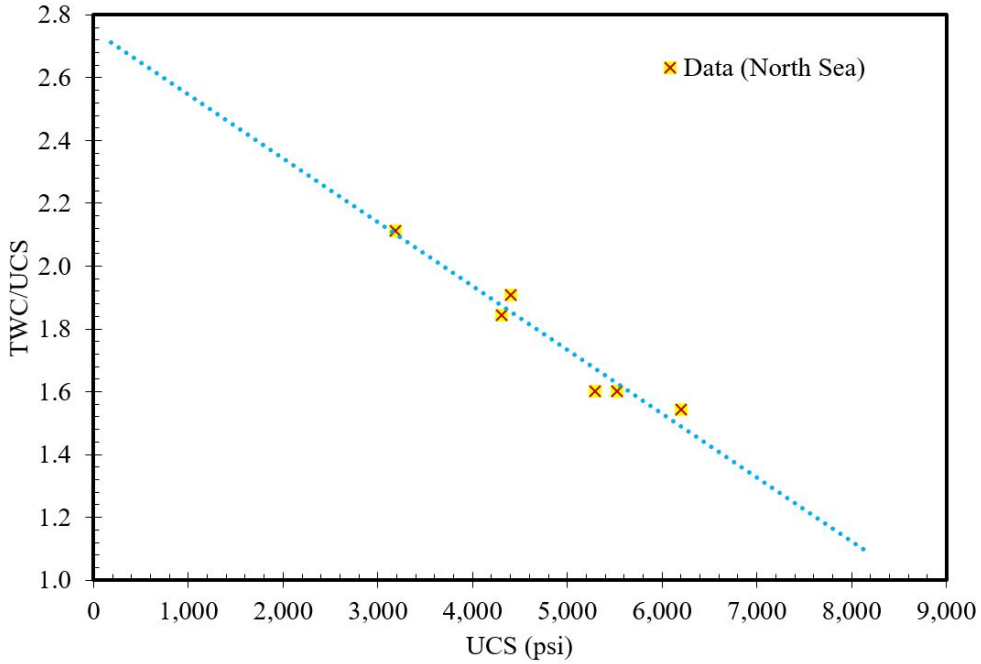

Figure 4.22: Correlation between TWC and UCS determined from experiments (from Dr. Nobuo Morita).

4.3.2 Results

All the six poly-axial experiments and their numerical simulations will be discussed in detail in this section. The results from experiments and simulations will be compared and the loading factor is determined for each one. All the three principal stresses are known whenever onset takes place and since the ratios of stresses is kept constant it will be easier to report it using any stress. Here, onset is reported with σ_R.

4.3.2.1 Case 01 - K_z = 1, K_r = 1/3

The first experiment being discussed here was carried out with no axial anisotropy and high lateral anisotropy of 1/3. The axial anisotropy is the ratio of vertical stress to maximum horizontal stress and the lateral anisotropy is the ratio of minimum horizontal stress to maximum horizontal stress. The specimens are saturated with 3.5% NaCl solution and kerosene oil is flowed through. The loading rate is 870 psi/hour and the fluid flow rate is maintained at 1.6 L/min. These data are shown with time in Fig. 4.23. The specimen properties are shown in Table 4.3.

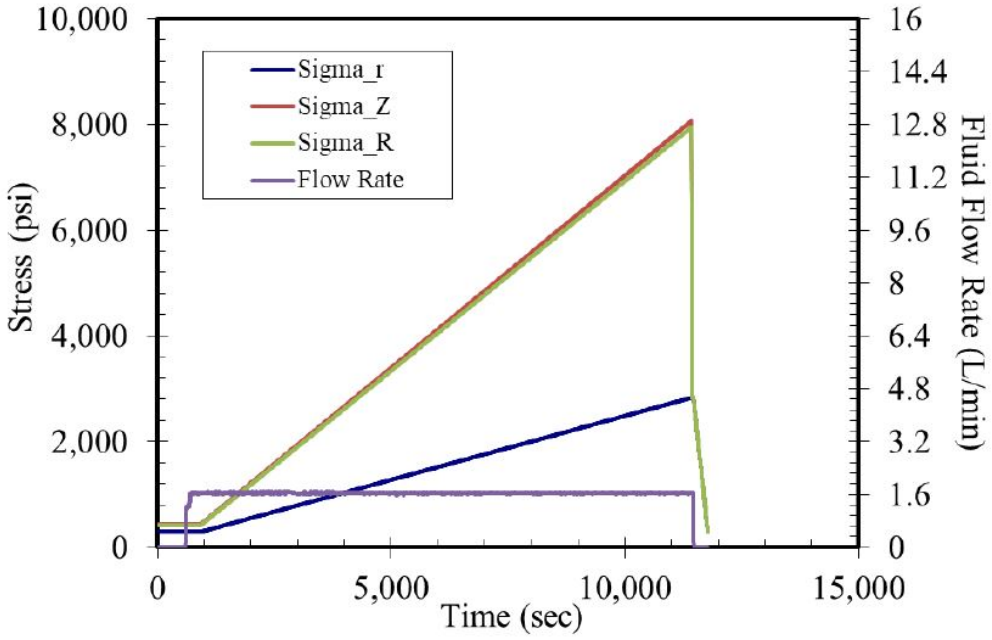

Figure 4.23: Three principal stresses and the fluid flow rate during the experimental run with K_z = 1 and K_r = 1/3.

Specimen Properties	
Rock	Castlegate sandstone (outcrop)
Specimen height	199.9 mm
Specimen internal diameter	19.9 mm
Specimen external diameter	199.5 mm
Angle of slabbed part	46.05°
Permeability	500 - 600 md
Porosity	32.5%
Fluid density	0.78 gm/cc
Fluid viscosity	1.4 cp
Solid density	2.65 gm/cc

Table 4.3: Specimen properties for poly-axial volumetric sand production experiment with K_z = 1 and K_r = 1/3.

The onset of sand production in the experiment is observed when σ_R is 3,480 psi. The sand rate varies a lot during the experiment. Hence, for regularity and reproducibility, 2 gm of cumulative produced sand is always referred to (in this dissertation) when the onset of sand production happens. The sand production during the experiment is shown in Fig. 4.24. The total run time is about 196 min in which the stresses are increased and sand production observed. The experiment was stopped before total collapse of the specimen due to safety reasons.

The numerical simulation is setup such that the stresses increase with an increment step of 200 psi and flow rate is maintained at 0.8 L/min due to vertical symmetry. Table 4.4 shows the simulation conditions. Fig. 4.25 shows the stresses and flow rate during the simulation.

Comparing the experimental and simulation's cumulative sand production, a loading factor A_1 is calculated. Note that Eq. 4.4 also provides us with a best fit loading factor along with lower and upper bounds from Eq. 4.5 and Eq. 4.6 respectively.

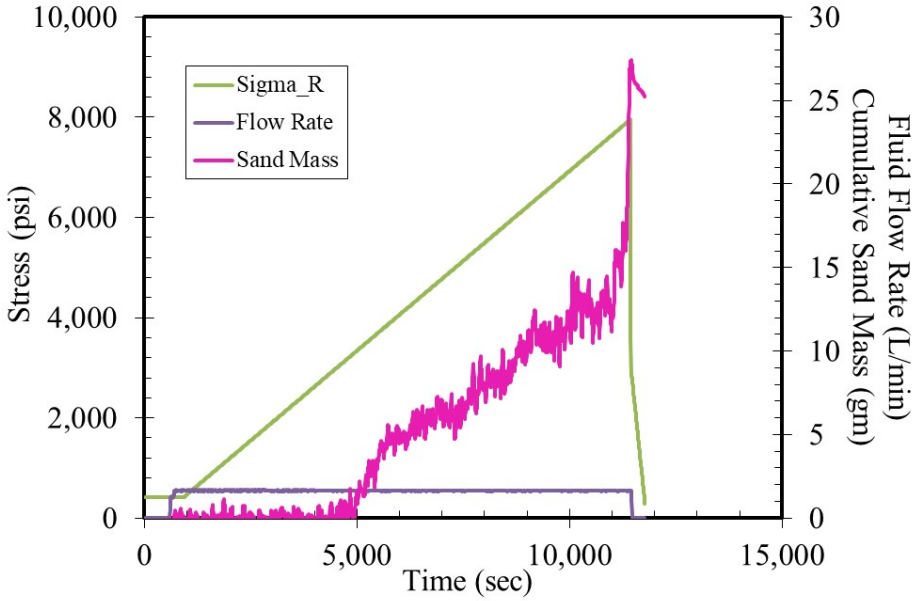

Figure 4.24: Three principal stresses and the fluid flow rate during the experimental run with K_z = 1 and K_r = 1/3.

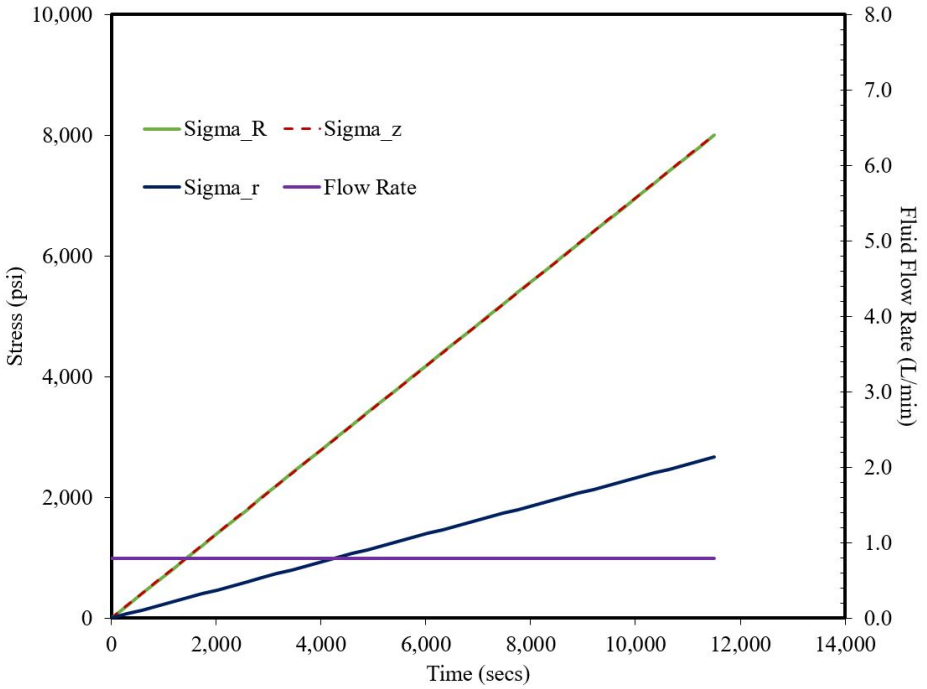

Figure 4.25: Three principal stresses and the fluid flow rate during the simulation run with K_z = 1 and K_r = 1/3.

Simulation Conditions	
Height	100 mm
Internal diameter	20 mm
External diameter	200 mm
Initial permeability	600 md
Initial Porosity	26%
Internal boundary pore pressure	0 psi
External boundary pore pressure	0.015 psi
Maximum σ_z	8,000 psi
Maximum σ_r	2,667 psi
Maximum σ_R	8,000 psi
Fluid density	0.78 gm/cc
Fluid viscosity	1.4 cp
Oil compressibility	1.068×10^{-5} 1/psi
Solid density	2.65 gm/cc
Failure criterion: Critical plastic strain (ε_c^p)	0.003671

Table 4.4: Simulation conditions for poly-axial volumetric sand production experiment with K_z = 1 and K_r = 1/3.

Fig. 4.26 shows the cumulative sand production from the experiment, numerical model with best A_1 (called original) and the one obtained from using the correlation Eq. 4.4 (called calibrated with bounds). The onset of sand production occurred when σ_R was 3,800 psi. The original A_1 strives to match the individual experimental result but the calibrated A_1 takes into account all the experimental results. Fig. 4.27 shows the comparison of sand rates between experiment and model.

Figs. A.2 - A.10 in Appendix A show the changes in ε^p, σ^e_{xx}, σ^e_{yy}, σ^e_{zz}, ε_{xx}, ε_{yy}, ε_{zz}, porosity and permeability between onset and end of simulation.

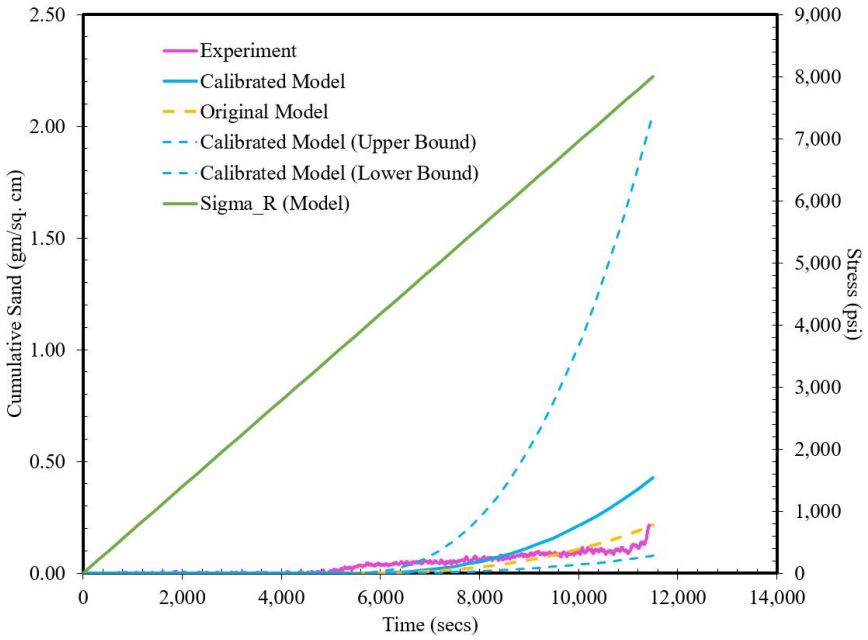

Figure 4.26: Cumulative sand mass comparison from experiment and numerical model with K_z = 1 and K_r = 1/3.

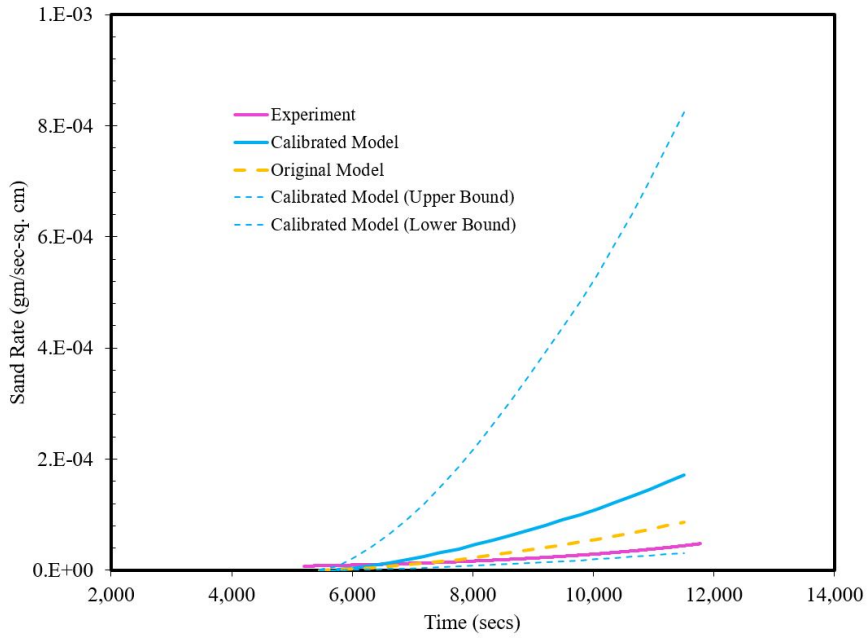

Figure 4.27: Sand rate comparison from experiment and numerical model with K_z = 1 and K_r = 1/3.

4.3.2.2 Case 02 - K_z = 1, K_r = 2/3

The second experiment being discussed here was carried out with no axial anisotropy and low lateral anisotropy of 2/3. The axial anisotropy is the ratio of vertical stress to maximum horizontal stress and the lateral anisotropy is the ratio of minimum horizontal stress to maximum horizontal stress. The specimen is saturated with 3.5% NaCl solution and kerosene oil is flowed through. The loading rate is 870 psi/hour and the fluid flow rate is maintained at 1.6 L/min. These data are shown with time in Fig. 4.28. The specimen properties are shown in Table 4.5.

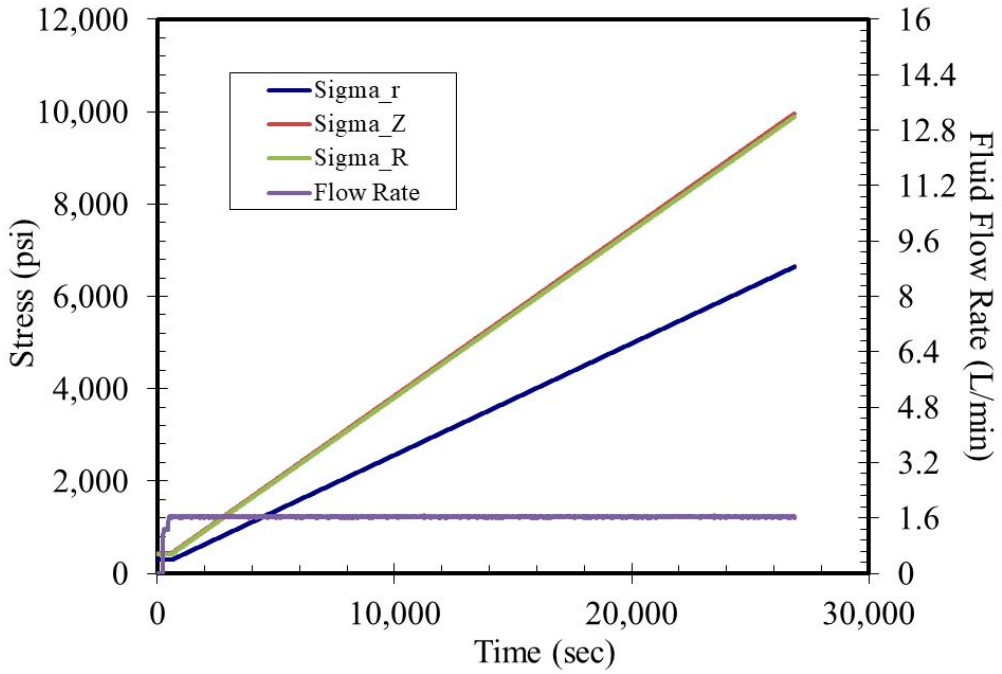

Figure 4.28: Three principal stresses and the fluid flow rate during the experimental run with K_z = 1 and K_r = 2/3.

The onset of sand production in the experiment is observed when σ_R is 4,351 psi. The sand rate varies a lot during the experiment run. Hence, for regularity and reproducibility, 2 gm of cumulative produced sand is always referred to (in this dissertation) when the onset of sand production happens. The sand production during the experiment is shown in Fig. 4.29. The total run time is

about 448 min in which the stresses are increased and sand production observed. The experiment is not run until total collapse of the specimen due to safety reasons.

Specimen Properties	
Rock	Castlegate sandstone (outcrop)
Specimen height	199.8 mm
Specimen internal diameter	19.9 mm
Specimen external diameter	199.8 mm
Angle of slabbed part	46.07°
Permeability	500 - 600 md
Porosity	26.6%
Fluid density	0.78 gm/cc
Fluid viscosity	1.4 cp
Solid density	2.65 gm/cc

Table 4.5: Specimen properties for poly-axial volumetric sand production experiment with K_z = 1 and K_r = 2/3.

The numerical simulation is setup such that the stresses increase with an increment step of 200 psi and flow rate is maintained at 0.8 L/min due to vertical symmetry. Table 4.6 shows the simulation conditions. Fig. 4.30 shows the stresses and flow rate during the simulation.

Comparing the experimental and simulation's cumulative sand production, a loading factor A_1 is calculated. Note that Eq. 4.4 also provides us with a best fit loading factor along with lower and upper bounds from Eq. 4.5 and Eq. 4.6 respectively. Fig. 4.31 shows the cumulative sand production from the experiment, numerical model with best A_1 (called original) and the one obtained from using the correlation Eq. 4.4 (called calibrated with bounds). The onset of sand production occurred when σ_R was 4,400 psi. The original A_1 strives to match the individual

experimental result but the calibrated A_1 takes into account all the experimental results. Fig. 4.32 shows the comparison of sand rates between experiment and model.

Figs. A.11 - A.19 in Appendix A show the changes in ε^p, σ^e_{xx}, σ^e_{yy}, σ^e_{zz}, ε_{xx}, ε_{yy}, ε_{zz}, porosity and permeability between onset and end of simulation.

Simulation Conditions	
Height	100 mm
Internal diameter	20 mm
External diameter	200 mm
Initial permeability	600 md
Initial Porosity	26%
Internal boundary pore pressure	0 psi
External boundary pore pressure	0.015 psi
Maximum σ_z	10,000 psi
Maximum σ_r	6,667 psi
Maximum σ_R	10,000 psi
Fluid density	0.78 gm/cc
Fluid viscosity	1.4 cp
Oil compressibility	1.068×10^{-5} 1/psi
Solid density	2.65 gm/cc
Failure criterion: Critical plastic strain (ε^p_c)	0.003671

Table 4.6: Simulation conditions for poly-axial volumetric sand production experiment with K_z = 1 and K_r = 2/3.

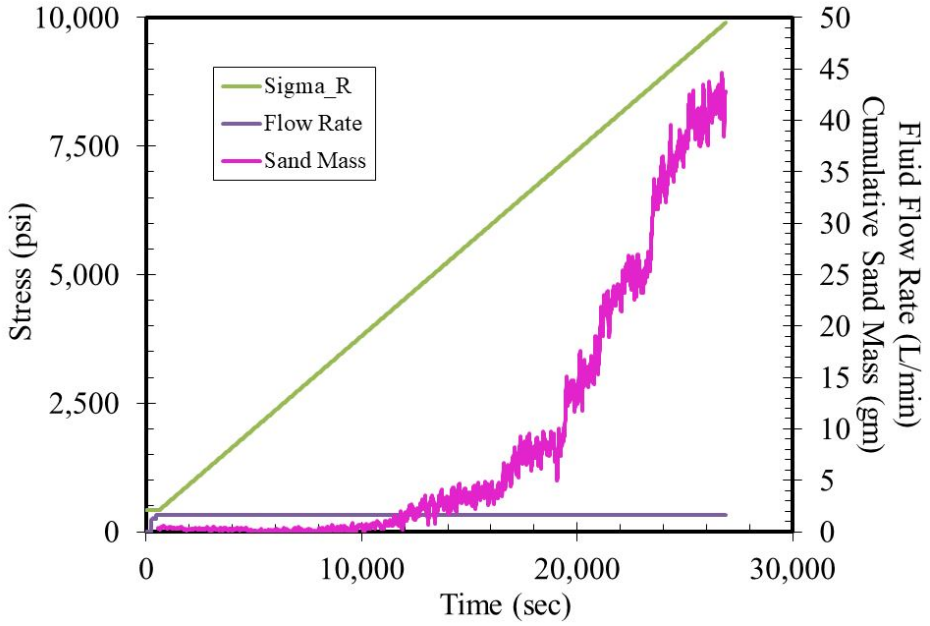

Figure 4.29: Three principal stresses and the fluid flow rate during the experimental run with K_z = 1 and K_r = 2/3.

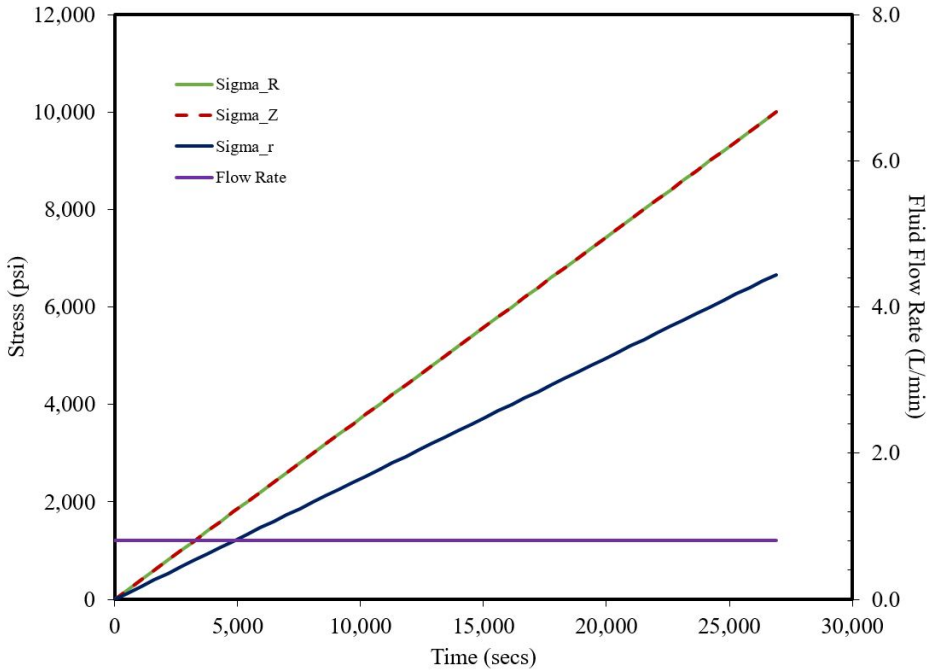

Figure 4.30: Three principal stresses and the fluid flow rate during the simulation run with K_z = 1 and K_r = 2/3.

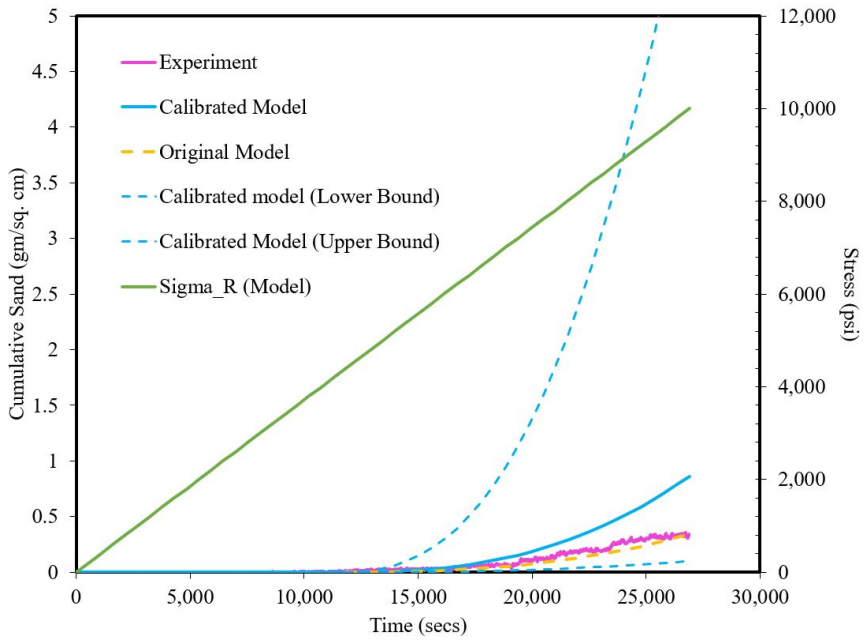

Figure 4.31: Cumulative sand mass comparison from experiment and numerical model with K_z = 1 and K_r = 2/3.

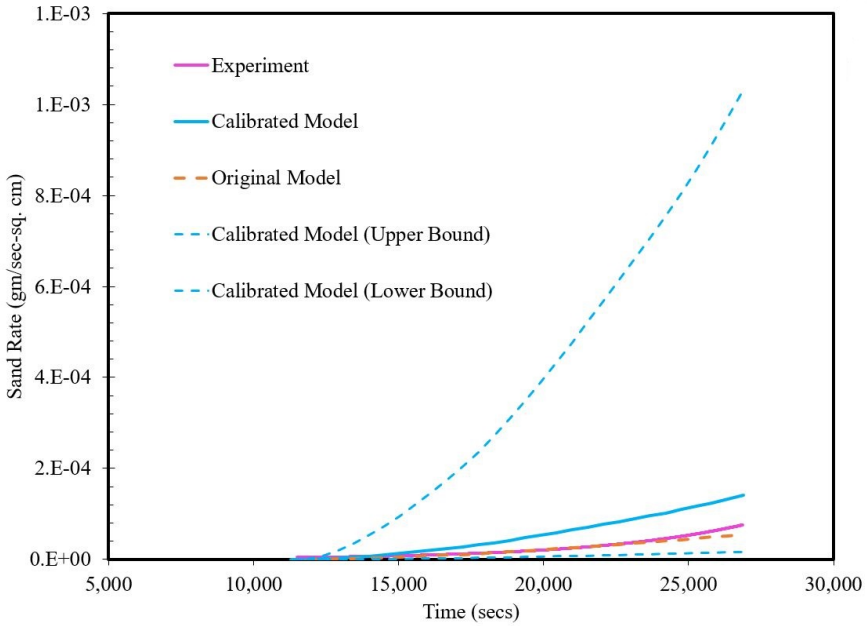

Figure 4.32: Sand rate comparison from experiment and numerical model with K_z = 1 and K_r = 2/3.

4.3.2.3 Case 03 - K_z = 2/3, K_r = 2/3

The third experiment being discussed here was carried out with low axial anisotropy and low lateral anisotropy of 2/3. The axial anisotropy is the ratio of vertical stress to maximum horizontal stress and the lateral anisotropy is the ratio of minimum horizontal stress to maximum horizontal stress. The specimens are saturated with 3.5% NaCl solution and kerosene oil is flowed through. The loading rate is 1,740 psi/hour and the fluid flow rate is maintained at 1.6 L/min. These data are shown with time in Fig. 4.33. The specimen properties are shown in Table 4.7.

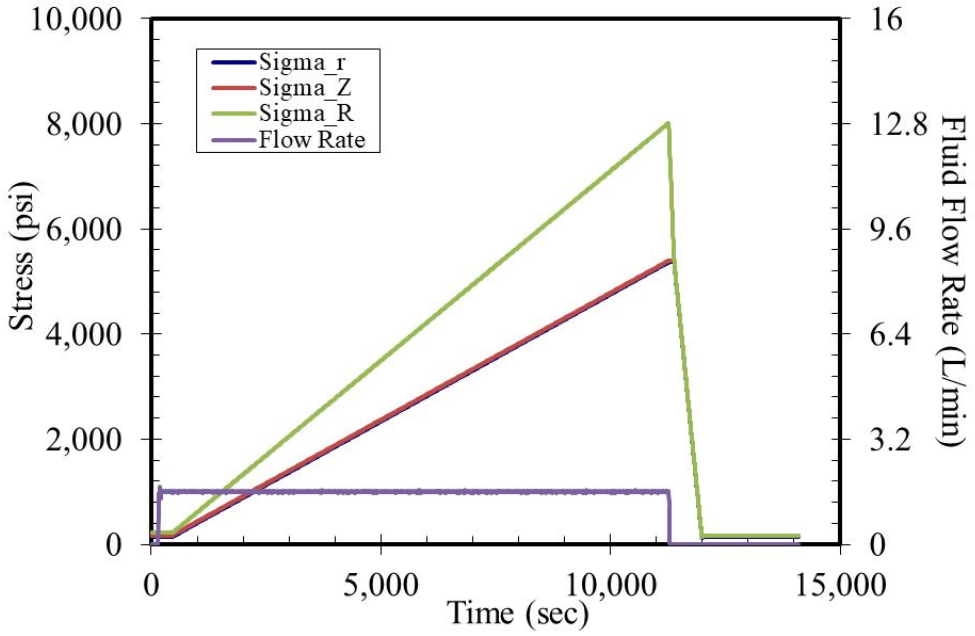

Figure 4.33: Three principal stresses and the fluid flow rate during the experimental run with K_z = 2/3 and K_r = 2/3.

The onset of sand production in the experiment is observed when σ_R was 4,786 psi. The sand rate varies a lot during the experiment run. Hence, for regularity and reproducibility, 2 gm of cumulative produced sand is always referred to (in this dissertation) when the onset of sand production happens. The sand production during the experiment is shown in Fig. 4.34. The total run time is about 235 min in which the stresses are increased and sand production is observed. The

experiment is not run until total collapse of the specimen due to safety reasons.

Specimen Properties	
Rock	Castlegate sandstone (outcrop)
Specimen height	199.7 mm
Specimen internal diameter	20.6 mm
Specimen external diameter	199.8 mm
Angle of slabbed part	46.20°
Permeability	500 - 600 md
Porosity	26.5%
Fluid density	0.78 gm/cc
Fluid viscosity	1.4 cp
Solid density	2.65 gm/cc

Table 4.7: Specimen properties for poly-axial volumetric sand production experiment with K_z = 2/3 and K_r = 2/3.

The numerical simulation is setup such that the stresses increase with an increment step of 200 psi and flow rate is maintained at 0.8 L/min due to vertical symmetry. Table 4.8 shows the simulation conditions. Fig. 4.35 shows the stresses and flow rate during the simulation.

Comparing the experimental and simulation's cumulative sand production, a loading factor A_1 is calculated. Note that Eq. 4.4 also provides us with a best fit loading factor along with lower and upper bounds from Eq. 4.5 and Eq. 4.6 respectively. Fig. 4.36 shows the cumulative sand production from the experiment, numerical model with best A_1 (called original) and the one obtained from using the correlation Eq. 4.4 (called calibrated with bounds). The onset of sand production occurred when σ_R was 4,400 psi. The original A_1 strives to match the individual experimental result but the calibrated A_1 takes into account all the experimental results. Fig. 4.37

shows the comparison of sand rates between experiment and model.

Figs. A.20 - A.28 in Appendix A show the changes in ε^p, σ^e_{xx}, σ^e_{yy}, σ^e_{zz}, ε_{xx}, ε_{yy}, ε_{zz}, porosity and permeability between onset and end of simulation.

Simulation Conditions	
Height	100 mm
Internal diameter	20 mm
External diameter	200 mm
Initial permeability	600 md
Initial Porosity	26%
Internal boundary pore pressure	0 psi
External boundary pore pressure	0.015 psi
Maximum σ_z	5,333 psi
Maximum σ_r	5,333 psi
Maximum σ_R	8,000 psi
Fluid density	0.78 gm/cc
Fluid viscosity	1.4 cp
Oil compressibility	1.068×10^{-5} 1/psi
Solid density	2.65 gm/cc
Failure criterion: Critical plastic strain (ε^p_c)	0.003671

Table 4.8: Simulation conditions for poly-axial volumetric sand production experiment with K_z = 2/3 and K_r = 2/3.

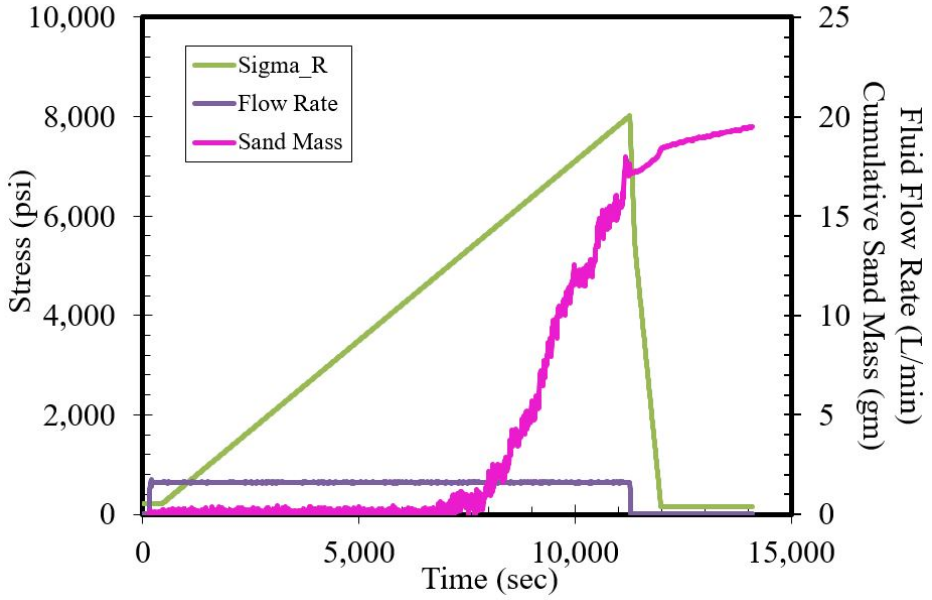

Figure 4.34: σ_R, cumulative sand production and the fluid flow rate during the experimental run with K_z = 2/3 and K_r = 2/3.

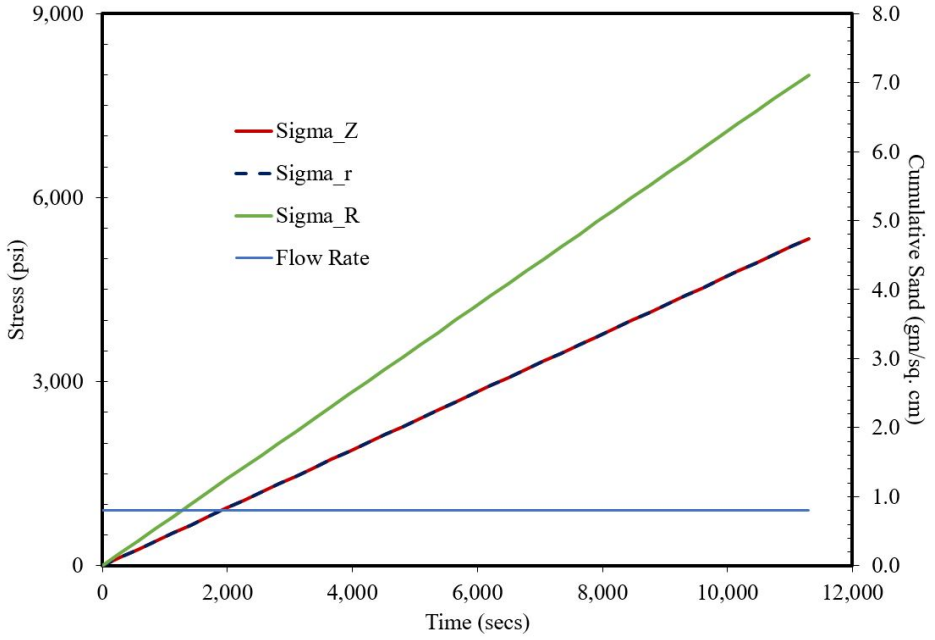

Figure 4.35: Three principal stresses and the fluid flow rate during the simulation run with K_z = 2/3 and K_r = 2/3.

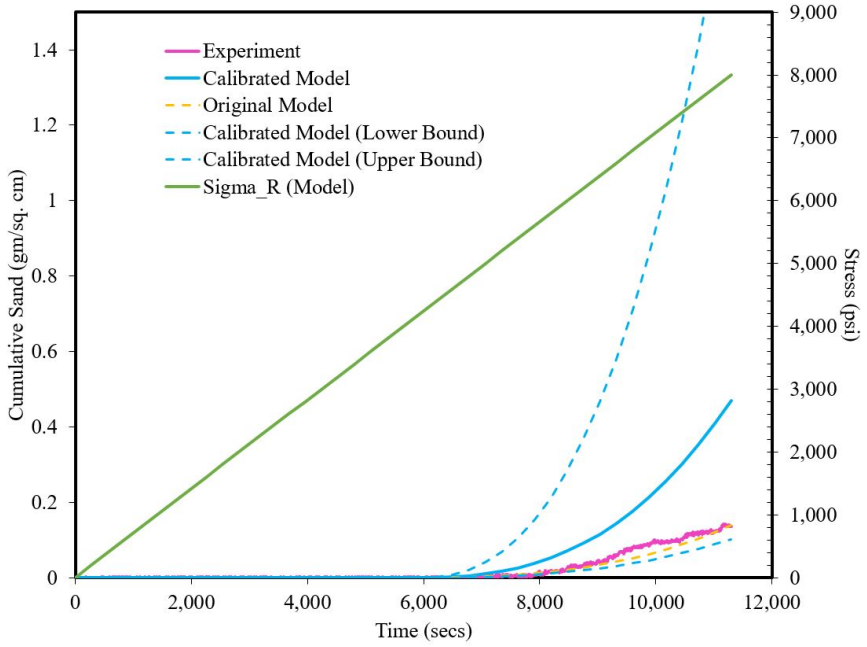

Figure 4.36: Cumulative sand mass comparison from experiment and numerical model with K_z = 2/3 and K_r = 2/3.

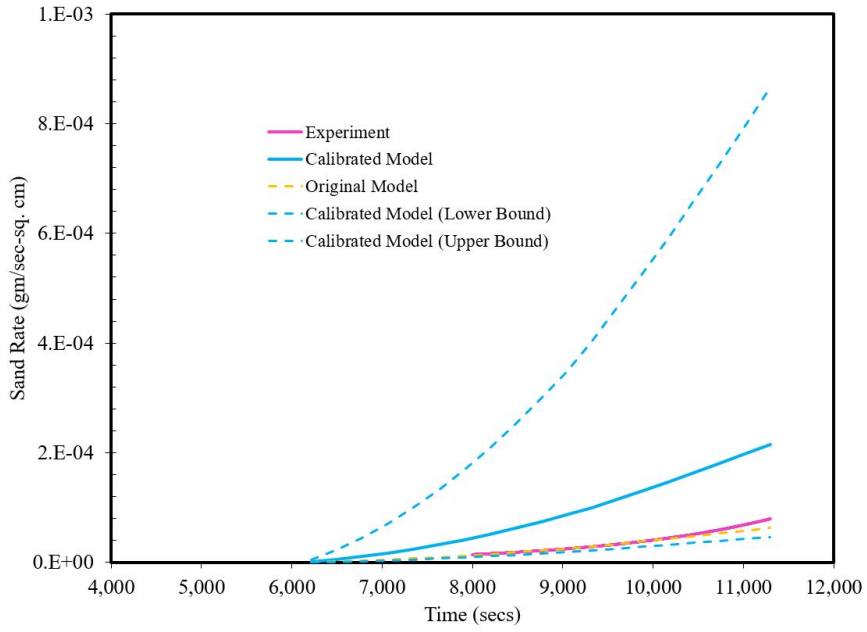

Figure 4.37: Sand rate comparison from experiment and numerical model with K_z = 2/3 and K_r = 2/3.

4.3.2.4 Case 04 - K_z = 4/3, K_r = 2/3

The fourth experiment being discussed here was carried out with low axial anisotropy of 4/3 and low lateral anisotropy of 2/3. The axial anisotropy is the ratio of vertical stress to maximum horizontal stress and the lateral anisotropy is the ratio of minimum horizontal stress to maximum horizontal stress. The specimen is saturated with 3.5% NaCl solution and kerosene oil is flowed through. The loading rate is 1,740 psi/hour and the fluid flow rate is maintained at 1.6 L/min. These data are shown with time in Fig. 4.38. The specimen properties are shown in Table 4.9.

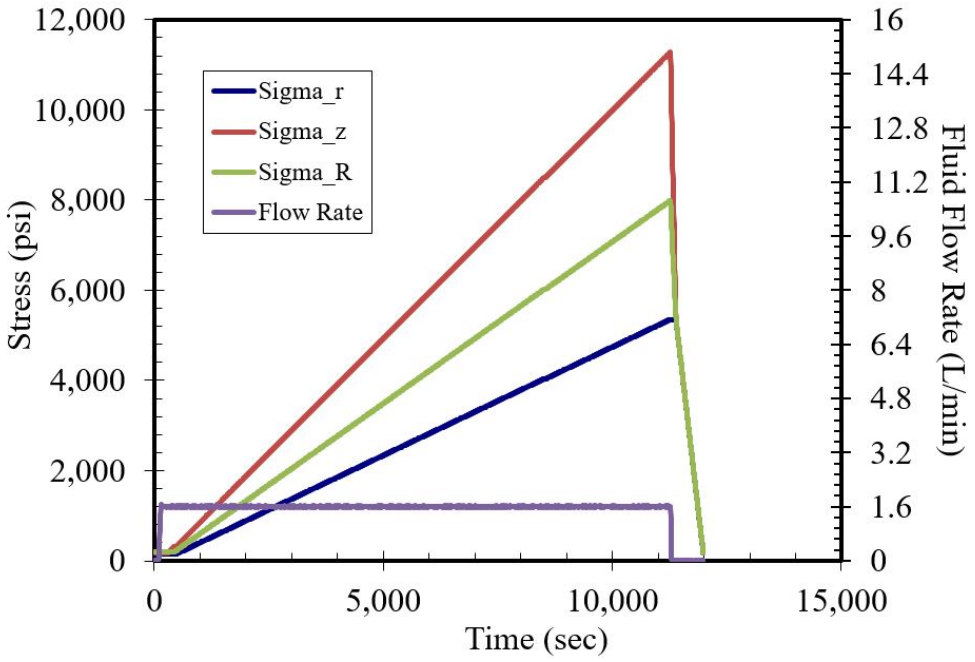

Figure 4.38: Three principal stresses and the fluid flow rate during the experimental run with K_z = 4/3 and K_r = 2/3.

The onset of sand production in the experiment is observed when σ_R was 4,496 psi. The sand rate varies a lot during the experiment. Hence, for regularity and reproducibility, 2 gm of cumulative produced sand is always referred to (in this dissertation) when the onset of sand production happens. The sand production during the experiment is shown in Fig. 4.39. The total run time is

about 200 min in which the stresses are increased and sand production is observed. The experiment is not run until the total collapse of the specimen due to safety reasons.

Specimen Properties	
Rock	Castlegate sandstone (outcrop)
Specimen height	199.8 mm
Specimen internal diameter	19.7 mm
Specimen external diameter	199.5 mm
Angle of slabbed part	46.04°
Permeability	500 - 600 md
Porosity	26.5%
Fluid density	0.78 gm/cc
Fluid viscosity	1.4 cp
Solid density	2.65 gm/cc

Table 4.9: Specimen properties for poly-axial volumetric sand production experiment with K_z = 2/3 and K_r = 2/3.

The numerical simulation is setup such that the stresses increase with an increment step of 200 psi and flow rate is maintained at 0.8 L/min due to vertical symmetry. Table 4.10 shows the simulation conditions. Fig. 4.40 shows the stresses and flow rate during the simulation.

Comparing the experimental and simulation's cumulative sand production, a loading factor A_1 is calculated. Note that Eq. 4.4 also provides us with a best fit loading factor along with lower and upper bounds from Eq. 4.5 and Eq. 4.6 respectively. Fig. 4.41 shows the cumulative sand production from the experiment, numerical model with best A_1 (called original) and the one obtained from using the correlation given by Eq. 4.4 (called calibrated with bounds). The onset of sand production is when σ_R is 4,350 psi. The original A_1 strives to match the individual

experimental result but the calibrated A_1 takes into account all the experimental results. Fig. 4.42 shows the comparison of sand rates between experiment and model.

Figs. A.29 - A.37 in Appendix A show the changes in ε^p, σ^e_{xx}, σ^e_{yy}, σ^e_{zz}, ε_{xx}, ε_{yy}, ε_{zz}, porosity and permeability between onset and end of simulation.

Simulation Conditions	
Height	100 mm
Internal diameter	20 mm
External diameter	200 mm
Initial permeability	600 md
Initial Porosity	26%
Internal boundary pore pressure	0 psi
External boundary pore pressure	0.015 psi
Maximum σ_z	10,800 psi
Maximum σ_r	5,400 psi
Maximum σ_R	8,100 psi
Fluid density	0.78 gm/cc
Fluid viscosity	1.4 cp
Oil compressibility	1.068×10^{-5} 1/psi
Solid density	2.65 gm/cc
Failure criterion: Critical plastic strain (ε^p_c)	0.003671

Table 4.10: Simulation conditions for poly-axial volumetric sand production experiment with K_z = 4/3 and K_r = 2/3.

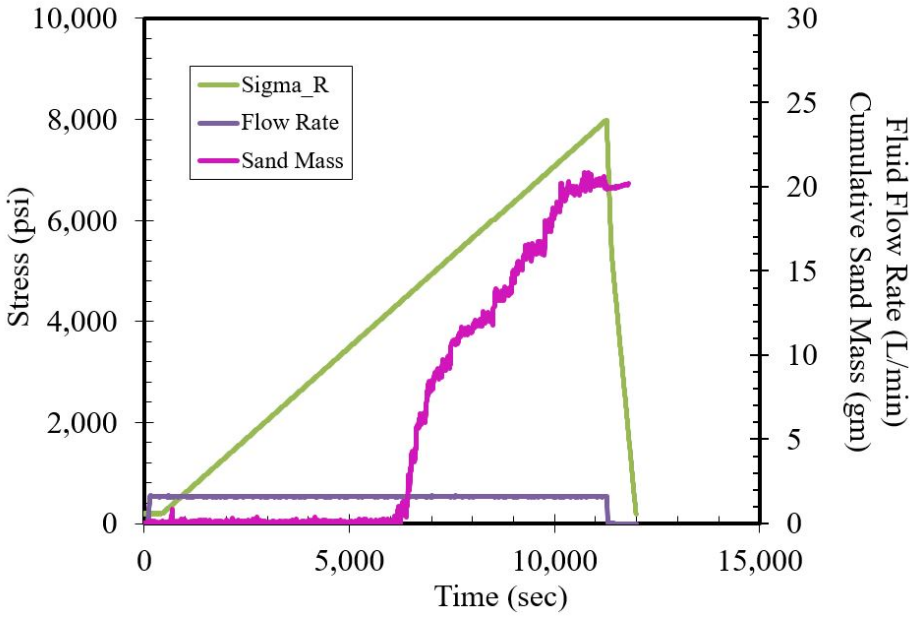

Figure 4.39: σ_R, cumulative sand production and the fluid flow rate during the experimental run with K_z = 4/3 and K_r = 2/3.

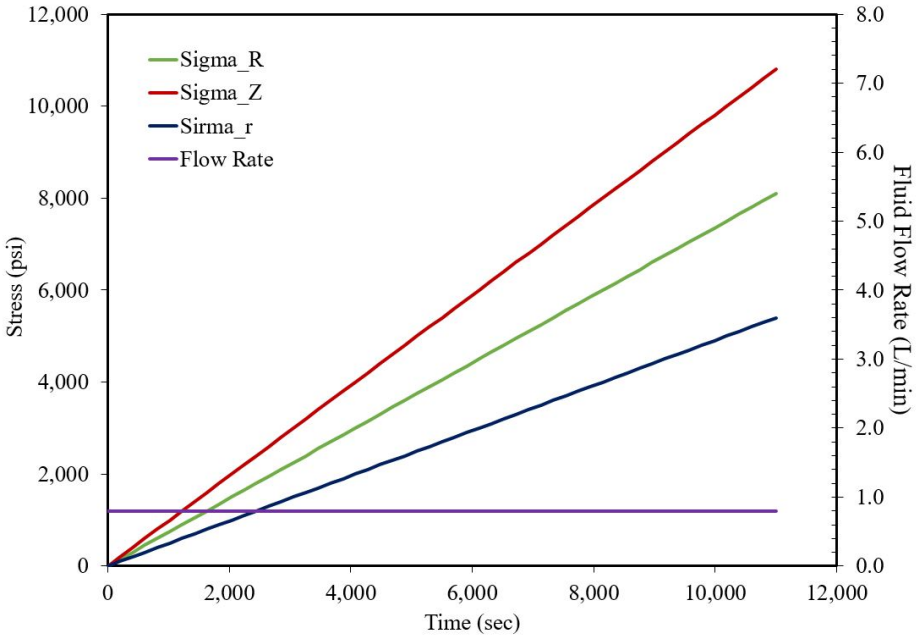

Figure 4.40: Three principal stresses and the fluid flow rate during the simulation run with K_z = 4/3 and K_r = 2/3.

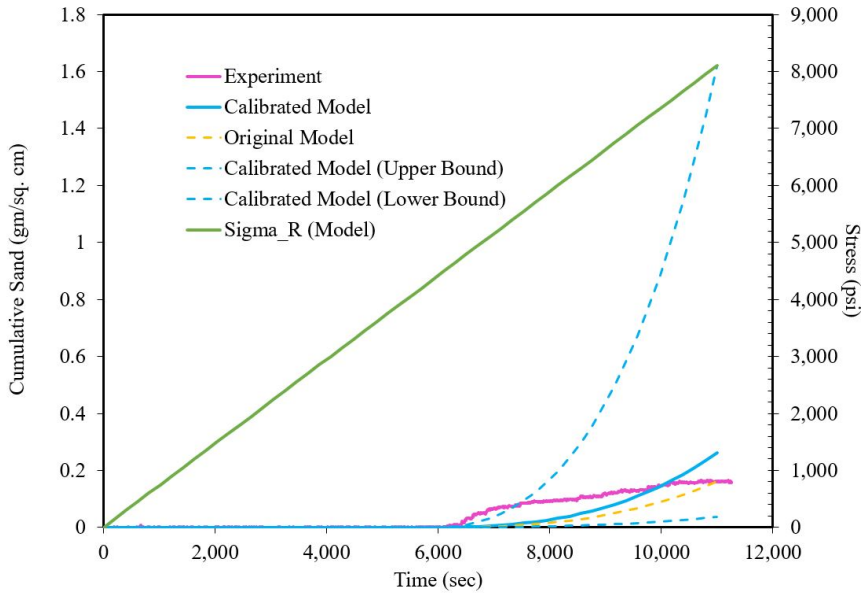

Figure 4.41: Cumulative sand mass comparison from experiment and numerical model with K_z = 4/3 and K_r = 2/3.

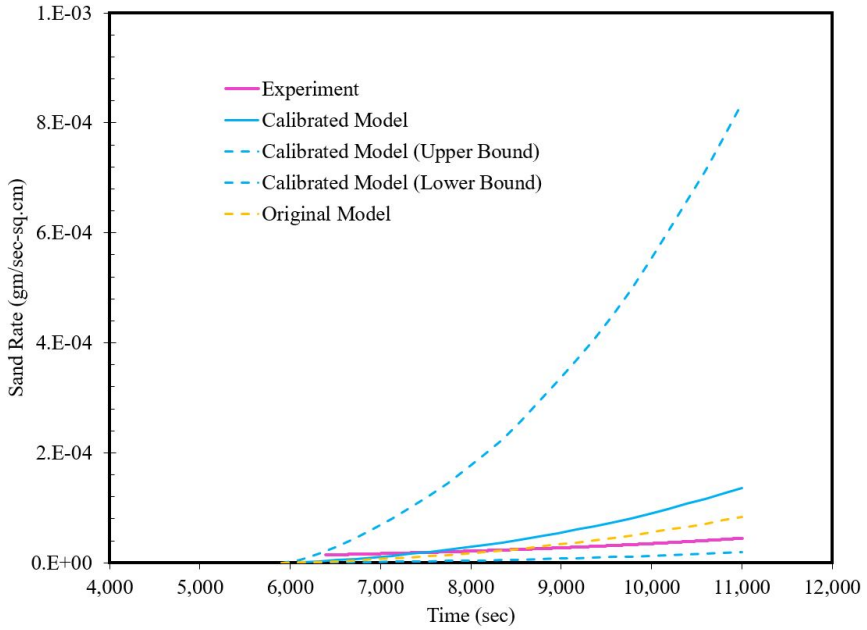

Figure 4.42: Sand rate comparison from experiment and numerical model with K_z = 2/3 and K_r = 2/3.

4.3.2.5 Case 05 - K_z = 2, K_r = 2/3

The fifth experiment being discussed here was carried out with high axial anisotropy of 2 and low lateral anisotropy of 2/3. The axial anisotropy is the ratio of vertical stress to maximum horizontal stress and the lateral anisotropy is the ratio of minimum horizontal stress to maximum horizontal stress. The specimen is saturated with 3.5% NaCl solution and kerosene oil is flowed through. The loading rate is 870 psi/hour and the fluid flow rate is maintained at 1.6 L/min. These data are shown with time in Fig. 4.43. The specimen properties are shown in Table 4.11.

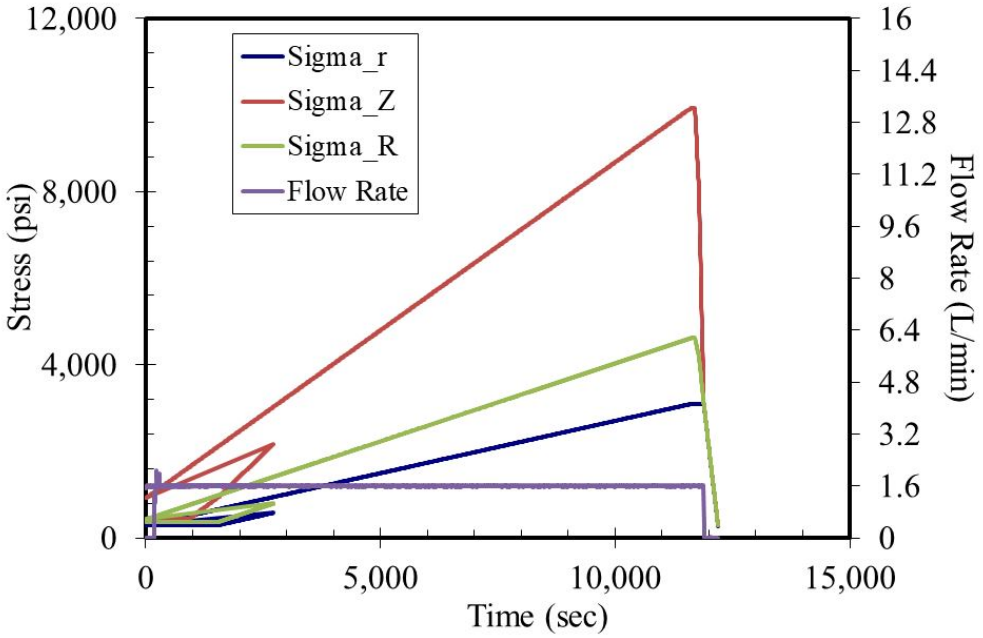

Figure 4.43: Three principal stresses and the fluid flow rate during the experimental run with K_z = 2 and K_r = 2/3.

The onset of sand production in the experiment is observed when σ_R was 3,771 psi. The sand rate varies a lot during the experiment. Hence, for regularity and reproducibility, 2 gm of cumulative produced sand is always referred to (in this dissertation) when the onset of sand production happens. The sand production during the experiment is shown in Fig. 4.44. The total run time is

about 200 min in which the stresses are increased and sand production is observed. The experiment is not run until the total collapse of the specimen due to safety reasons.

Specimen Properties	
Rock	Castlegate sandstone (outcrop)
Specimen height	200.0 mm
Specimen internal diameter	19.9 mm
Specimen external diameter	199.7 mm
Angle of slabbed part	45.96°
Permeability	500 - 600 md
Porosity	26.3%
Fluid density	0.78 gm/cc
Fluid viscosity	1.4 cp
Solid density	2.65 gm/cc

Table 4.11: Specimen properties for poly-axial volumetric sand production experiment with K_z = 2 and K_r = 2/3.

The numerical simulation is setup such that the stresses increase with an increment step of 200 psi and flow rate is maintained at 0.8 L/min due to vertical symmetry. Table 4.12 shows the simulation conditions. Fig. 4.45 shows the stresses and flow rate during the simulation.

Comparing the experimental and simulation's cumulative sand production, a loading factor A_1 is calculated. Note that Eq. 4.4 also provides us with a best fit loading factor along with lower and upper bounds from Eq. 4.5 and Eq. 4.6. Fig. 4.46 shows the cumulative sand production from the experiment, numerical model with best A_1 (called original) and the one obtained from using the correlation given by Eq. 4.4 (called calibrated with bounds). The onset of sand production occurred when σ_R was 3,900 psi. The original A_1 strives to match the individual experimental

result but the calibrated A_1 takes into account all the experimental results. Fig. 4.47 shows the comparison of sand rates between experiment and model.

Figs. A.38 - A.46 in Appendix A show the changes in ε^p, σ^e_{xx}, σ^e_{yy}, σ^e_{zz}, ε_{xx}, ε_{yy}, ε_{zz}, porosity and permeability between onset and end of simulation.

Simulation Conditions	
Height	100 mm
Internal diameter	20 mm
External diameter	200 mm
Initial permeability	600 md
Initial Porosity	26%
Internal boundary pore pressure	0 psi
External boundary pore pressure	0.015 psi
Maximum σ_z	10,000 psi
Maximum σ_r	3,333 psi
Maximum σ_R	5,000 psi
Fluid density	0.78 gm/cc
Fluid viscosity	1.4 cp
Oil compressibility	1.068×10^{-5} 1/psi
Solid density	2.65 gm/cc
Failure criterion: Critical plastic strain (ε^p_c)	0.003671

Table 4.12: Simulation conditions for poly-axial volumetric sand production experiment with K_z = 2 and K_r = 2/3.

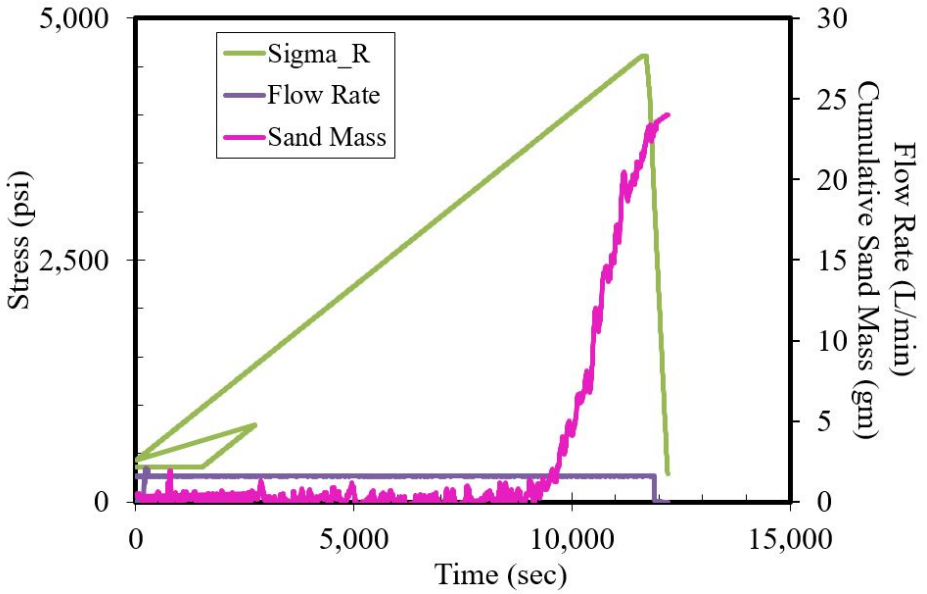

Figure 4.44: σ_R, cumulative sand production and the fluid flow rate during the experimental run with K_z = 2 and K_r = 2/3.

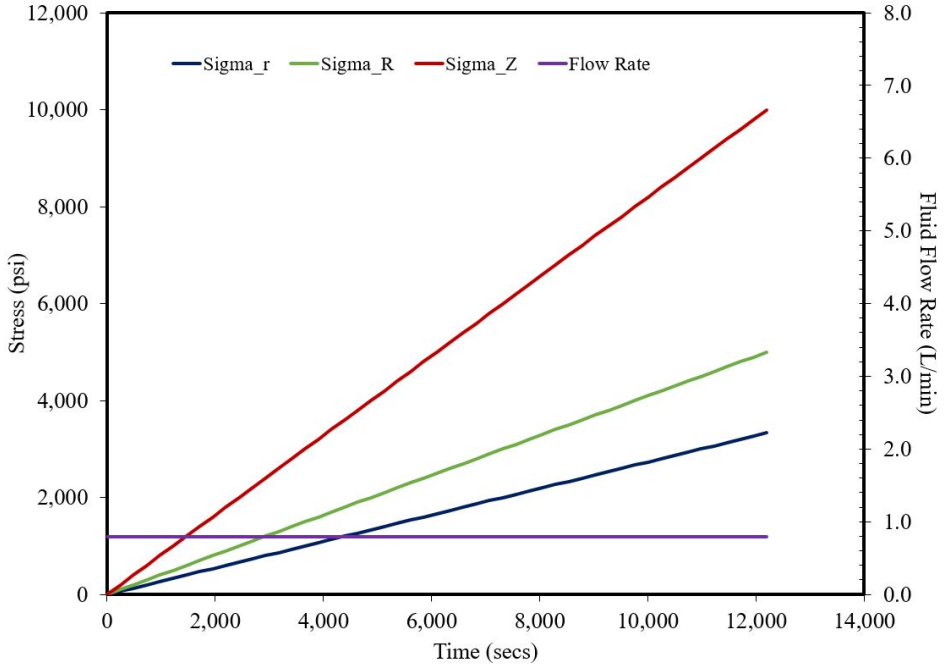

Figure 4.45: Three principal stresses and the fluid flow rate during the simulation run with K_z = 2 and K_r = 2/3.

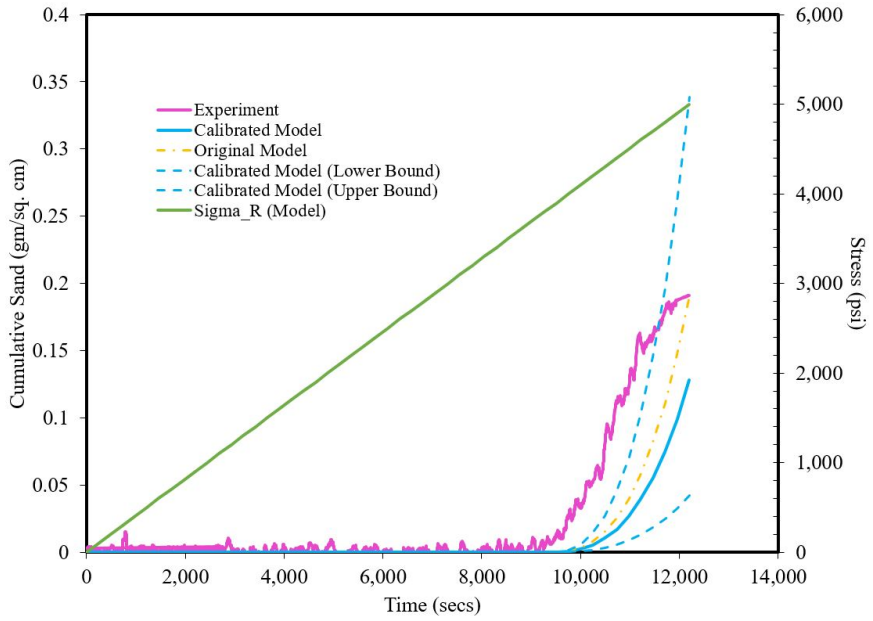

Figure 4.46: Cumulative sand mass comparison from experiment and numerical model with K_z = 2 and K_r = 2/3.

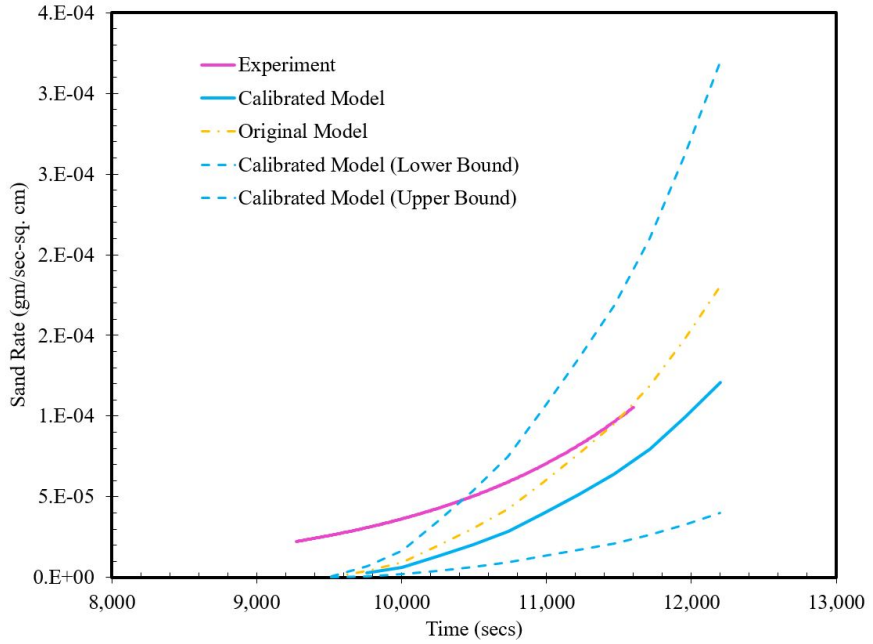

Figure 4.47: Sand rate comparison from experiment and numerical model with K_z = 2 and K_r = 2/3.

4.3.2.6 *Case 06 - K_z = 1, K_r = 1*

The last experiment being discussed here was carried out with neither axial nor lateral anisotropy. The axial anisotropy is the ratio of vertical stress to maximum horizontal stress and the lateral anisotropy is the ratio of minimum horizontal stress to maximum horizontal stress. The specimen is saturated with 3.5% NaCl solution and kerosene oil is flowed through. The loading rate is 2,900 psi/hour initially and 1,450 psi/hour later. This was done since the test was restarted due to confining pressure bleeding. The fluid flow rate is maintained at 1.6 L/min. These data are shown with time in Fig. 4.48. The specimen properties are shown in Table 4.13.

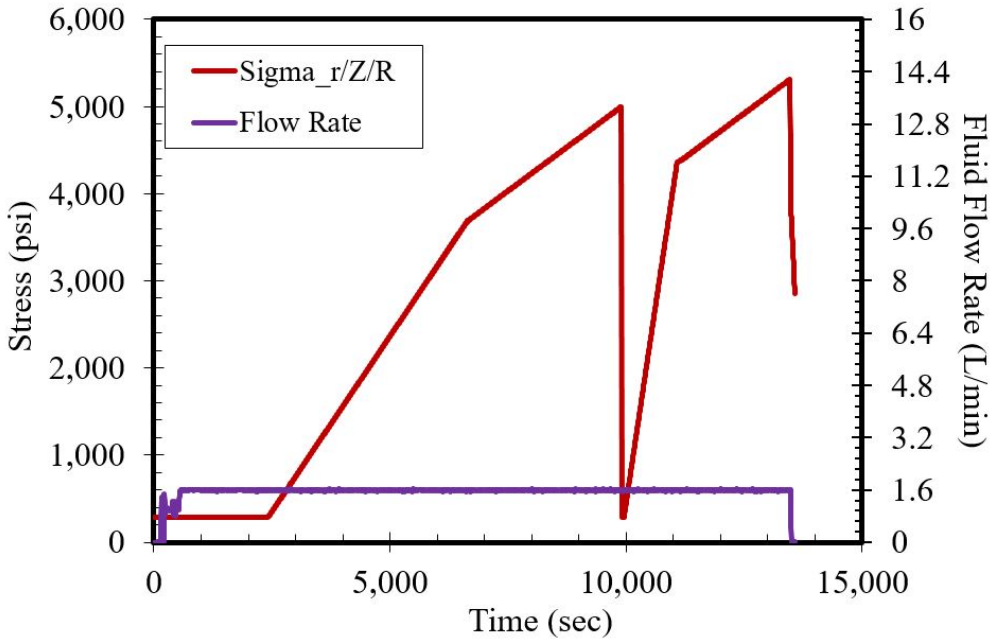

Figure 4.48: Three principal stresses and the fluid flow rate during the experimental run with K_z = 1 and K_r = 1.

The onset of sand production in the experiment is observed when σ_R was 4,931 psi. The sand rate varies a lot during the experiment. Hence, for regularity and reproducibility, 2 gm of cumulative produced sand is always referred to (in this dissertation) when the onset of sand production happens. The sand production during the experiment is shown in Fig. 4.49. The total run time

is about 175 min excluding the restart in which the stresses are increased and sand production observed. The experiment is not run until the total collapse of the specimen due to safety reasons.

Specimen Properties	
Rock	Castlegate sandstone (outcrop)
Specimen height	200.0 mm
Specimen internal diameter	19.9 mm
Specimen external diameter	199.7 mm
Angle of slabbed part	46.09°
Permeability	500 - 600 md
Porosity	26.3%
Fluid density	0.78 gm/cc
Fluid viscosity	1.4 cp
Solid density	2.65 gm/cc

Table 4.13: Specimen properties for poly-axial volumetric sand production experiment with K_z = 1 and K_r = 1.

The numerical simulation is setup such that the stresses increase with an increment step of 200 psi until they reach 5,000 psi and thereafter with a step of 40 psi. The flow rate is maintained at 0.8 L/min due to vertical symmetry. Table 4.14 shows the simulation conditions. Fig. 4.50 shows the stresses and flow rate during the simulation.

Comparing the experimental and simulation's cumulative sand production, a loading factor A_1 is calculated. Note that Eq. 4.4 also provides us with a best fit loading factor along with lower and upper bounds from Eq. 4.5 and Eq. 4.6 respectively. Fig. 4.51 shows the cumulative sand production from the experiment, numerical model with best A_1 (called original) and the one obtained from using the correlation given by Eq. 4.4 (called calibrated with bounds). The onset of

sand production occurred when σ_R was 5,120 psi. The original A_1 strives to match the individual experimental result but the calibrated A_1 takes into account all the experimental results. Fig. 4.52 shows the comparison of sand rates between experiment and model.

Figs. A.47 - A.55 in Appendix A show the changes in ε^p, σ^e_{xx}, σ^e_{yy}, σ^e_{zz}, ε_{xx}, ε_{yy}, ε_{zz}, porosity and permeability between onset and end of simulation.

Simulation Conditions	
Height	100 mm
Internal diameter	20 mm
External diameter	200 mm
Initial permeability	600 md
Initial Porosity	26%
Internal boundary pore pressure	0 psi
External boundary pore pressure	0.015 psi
Maximum σ_z	5,400 psi
Maximum σ_r	5,400 psi
Maximum σ_R	5,400 psi
Fluid density	0.78 gm/cc
Fluid viscosity	1.4 cp
Oil compressibility	1.068×10^{-5} 1/psi
Solid density	2.65 gm/cc
Failure criterion: Critical plastic strain (ε^p_c)	0.003671

Table 4.14: Simulation conditions for poly-axial volumetric sand production experiment with K_z = 1 and K_r = 1.

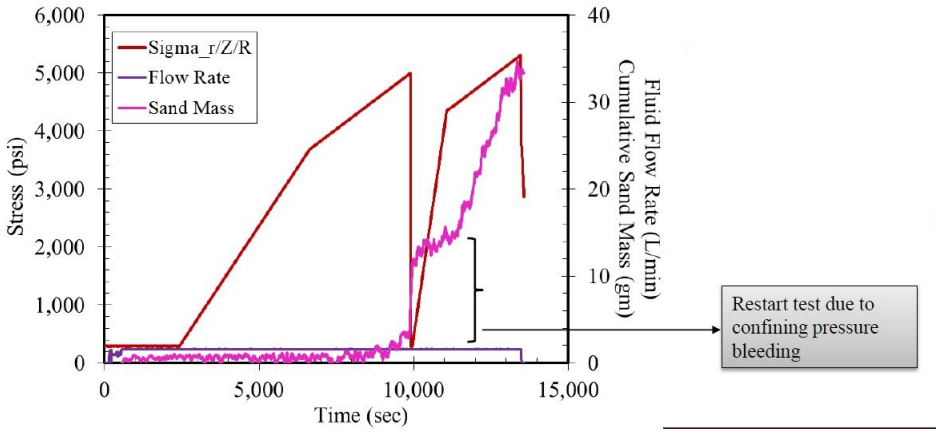

Figure 4.49: σ_R, cumulative sand production and the fluid flow rate during the experimental run with K_z = 1 and K_r = 1.

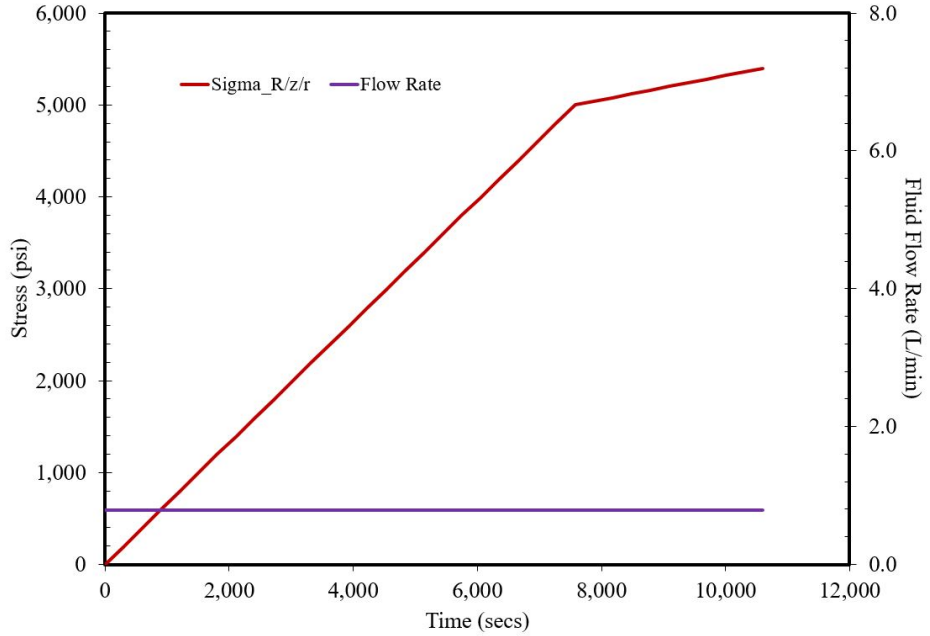

Figure 4.50: Three principal stresses and the fluid flow rate during the simulation run with K_z = 1 and K_r = 1.

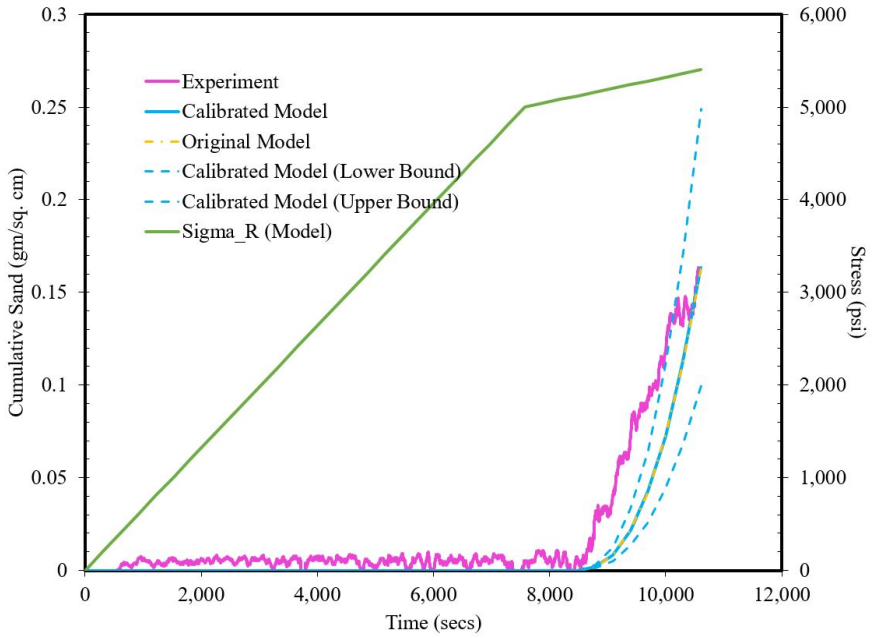

Figure 4.51: Cumulative sand mass comparison from experiment and numerical model with K_z = 1 and K_r = 1.

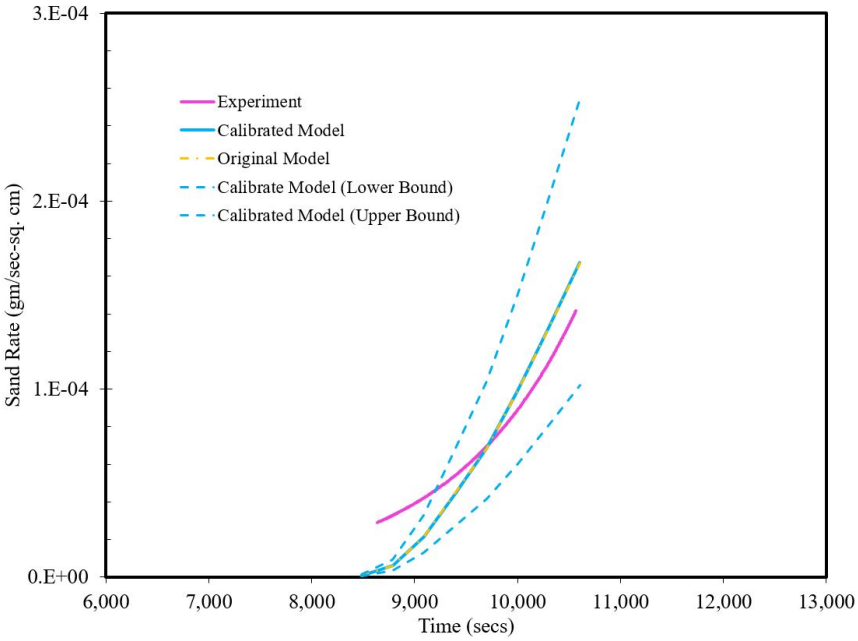

Figure 4.52: Sand rate comparison from experiment and numerical model with K_z = 1 and K_r = 1.

4.3.2.7 *Results Comparison*

In the previous sections results for individual experiment and simulation were shared in detail. One of the objective of this study is to determine the effect of axial and lateral anisotropy on onset of sand production and their rates. In experiments and simulations alike, the anisotropy in both the directions are kept constant throughout their runtime. However during field operations, this may not be the case. The axial and lateral stress anisotropies may change with reservoir depletion and this may affect the onset of sand production. Fig. 4.53 shows the comparison of all the experiments and their simulation onset results. Looking at the figure, one can conclude that the model is well equipped with estimating the onset of sand production. The prediction accuracy of the model for onset is within $\pm 10\%$. There is no indication that experimental results are consistently higher or lower than that of models'. σ_R is being used for comparisons here.

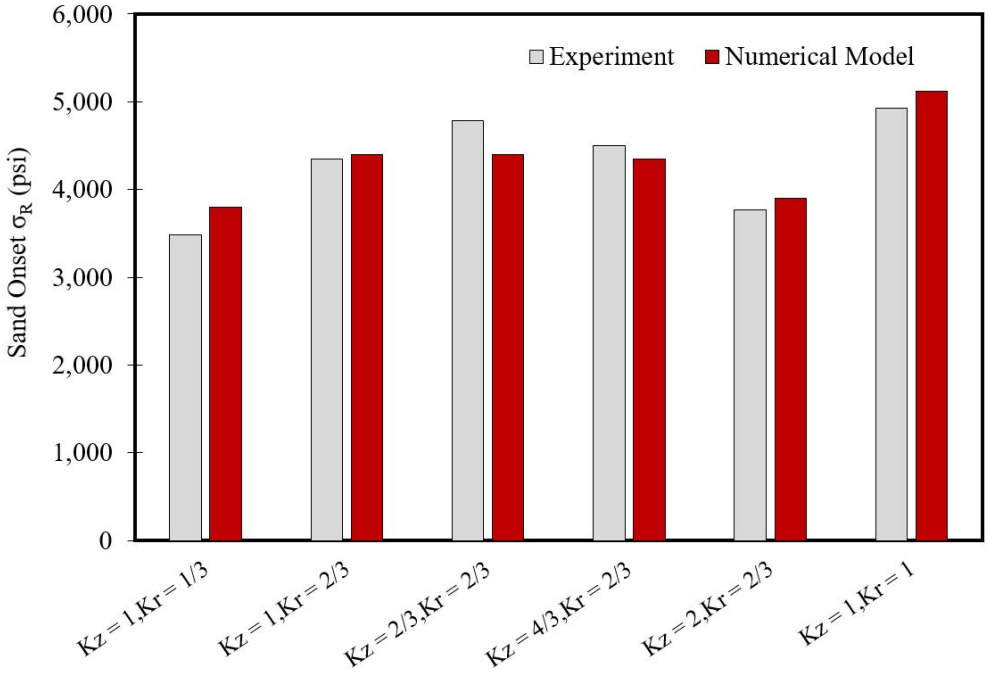

Figure 4.53: Sand onset comparison between all the experiments and numerical models.

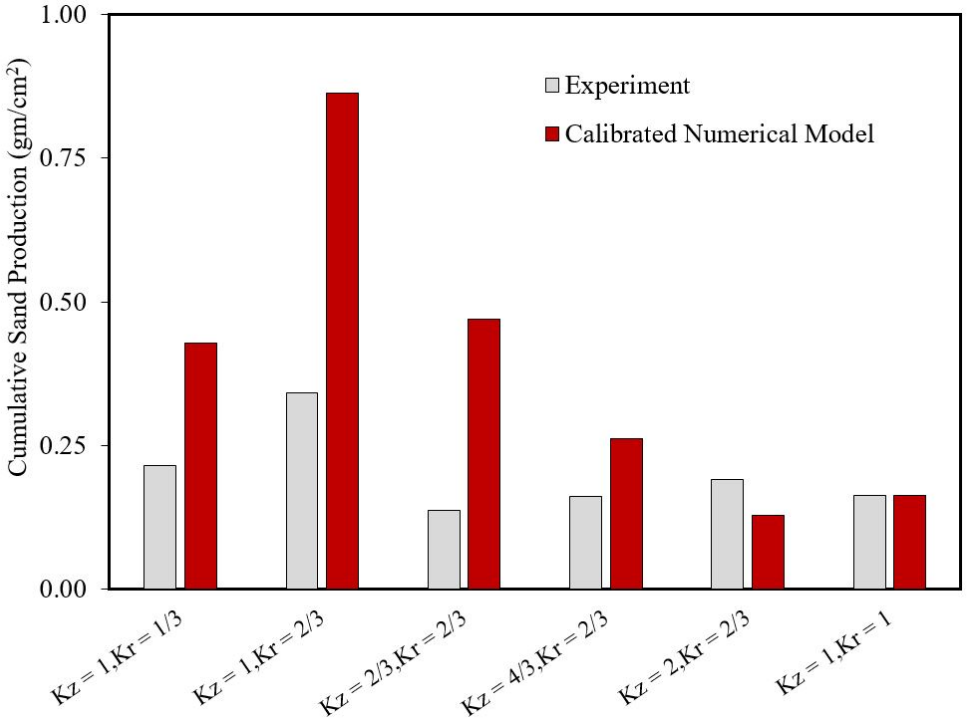

Figure 4.54: Cumulative sand production comparison between all the experiments and calibrated numerical models.

Fig. 4.54 shows the comparison between cumulative sand production from experiments and calibrated numerical models. There are several sources of errors involved during the measurement of sand rates during the experiments. Such as incorrect calibration of sand trap due to overuse, geometric and material properties differences among specimens, loading rates etc. The combination of all these factors produce highly variable experimental sand rates over time. Thus the process of exactly matching sand rates is still elusive and a better approach is to look at cumulative production of sand. The average ratio of produced sand from experiment and calibrated model given by Eq. 4.8 is calculated to be 0.72.

$$\frac{1}{6}\sum_{i=1}^{6}\frac{M_{exp}^{i}}{M_{model}^{i}} \tag{4.8}$$

where M_{exp} and M_{model} are the cumulative sand mass produced from experiment and calibrated model respectively. The lower and upper bounds of this ratio are found to be 0.25 and 3 respectively.

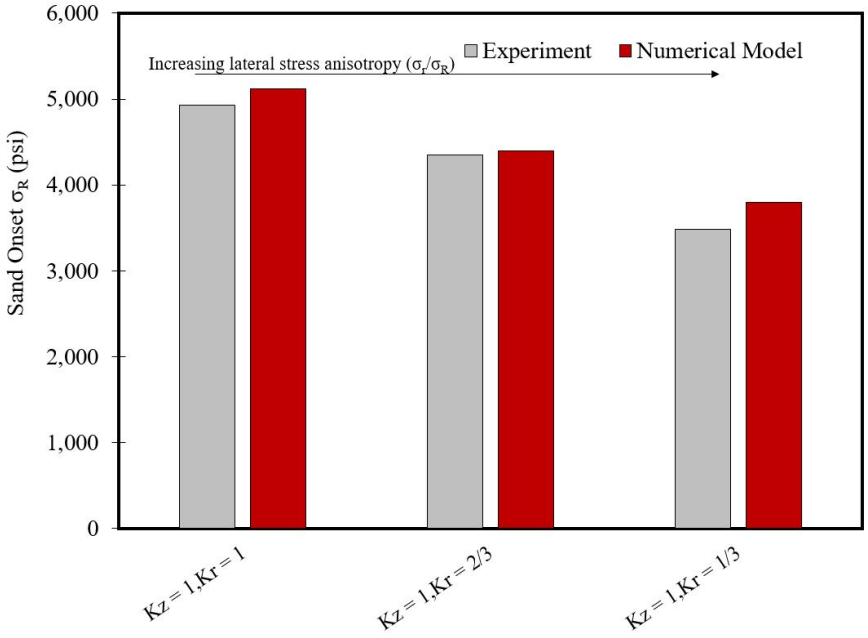

Figure 4.55: Sand onset comparison between all the experiments and numerical models due to lateral anisotropy.

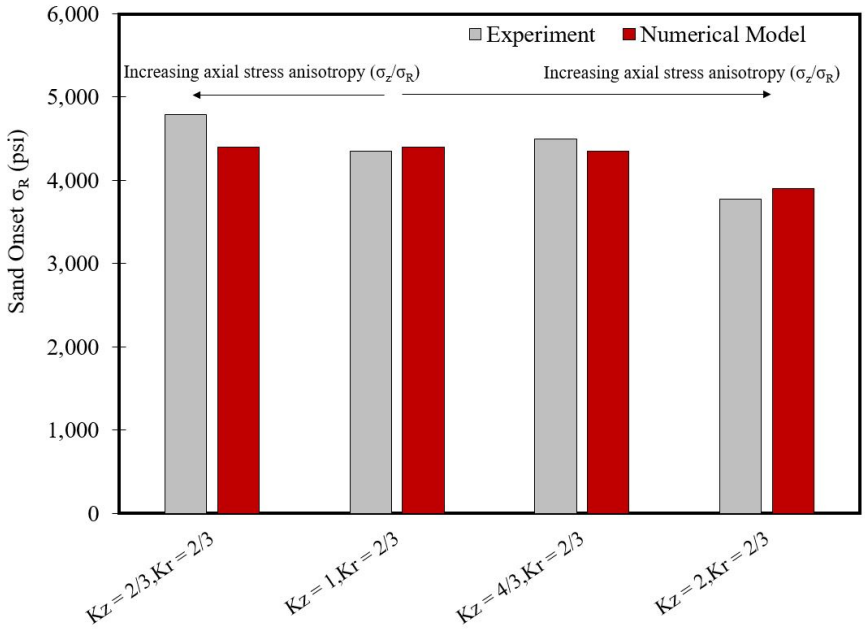

Figure 4.56: Sand onset comparison between all the experiments and numerical models due to axial anisotropy.

The effect of lateral and axial anisotropies can be judged from Fig. 4.55 and 4.56 respectively. The resulting trends from experiments and numerical models are similar. It can be observed that with increasing lateral anisotropy, while axial is kept constant, onset stress decreases. In turn, it would increase sand production potential and will result in earlier sand production. On the other hand, effect of increasing axial anisotropy (keeping lateral constant) on sand onset is ambiguous.

For this purpose, a separate study was done where numerical models were run with change in axial anisotropy keeping that of lateral constant. The material constitutive relations are that of Castlegate outcrop sandstone. The summary of all the model runs are included in Table 4.15.

ID	**Material**	$\mathbf{K_z}(\frac{\sigma_z}{\sigma_R})$	$\mathbf{K_r}(\frac{\sigma_r}{\sigma_R})$
01	Castlegate	1/3	1, 1/3
02	Castlegate	2/3	1, 1/3
03	Castlegate	4/5	1, 1/3
04	Castlegate	1	1, 1/3
05	Castlegate	4/3	1, 1/3
06	Castlegate	5/3	1, 1/3
07	Castlegate	7/4	1, 1/3
08	Castlegate	2	1, 1/3
09	Castlegate	9/4	1, 1/3

Table 4.15: Summary of the numerical models for undersanding the effect of varying axial stress anisotropy.

Many of the simulation conditions are common in all the runs as listed in Table 4.16. The numerical simulation is setup such that the σ_R increase with an increment step of 200 psi and the flow rate is maintained at 0.8 L/min due to vertical symmetry.

Simulation Conditions	
Height	100 mm
Internal diameter	20 mm
External diameter	200 mm
Initial permeability	600 md
Initial Porosity	26%
Internal boundary pore pressure	0 psi
External boundary pore pressure	0.015 psi
Fluid density	0.78 gm/cc
Fluid viscosity	1.4 cp
Oil compressibility	1.068×10^{-5} 1/psi
Solid density	2.65 gm/cc
Failure criterion: Critical plastic strain (ε_c^p)	0.003671

Table 4.16: Simulation conditions for poly-axial volumetric sand production numerical models summarized in Table 4.15.

The results from the cases run are unambiguous and ascertain that increasing axial anisotropy increases sand production potential and leads to earlier sand onset. Fig. 4.57 and 4.58 show the onset of sand production from the simulation in terms of σ_R. The stress steps are taken at 200 psi hence all the onsets are estimated in multiples of 200 psi. The model's prediction accuracy for sand onset has been previously calculated to be $\pm 10\%$. This is applicable here too. The effect of high lateral anisotropy is evident in Fig. 4.58 where onset is earlier as compared to 4.57.

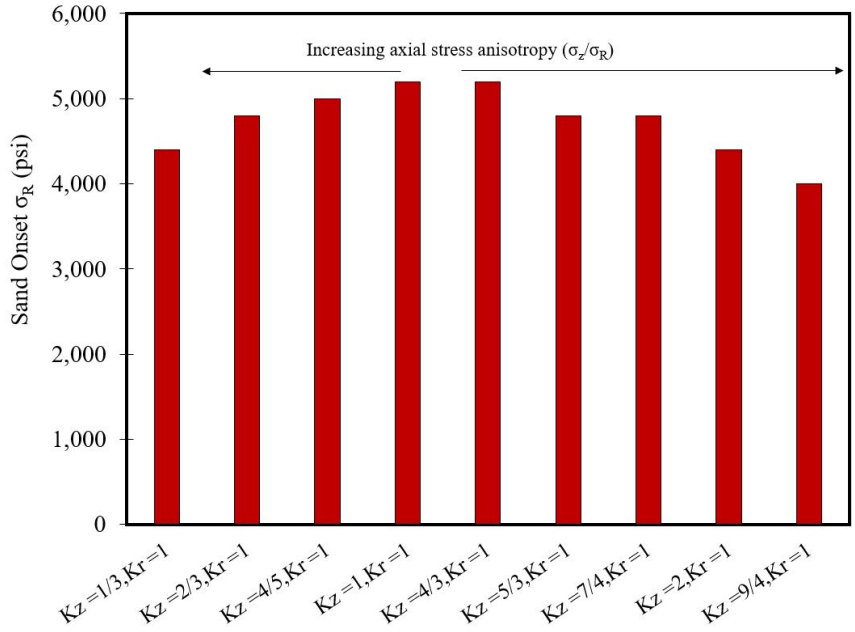

Figure 4.57: Sand onset comparison between the nine numerical models due to axial anisotropy; with K_r = 1.

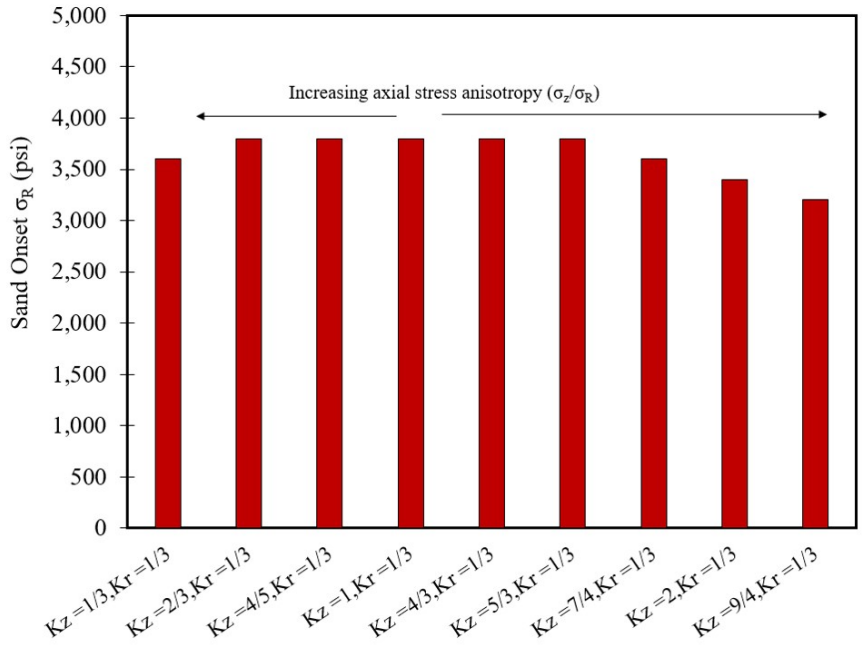

Figure 4.58: Sand onset comparison between the nine numerical models due to axial anisotropy; with K_r = 1/3.

Fig. 4.59 - 4.60 show the comparison of sand rates obtained from the numerical models with no stress anisotropy in lateral direction (K_r = 1) and high stress anisotropy (K_r = 1/3). The sand rates are plotted against normalized σ_R i.e. $(\sigma_R - \sigma_R^o)/\sigma_R^o$ where σ_R^o is the σ_R at sand onset. It can be observed that in plot (a), $\sigma_R > \sigma_z$ and in plot (b), $\sigma_R < \sigma_z$. Comparing sand rates is not as straightforward as onset of sand production. Factors like failed surface area and post-failure plastic strain also play a role in calculating sand rates. However from this study it can be concluded that, as axial anisotropy increases, sand rates decrease at a particular normalized σ_R. Lateral anisotropy also plays a dominant role in Fig. 4.60(a) where sand rates are estimated very close to one another. This is not the case with none lateral anisotropy in Fig. 4.59(a).

Similarly, numerical simulations were run with change in lateral anisotropy keeping that of axial constant. The material constitutive relations are that of Castlegate outcrop sandstone. The summary of all the model runs are included in Table 4.17. Simulation conditions are common in all the runs as listed in Table 4.16. The numerical simulation is setup such that the σ_R increase with an increment step of 200 psi and the flow rate is maintained at 0.8 L/min due to vertical symmetry.

ID	**Material**	$\mathbf{K_z}(\frac{\sigma_z}{\sigma_R})$	$\mathbf{K_r}(\frac{\sigma_r}{\sigma_R})$
01	Castlegate	1/3	1, 2/3, 1/3
02	Castlegate	2/3	1, 2/3, 1/3
03	Castlegate	4/5	1, 2/3, 1/3
04	Castlegate	1	1, 2/3, 1/3
05	Castlegate	4/3	1, 2/3, 1/3
06	Castlegate	5/3	1, 2/3, 1/3
07	Castlegate	7/4	1, 2/3, 1/3
08	Castlegate	2	1, 2/3, 1/3
09	Castlegate	9/4	1, 2/3, 1/3

Table 4.17: The numerical simulations summary for undersanding the effect of varying lateral anisotropy.

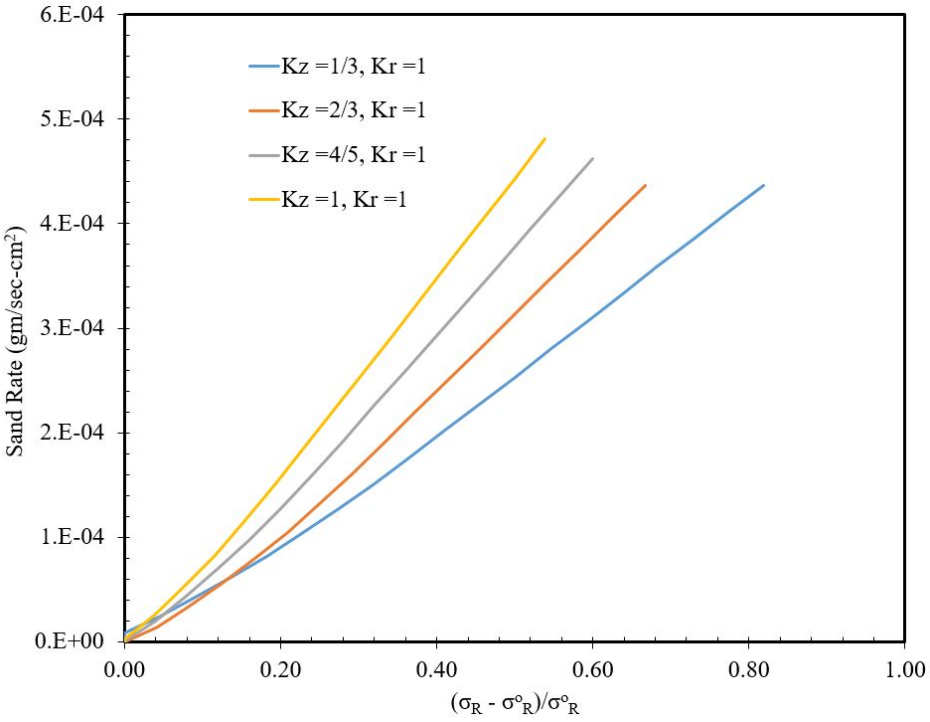

(a)

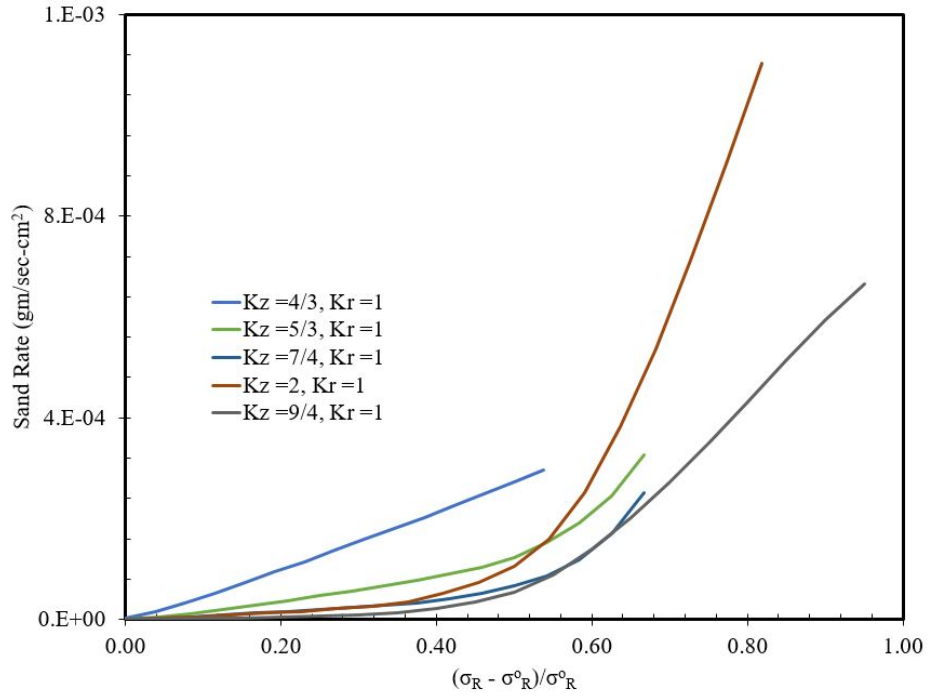

(b)

Figure 4.59: Sand rate comparison between the nine numerical models due to axial anisotropy; with K_r = 1.

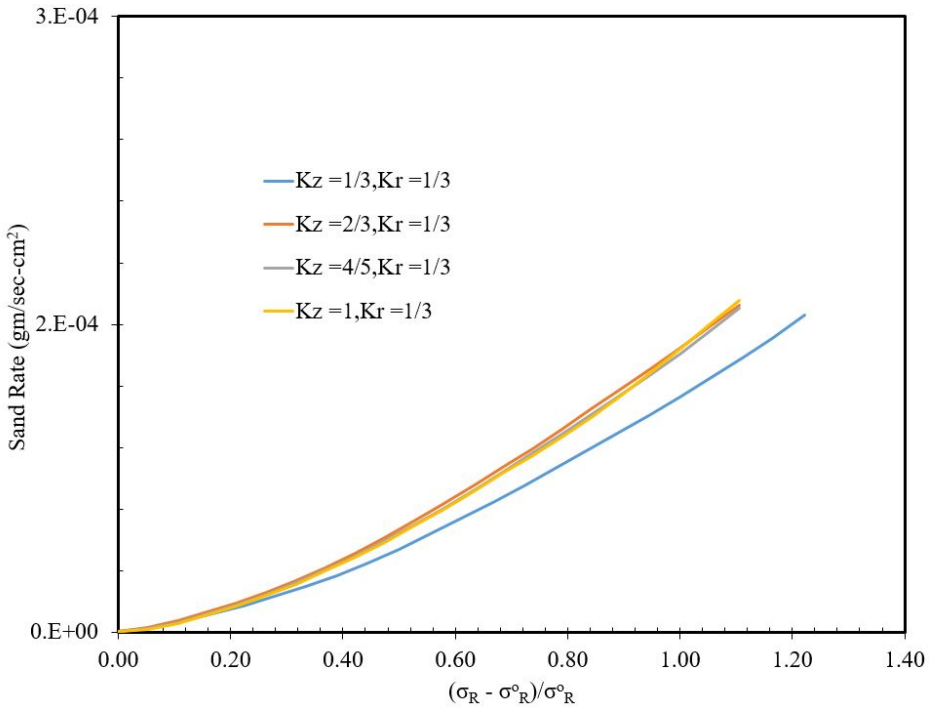

(a)

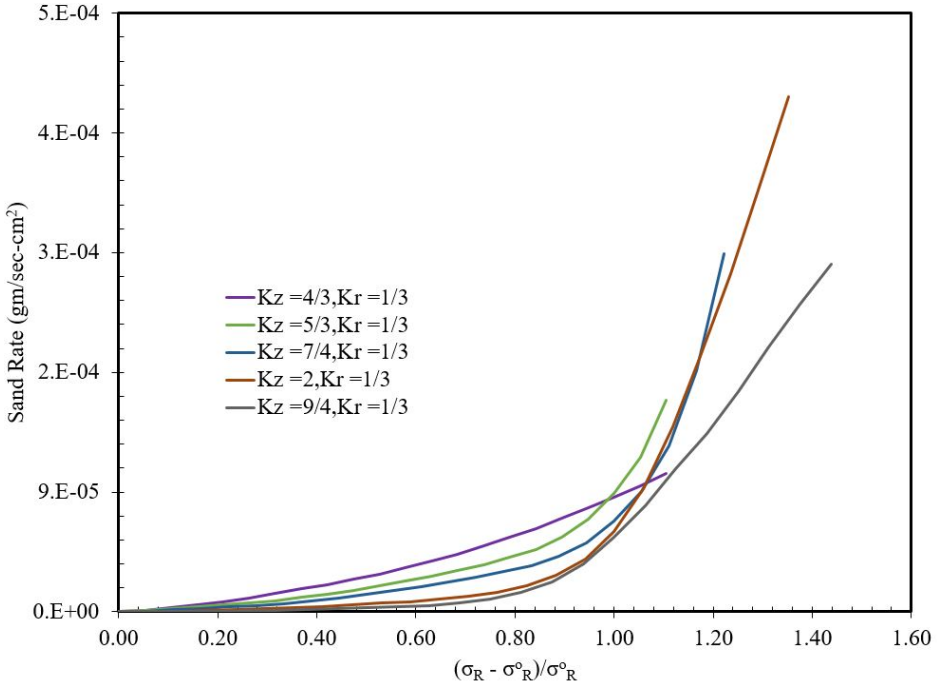

(b)

Figure 4.60: Sand rate comparison between the nine numerical models due to axial anisotropy; with K_r = 1/3.

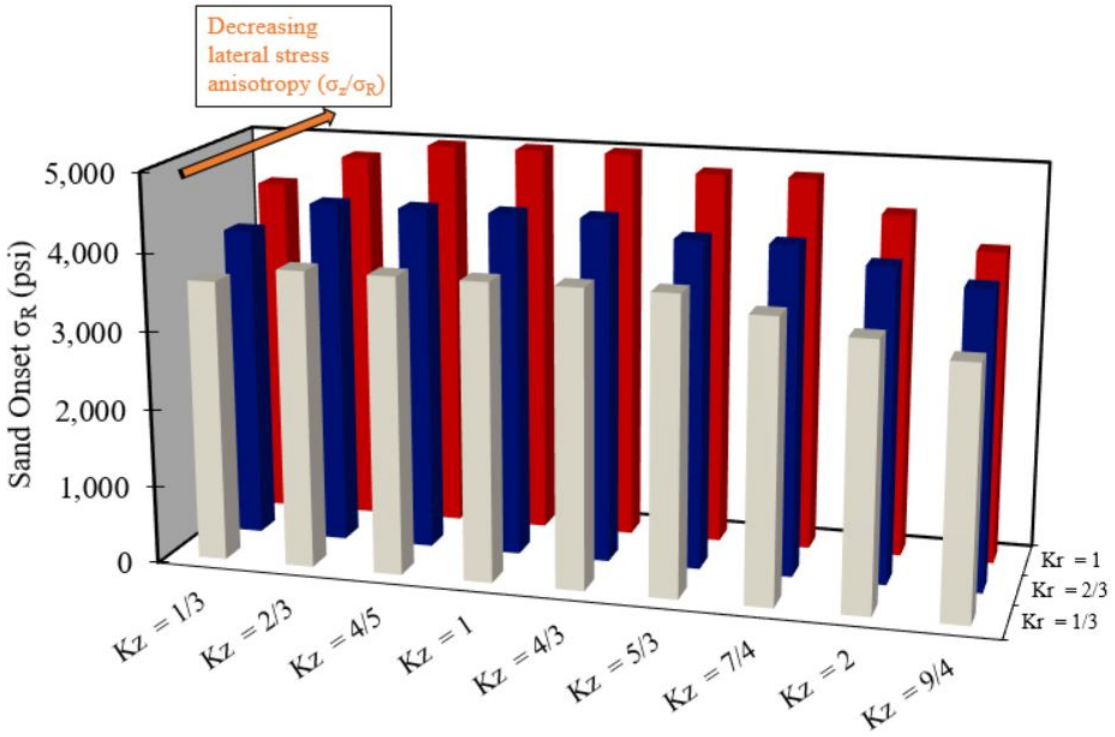

Figure 4.61: Sand onset comparison between the numerical models due to change in lateral anisotropy.

The results are unambiguous and ascertain that increasing lateral anisotropy increases sand production potential and leads to earlier sand onset (Fig. 4.61). For sand rate comparison, although estimated in all simulations, only two extreme cases are shown for brevity (K_z = 1/3 & K_z = 2) in Fig. 4.62. It can be concluded that, as lateral anisotropy increases, sand rates decrease at a particular normalized σ_R.

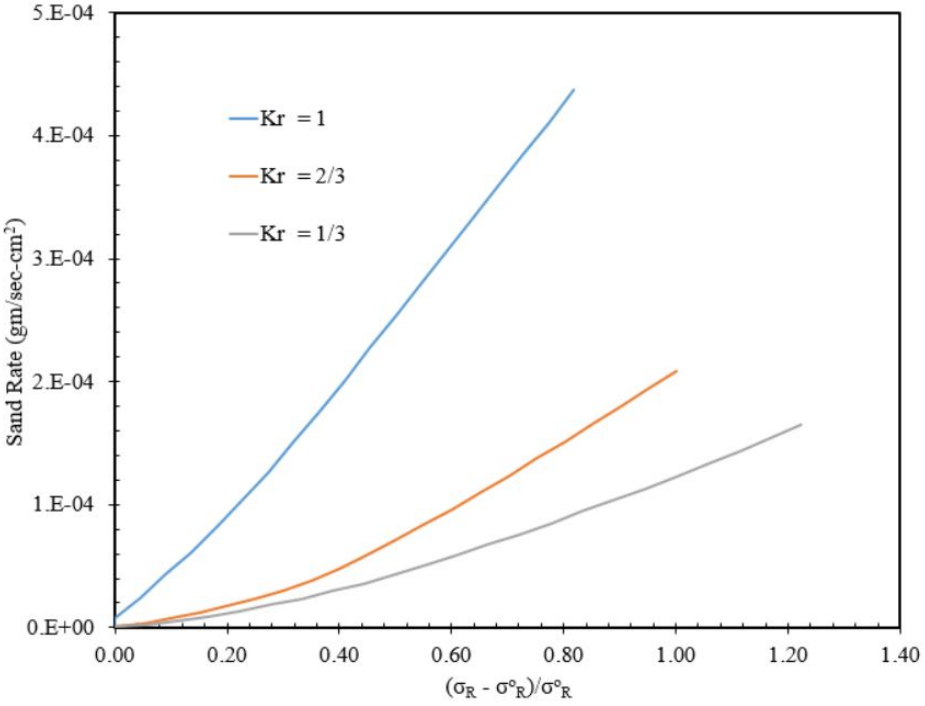

(a) K_z = 1/3

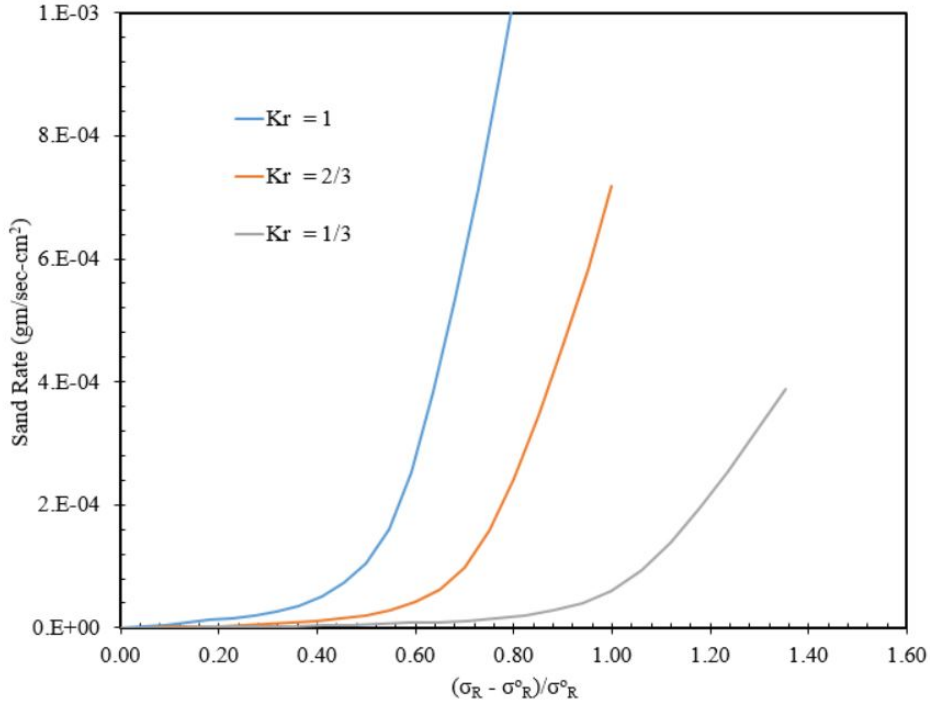

(b) K_z = 2

Figure 4.62: Sand rate comparison between the numerical models due to change in lateral stress anisotropy.

5. SAND RATE PREDICTION FOR AN OFFSHORE FIELD

5.1 Introduction

In this chapter, a case from an offshore[1] field is presented. Triaxial tests[2] were performed on cores obtained from two wells and sand production potential was studied. The reservoir did not produce a significant amount of sand rate that could prove hazardous to the surface facilities. Hence, there was no sand rate measurement done at the field. The purpose of this study is to show that the results from numerical analysis qualitatively replicate the field situation.

5.2 Background of the Offshore Field

The offshore field is considered one of the major oil fields in the Middle East region. The field has significant dimensions of about 20 and 8 km in length and width respectively.

The subject of this study are two sandstone reservoirs, upper and lower. The upper sandstone reservoir lies at a depth of about 5,000 ft below sea floor and was discovered in 1960. Underlying the upper sandstone, there is another sandstone reservoir at a depth of about 5,400 ft below sea floor. The average gross thickness of the upper reservoir is about 190 ft and that of the lower one is about 650 ft. The upper reservoir is of Middle Cretaceous geologic age. The upper sand is separated from the lower one by a thick shale bed of about 200 ft. Fig. 5.1 shows that the both the reservoirs had the same original oil-water contact level.

Both the upper and lower sandstone reservoirs can be classified as strong waterdrive that are able to maintain reservoir pressure well above the bubble point. However, there is also an adverse water-to-oil mobility ratio of 2 to 4 with high formation permeability. Hence, water production was difficult to avoid. Typically, water production begins from the peripheral wells located near

[1] Name undisclosed due to confidentiality agreement
[2] Data gathered from a report

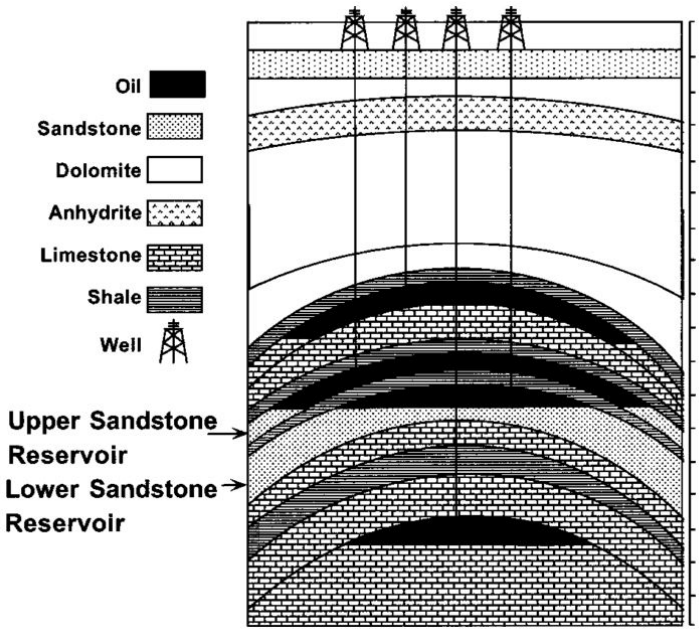

Figure 5.1: Subsurface profile of the offshore oil field (after Japan Oil Engineering Co. (2000)).

the oil-water contact in an edge-water drive reservoir. In this case, some wells located in the central region of upper reservoir started producing formation water well before the wells located in the flank area. Japan Oil Engineering Co. (2000) concluded that this early water breakthrough is due to communication between the upper and lower sandstone reservoirs through faults (Fig. 5.2).

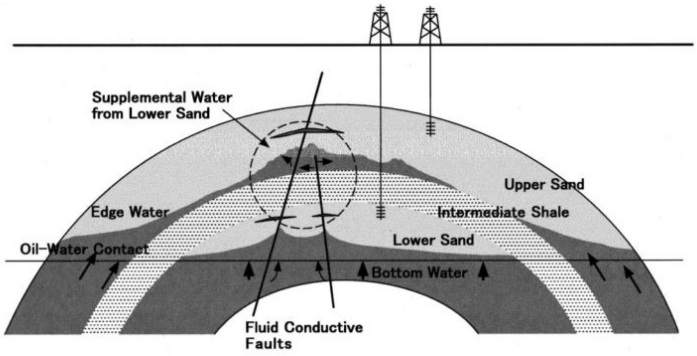

Figure 5.2: Depiction of conceptual communication between the upper and lower sand resulting into early waterbreakthrough in central region wells of upper sand (after Japan Oil Engineering Co. (2000)).

The upper sand consists mainly of sandstone-dominated sandstone and shale sequences. The depositional environment is complex, with shore face and tide-influenced fluvial channels. It has an anticline structure (Fig. 5.3) with the major axis running northeast to southwest. The dip is gentle at about 3°on the northwestern flank and about 2°on the southeastern flank. Japan Oil Engineering Co. (2000) divide the upper sand into 7 geological layers (Fig. 5.4) from top to bottom based on well-to-well correlation. The main sand body has an average shaliness of about 9%. The depositional environment of the main sand body is interpreted as channel fill in a huge incised valley since it does not yield any marine fossils, from northwest to southeast. The average reservoir porosity varies between 21 to 28% and the average permeability between 1,200 and 3,500 md.

The lower sand reservoir has alternating beds of sandstone and shale with relatively continuous coal layers. It also does not yield any marine fossils except the lower most layers. The lower sand is divided into 23 geological layers. The sedimentary environment could be generally interpreted to be fluvial channel on a delta plane.

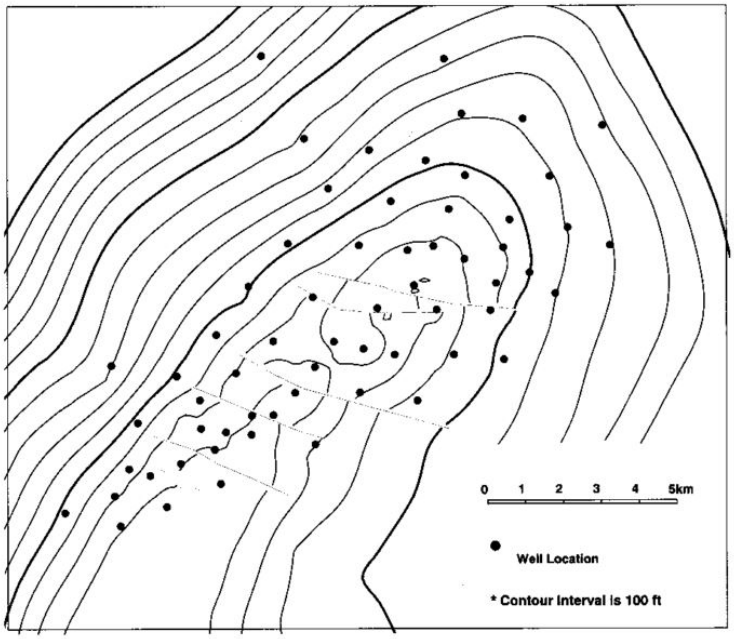

Figure 5.3: Top structural map of the upper sand reservoir with well locations (after Japan Oil Engineering Co. (2000)).

The sandwiched shale layer is composed mainly of shale with thin sandstone beds. It is divided into seven geological layers. Sandstone beds are developed relatively well in southwest and northeast offshore field and are interpreted to previously being belonged to the upper reservoir.

The upper sand commenced production in 1961 with undersaturated oil of about 28°API gravity with oil viscosity about 4 cp at reservoir conditions. Since the upper sand is supported by a strong edge-water drive, the average reservoir pressure has dropped only about 500 psi. However, water production was inevitable due to the adverse water-to-oil mobility ratio from 2 to 4. Efforts were made to maximize oil recovery without water encroachment and thus horizontal completions and re-completions with plug and shut-off of water producing perforations were used for that purpose. There was a long water free production period; and water production started when cumulative oil production exceeded 800 MMSTB (Fig. 5.5).

Layer Name	Average Reservoir Properties		
	Porosity, %	Permeability, md	Gross thickness, ft
Sand 1A	23	1,970	21
Shale 1A			
Sand 1B	23	2,140	20
Shale 1B			
Sand 2A	25	2,410	19
Shale 2A			
Sand 2B	26	2,560	19
Shale 2B			
Sand 3	28	3,490	112
Sand 4			
Sand 5			
Shale 5			
Sand 6	21	1,240	28
Shale 6			
Sand7	26	1,580	43
Intermediate Shale			142

Figure 5.4: Geological layers of the upper sand reservoir with average reservoir properties (after Japan Oil Engineering Co. (2000)).

The upper and lower are two highly permeable sandstone reservoirs from where the bulk of production was achieved. Some wells were completed with cemented perforated liner. The perforation cavity stability is an issue with such high permeability and water breakthrough occurring in the upper sand reservoir. The pressure did not deplete due to the strong water drive and thus not a damaging sand rate is observed in the field.

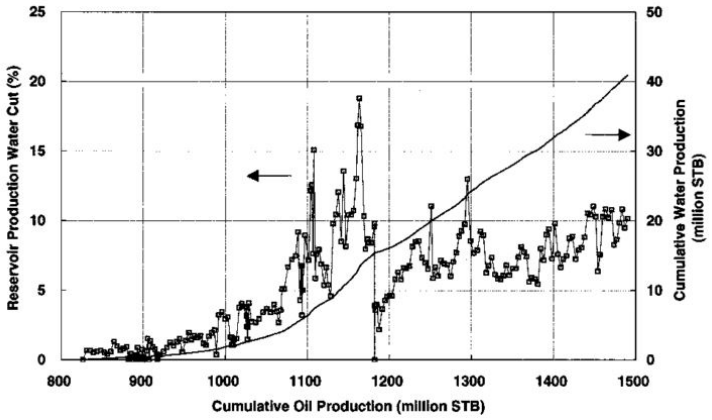

Figure 5.5: Production water cut and cumulative water production from the upper sand reservoir (after Japan Oil Engineering Co. (2000)).

5.3 Sand Production Prediction in the Offshore Field

The two sandstone layers (upper B1, lower B2) are the main producing zones in the oil field. There are some producing wells drilled in the adjacent limestone and carbonate layers as well but our focus will be on B1 and B2 layers. Since the beginning of production in 1960, wells in these sandstone layers have produced an average of 250,000 - 300,000 STB/day (Fig. 5.6). The average initial water saturation is very low (4 - 10%). The dissolved gas amount is about 200 - 250 SCF/STB which is small, thus making the oil undersaturated. The initial reservoir pressure of the two layers is between 2,600 - 2,700 psig with bubble point pressure about 600 - 800 psig. The formation volume factor is between 1.1 - 1.16 RB/STB. The PVT data from the depth of 5,065 ft. is presented in Figs. 5.7 - 5.9.

There were few indications of perforation cavity failure and sand production in the offshore oil field for the first 30 years of production. In the 1990s sand production was observed at well head and at gas lift valve. There was one horizontal well which had catastrophic sand production in the production test after completion and was thus suspended. Also, there were 8 injection wells through which ground water of B2 layer was injected to the carbonate reservoir. In one of these wells, sand was accumulated in the wellbore and gravel packing was done as a remedy.

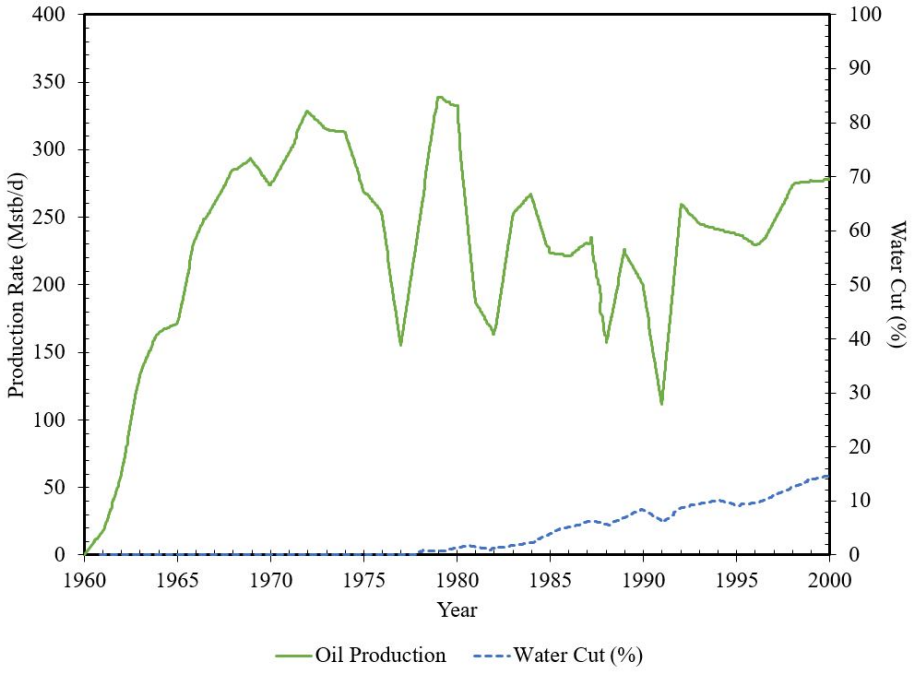

Figure 5.6: Oil Production history and water cut between 1960 and 2000.

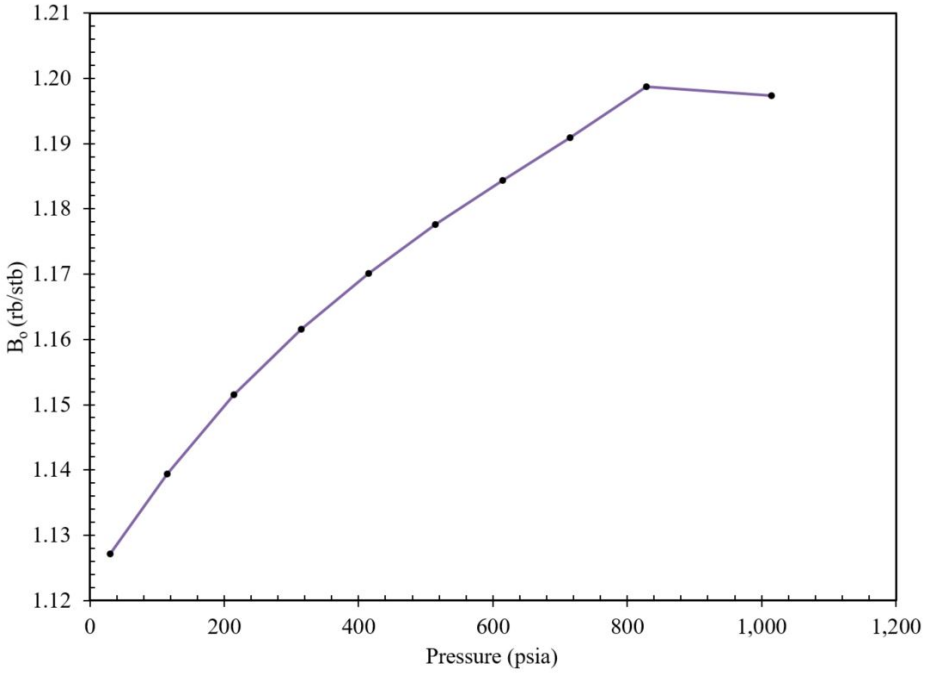

Figure 5.7: Formation volume factor from PVT analysis at depth of 5,065 ft.

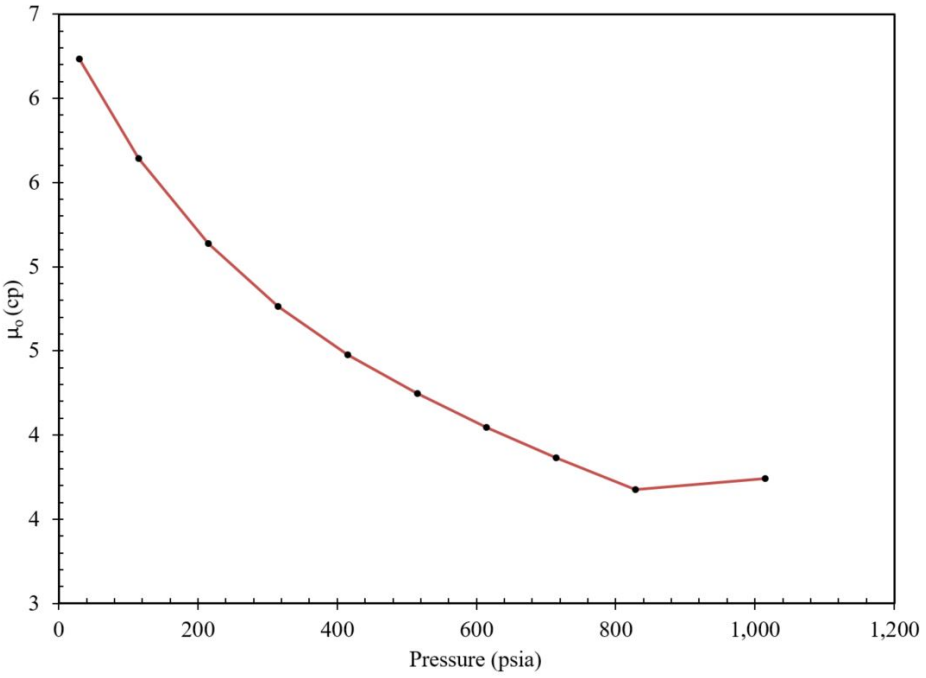

Figure 5.8: Viscosity of oil from PVT analysis at depth of 5,065 ft.

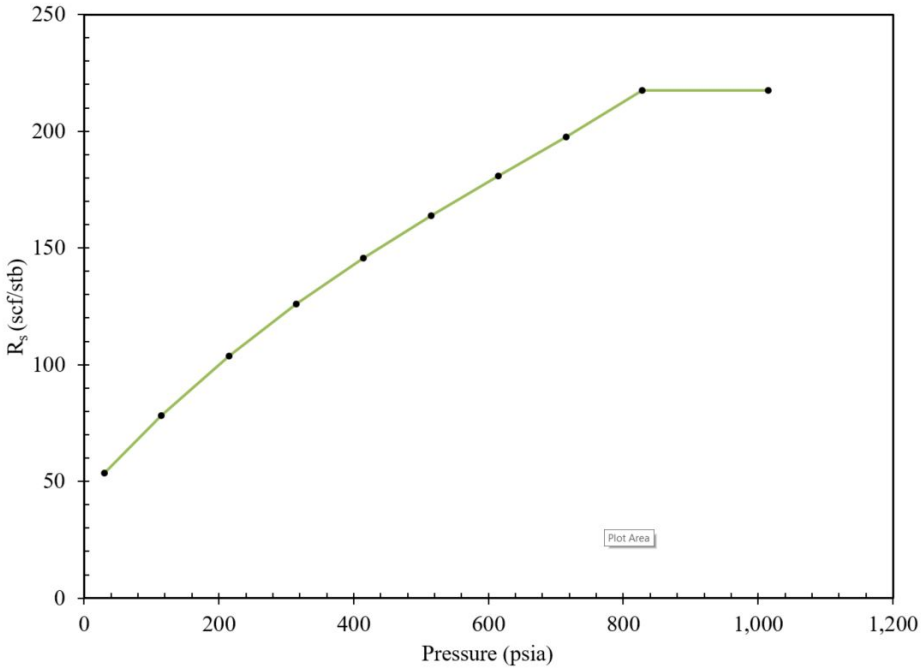

Figure 5.9: Solution gas-oil ratio from PVT analysis at depth of 5,065 ft.

Field data was collected by the operator to conduct a thorough study to estimate the severity of sand production in the future. In this section and later, we use that data to estimate sand rates from B1 sandstone layer.

5.3.1 Description of Data

A test program was established in 1998-99 and data was collected from two wells. Rock mechanical properties were measured using triaxial tests on cores drilled from these wells from B1 and B2 sandstone layers. These tests were performed till failure. Additionally, micro-frac tests were performed to estimate the in-situ stress state.

Triaxial tests were performed on various cores obtained from the field at several confining pressures. These cores were obtained both from B1 and B2 sandstone layers. Constitutive material modeling is done using this test data. The experimental results are explained below.

5.3.1.1 Triaxial Test Results

Five core triaxial results are reported here which are used for constitutive material modeling. The cores were tested at 0, 50, 250, 500 and 1,500 psi confining pressures. At 0 psi confining pressure, unconfined compressive strength (UCS) is measured.

- B1 Sandstone Layer
  - UCS 817 psi: Table 5.1 shows the test data. Fig. 5.10 shows the stress-strain curve and Fig. 5.7 shows the specimens.
  - UCS 2,082 psi: Table 5.2, 5.3 and 5.4 show the test data. Figs. 5.8 - 5.10 show the stress-strain curves and Fig. 5.16 shows the specimens.
  - UCS 2,575 psi: Table 5.5 shows the test data. Fig. 5.11 shows the stress-strain curve.
- B2 Sandstone Layer
  - UCS 1,230 psi: Table 5.6 shows the test data. Fig. 5.12 shows the stress-strain curve.
  - UCS 1,725 psi: Table 5.7 shows the test data. Fig. 5.13 shows the stress-strain curve.
  - UCS 2,134 psi: Table 5.8 shows the test data. Fig. 5.14 shows the stress-strain curve.
  - UCS 2,853 psi: Table 5.9 shows the test data. Fig. 5.15 shows the stress-strain curve.

ID	**Depth (ft.)**	**Confining Pressure (psi)**	**Maximum Axial Stress (psi)**
01	5,127 - 5,130	50	1,120
02	5,127 - 5,130	200	2,800
03	5,127 - 5,130	1,000	5,150
04	5,127 - 5,130	2,000	10,300
05	5,127 - 5,130	3,000	11,300

Table 5.1: Triaxial test data for cores in B1 layer with UCS: 817 psi.

ID	Depth (ft.)	Confining Pressure (psi)	Maximum Axial Stress (psi)
01	5,109 - 5,112	50	1,520
02	5,109 - 5,112	200	5,150
03	5,109 - 5,112	1,000	10,300
04	5,109 - 5,112	3,000	11,300

Table 5.2: Triaxial test data for cores in B1 layer with UCS: 2,082 psi.

ID	Depth (ft.)	Confining Pressure (psi)	Maximum Axial Stress (psi)
01	5,111	51	2,250
02	5,111	256	3,965
03	5,111	511	5,090
04	5,111	1,501	7,400

Table 5.3: Triaxial test data for cores in B1 layer with UCS: 2,082 psi.

ID	Depth (ft.)	Confining Pressure (psi)	Maximum Axial Stress (psi)
01	5,127.7	51	2,785
02	5,127.7	256	3,970
03	5,127.7	513	5,675
04	5,127.7	1,538	8,680

Table 5.4: Triaxial test data for cores in B1 layer with UCS: 2,082 psi.

ID	Depth (ft.)	Confining Pressure (psi)	Maximum Axial Stress (psi)
01	4,874	49	2,969
02	4,874	244	3,838
03	4,874	488	5,218
04	4,874	1,463	9,677

Table 5.5: Triaxial test data for cores in B1 layer with UCS: 2,575 psi.

ID	Depth (ft.)	Confining Pressure (psi)	Maximum Axial Stress (psi)
01	5,511	55	1,795
02	5,511	276	4,065
03	5,511	551	4,720
04	5,511	1,654	9,260

Table 5.6: Triaxial test data for cores in B2 layer with UCS: 1,230 psi.

ID	Depth (ft.)	Confining Pressure (psi)	Maximum Axial Stress (psi)
01	5,555.3	56	2,580
02	5,555.3	278	4,075
03	5,555.3	556	4,920
04	5,555.3	1,667	9,490

Table 5.7: Triaxial test data for cores in B2 layer with UCS: 1,725 psi.

ID	Depth (ft.)	Confining Pressure (psi)	Maximum Axial Stress (psi)
01	5,199.7	52	2,269
02	5,199.7	260	4,435
03	5,199.7	520	5,816
04	5,199.7	1,560	9,828

Table 5.8: Triaxial test data for cores in B2 layer with UCS: 2,134 psi.

ID	Depth (ft.)	Confining Pressure (psi)	Maximum Axial Stress (psi)
01	5,371.7	53	3,666
02	5,371.7	268	4,822
03	5,371.7	537	7,726
04	5,371.7	1,611	11,282

Table 5.9: Triaxial test data for cores in B2 layer with UCS: 2,853 psi.

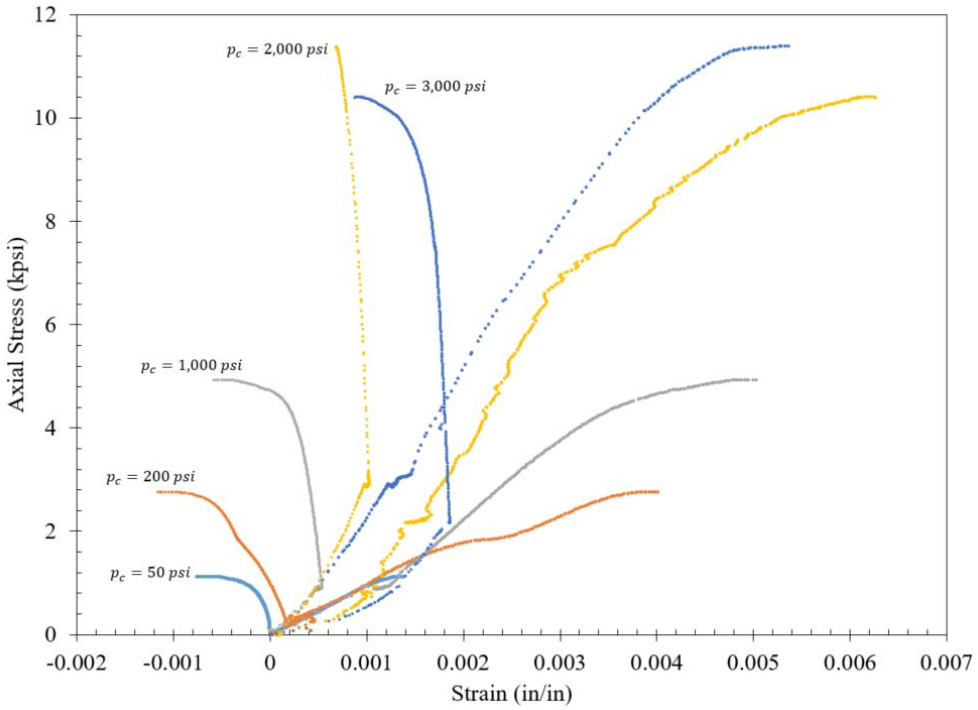

Figure 5.10: Stress - Strain curve from triaxial tests on cores with UCS - 817 psi from B1 layer.

Figure 5.11: Pictures of cores with UCS - 817 psi from B1 layer.

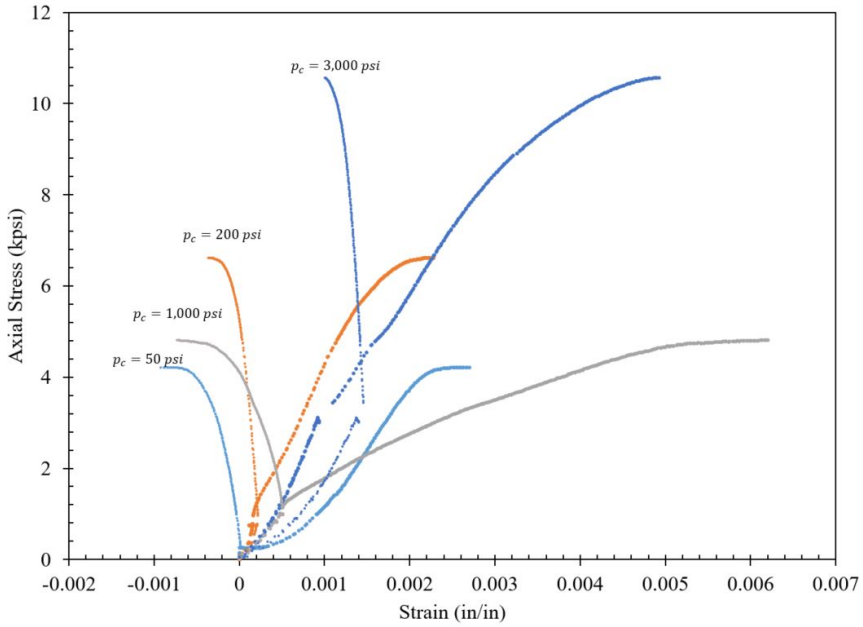

Figure 5.12: Stress - Strain curve from triaxial tests on cores with UCS - 2,082 psi from B1 layer (Depth of 5,109 - 5,112 ft.).

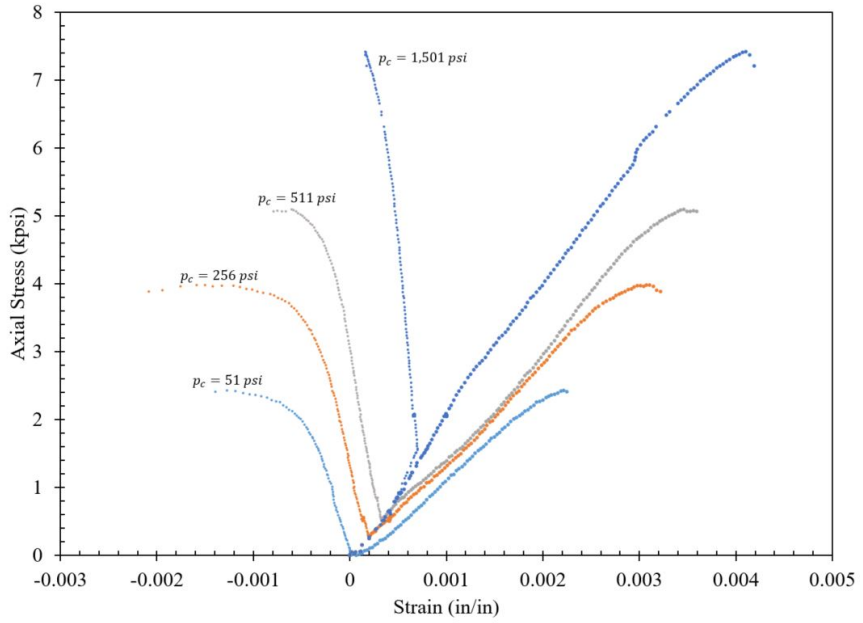

Figure 5.13: Stress - Strain curve from triaxial tests on cores with UCS - 2,082 psi from B1 layer (Depth of 5,111 ft.).

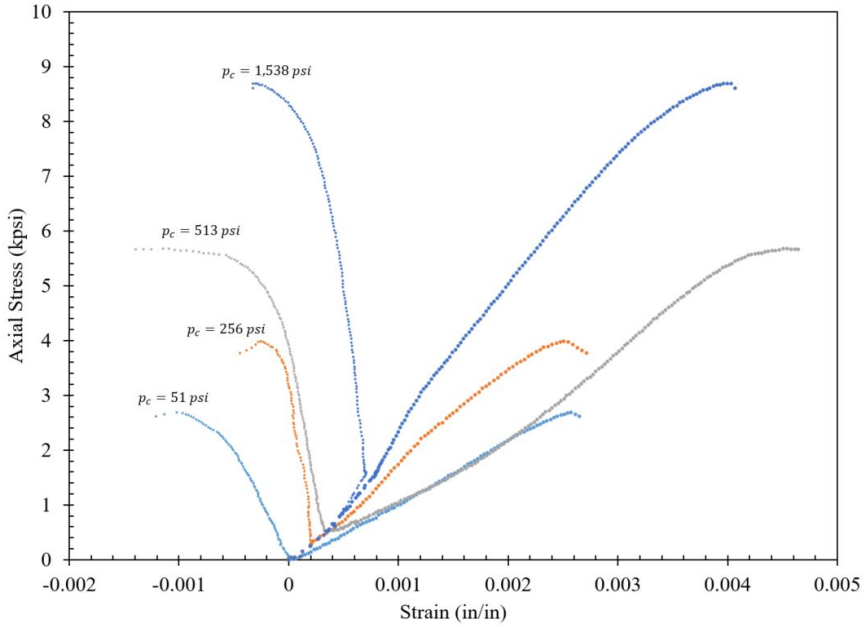

Figure 5.14: Stress - Strain curve from triaxial tests on cores with UCS - 2,082 psi from B1 layer (Depth of 5,127.7 ft.).

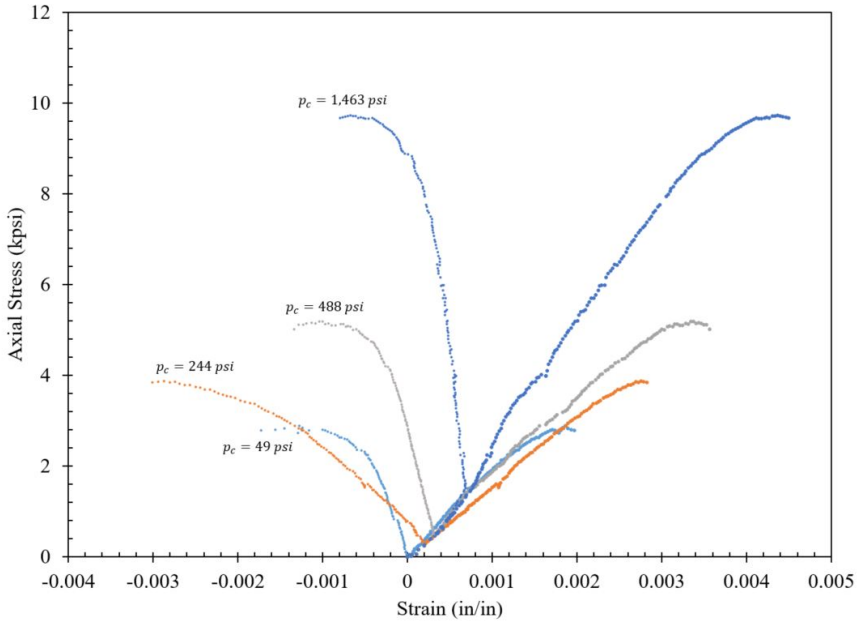

Figure 5.15: Stress - Strain curve from triaxial tests on cores with UCS - 2,575 psi from B1 layer (Depth of 5,127.7 ft.).

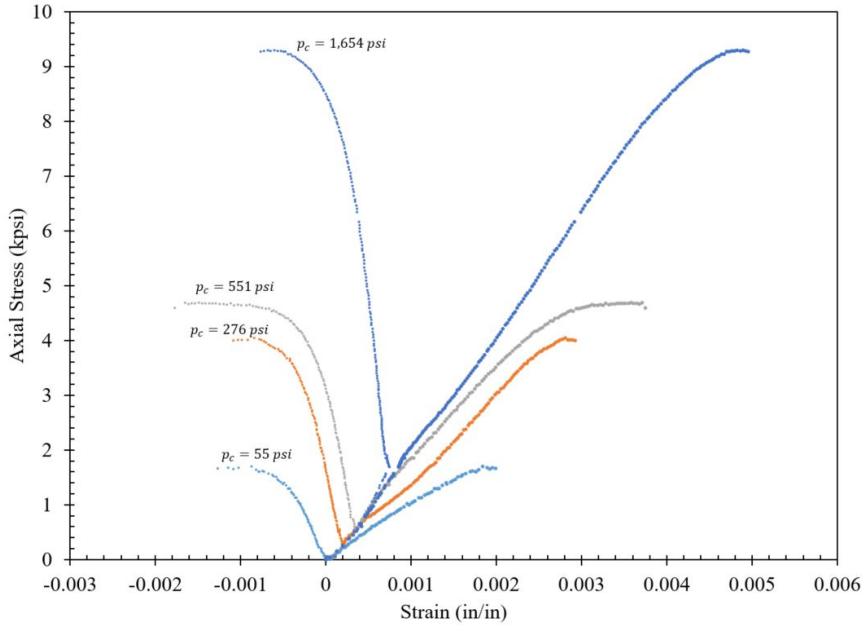

Figure 5.16: Stress - Strain curve from triaxial tests on cores with UCS - 1,230 psi from B2 layer (Depth of 5,511 ft.).

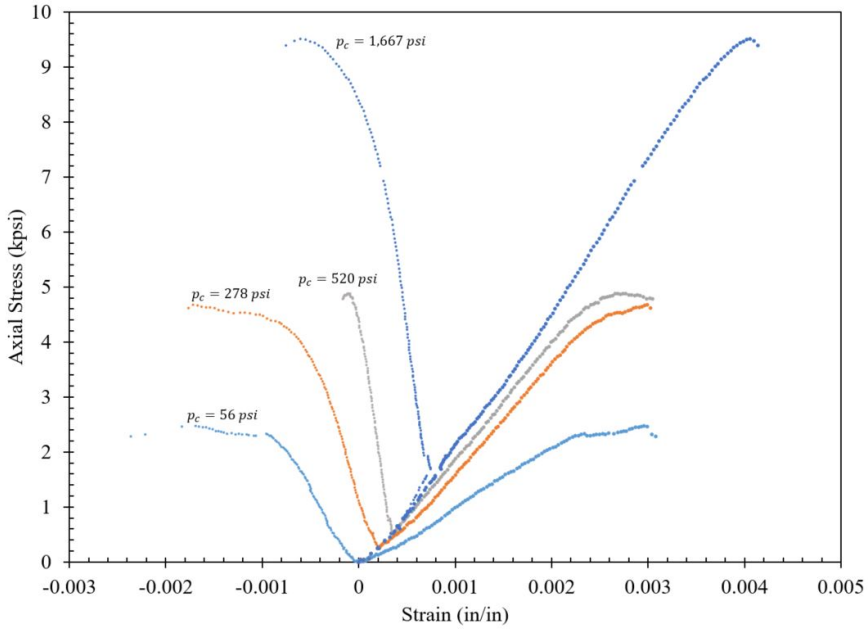

Figure 5.17: Stress - Strain curve from triaxial tests on cores with UCS - 1,725 psi from B2 layer (Depth of 5,555.3 ft.).

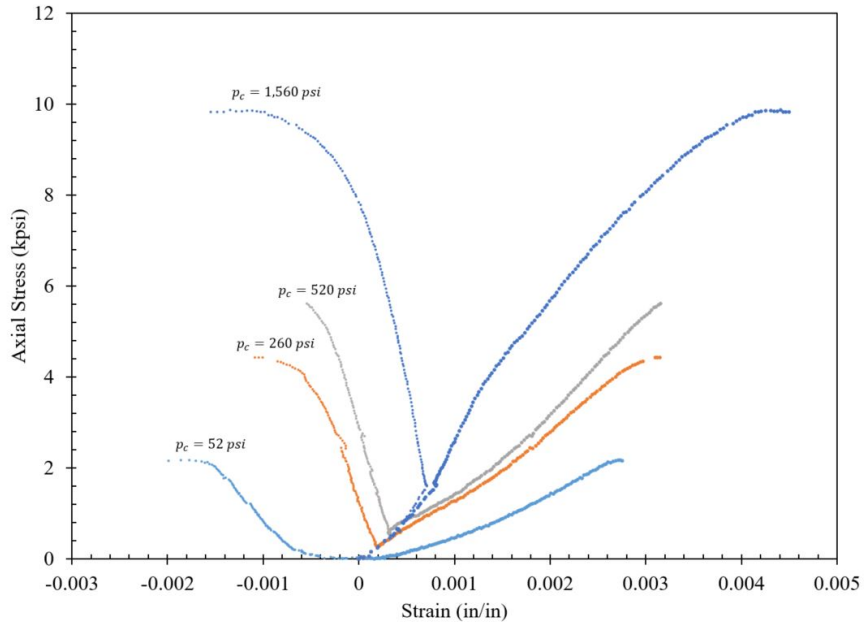

Figure 5.18: Stress - Strain curve from triaxial tests on cores with UCS - 2,134 psi from B2 layer (Depth of 5,199.7 ft.).

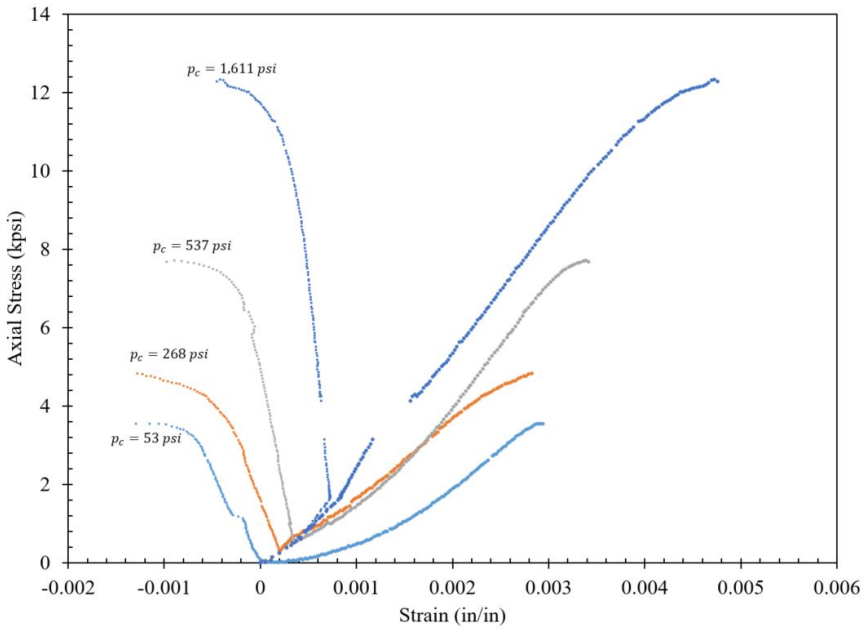

Figure 5.19: Stress - Strain curve from triaxial tests on cores with UCS - 2,853 psi from B2 layer (Depth of 5,371.7 ft.) (some data is missing for p_c = 1,611 psi).

Figure 5.20: Pictures of cores with UCS - 2,082 psi from B1 layer.

5.3.1.2 Reservoir Data Used in Modeling

The PVT data has been presented in Figs. 5.7 - 5.9. The permeabilities k_x, k_y and k_z in the three principal directions has been taken as equal to $1,000$ md. The porosity of 30% has been used.

The non-Darcy factor is important in the analysis of turbulent flow near the perforation cavity. It is calculated using Eq. 5.1.

$$\beta = \left(\frac{5.5 \times 10^9}{k^{1.2}(\phi S_{hc})^{0.75}} \right) \tag{5.1}$$

where S_{hc} is the initial hydrocarbon saturation, k is the permeability and ϕ is the porosity. The initial water saturation is low so the value of S_{hc} is taken as 80%.

The fluid density (ρ_o) is taken to be 0.7504 gm/cc and the compressibility of oil (c_o) is used as 1.068×10^{-5}. The viscosity of oil is used as 4.5 cp.

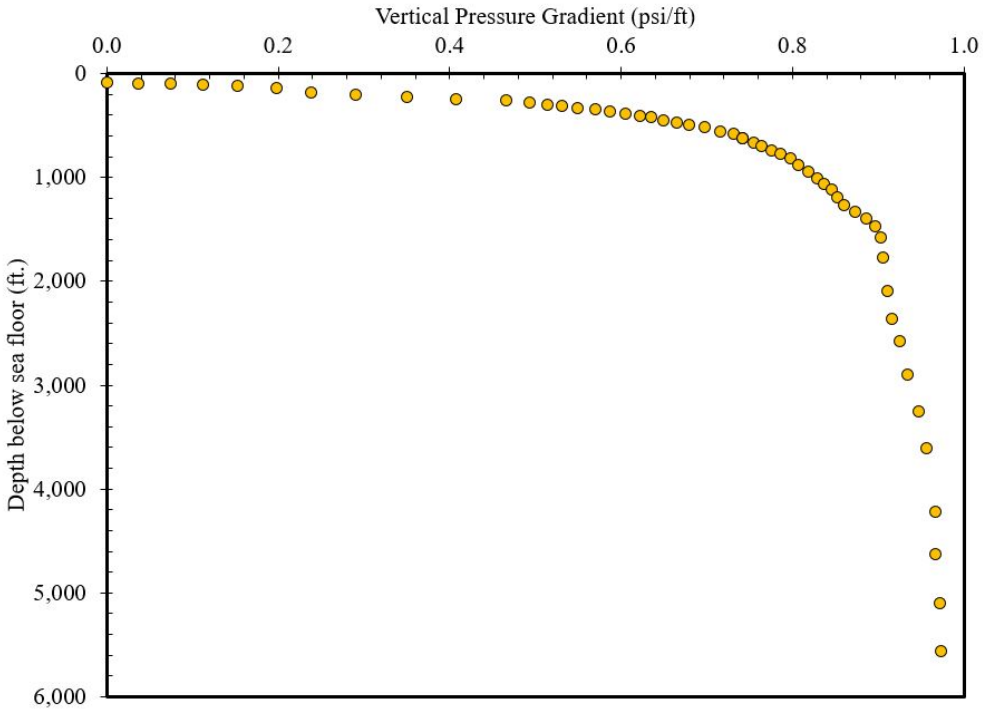

Figure 5.21: Vertical pressure gradient with depth below sea floor.

The vertical pressure gradient was estimated from logging (Fig. 5.21) and is used as 0.972 psi/ft for both the B1 and B2 layers. The average reservoir pressure in both the B1 and B2 sandstone layers was continually monitored. The reservoir system has natural edge-water drive due to which the pressure is maintained above bubble point. B1 layer is depleted by 520 psi and the B2 layer by

270 psi between 1960 and 2000 (Fig. 5.22). Such low depletion rates are advantageous in reducing sand production potential of the field in general. It is one of the reasons that sand production from this field is not a serious problem even after the field had produced from friable sandstones for more than 40 years. The production history along with the water cut data is shown in Fig. 5.6.

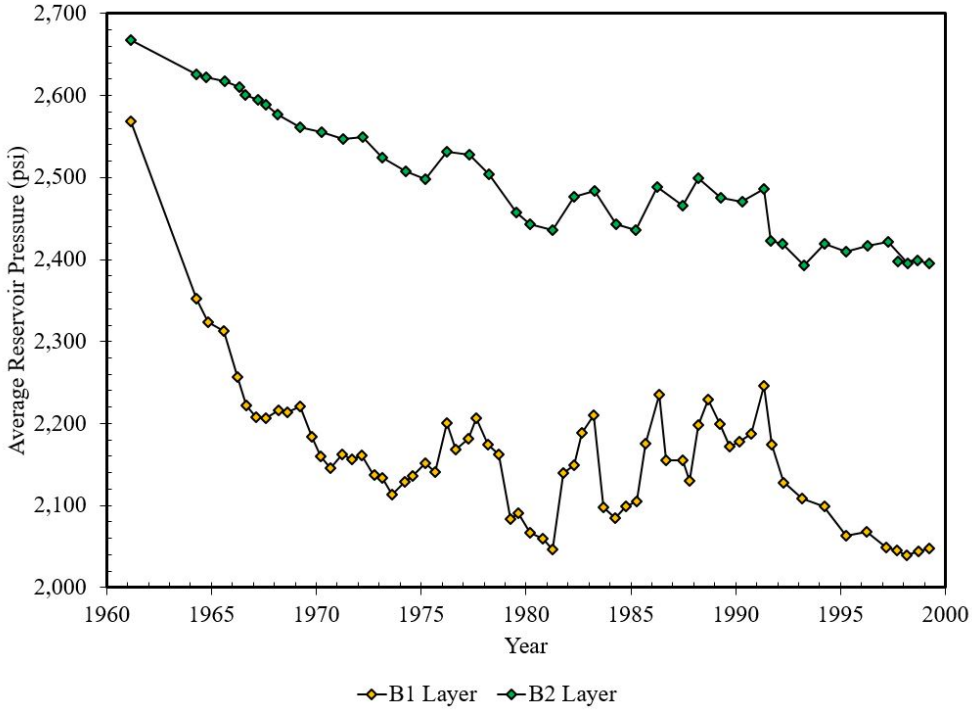

Figure 5.22: Average reservoir pressure in the B1 and B2 sandstone layers between 1960 and 2000.

5.3.2 Preliminary Sand Rate Prediction

The offshore field did not produce significant amount of sand as to the level of damaging surface facilities. The water drive helped to keep the reservoir pressure above bubble point and there was not much depletion to destabilize the perforation cavities in stronger rocks. Although some signs of sand production were continually seen at the wellhead, there was no data collected on sand rate measurements. The objective of the simulation runs is to compare the results qualitatively with that of field observations; and show that the friable sandstones did not produce damaging

amount of sand.

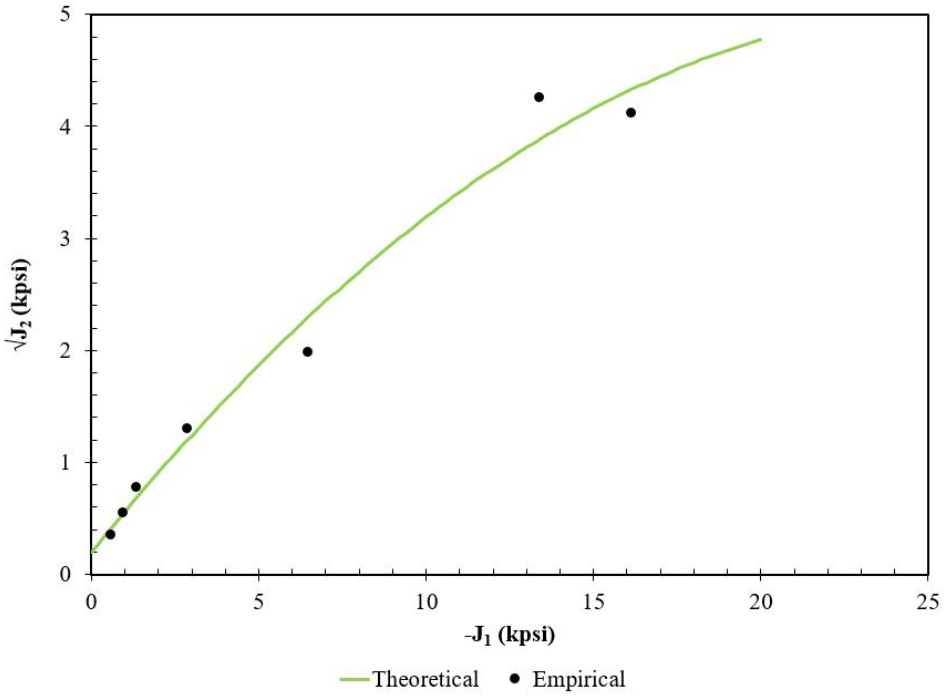

Figure 5.23: Drucker-Prager yield envelope for the material with UCS = 817 psi.

The sand production potential and sand rates from four rocks with UCS 817, 1230, 1725 and 2082 psi are studied for the B1 layer. The constitutive relations for the four rocks are different. The Drucker-Prager yield envelopes for all the rocks are shown in Figs. 5.23 - 5.26. The critical plastic strain criterion is used for judging failure and is calculated to be 0.00343. The failure envelopes for all the rocks are shown in Figs. 5.27 - 5.30. Since the number of samples are small for each rock, the average of all the samples is taken to determine the critical plastic strain (Fig. 5.31).

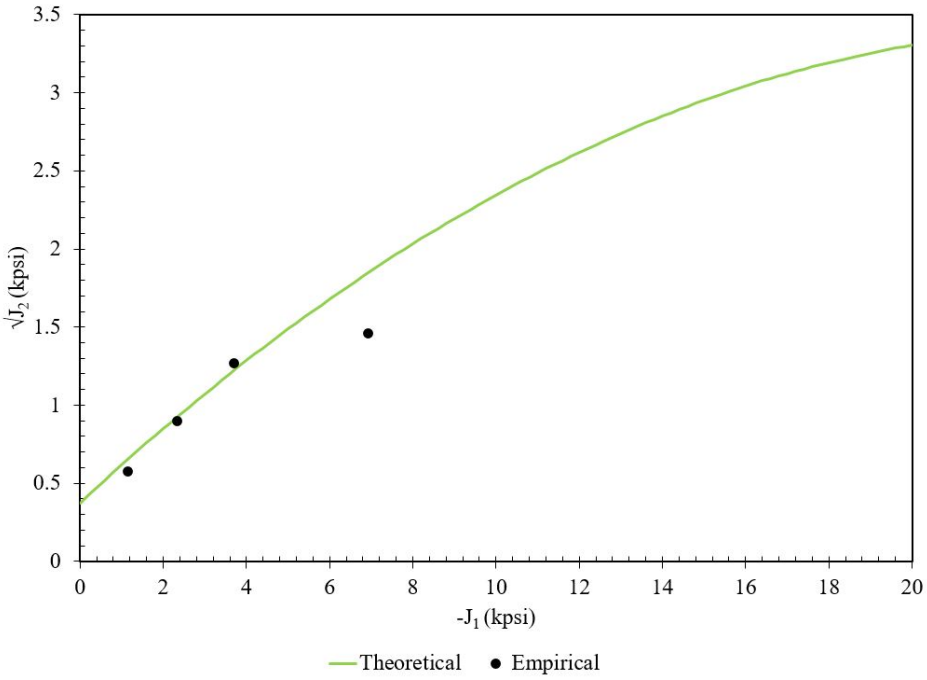

Figure 5.24: Drucker-Prager yield envelope for the material with UCS = $1,230$ psi.

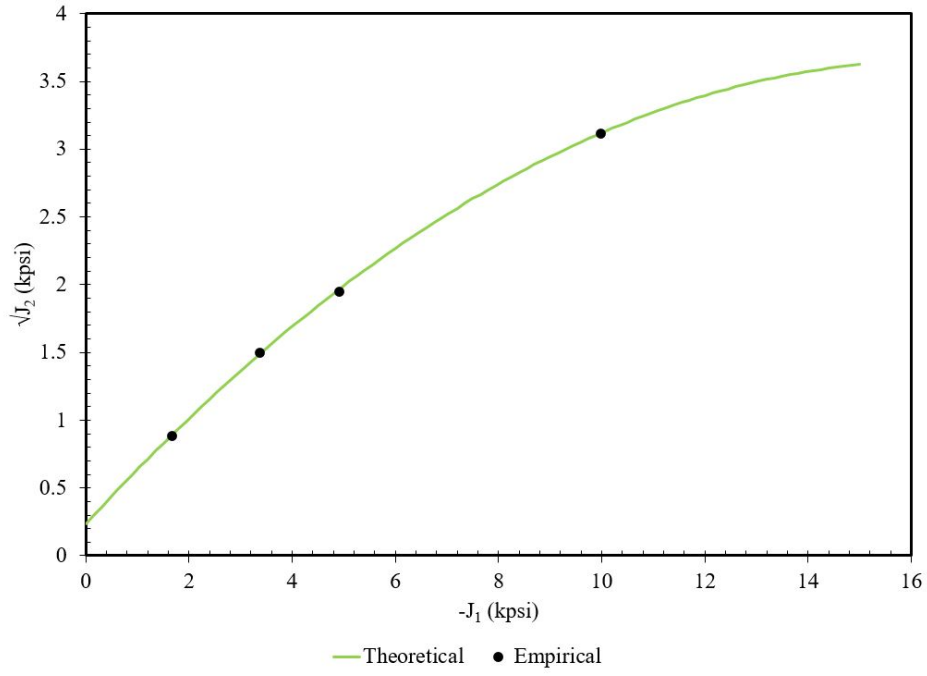

Figure 5.25: Drucker-Prager yield envelope for the material with UCS = $1,725$ psi.

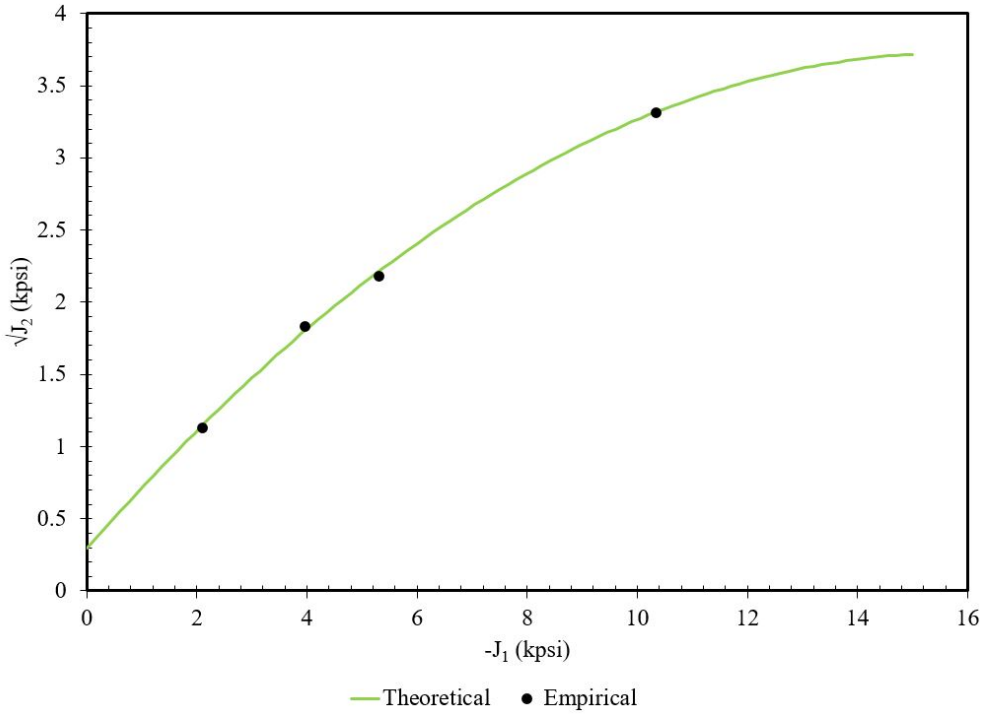

Figure 5.26: Drucker-Prager yield envelope for the material with UCS = $2,082$ psi.

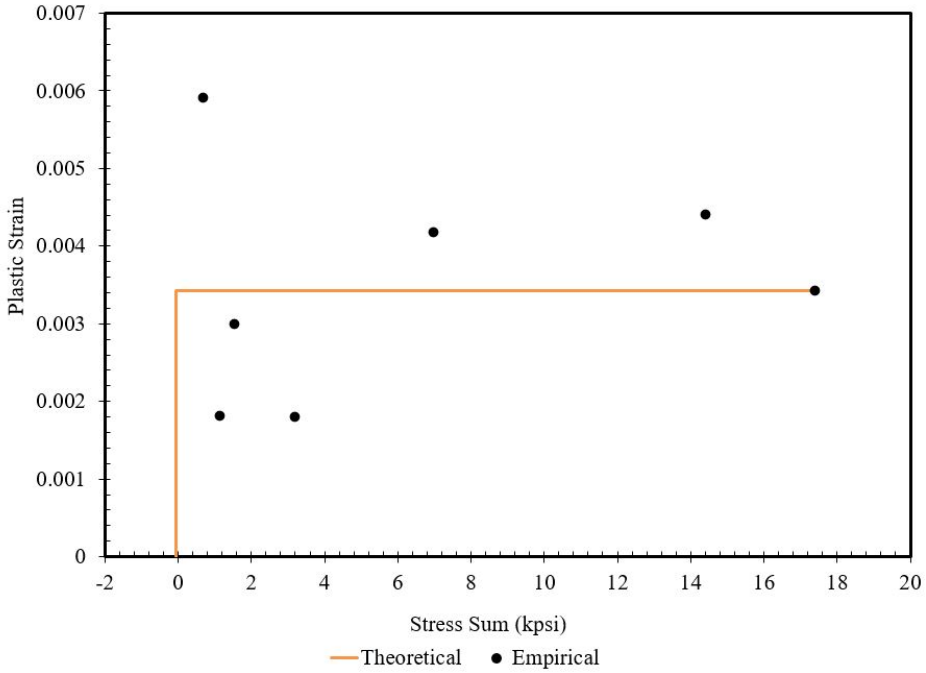

Figure 5.27: Critical plastic strain failure envelope for the material with UCS = 817 psi.

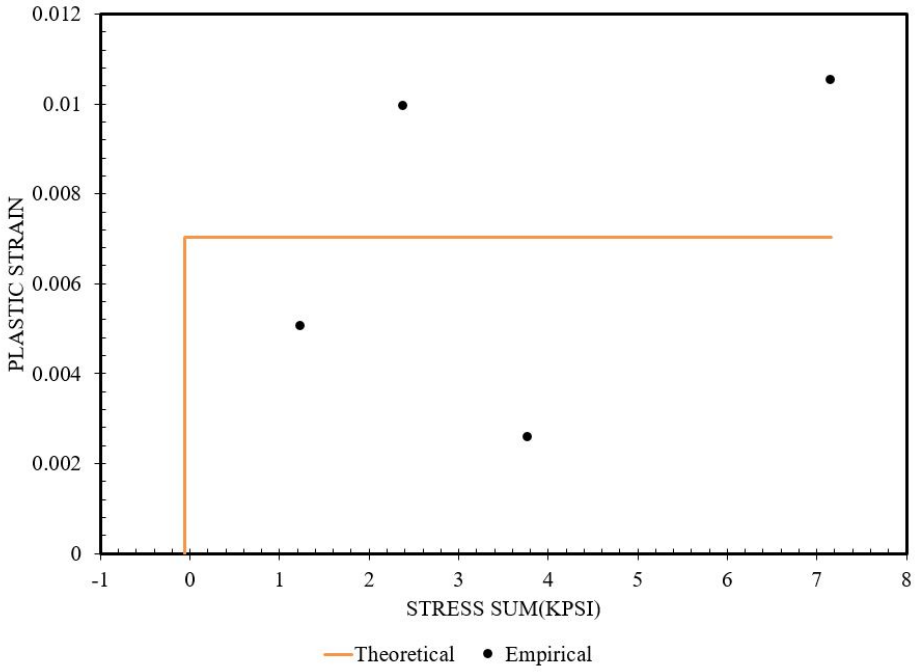

Figure 5.28: Critical plastic strain failure envelope for the material with UCS = $1,230$ psi.

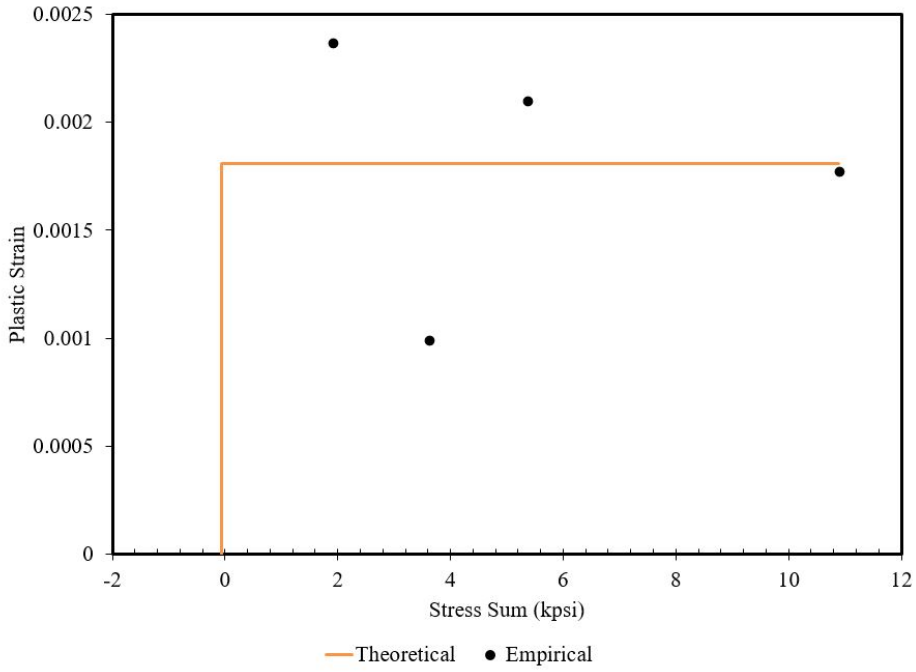

Figure 5.29: Critical plastic strain failure envelope for the material with UCS = $1,725$ psi.

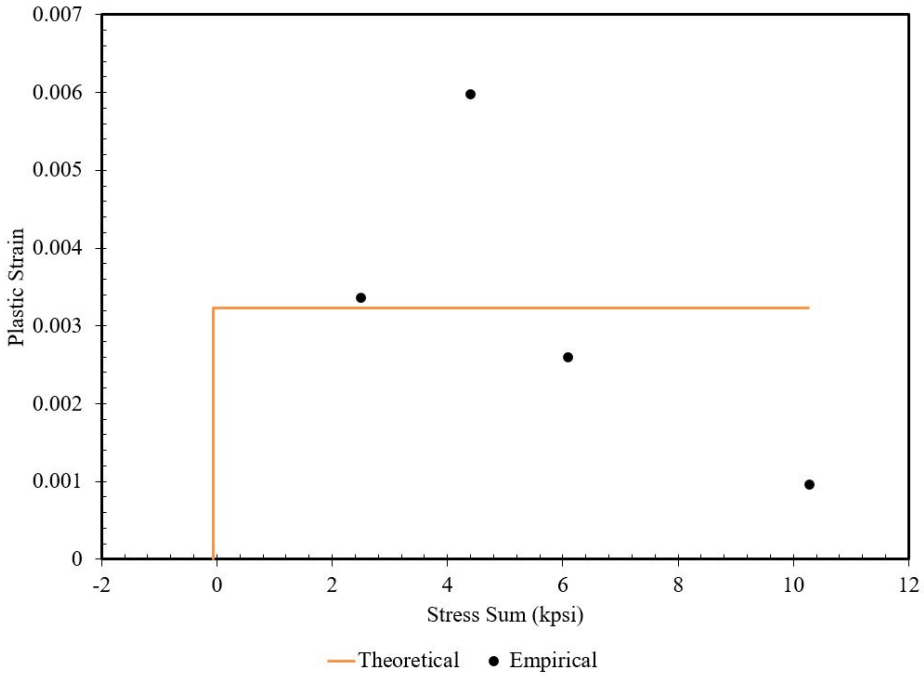

Figure 5.30: Critical plastic strain failure envelope for the material with UCS = $2,082$ psi.

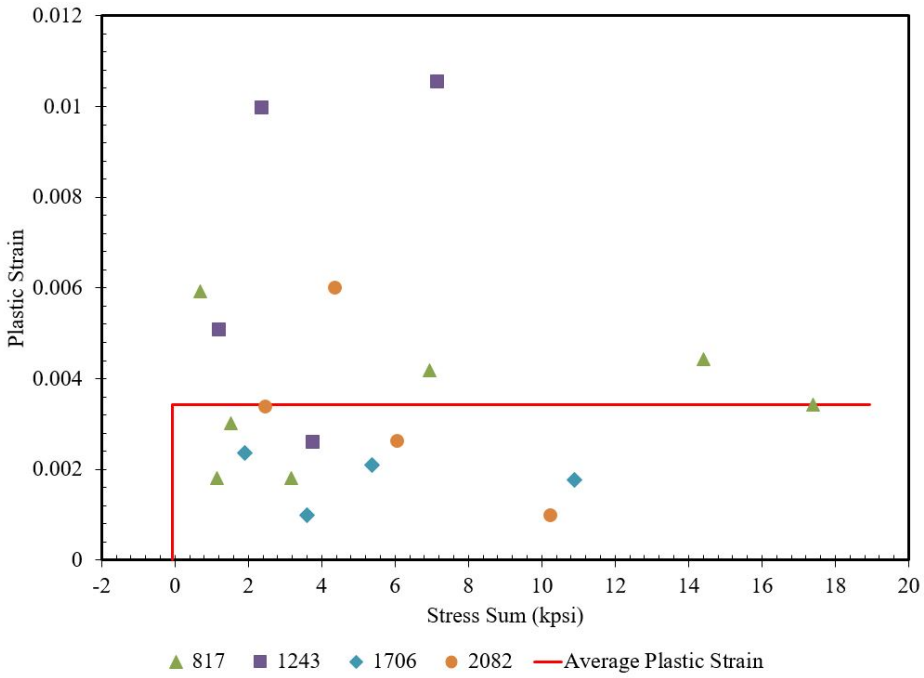

Figure 5.31: Average of all the plastic strains is used as the critical plastic strain for all the material.

The mesh geometry is very complex since multiple perforations are considered. Staggered perforation pattern shot density of 6 spf (shots per foot) at 120° phasing is used in this analysis. There are total of 18 perforations in 6 layers (Fig. 5.32). The perforation layers are shown zoomed in Fig. 5.33 .The total depth of the section is 3 feet. External boundary is considered to be infinite. The top and bottom two layers are used only for perforation interaction. The number of elements is about 25,000 and thus to reduce the computation effort and time, only the middle two layers of perforations are assigned non-linear elasto-plastic rock properties (Fig. 5.34). 12-node infinite elements are used on the outer boundary whereas 20-node hexahedral elements are used elsewhere.

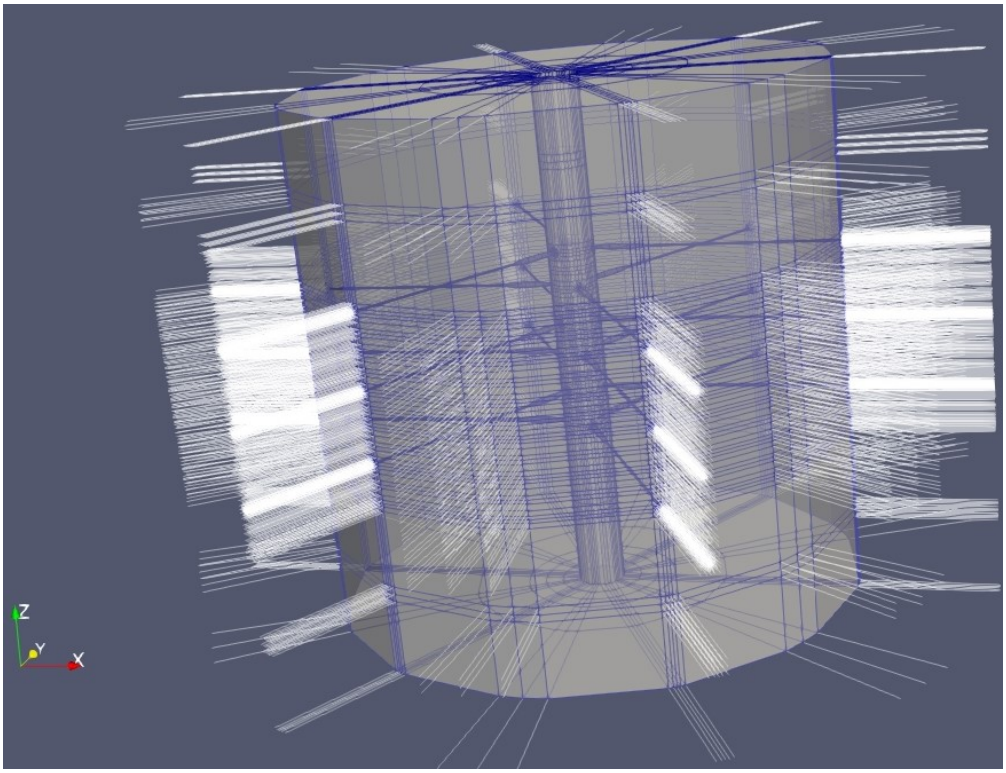

Figure 5.32: Mesh used in sand rate numerical analysis with 6 spf and 120° phasing.

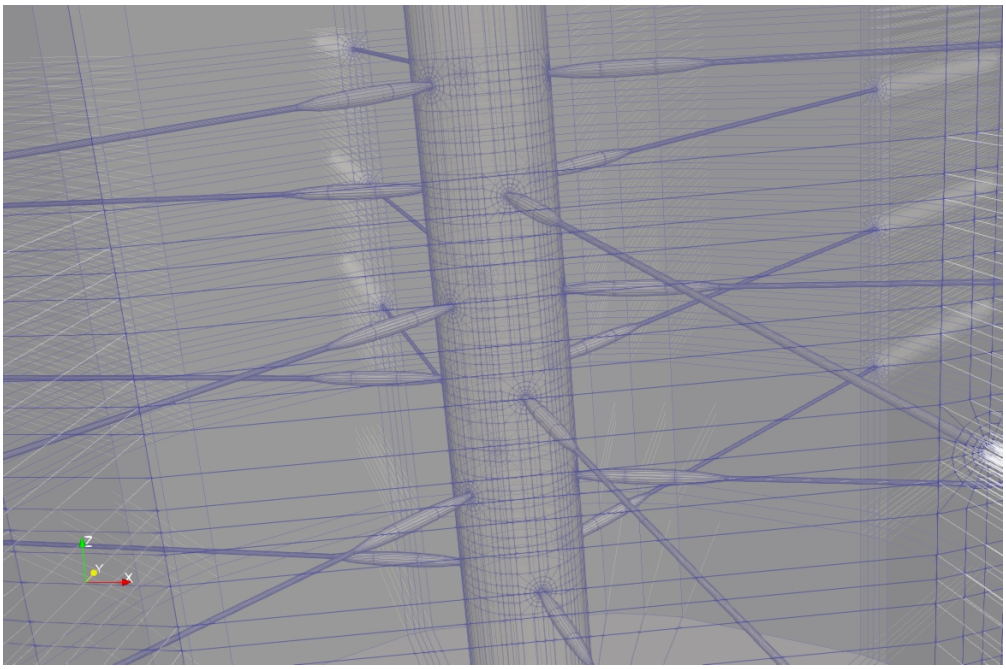

Figure 5.33: All the six perforation layers are shown zoomed in.

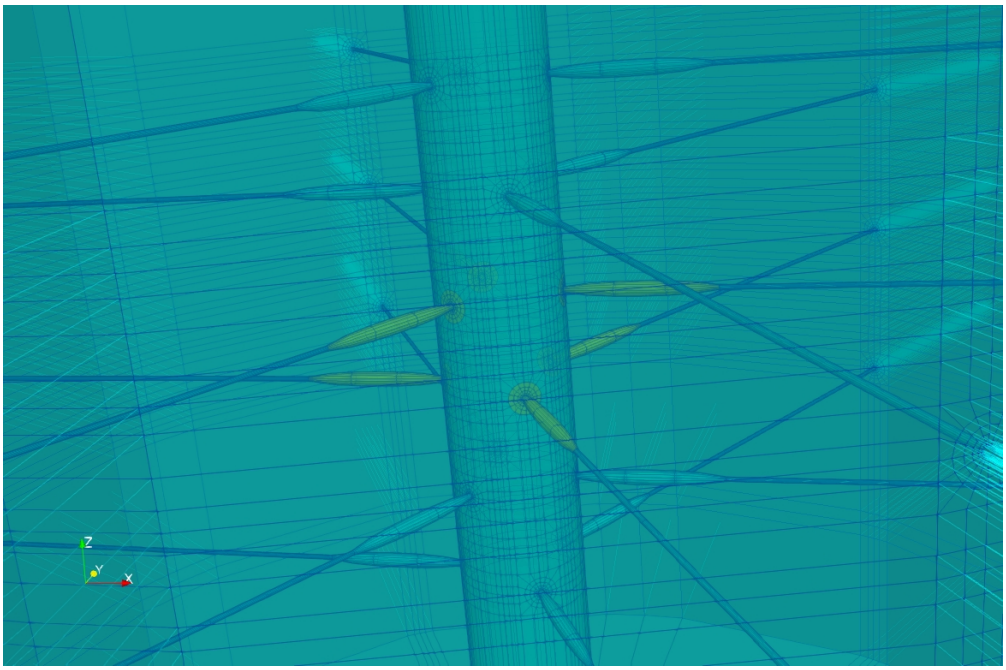

Figure 5.34: Zoomed-in perforation layers with middle two layers showing non-linear elasto-plastic material.

From the preliminary analysis, it was found that the rocks with UCS 1,725 and above do not fail in the 40 years of production period. The UCS distribution with depth for the vertical well is shown in Fig. 5.35. This distribution was provided with the data and estimated from uniaxial test results by employing a neural network algorithm. The details of the algorithm are beyond the scope of this work. It is evident from the figure that the UCS in B1 layer varies from 282 psi to 3,591 psi. Since no rock with UCS above 1,725 psi would fail under the production conditions, this study is concerned with rocks having UCS between 282 psi and 1,725 psi. The first step would be to determine at what strength the formation would fail. For this analysis, artificial constitutive relations for UCS between 817 psi and 1,725 were prepared (Table 5.10). These artificial constitutive relations are linear interpolation/extrapolation of constitutive coefficients from the two rocks. The first three rocks are prepared using extrapolation and the next two by interpolation. The stress-strain curves for the artificial rocks are shown in Figs. 5.36 - 5.40. Sand rate prediction from the B1 layer can be estimated by considering the cumulative from all these artificial rocks. The thickness for all the six rocks (one original and five artificial) are calculated from Fig. 5.35 and shown in Table 5.11. The lower UCS and upper UCS are the range of rock strengths considered in that particular model. It was found that the rock with 1,410 psi UCS fails and produces sand. Hence, all the rocks below this strength will produce sand. The detailed analysis of sand production from B1 layer is presented in the next section.

ID	**UCS (psi)**
01	282
02	460
03	638
04	1,113
05	1,410

Table 5.10: UCS for artificial rocks prepared for offshore field from available triaxial data.

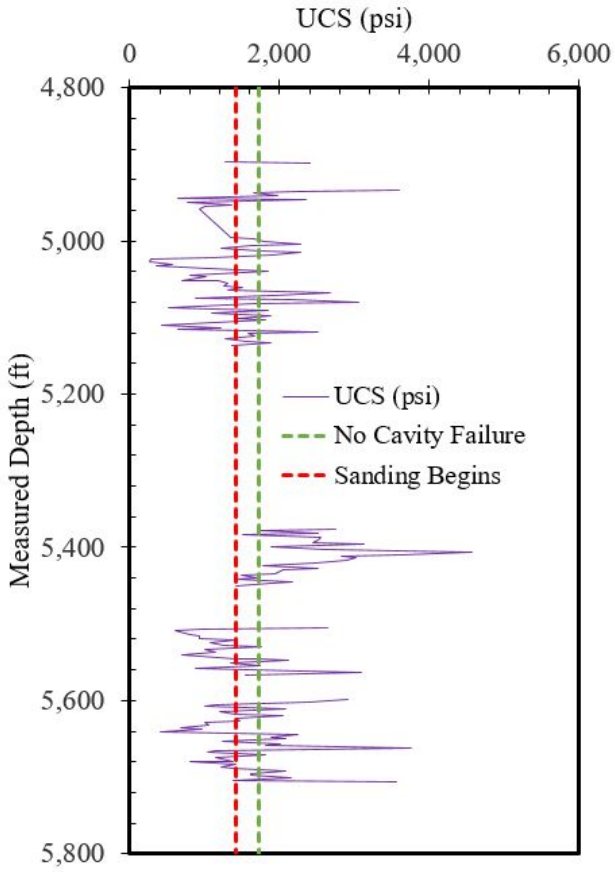

Figure 5.35: UCS distribution for B1 and B2 layer for a vertical well in the offshore field.

ID	UCS (psi)	Lower UCS (psi)	Upper UCS (psi)	Thickness (ft)	Percent of Total
01	282	282	371	4.82	4%
02	460	371	549	6.68	6%
03	638	549	727.5	5.94	5%
04	817	727.5	965	19.60	18%
05	1,113	965	1261.5	51.14	46%
06	1,410	1261.5	1410	24.03	21%

Table 5.11: Thickness of the rock formations in the B1 layer calculated from Fig. 5.35.

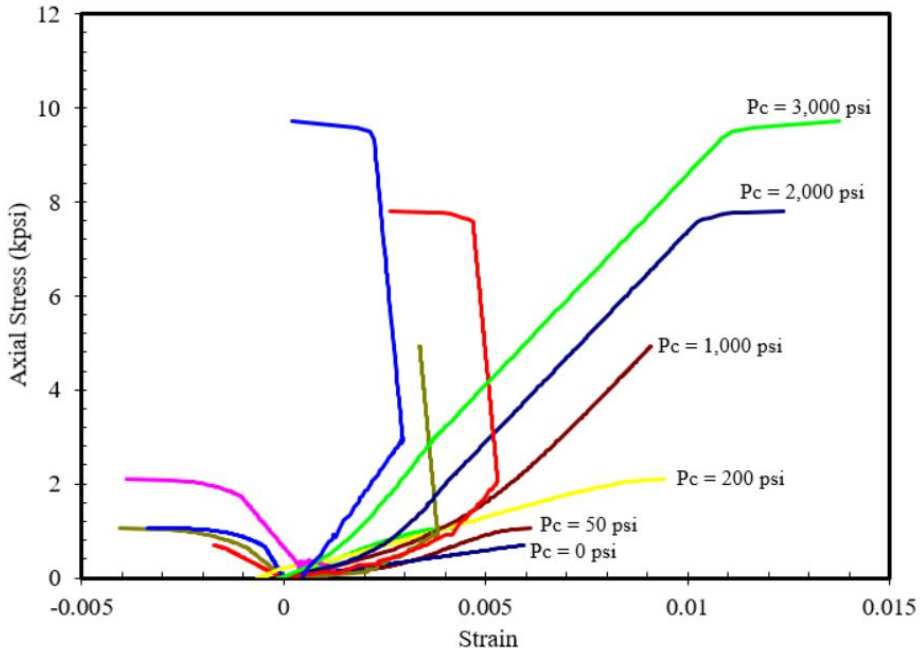

Figure 5.36: Stress - Strain curve for an artificial rock with UCS - 282 psi from B1 layer.

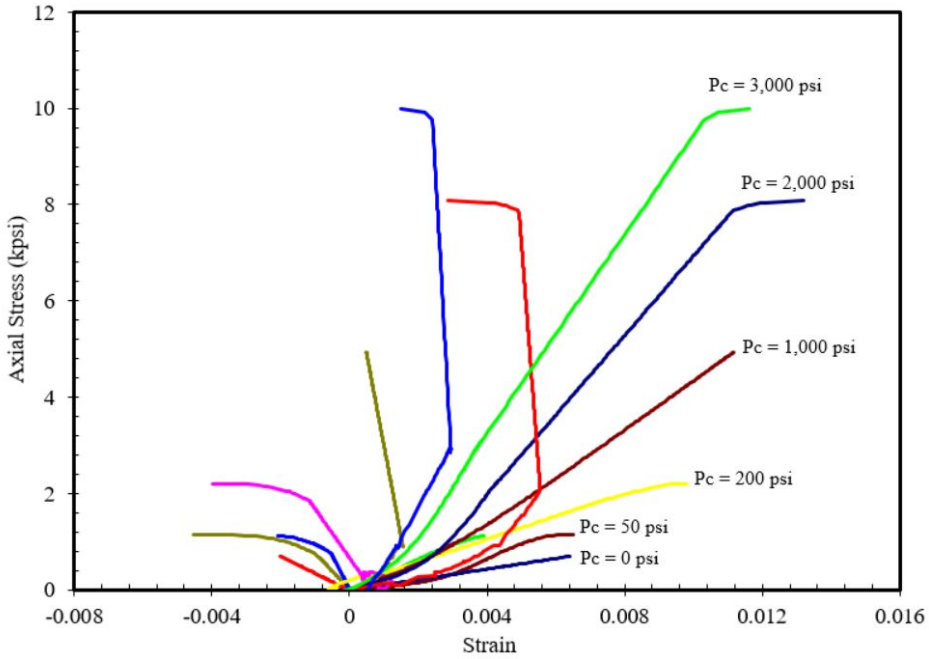

Figure 5.37: Stress - Strain curve for an artificial rock with UCS - 460 psi from B1 layer.

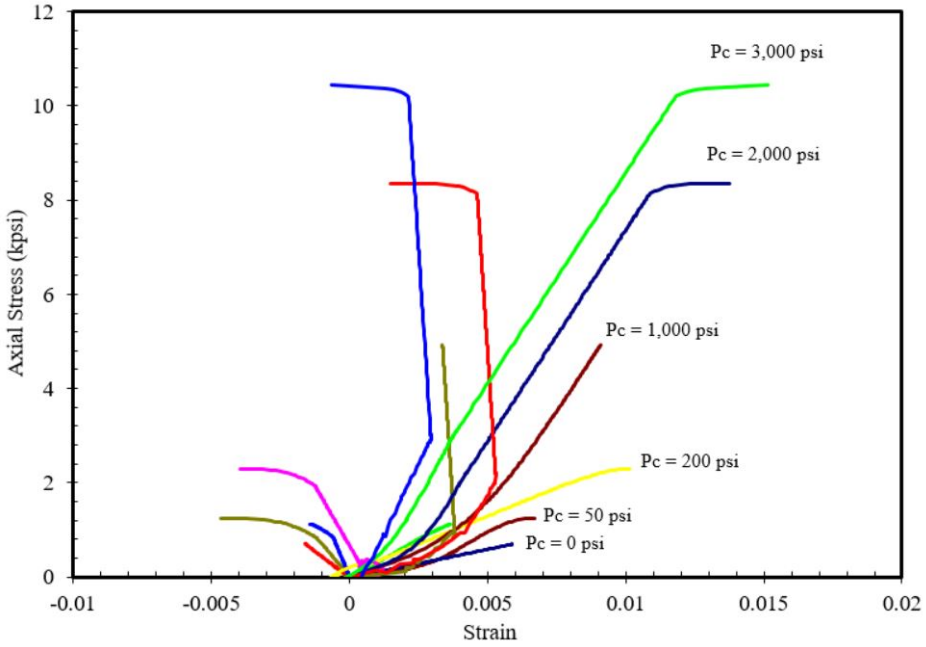

Figure 5.38: Stress - Strain curve for an artificial rock with UCS - 638 psi from B1 layer.

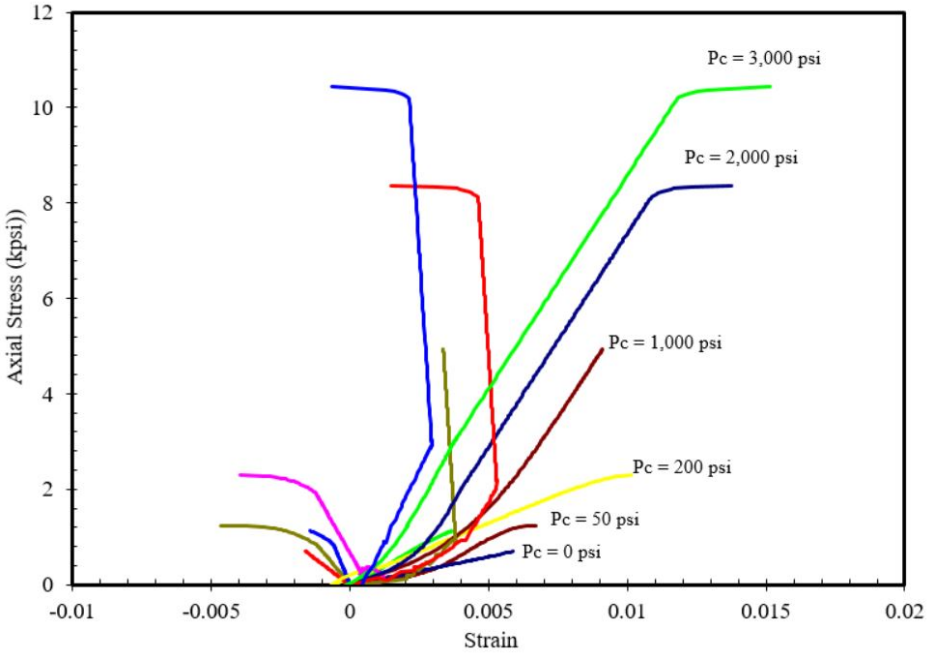

Figure 5.39: Stress - Strain curve for an artificial rock with UCS - 1,113 psi from B1 layer.

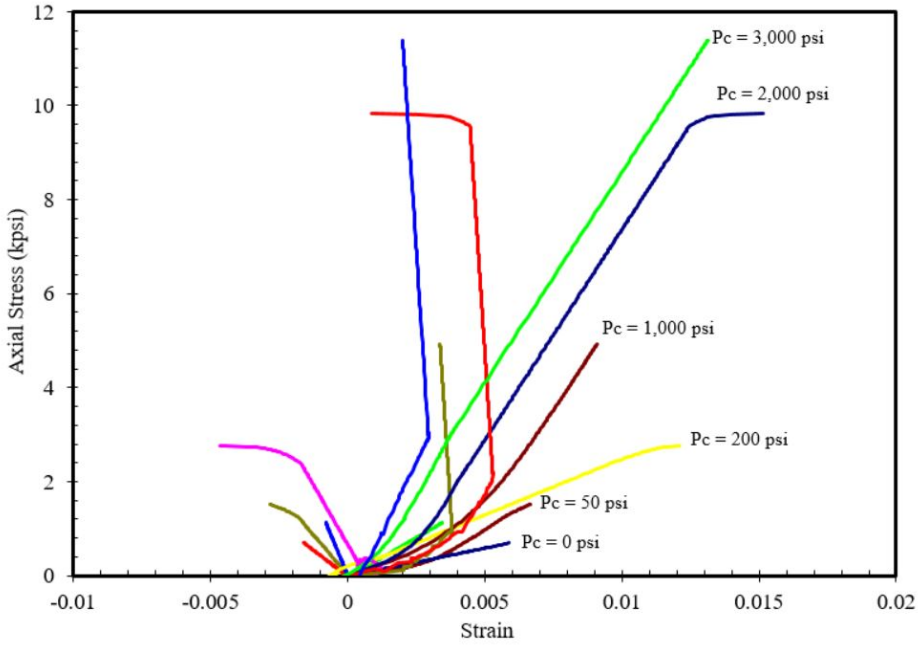

Figure 5.40: Stress - Strain curve for an artificial rock with UCS - 1,410 psi from B1 layer.

5.4 Detailed Sand Rate Prediction

The sand production potential and sand rates from six rocks with UCS 282, 460, 638, 817, 1113 and 1410 psi are studied for the B1 layer. The B1 layer consists of rocks with strength ranging from 282 psi to 3,591 psi but not all rocks fail and produce sand. Rocks with UCS below 1,410 psi show the presence of sand production potential and will be studied here in detail. Staggered perforation pattern shot density of 6 spf (shots per foot) at 120° phasing is used in this analysis. There are total of 18 perforations in 6 layers. The top and bottom 6 perforations are included to interact with the central ones and do not produce sand. The total depth of the formation that may produce sand is 112.2 ft with different strengths of rocks.

5.4.1 Case I - 1,410 psi UCS

This is the strongest of the artificial sandstone rock prepared from the available triaxial data. The stress-strain curves are shown in Fig. 5.40. The constitutive relations are derived from extrapolating the triaxial data. The simulation is carried on for a vertical well with x, y and z axes aligned

with minimum horizontal, maximum horizontal and vertical stresses respectively. The sand rate simulation conditions are stated in Table 5.12.

Simulation Conditions	
Depth	5,082 ft.
Well diameter	8.5 in.
Permeability	1,000 md
Porosity	30%
S_{wi}	20%
Fluid Density	0.7504 gm/cc
Fluid Viscosity	4.5 cp
Oil Compressibility	1.068×10^{-5} 1/psi
Vertical pressure gradient	0.972 psi/ft
Initial reservoir pressure	2,568 psi
Initial stress ratio (σ_h/σ_v)	0.274
Initial stress ratio (σ_H/σ_v)	0.374
Ratio of effective stress change during depletion ($\Delta\sigma_h^e/\Delta\sigma_v^e$)	0.3
Failure criterion: Critical plastic strain (ε_c^p)	0.00343
Perforation hole length	10 in.
Perforation shot density	6 spf
Perforation phasing	120°

Table 5.12: Simulation reservoir conditions for Case I in B1 layer with UCS: 1,410 psi.

Initially, the simulation was planned for 40 years with 480 psi depletion but after a certain number of iterations remeshing the perforation cavity is not numerically feasible. The shape of the perforation becomes much distorted for any meaningful calculations to take place. Hence, the

simulation is carried on for 38 years with a total depletion of 456 psi. A drawdown of 500 psi is applied at the perforation face. The stresses are shown in Fig. 5.41.

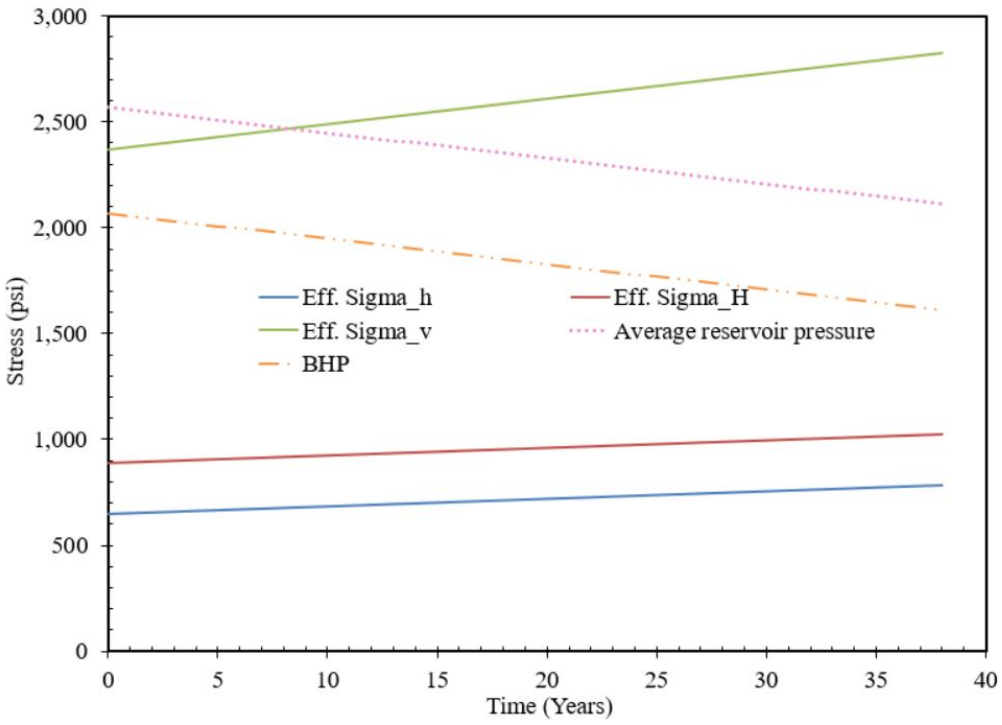

Figure 5.41: Stress states during the simulation of sand rate prediction for the rock with UCS of 1,410 psi for 500 psi drawdown.

The results show that failure starts to occur in the seventh year of oil production but the cavity disintegration and sand production does not start until eighteen years (Fig. 5.42). The calibration factor A_1 is determined using the Eq. 4.4 which was derived from polyaxial experimental test results. The effective stress change in the maximum principal stress direction after the onset ($\Delta\sigma^e_{max}$) is 240 psi and the thick-walled cylinder strength is 3,478 psi from Fig. 4.22. Hence, A_1 came out to be 11.1695×10^{-2}. From Eq. 4.5 and 4.6, 95% confidence interval of A_1 can be calculated which comes out to be 6.496×10^{-2} and 16.7516×10^{-2}. The estimated range of cumulative sand production from 24 feet of this rock is between 18 and 48 tons over a period of 38 years.

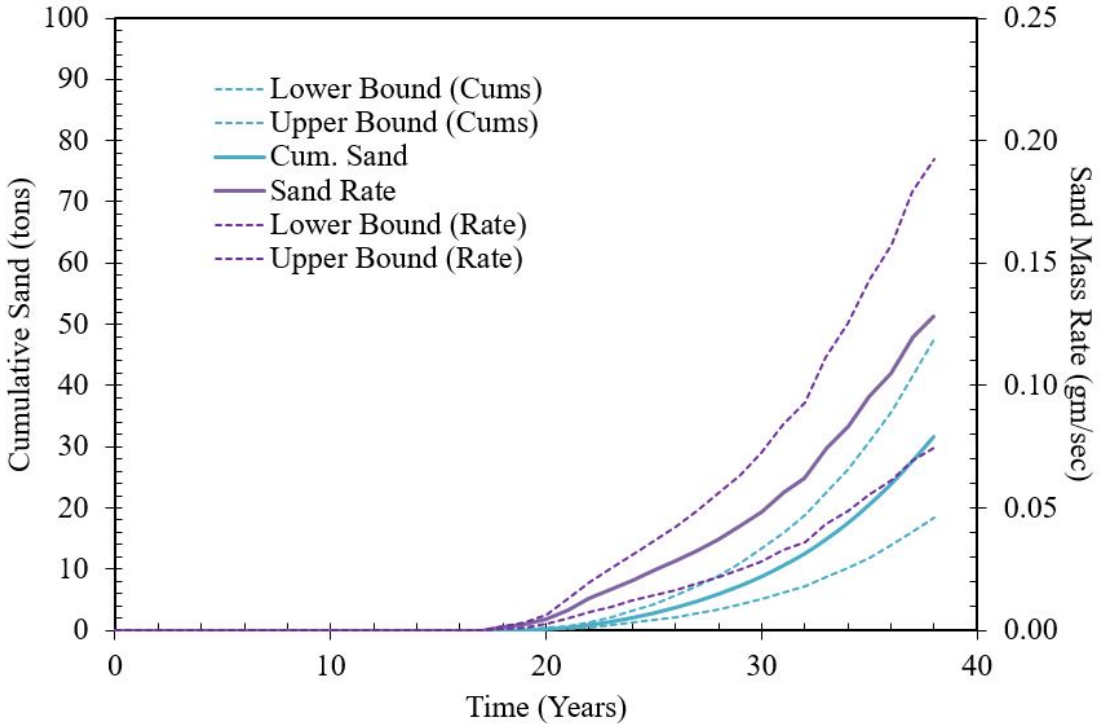

Figure 5.42: Sand rate prediction for the rock with UCS of 1,410 psi with 500 psi of drawdown.

Critical plastic stain criterion is used for the judgment of failure. The failure does not automatically triggers onset of sand production. As discussed in previous chapters, a stable arch is shown to be formed even after failure; which needs to be disintegrated with a critical flow rate. Figs. 5.43 show the increase in failed gauss points over the span of simulation run at 7 and 38 years. It clearly indicates that the failure starts to occur around the sides of the perforations and continues in that direction. After remeshing, the perforation takes the shape of an ellipsoidal balloon slightly squeezed in vertical direction.

Similarly, the simulation is run for a drawdown of 300 psi with stress states depicted in Fig. 5.44 . The results show that failure starts to occur in the 9th year of oil production but the cavity disintegration and sand production does not start until 22nd year (Fig. 5.45). The estimated range of cumulative sand production from 24 feet of this rock is between 8 and 20 tons over a period of 40 years for 300 psi drawdown. Figs. 5.46 show the increase in failed gauss points over the span

of simulation run at 9 and 40 years.

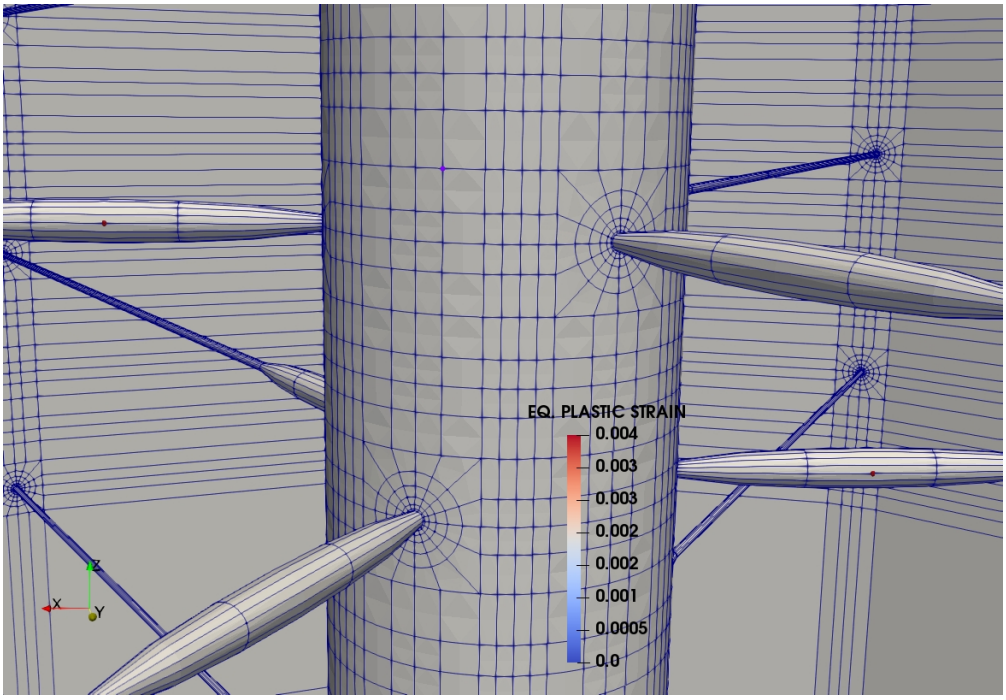

(a) At 7 years of production.

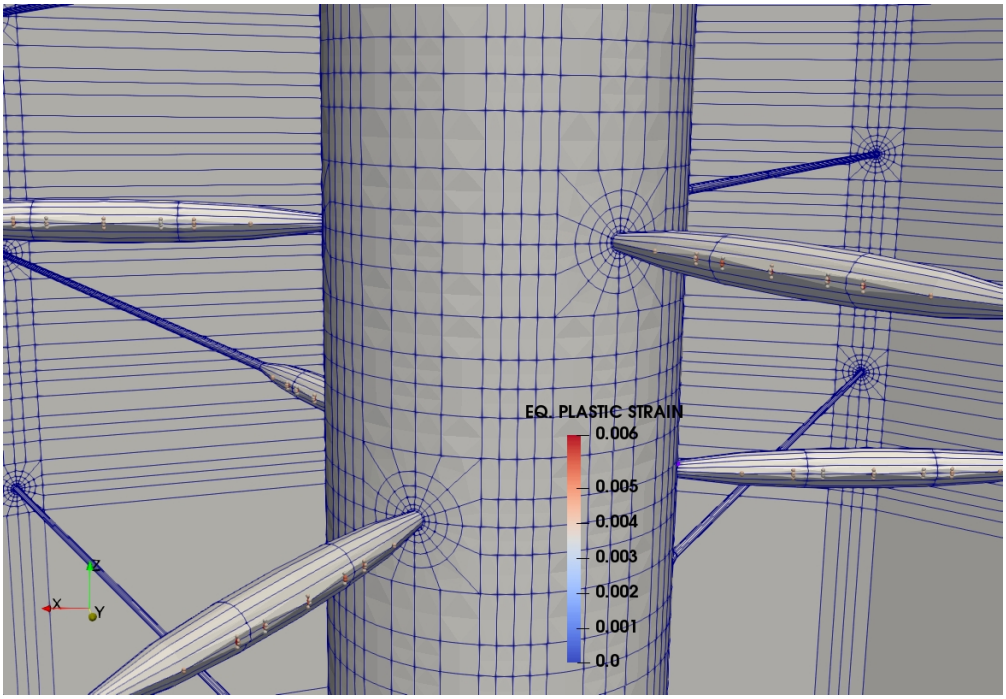

(b) At 38 years of production.

Figure 5.43: ε^p around the perforations at failed gauss points for Case I of UCS 1,410 psi.

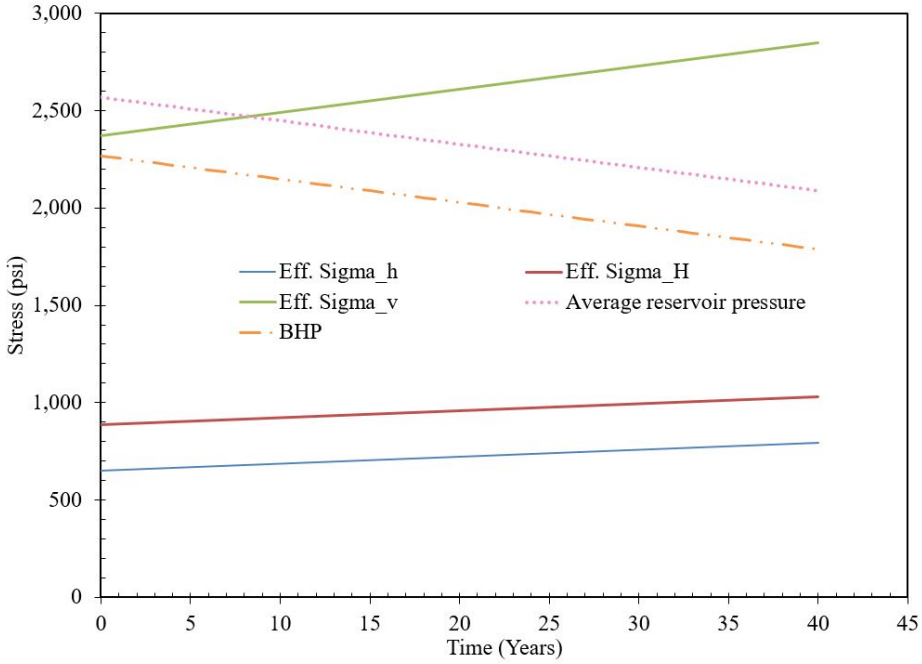

Figure 5.44: Stress states during the simulation of sand rate prediction for the rock with UCS of 1,410 psi for 300 psi drawdown.

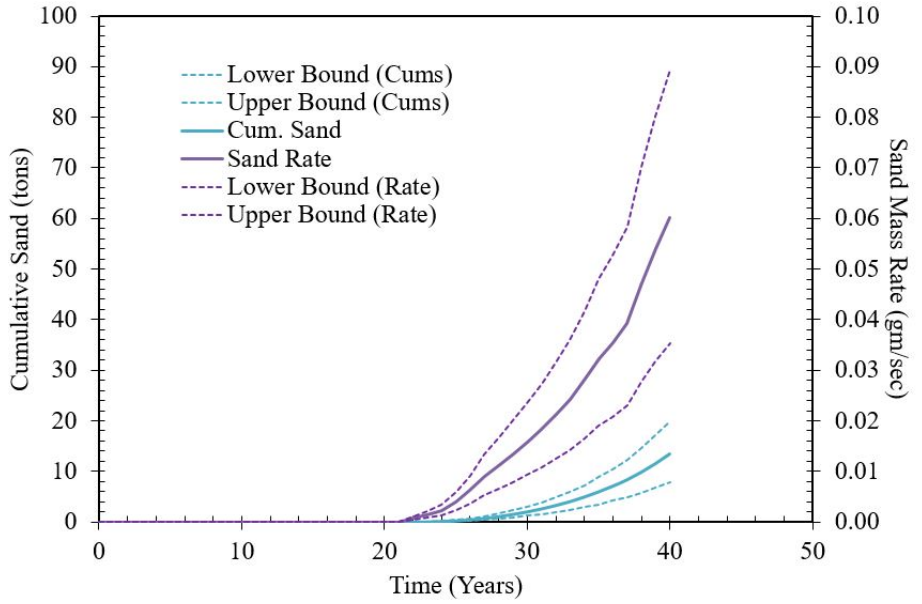

Figure 5.45: Sand rate prediction for the rock with UCS of 1,410 psi with 300 psi of drawdown.

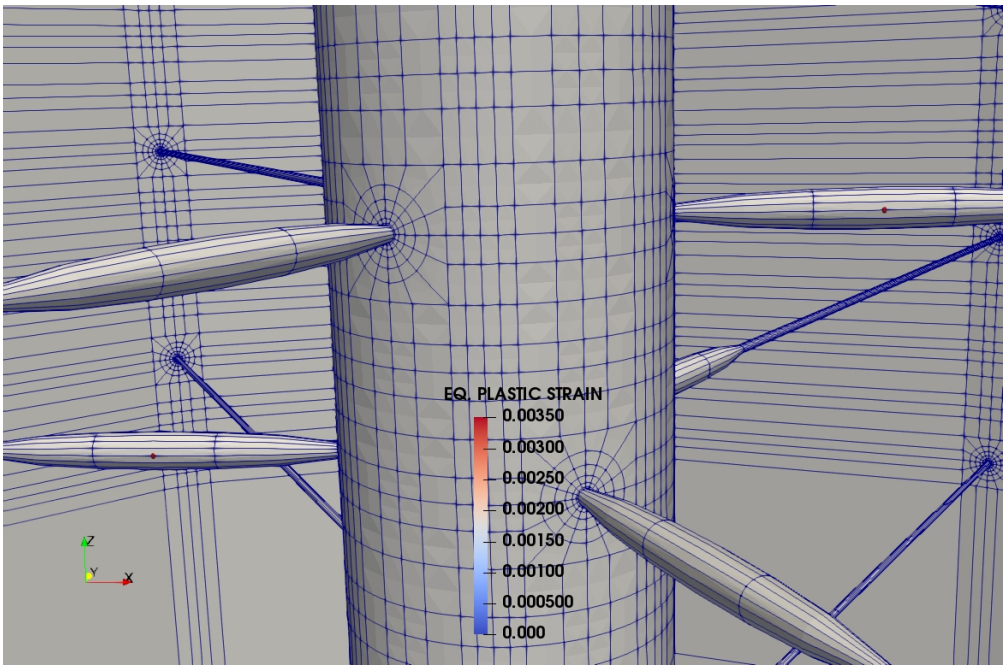

(a) At 9 years of production.

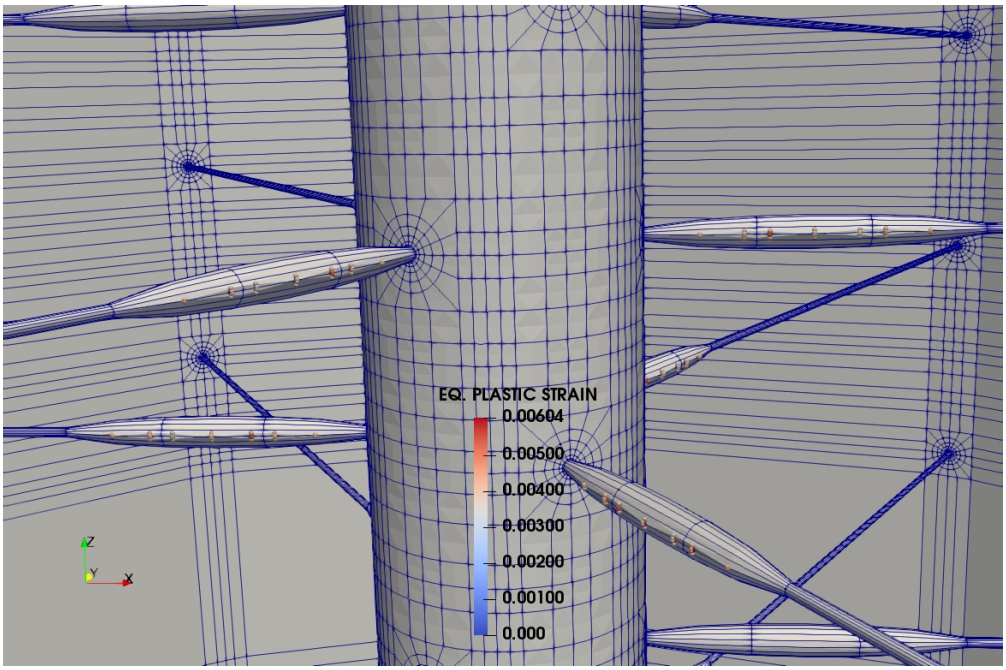

(b) At 40 years of production.

Figure 5.46: ε^p around the perforations at failed gauss points for Case I of UCS 1,410 psi for 300 psi drawdown.

5.4.2 Case II - 1,113 psi UCS

This is one of the stronger artificial sandstone rock prepared from the available triaxial data. The stress-strain curves are shown in Fig. 5.39. The constitutive relations are derived from extrapolating the triaxial data. The simulation is carried on for a vertical well with x, y and z axes aligned with minimum horizontal, maximum horizontal and vertical stresses respectively. The sand rate simulation conditions are stated in Table 5.13.

Simulation Conditions	
Depth	5,082 ft.
Well diameter	8.5 in.
Permeability	1,000 md
Porosity	30%
S_{wi}	20%
Fluid Density	0.7504 gm/cc
Fluid Viscosity	4.5 cp
Oil Compressibility	1.068×10^{-5} 1/psi
Vertical pressure gradient	0.972 psi/ft
Initial reservoir pressure	2,568 psi
Initial stress ratio (σ_h/σ_v)	0.274
Initial stress ratio (σ_H/σ_v)	0.374
Ratio of effective stress change during depletion ($\Delta\sigma_h^e/\Delta\sigma_v^e$)	0.3
Failure criterion: Critical plastic strain (ε_c^p)	0.00343
Perforation hole length	10 in.
Perforation shot density	6 spf
Perforation phasing	120°

Table 5.13: Simulation reservoir conditions for Case II in B1 layer with UCS: 1,113 psi.

Initially, the simulation was planned for 40 years with 480 psi depletion but after a certain number of iterations remeshing the perforation cavity is not numerically feasible. The shape of the perforation becomes much distorted for any meaningful calculations to take place. Hence, the simulation is carried on for 35 years with a total depletion of 420 psi. A drawdown of 500 psi is applied at the perforation face. The stresses are shown in Fig. 5.47.

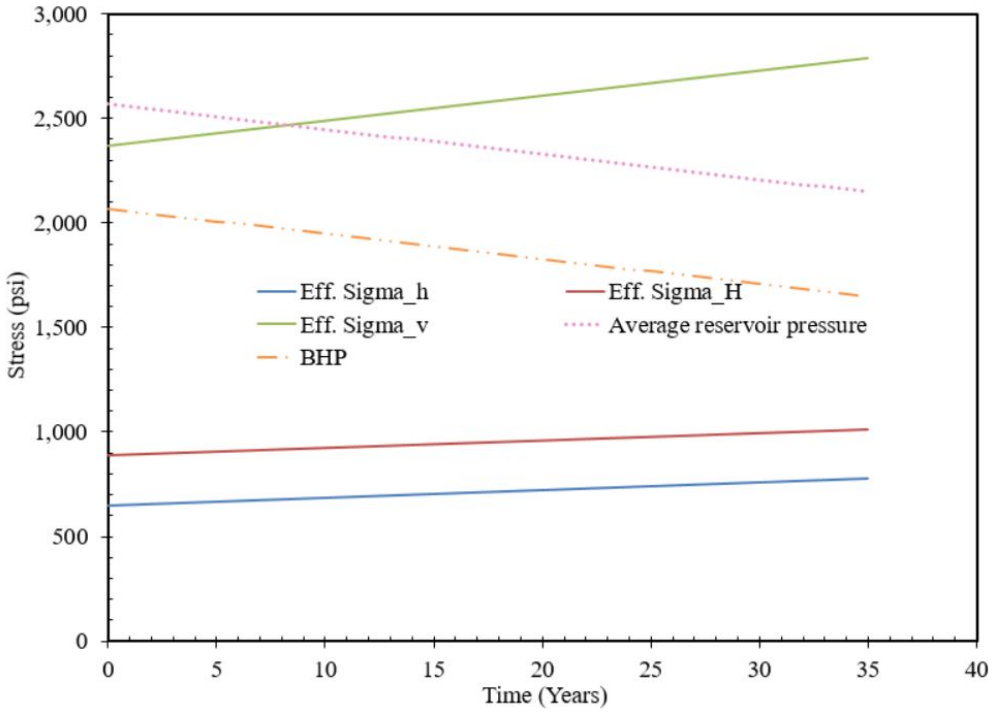

Figure 5.47: Stress states during the simulation of sand rate prediction for the rock with UCS of 1,113 psi for 500 psi drawdown.

The results show that failure starts to occur in the first year of oil production but the cavity disintegration and sand production does not start until third year (Fig. 5.48). The calibration factor A_1 is determined using the Eq. 4.4 which was derived from polyaxial experimental test results. The effective stress change in the maximum principal stress direction after the onset ($\Delta\sigma^e_{max}$) is 396 psi and the thick-walled cylinder strength is 2,812 psi from Fig. 4.22. Hence, A_1 came out to be 9.3059×10^{-2}. From Eq. 4.5 and 4.6, 95% confidence interval of A_1 can be calculated

which comes out to be 4.8764×10^{-2} and 15.4899×10^{-2}. The estimated range of cumulative sand production from 51 feet of this rock is between 153 and 486 tons over a period of 35 years.

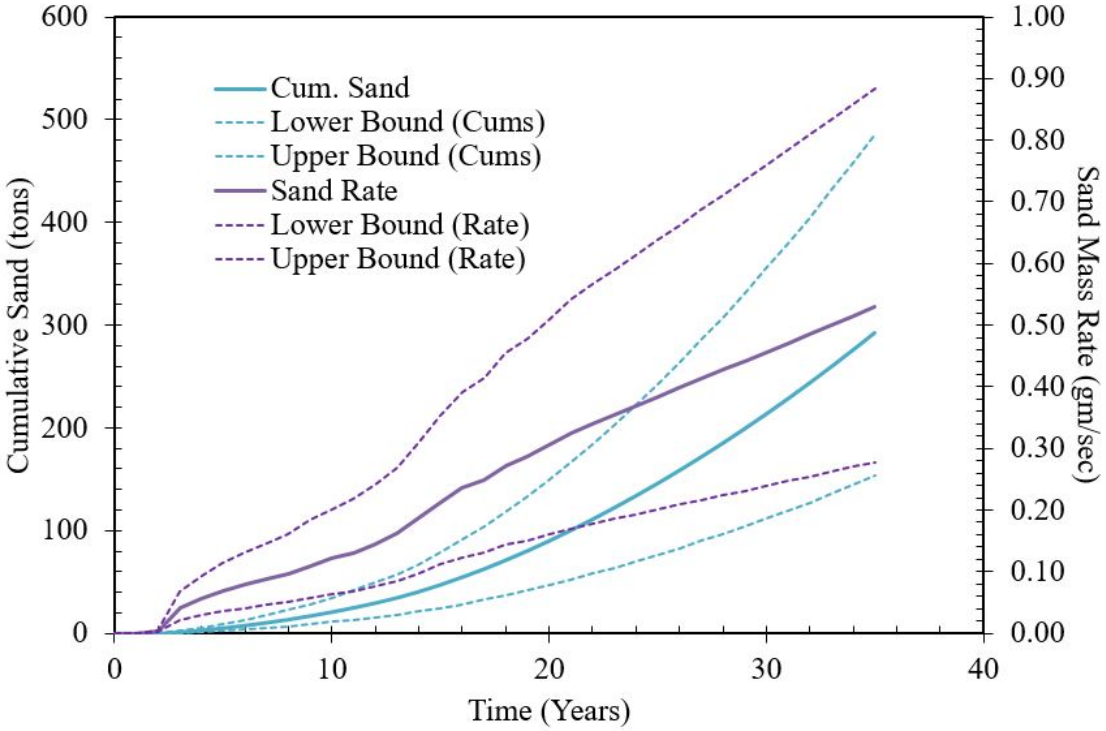

Figure 5.48: Sand rate prediction for the rock with UCS of 1,113 psi with 500 psi of drawdown.

Critical plastic stain criterion is used for the judgment of failure. The failure does not automatically triggers onset of sand production. As discussed in previous chapters, a stable arch is shown to be formed even after failure; which needs to be disintegrated with a critical flow rate. Figs. 5.49 show the increase in failed gauss points over the span of simulation run at 3 and 35 years. It clearly indicates that the failure starts to occur around the sides of the perforations and continues in that direction. After remeshing, the perforation takes the shape of an ellipsoidal balloon slightly squeezed in vertical direction.

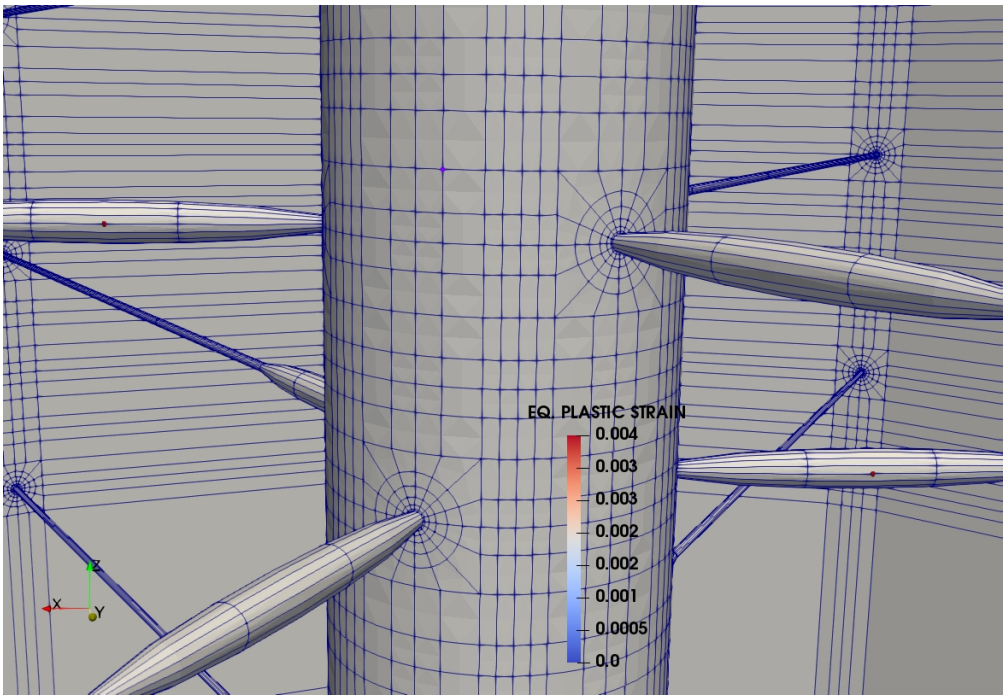

(a) After first year of production.

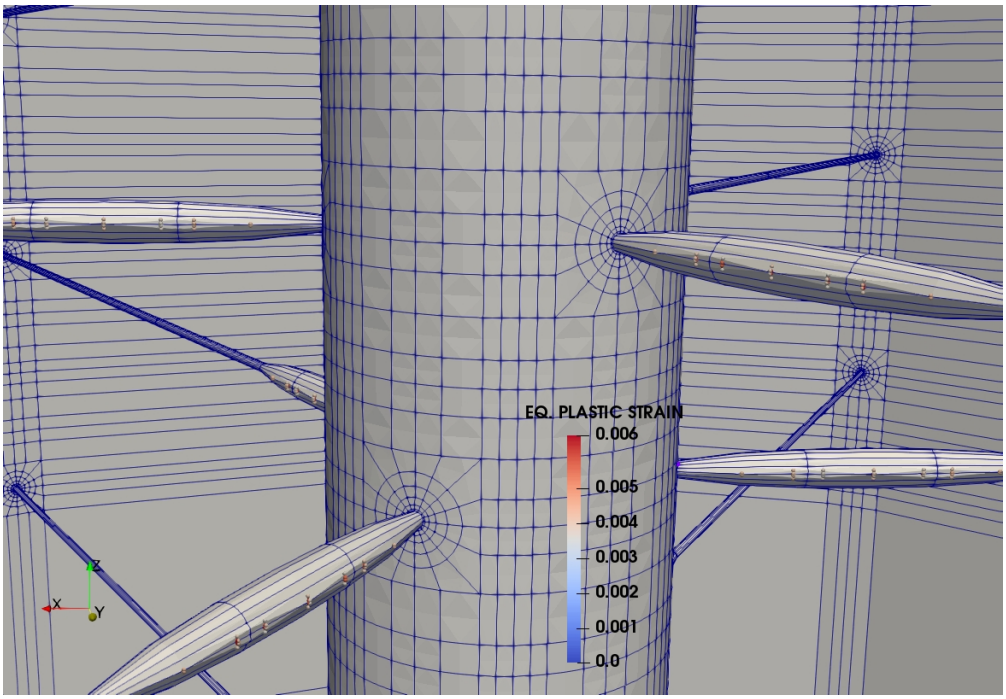

(b) At 35 years of production.

Figure 5.49: ε^p around the perforations at failed gauss points for Case II of UCS 1,113 psi for 500 psi drawdown.

Similarly, the simulation is run for a drawdown of 300 psi with stress states depicted in Fig. 5.50 . The results show that failure starts to occur in the 1st year of oil production but the cavity disintegration and sand production does not start until 5th year (Fig. 5.51). The estimated range of cumulative sand production from 51 feet of this rock is between 83 and 249 tons over a period of 33 years for 300 psi drawdown. Figs. 5.52 show the increase in failed gauss points over the span of simulation run at 1 and 33 years.

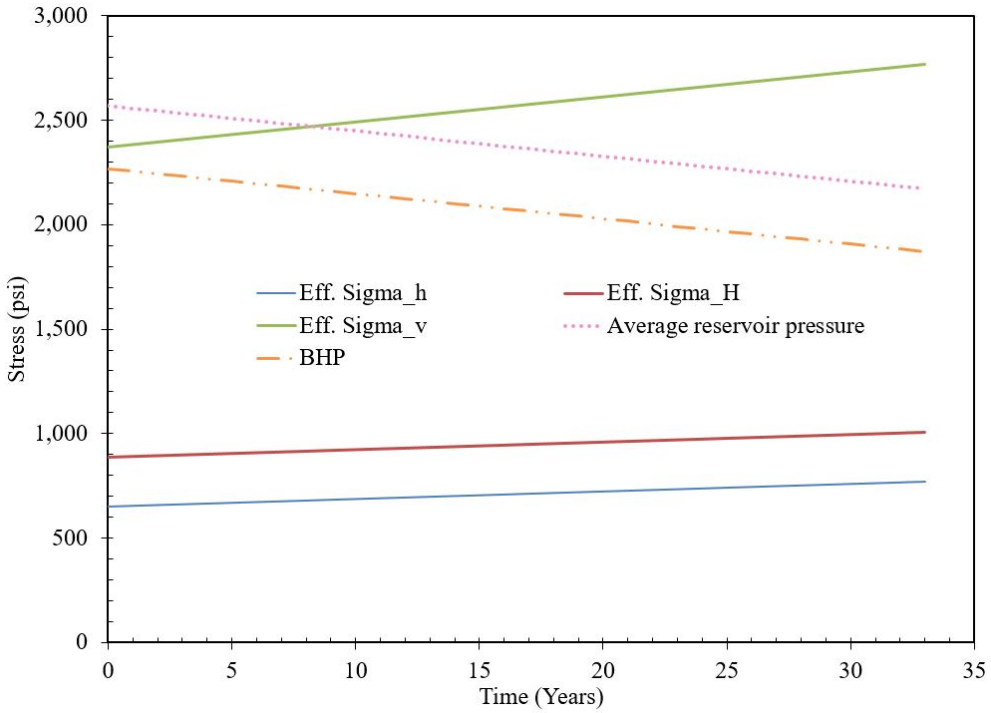

Figure 5.50: Stress states during the simulation of sand rate prediction for the rock with UCS of 1,113 psi for 300 psi drawdown.

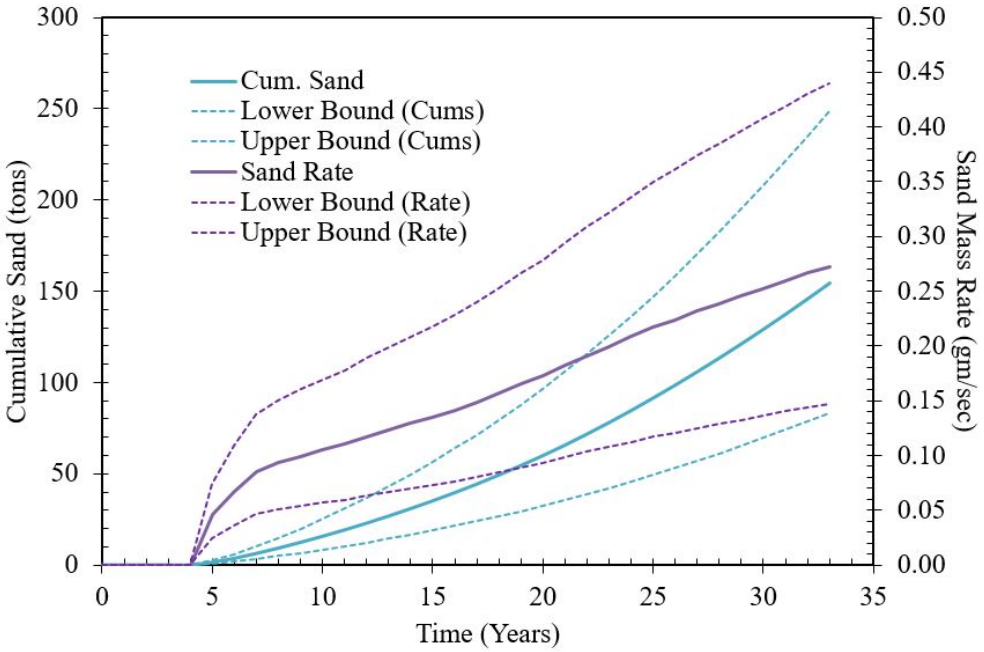

Figure 5.51: Sand rate prediction for the rock with UCS of 1,113 psi with 300 psi of drawdown.

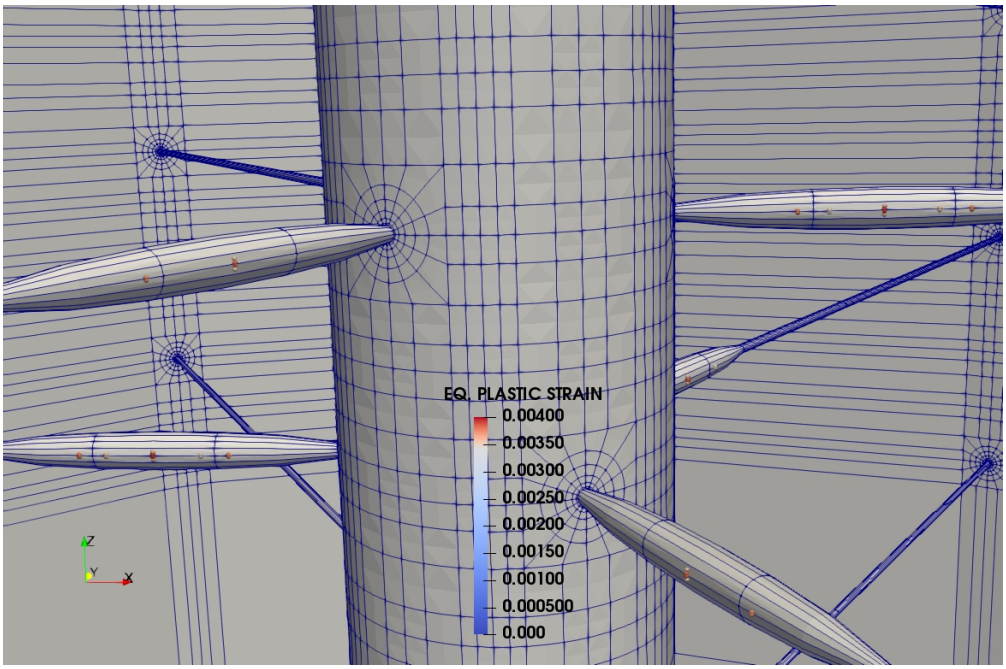

(a) After first year of production.

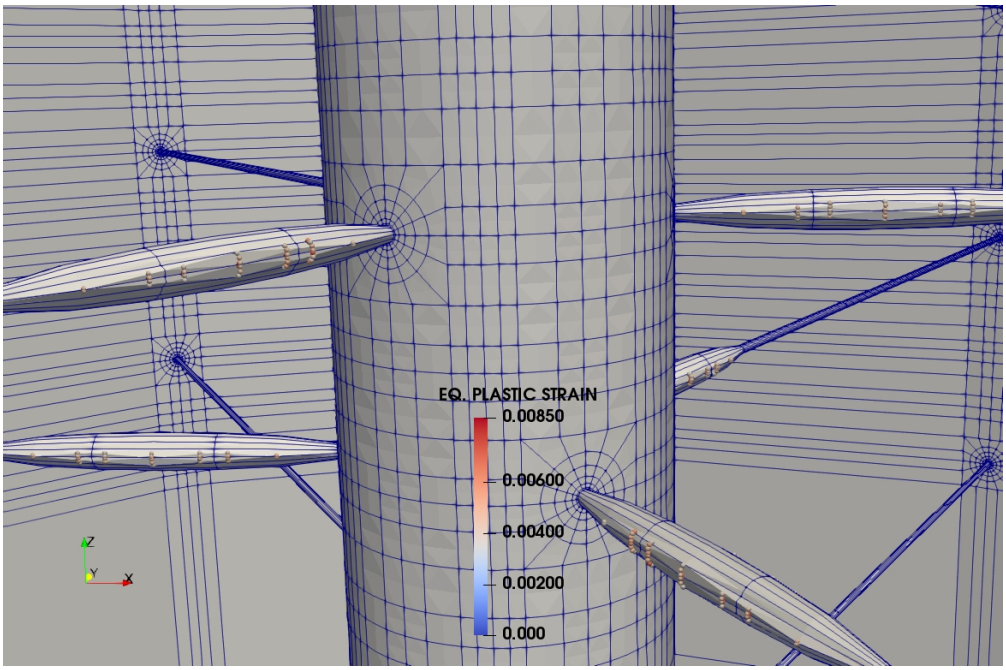

(b) At 33 years of production.

Figure 5.52: ε^p around the perforations at failed gauss points for Case II of UCS 1,113 psi for 300 psi drawdown.

5.4.3 Case III - 817 psi UCS

This is one of the original sandstone rock data from the available triaxial core analysis. The stress-strain curves are shown in Fig. 5.10. The constitutive relations are derived from the triaxial data. The simulation is carried on for a vertical well with x, y and z axes aligned with minimum horizontal, maximum horizontal and vertical stresses respectively. The sand rate simulation conditions are stated in Table 5.14.

Simulation Conditions	
Depth	5,082 ft.
Well diameter	8.5 in.
Permeability	1,000 md
Porosity	30%
S_{wi}	20%
Fluid Density	0.7504 gm/cc
Fluid Viscosity	4.5 cp
Oil Compressibility	1.068×10^{-5} 1/psi
Vertical pressure gradient	0.972 psi/ft
Initial reservoir pressure	2,568 psi
Initial stress ratio (σ_h/σ_v)	0.274
Initial stress ratio (σ_H/σ_v)	0.374
Ratio of effective stress change during depletion ($\Delta\sigma_h^e/\Delta\sigma_v^e$)	0.3
Failure criterion: Critical plastic strain (ε_c^p)	0.00343
Perforation hole length	10 in.
Perforation shot density	6 spf
Perforation phasing	120°

Table 5.14: Simulation reservoir conditions for Case III in B1 layer with UCS: 817 psi.

Initially, the simulation was planned for 40 years with 480 psi depletion but after a certain number of iterations remeshing the perforation cavity is not numerically feasible. The shape of the perforation becomes much distorted for any meaningful calculations to take place. Hence, the simulation is carried on for 33 years with a total depletion of 396 psi. A drawdown of 500 psi is applied at the perforation face. The stresses are shown in Fig. 5.53.

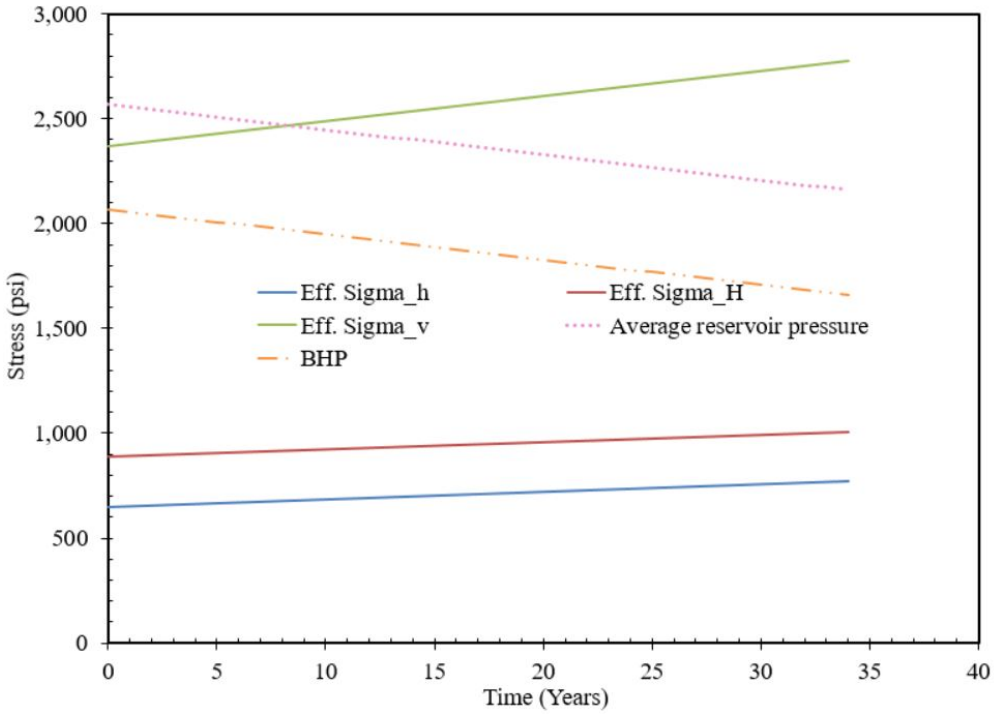

Figure 5.53: Stress states during the simulation of sand rate prediction for the rock with UCS of 817 psi for 500 psi drawdown.

The results show that failure starts to occur in the first year of oil production but the cavity disintegration and sand production does not start until third year (Fig. 5.54). The calibration factor A_1 is determined using the Eq. 4.4 which was derived from polyaxial experimental test results. The effective stress change in the maximum principal stress direction after the onset ($\Delta\sigma^e_{max}$) is 324 psi and the thick-walled cylinder strength is 2,112 psi from Fig. 4.22. Hence, A_1 came out to be 9.0139×10^{-2}. From Eq. 4.5 and 4.6, 95% confidence interval of A_1 can be calculated

which comes out to be 4.6382×10^{-2} and 15.2795×10^{-2}. The estimated range of cumulative sand production from 20 feet of this rock is between 25 and 83 tons over a period of 33 years.

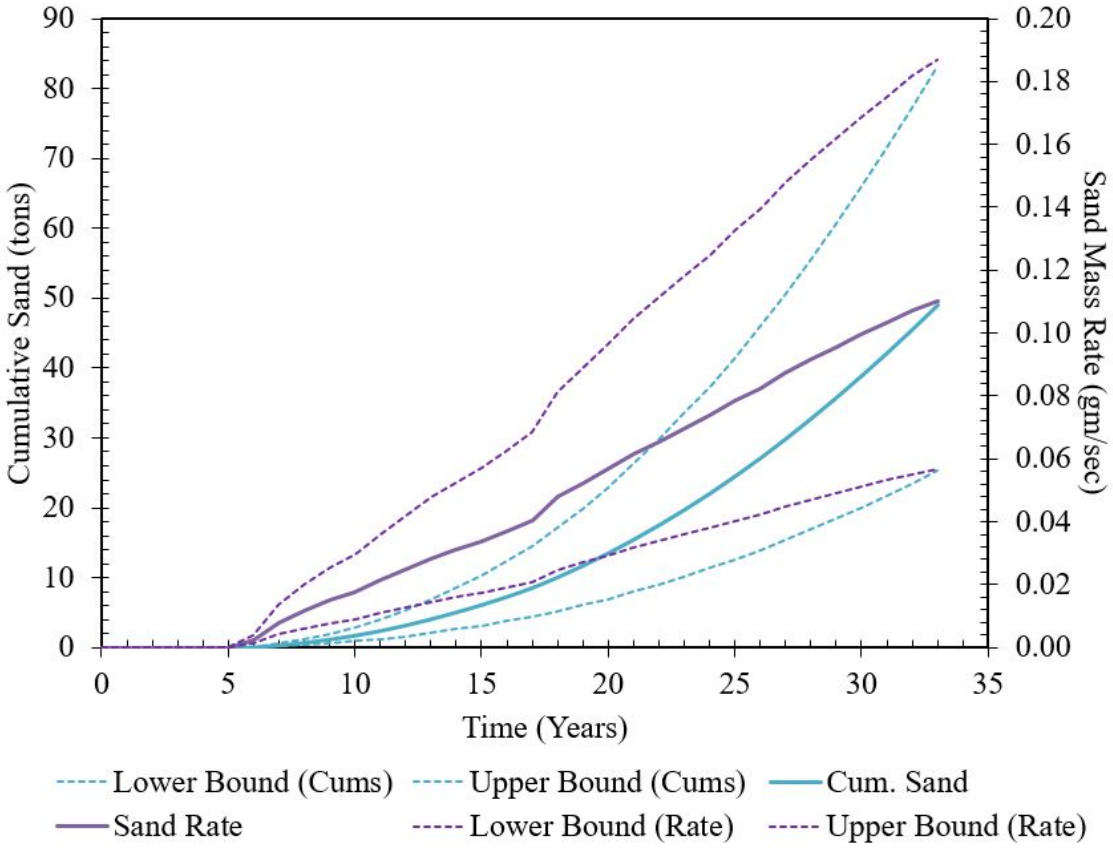

Figure 5.54: Sand rate prediction for the rock with UCS of 817 psi with 500 psi of drawdown.

Critical plastic stain criterion is used for the judgment of failure. The failure does not automatically triggers onset of sand production. As discussed in previous chapters, a stable arch is shown to be formed even after failure; which needs to be disintegrated with a critical flow rate. Figs. 5.55 show the increase in failed gauss points over the span of simulation run at 1 and 33 years. It clearly indicates that the failure starts to occur around the sides of the perforations and continues in that direction. After remeshing, the perforation takes the shape of an ellipsoidal balloon slightly squeezed in vertical direction.

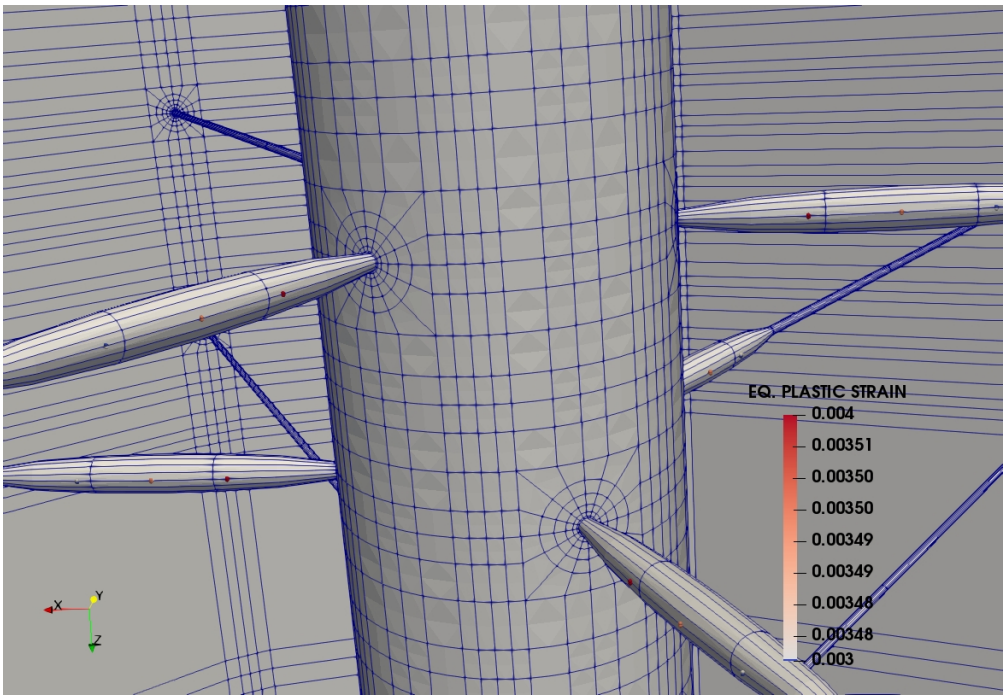

(a) After first year of production.

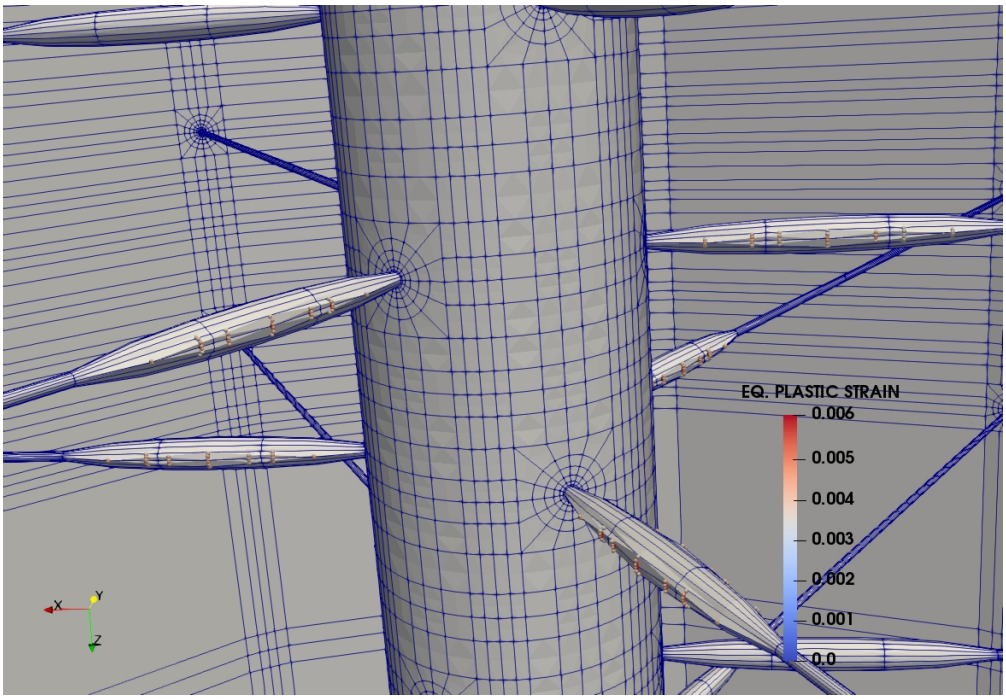

(b) At 33 years of production.

Figure 5.55: ε^p around the perforations at failed gauss points for Case III of UCS 817 psi for 500 psi drawdown.

Similarly, the simulation is run for a drawdown of 300 psi with stress states depicted in Fig. 5.56 . The results show that failure starts to occur in the 1st year of oil production but the cavity disintegration and sand production does not start until 10th year (Fig. 5.57). The estimated range of cumulative sand production from 20 feet of this rock is between 14 and 47 tons over a period of 36 years for 300 psi drawdown. Figs. 5.58 show the increase in failed gauss points over the span of simulation run at 1 and 36 years.

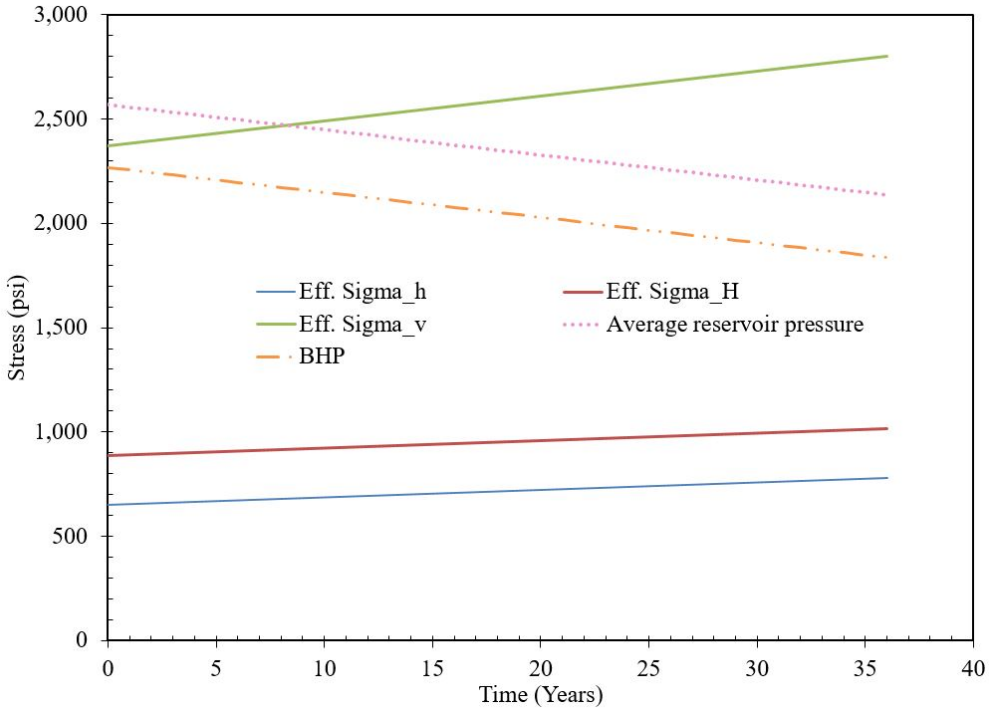

Figure 5.56: Stress states during the simulation of sand rate prediction for the rock with UCS of 817 psi for 300 psi drawdown.

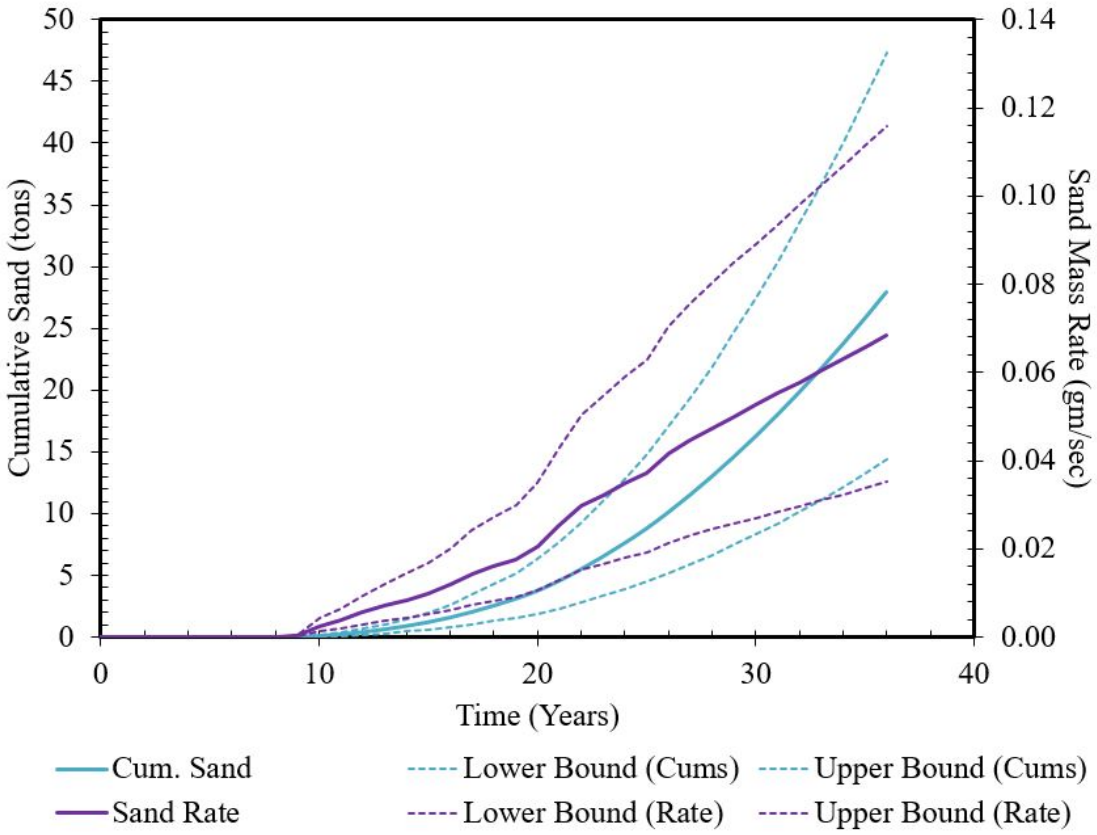

Figure 5.57: Sand rate prediction for the rock with UCS of 817 psi with 300 psi of drawdown.

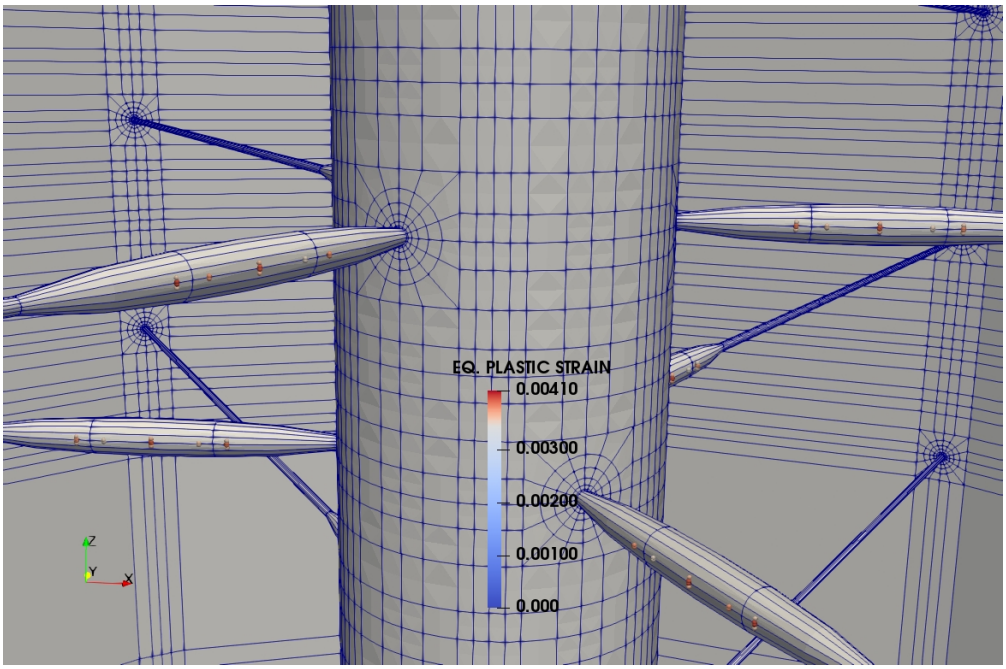

(a) After first year of production.

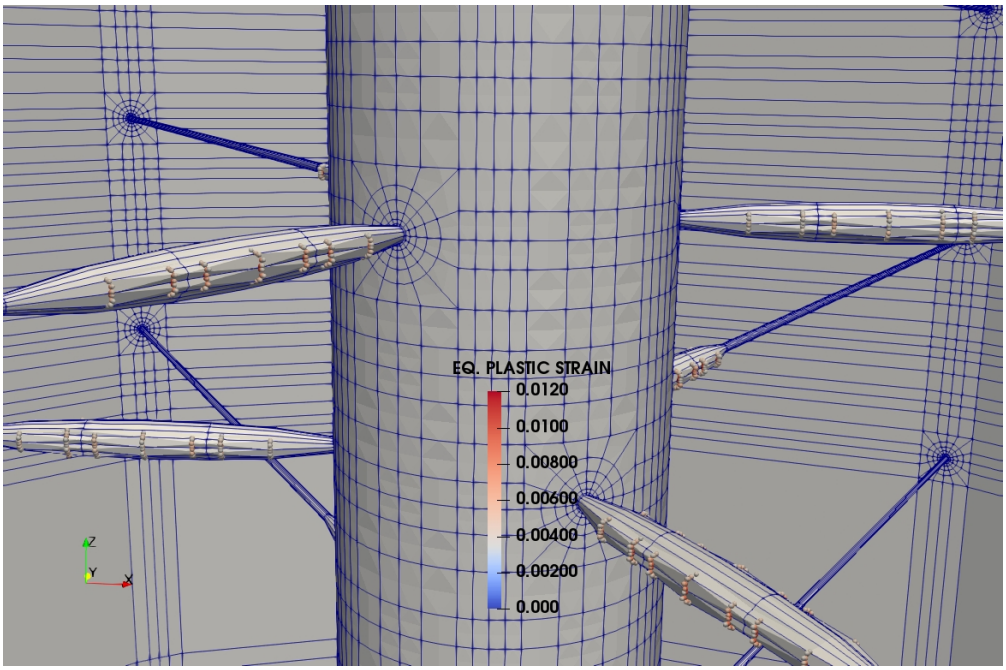

(b) At 36 years of production.

Figure 5.58: ε^p around the perforations at failed gauss points for Case III of UCS 817 psi for 300 psi drawdown.

5.4.4 Case IV - 638 psi UCS

This is an artificial sandstone rock data prepared from the available triaxial core analysis. The stress-strain curves are shown in Fig. 5.38. The constitutive relations are derived from the triaxial data. The simulation is carried on for a vertical well with x, y and z axes aligned with minimum horizontal, maximum horizontal and vertical stresses respectively. The sand rate simulation conditions are stated in Table 5.15.

Simulation Conditions	
Depth	5,082 ft.
Well diameter	8.5 in.
Permeability	1,000 md
Porosity	30%
S_{wi}	20%
Fluid Density	0.7504 gm/cc
Fluid Viscosity	4.5 cp
Oil Compressibility	1.068×10^{-5} 1/psi
Vertical pressure gradient	0.972 psi/ft
Initial reservoir pressure	2,568 psi
Initial stress ratio (σ_h/σ_v)	0.274
Initial stress ratio (σ_H/σ_v)	0.374
Ratio of effective stress change during depletion ($\Delta\sigma_h^e/\Delta\sigma_v^e$)	0.3
Failure criterion: Critical plastic strain (ε_c^p)	0.00343
Perforation hole length	10 in.
Perforation shot density	6 spf
Perforation phasing	120°

Table 5.15: Simulation reservoir conditions for Case IV in B1 layer with UCS: 638 psi.

The simulation runs for a period of 40 years. A drawdown of 500 psi is applied at the perforation face. The stresses are shown in Fig. 5.59.

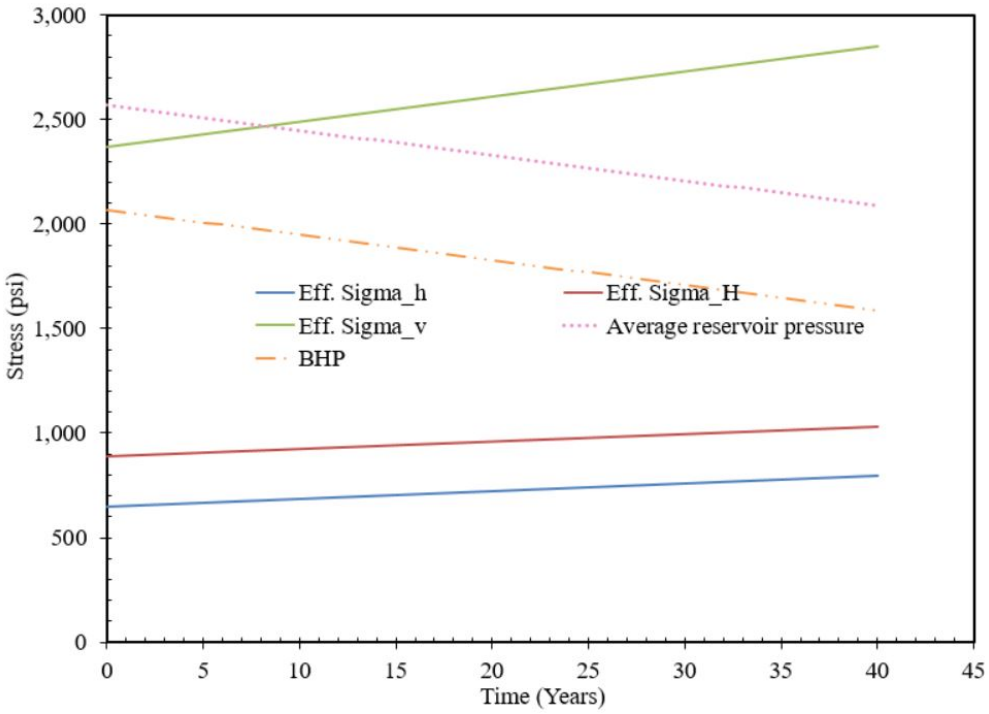

Figure 5.59: Stress states during the simulation of sand rate prediction for the rock with UCS of 638 psi for 500 psi drawdown.

The results show that failure starts to occur in the first year of oil production and the cavity disintegration and sand production also start in the same year (Fig. 5.60). The calibration factor A_1 is determined using the Eq. 4.4 which was derived from polyaxial experimental test results. The effective stress change in the maximum principal stress direction after the onset ($\Delta\sigma^e_{max}$) is 468 psi and the thick-walled cylinder strength is 1,782 psi from Fig. 4.22. Hence, A_1 came out to be 6.8283×10^{-2}. From Eq. 4.5 and 4.6, 95% confidence interval of A_1 can be calculated which comes out to be 2.9984×10^{-2} and 13.5636×10^{-2}. The estimated range of cumulative sand production from 6 feet of this rock is between 64 and 291 tons over a period of 40 years.

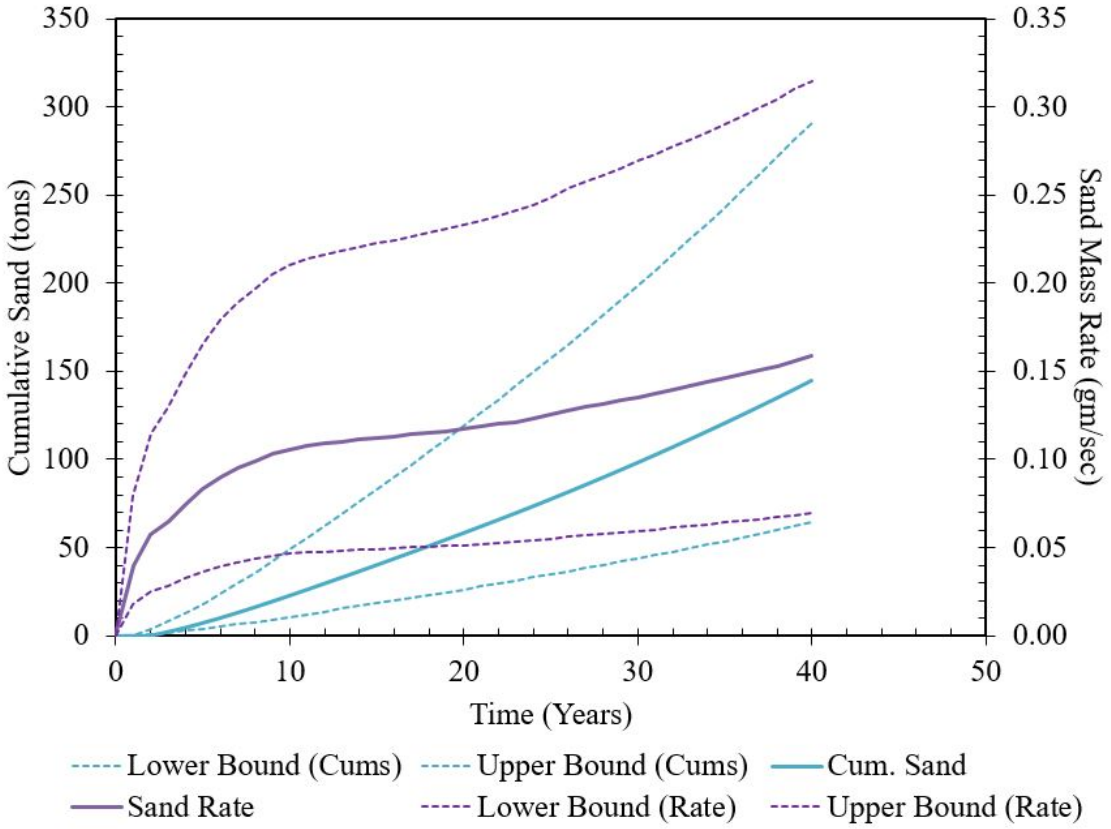

Figure 5.60: Sand rate prediction for the rock with UCS of 638 psi with 500 psi of drawdown.

Critical plastic stain criterion is used for the judgment of failure. The failure does not automatically triggers onset of sand production. As discussed in previous chapters, a stable arch is shown to be formed even after failure; which needs to be disintegrated with a critical flow rate. Figs. 5.61 show the increase in failed gauss points over the span of simulation run at 1 and 40 years. It clearly indicates that the failure starts to occur around the sides of the perforations and continues in that direction. After remeshing, the perforation takes the shape of an ellipsoidal balloon slightly squeezed in vertical direction.

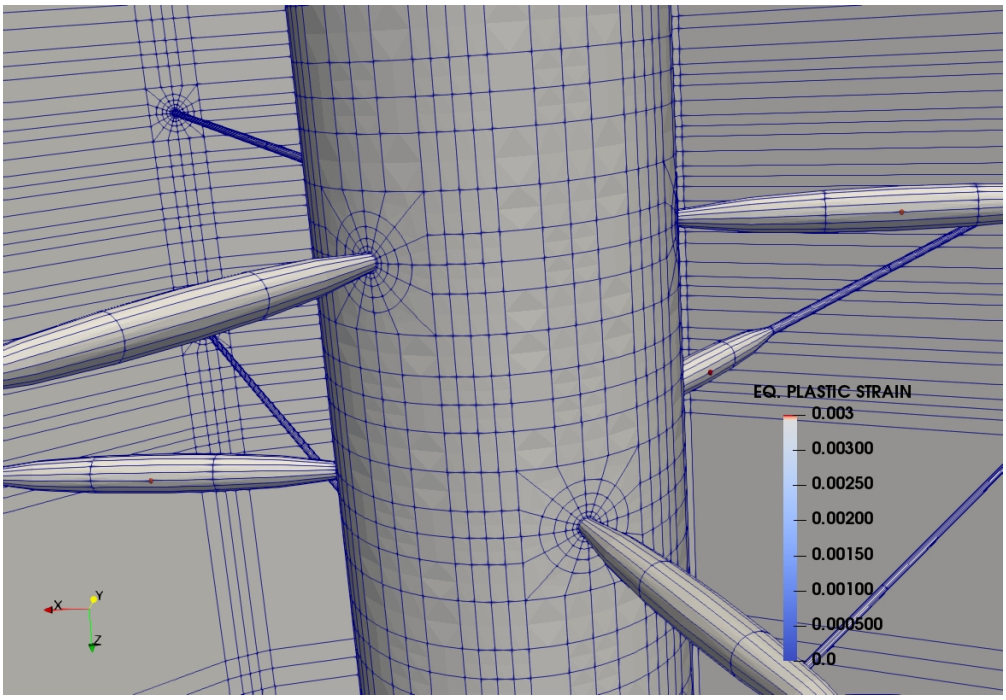

(a) After first year of production.

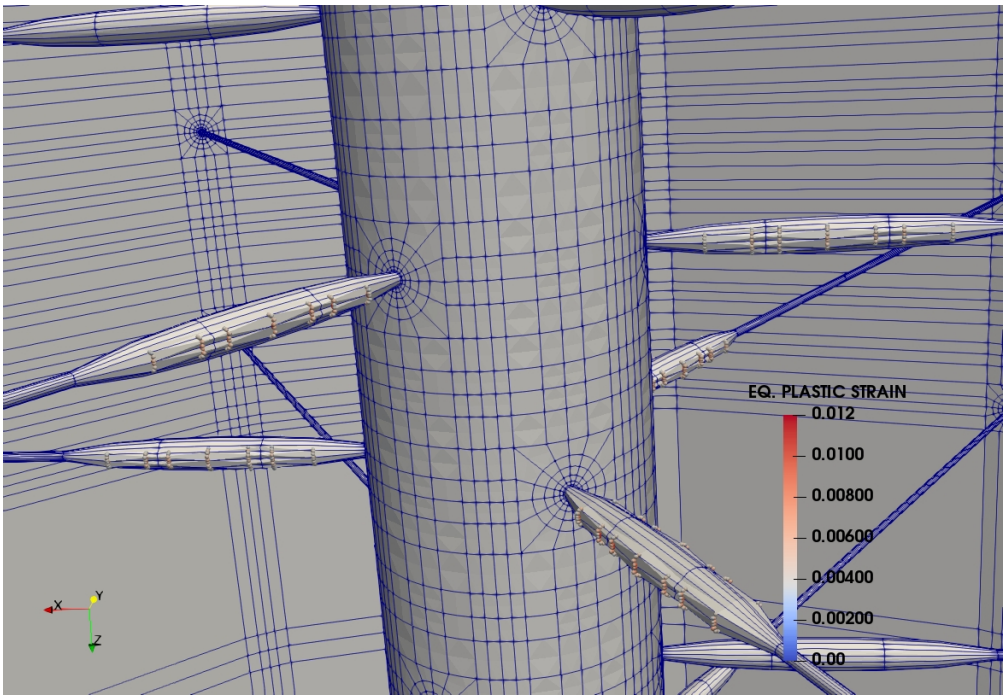

(b) At 40 years of production.

Figure 5.61: ε^p around the perforations at failed gauss points for Case IV of UCS 638 psi for 500 psi drawdown.

Similarly, the simulation is run for a drawdown of 300 psi with stress states depicted in Fig. 5.62 . The results show that failure starts to occur in the first year of oil production and the cavity disintegration and sand production also start in the same year (Fig. 5.63). The estimated range of cumulative sand production from 6 feet of this rock is between 28 and 127 tons over a period of 40 years for 300 psi drawdown. Figs. 5.64 show the increase in failed gauss points over the span of simulation run at 1 and 40 years.

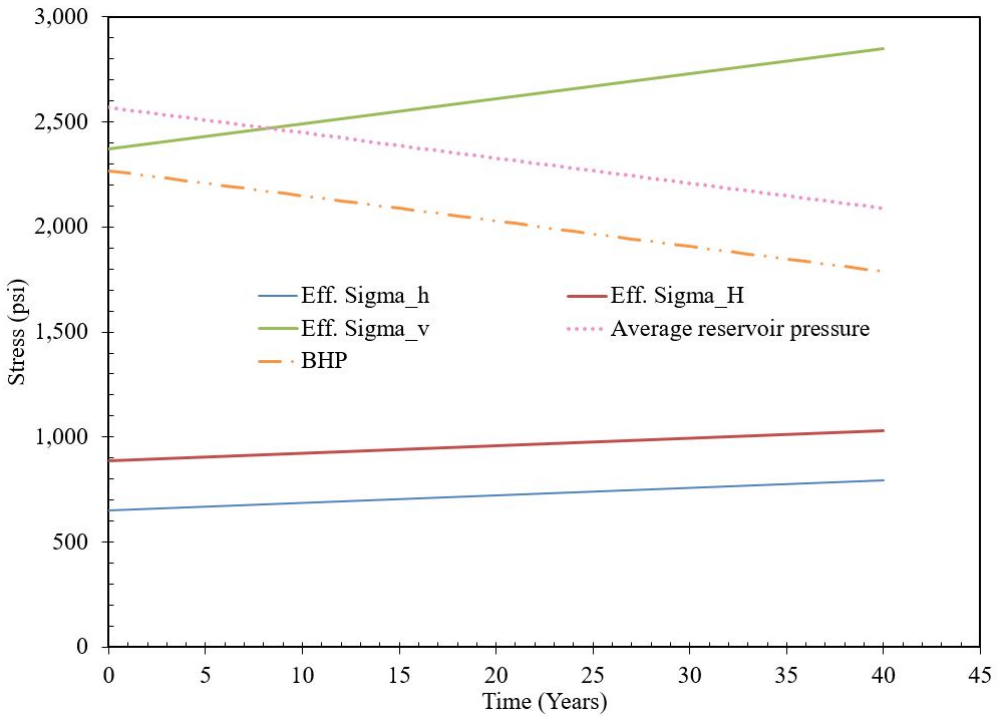

Figure 5.62: Stress states during the simulation of sand rate prediction for the rock with UCS of 638 psi for 300 psi drawdown.

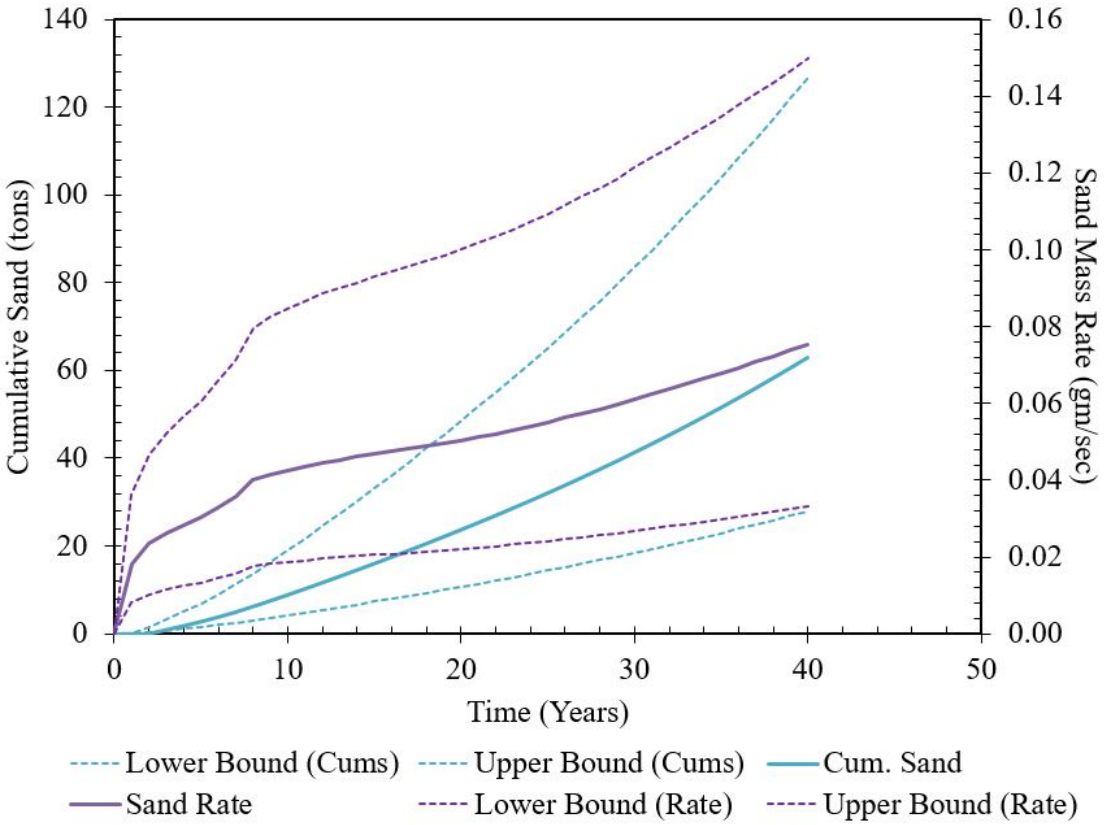

Figure 5.63: Sand rate prediction for the rock with UCS of 638 psi with 300 psi of drawdown.

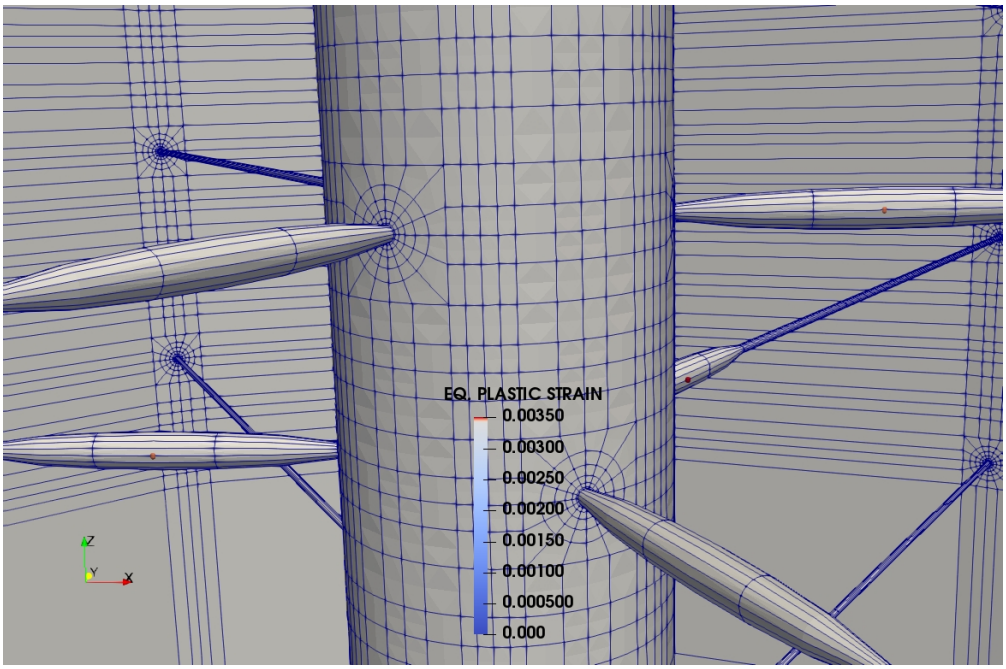

(a) After first year of production.

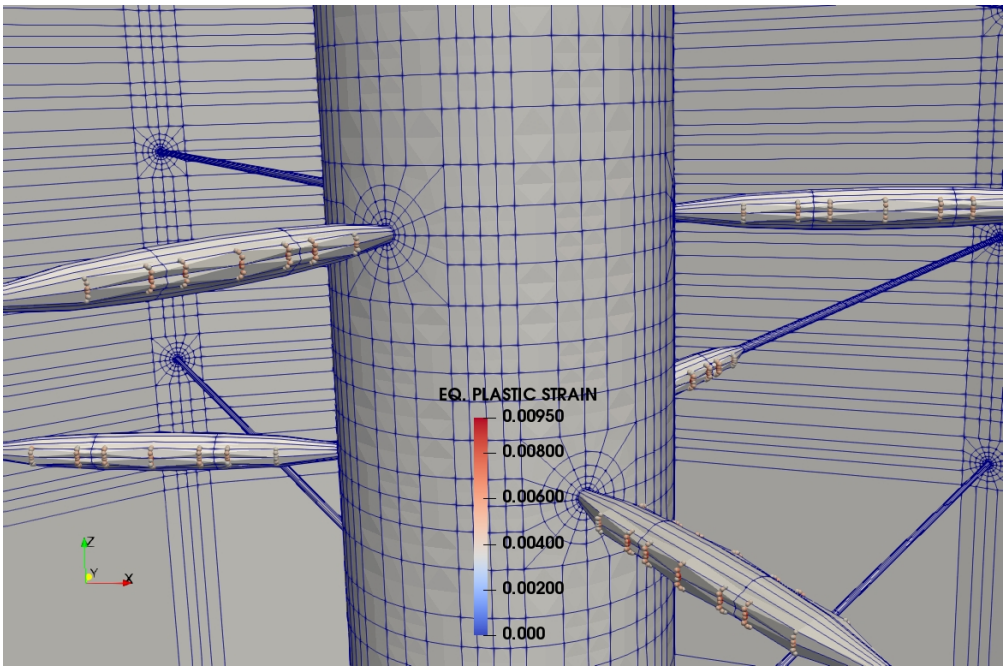

(b) At 40 years of production.

Figure 5.64: ε^p around the perforations at failed gauss points for Case IV of UCS 638 psi for 300 psi drawdown.

5.4.5 Case V - 460 psi UCS

This is an artificial sandstone rock data prepared from the available triaxial core analysis. The stress-strain curves are shown in Fig. 5.37. The constitutive relations are derived from the triaxial data. The simulation is carried on for a vertical well with x, y and z axes aligned with minimum horizontal, maximum horizontal and vertical stresses respectively. The sand rate simulation conditions are stated in Table 5.16.

Simulation Conditions	
Depth	5,082 ft.
Well diameter	8.5 in.
Permeability	1,000 md
Porosity	30%
S_{wi}	20%
Fluid Density	0.7504 gm/cc
Fluid Viscosity	4.5 cp
Oil Compressibility	1.068×10^{-5} 1/psi
Vertical pressure gradient	0.972 psi/ft
Initial reservoir pressure	2,568 psi
Initial stress ratio (σ_h/σ_v)	0.274
Initial stress ratio (σ_H/σ_v)	0.374
Ratio of effective stress change during depletion ($\Delta\sigma_h^e/\Delta\sigma_v^e$)	0.3
Failure criterion: Critical plastic strain (ε_c^p)	0.00343
Perforation hole length	10 in.
Perforation shot density	6 spf
Perforation phasing	120°

Table 5.16: Simulation reservoir conditions for Case V in B1 layer with UCS: 460 psi.

Initially, the simulation was planned for 40 years with 480 psi depletion but after a certain number of iterations remeshing the perforation cavity is not numerically feasible. The shape of the perforation becomes much distorted for any meaningful calculations to take place. Hence, the simulation is carried on for 37 years with a total depletion of 444 psi. A drawdown of 500 psi is applied at the perforation face. The stresses are shown in Fig. 5.65.

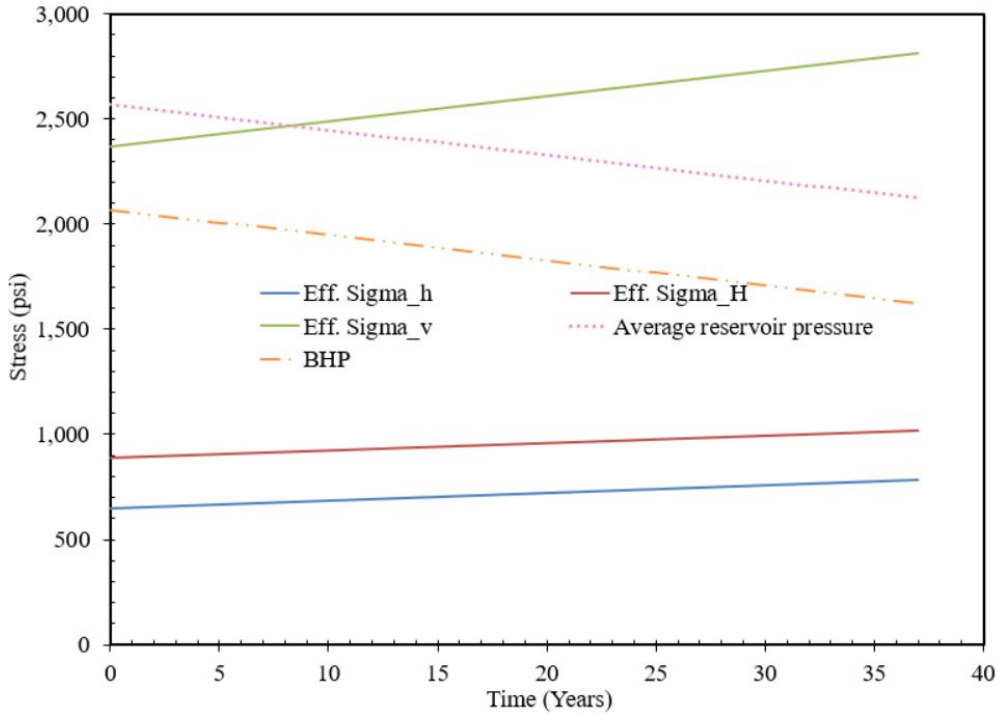

Figure 5.65: Stress states during the simulation of sand rate prediction for the rock with UCS of 460 psi for 500 psi drawdown.

The results show that failure starts to occur in the first year of oil production and the cavity disintegration and sand production also start in the first year (Fig. 5.66). The calibration factor A_1 is determined using the Eq. 4.4 which was derived from polyaxial experimental test results. The effective stress change in the maximum principal stress direction after the onset ($\Delta\sigma^e_{max}$) is 432 psi and the thick-walled cylinder strength is 1,222 psi from Fig. 4.22. Hence, A_1 came out to be 5.4214×10^{-2}. From Eq. 4.5 and 4.6, 95% confidence interval of A_1 can be calculated

which comes out to be 2.0867×10^{-2} and 12.2855×10^{-2}. The estimated range of cumulative sand production from 7 feet of this rock is between 109 and 639 tons over a period of 37 years.

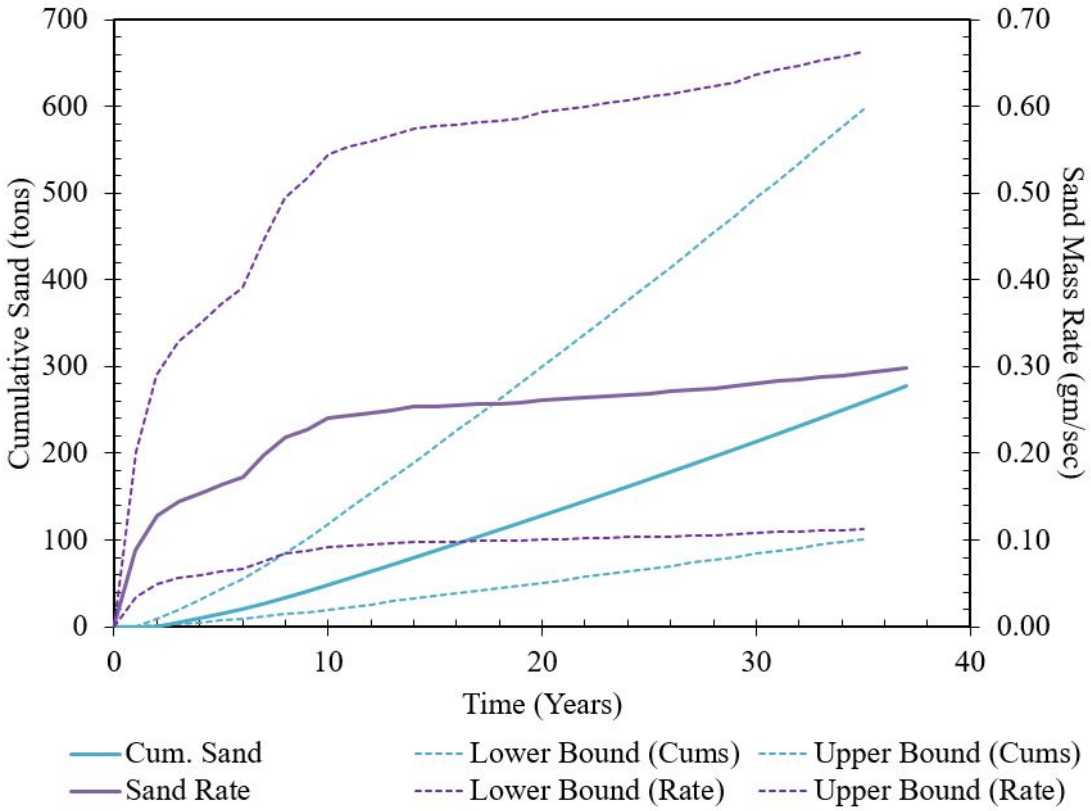

Figure 5.66: Sand rate prediction for the rock with UCS of 460 psi with 500 psi of drawdown.

Critical plastic stain criterion is used for the judgment of failure. The failure does not automatically triggers onset of sand production. As discussed in previous chapters, a stable arch is shown to be formed even after failure; which needs to be disintegrated with a critical flow rate. Figs. 5.67 show the increase in failed gauss points over the span of simulation run at 1 and 37 years. It clearly indicates that the failure starts to occur around the sides of the perforations and continues in that direction. After remeshing, the perforation takes the shape of an ellipsoidal balloon slightly squeezed in vertical direction.

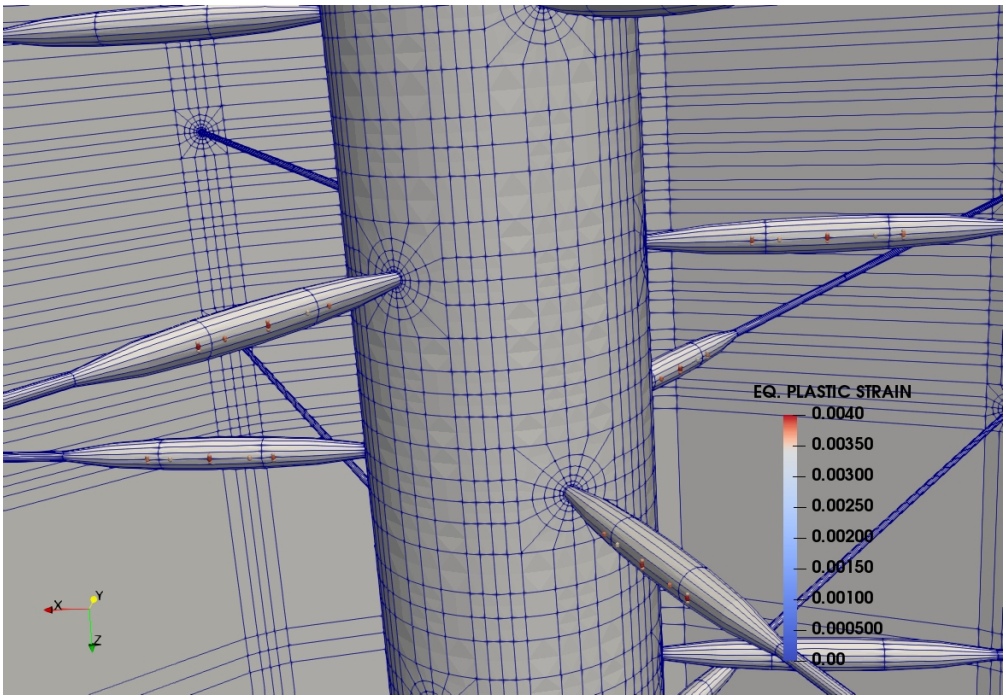

(a) After first year of production.

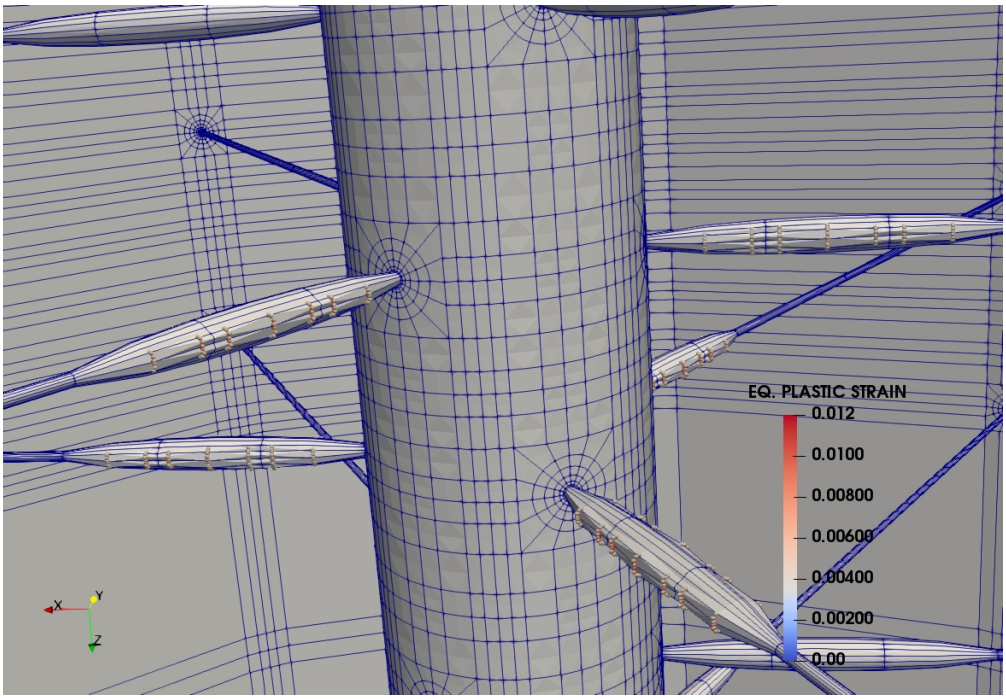

(b) At 37 years of production.

Figure 5.67: ε^p around the perforations at failed gauss points for Case V of UCS 460 psi for 500 psi drawdown.

Similarly, the simulation is run for a drawdown of 300 psi with stress states depicted in Fig. 5.68 . The results show that failure starts to occur in the first year of oil production and the cavity disintegration and sand production also start in the same year (Fig. 5.69). The estimated range of cumulative sand production from 7 feet of this rock is between 39 and 247 tons over a period of 40 years for 300 psi drawdown. Figs. 5.70 show the increase in failed gauss points over the span of simulation run at 1 and 40 years.

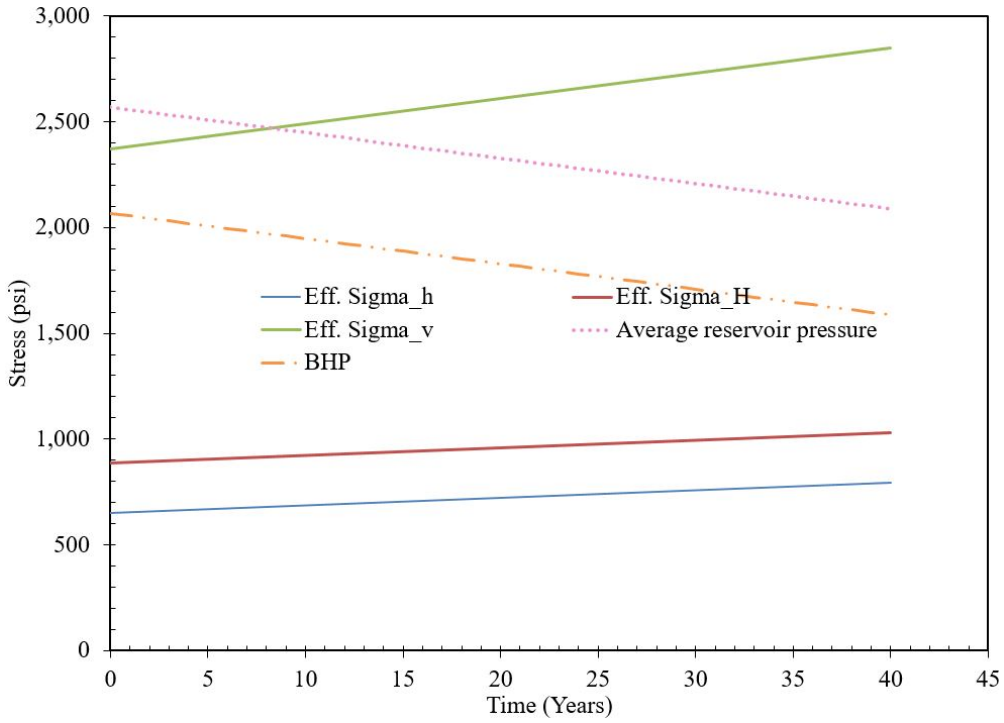

Figure 5.68: Stress states during the simulation of sand rate prediction for the rock with UCS of 460 psi for 300 psi drawdown.

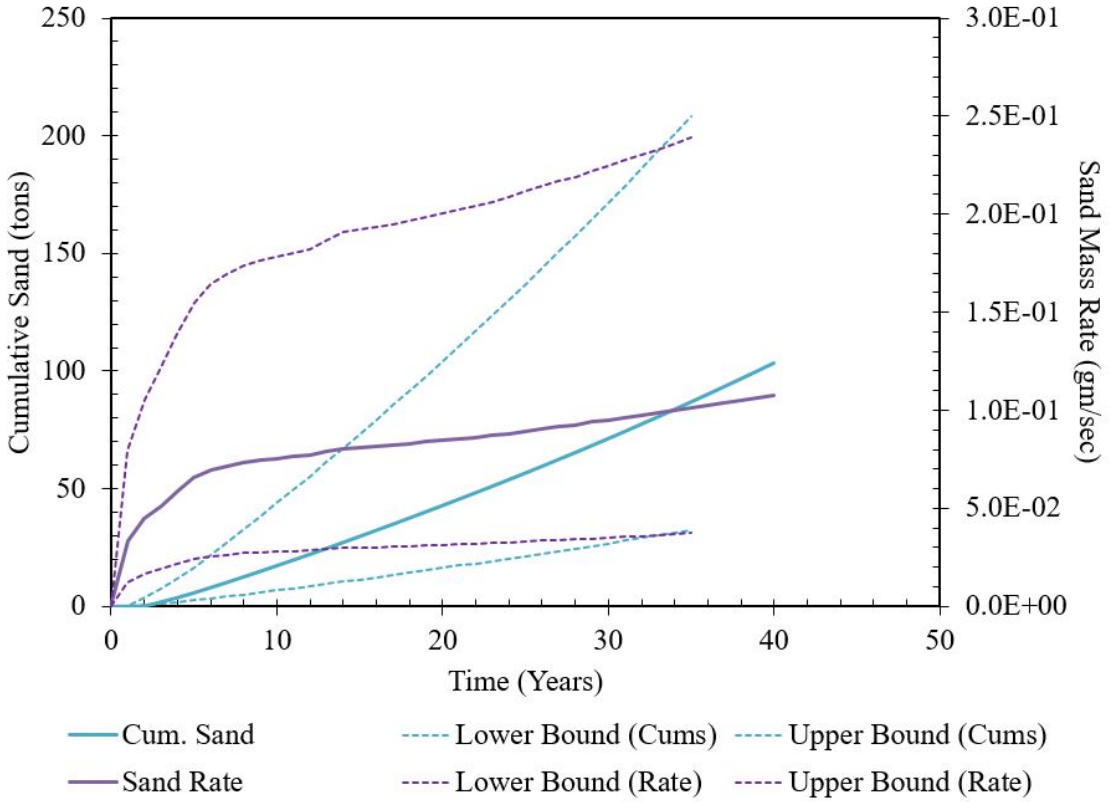

Figure 5.69: Sand rate prediction for the rock with UCS of 460 psi with 300 psi of drawdown.

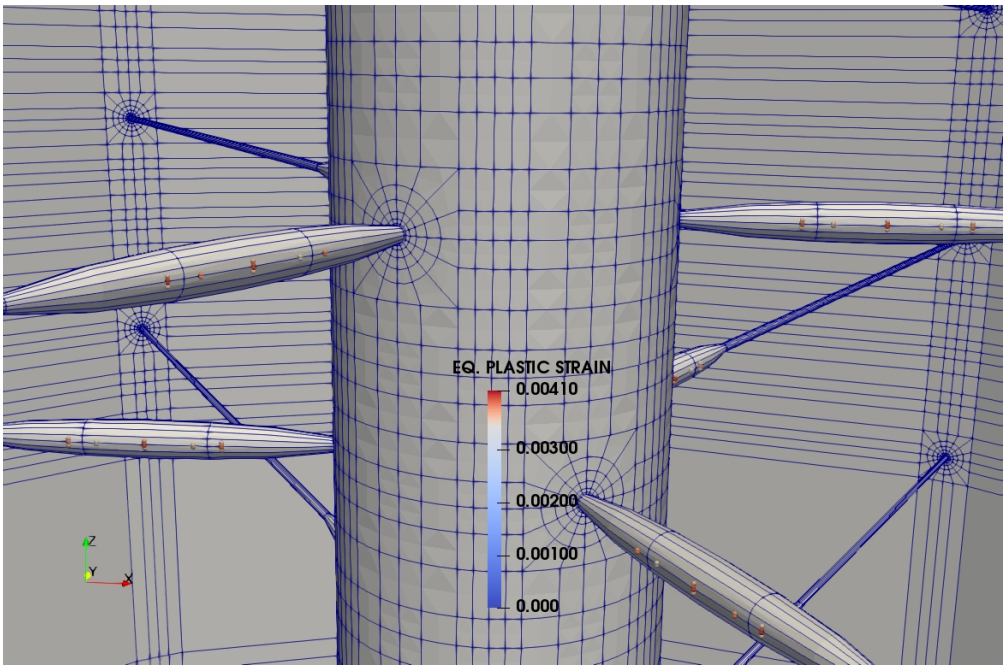

(a) After first year of production.

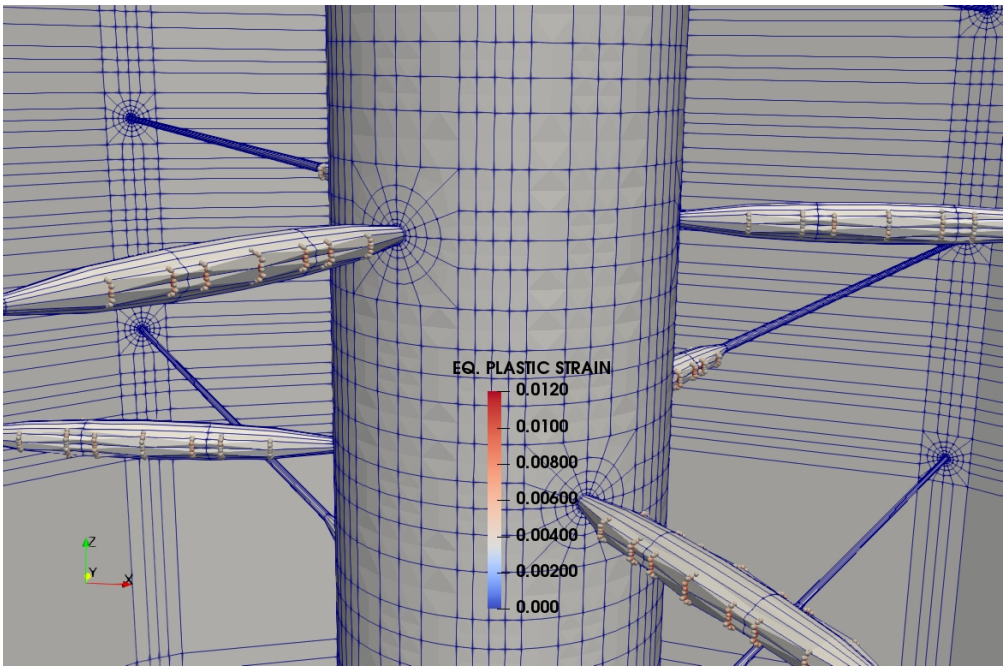

(b) At 40 years of production.

Figure 5.70: ε^p around the perforations at failed gauss points for Case V of UCS 460 psi for 300 psi drawdown.

5.4.6 Case VI - 282 psi UCS

This is an artificial sandstone rock data prepared from the available triaxial core analysis. The stress-strain curves are shown in Fig. 5.36. The constitutive relations are derived from the triaxial data. The simulation is carried on for a vertical well with x, y and z axes aligned with minimum horizontal, maximum horizontal and vertical stresses respectively. The sand rate simulation conditions are stated in Table 5.17.

Simulation Conditions	
Depth	5,082 ft.
Well diameter	8.5 in.
Permeability	1,000 md
Porosity	30%
S_{wi}	20%
Fluid Density	0.7504 gm/cc
Fluid Viscosity	4.5 cp
Oil Compressibility	1.068×10^{-5} 1/psi
Vertical pressure gradient	0.972 psi/ft
Initial reservoir pressure	2,568 psi
Initial stress ratio (σ_h/σ_v)	0.274
Initial stress ratio (σ_H/σ_v)	0.374
Ratio of effective stress change during depletion ($\Delta\sigma_h^e/\Delta\sigma_v^e$)	0.3
Failure criterion: Critical plastic strain (ε_c^p)	0.00343
Perforation hole length	10 in.
Perforation shot density	6 spf
Perforation phasing	120°

Table 5.17: Simulation reservoir conditions for Case VI in B1 layer with UCS: 282 psi.

Initially, the simulation was planned for 40 years with 480 psi depletion but after a certain number of iterations remeshing the perforation cavity is not numerically feasible. The shape of the perforation becomes much distorted for any meaningful calculations to take place. Hence, the simulation is carried on for 35 years with a total depletion of 420 psi. A drawdown of 500 psi is applied at the perforation face. The stresses are shown in Fig. 5.71.

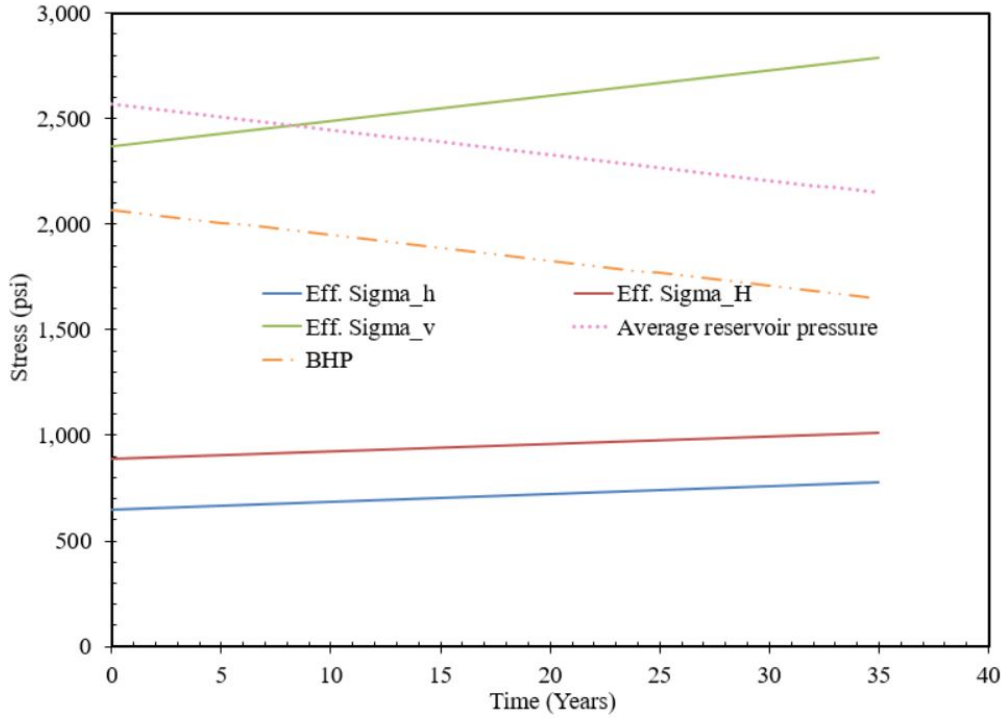

Figure 5.71: Stress states during the simulation of sand rate prediction for the rock with UCS of 282 psi for 500 psi drawdown.

The results show that failure starts to occur in the first year of oil production and the cavity disintegration and sand production also start in the first year (Fig. 5.72). The calibration factor A_1 is determined using the Eq. 4.4 which was derived from polyaxial experimental test results. The effective stress change in the maximum principal stress direction after the onset ($\Delta\sigma^e_{max}$) is 408 psi and the thick-walled cylinder strength is 759 psi from Fig. 4.22. Hence, A_1 came out to be 3.3978×10^{-2}. From Eq. 4.5 and 4.6, 95% confidence interval of A_1 can be calculated which

comes out to be 1.0015×10^{-2} and 10.0542×10^{-2}. The estimated range of cumulative sand production from 5 feet of this rock is between 160 and 1,603 tons over a period of 35 years.

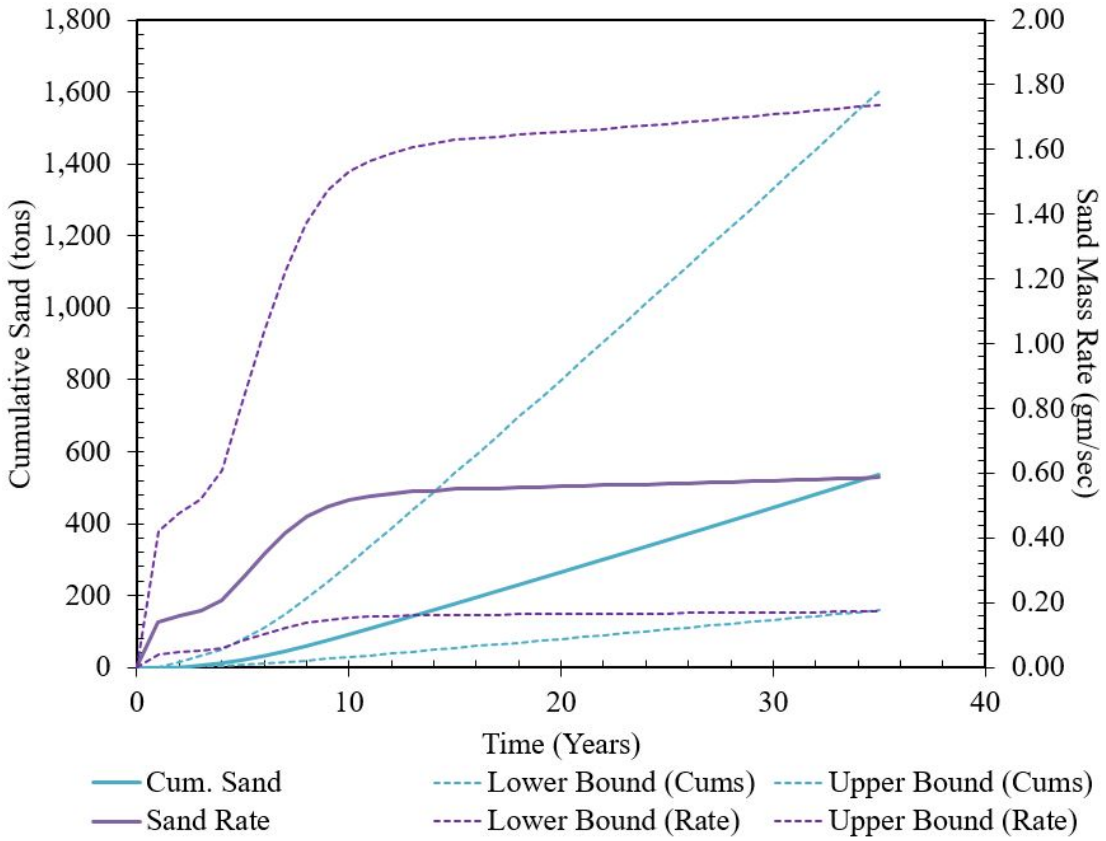

Figure 5.72: Sand rate prediction for the rock with UCS of 282 psi with 500 psi of drawdown.

Critical plastic stain criterion is used for the judgment of failure. The failure does not automatically triggers onset of sand production. As discussed in previous chapters, a stable arch is shown to be formed even after failure; which needs to be disintegrated with a critical flow rate. Figs. 5.73 show the increase in failed gauss points over the span of simulation run at 1 and 35 years. It clearly indicates that the failure starts to occur around the sides of the perforations and continues in that direction. After remeshing, the perforation takes the shape of an ellipsoidal balloon slightly squeezed in vertical direction.

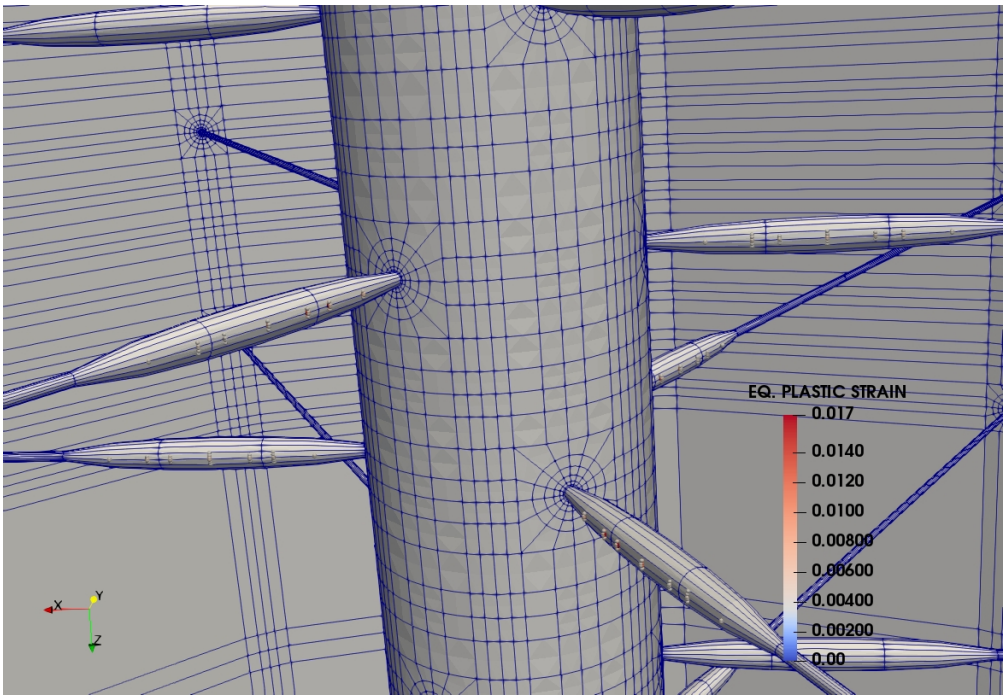

(a) After first year of production.

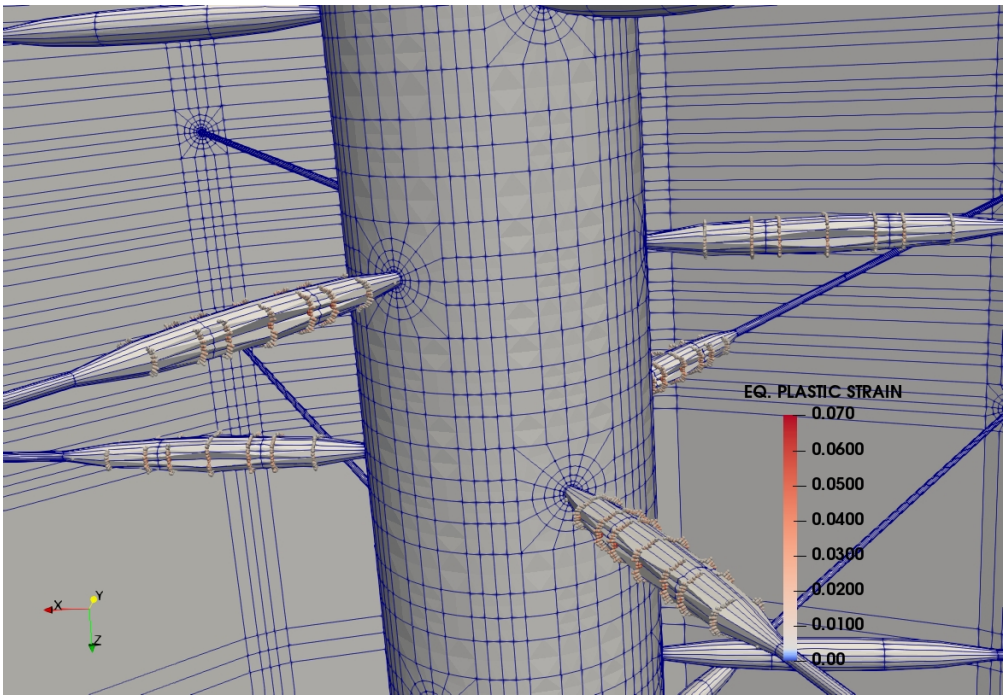

(b) At 35 years of production.

Figure 5.73: ε^p around the perforations at failed gauss points for Case VI of UCS 282 psi for 500 psi drawdown.

Similarly, the simulation is run for a drawdown of 300 psi with stress states depicted in Fig. 5.74 . The results show that failure starts to occur in the first year of oil production and the cavity disintegration and sand production also start in the same year (Fig. 5.75). The estimated range of cumulative sand production from 5 feet of this rock is between 64 and 645 tons over a period of 35 years for 300 psi drawdown. Figs. 5.76 show the increase in failed gauss points over the span of simulation run at 1 and 35 years.

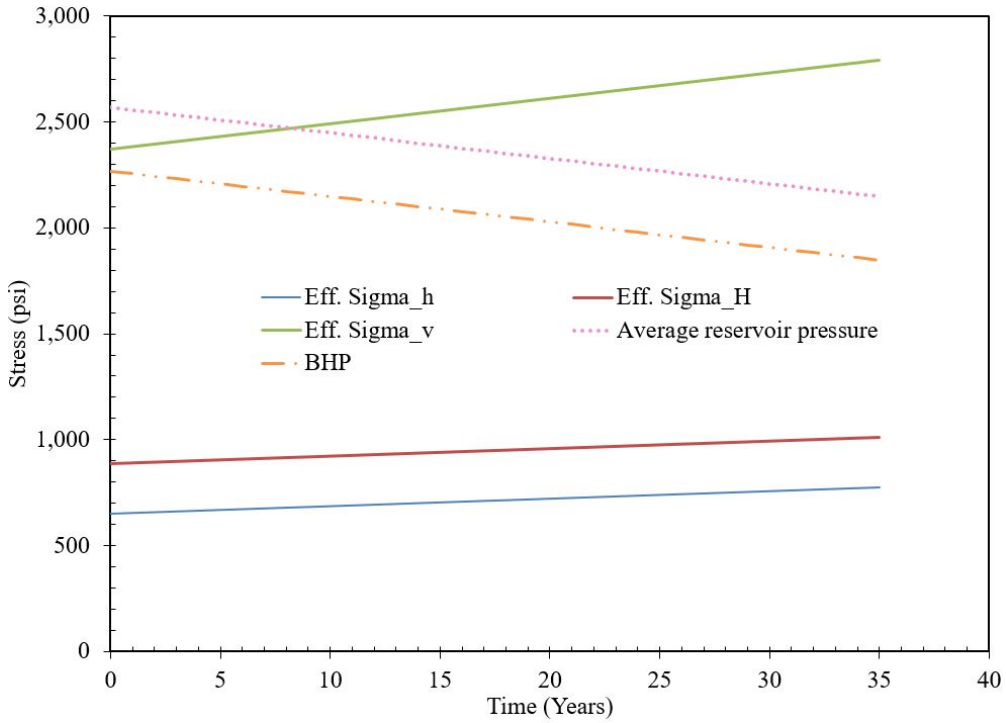

Figure 5.74: Stress states during the simulation of sand rate prediction for the rock with UCS of 282 psi for 300 psi drawdown.

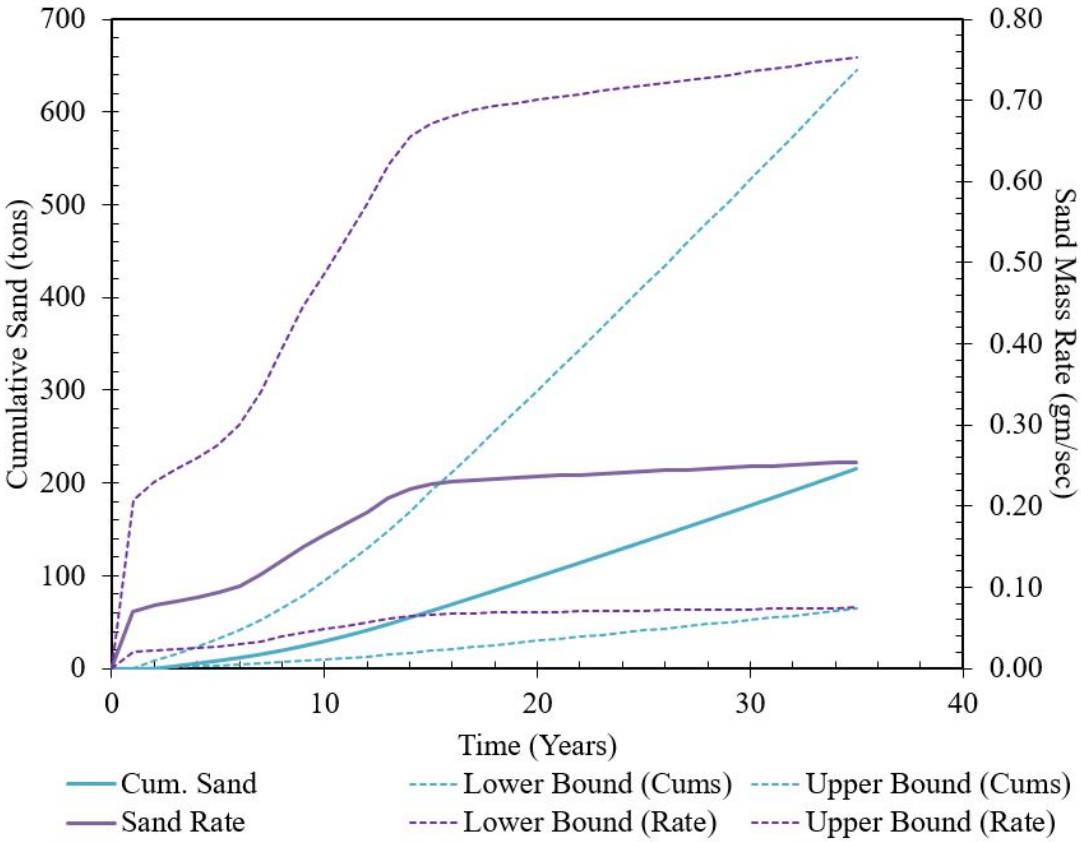

Figure 5.75: Sand rate prediction for the rock with UCS of 282 psi with 300 psi of drawdown.

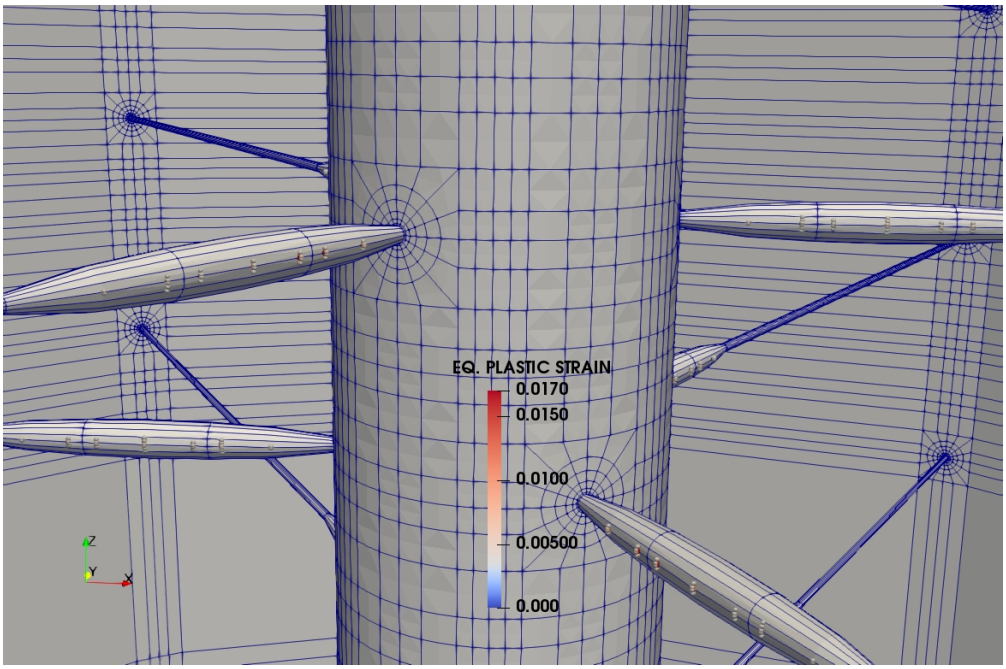

(a) After first year of production.

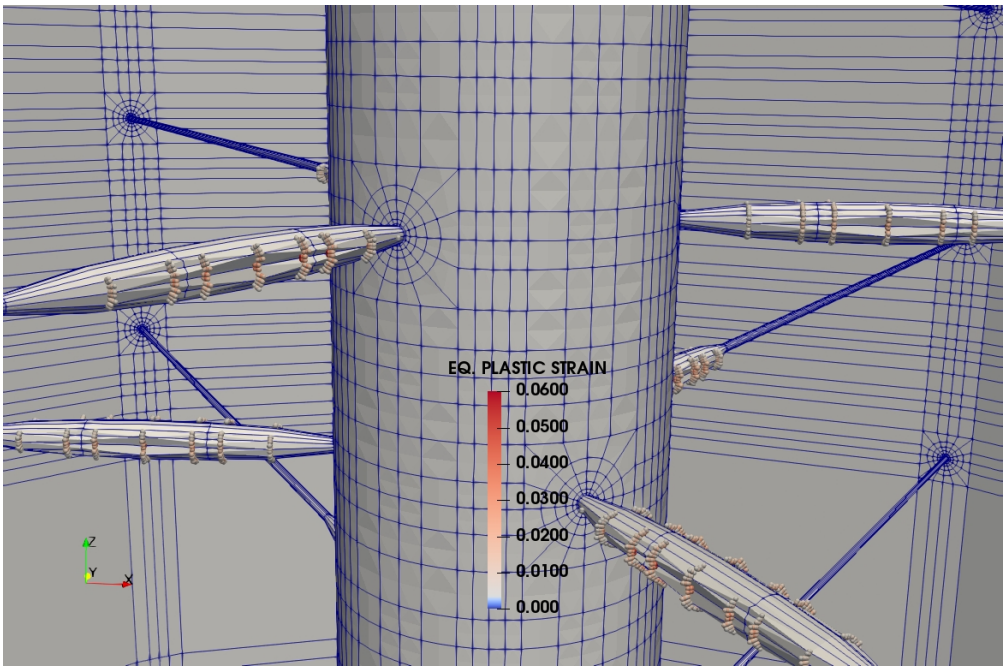

(b) At 35 years of production.

Figure 5.76: ε^p around the perforations at failed gauss points for Case VI of UCS 282 psi for 300 psi drawdown.

5.4.7 Total sand Rate from B1 Layer

The six simulations that are explained in above sections are run for different periods. This is due to the limitations of remeshing an ellipsoidal perforation so that it does not distort to a level where sharp kinks develop and calculations fail to converge. The lowest number of years is 33 years for which sand rates are estimated for all the cases using 500 psi drawdown. Assuming that B1 layer is perforated throughout with 6 spf, total sand rate and cumulative sand production is estimated and shown in Fig. 5.77 and 5.78 for 500 psi and 300 psi drawdown respectively.

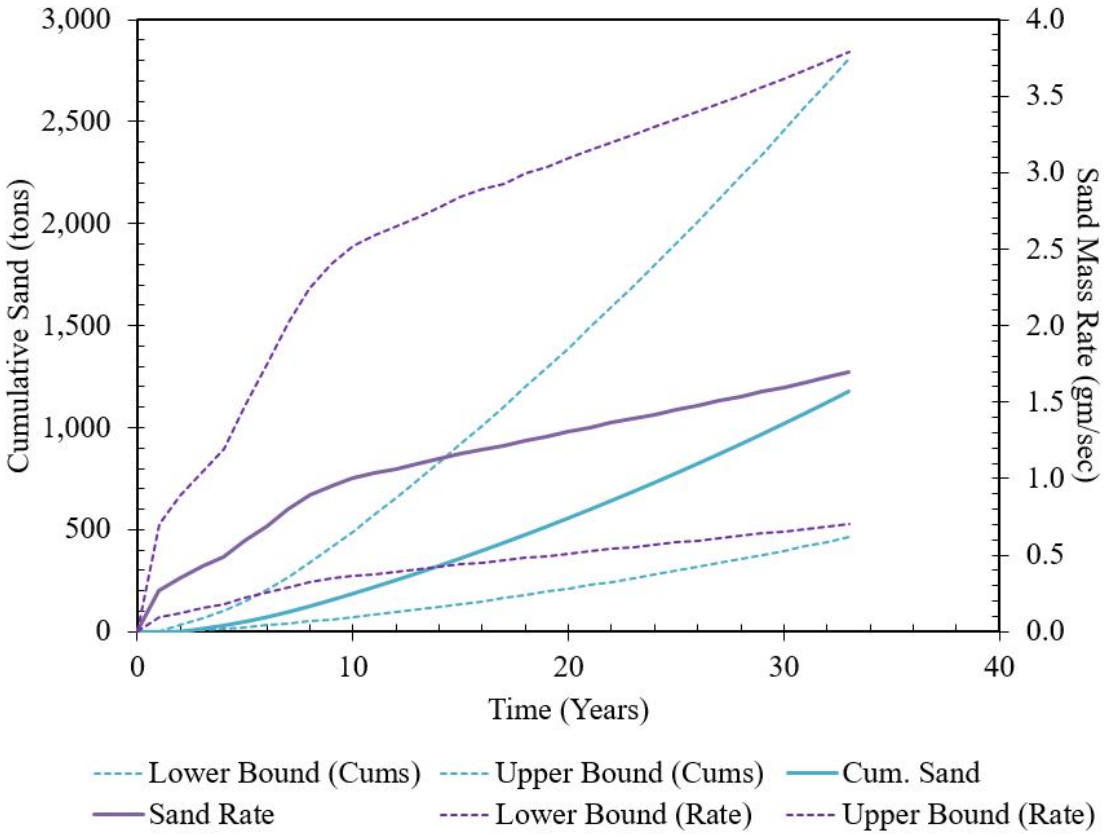

Figure 5.77: Total sand rate and cumulative prediction for B1 layer with 500 psi of drawdown.

The flow simulation results in a constant flow rate of 1,280 cc/sec from the 3 feet of wellbore section for 300 psi drawdown. Since sand production is only considered from the middle six

perforations, downhole production rate from the perforated B1 layer (112.2 ft.) is 26,000 rb/day. Similarly, the flow simulation for 500 psi drawdown results in 43,300 rb/day. For light crude oil, the standard acceptable sand production is that of 10 lb for 1,000 bbl of oil.

The expected cumulative production over a span of 33 years is 508 and 1,175 tons for 300 psi and 500 psi drawdown respectively. That is 0.001% (by weight) or 0.0004% (by volume) for 300 psi and 0.002% (by weight) or 0.0005% (by volume) of the total production. Thus with 300 psi drawdown, it is estimated that 3.5 lb of sand production will occur for 1,000 bbl of crude oil. However with 500 psi drawdown, 5 lb of sand production per 1,000 bbl of crude oil is estimated. In these scenarios, produced sand rate is not harmful to the production facilities though, the separator needs cleaning and removal of debris periodically.

In view of the field observation of low sand production, the simulation results seem reasonable. However, sand rates are still higher than expected. The reasons for this occurrence are multifaceted. First of all, only a few triaxial tests were performed on core samples and the UCS distribution was estimated using neural network. There may be a discrepancy between predicted and actual rock strength as the lowest measured UCS from triaxial test and neural network were 817 and 282 psi respectively. Additionally, formation strength varies for each well. For example, it was reported that a well was suspended since it produced large amount of sand from the very first day. On the other hand, average wells were generally free from sand for a long time. Similarly, it is probable that the data collected from the cores of two wells K-188 and K-191 are anomalous to the field data in general. That is, these wells are prone to low-medium sand rates as predicted from sand rate model whereas the general trend of the field is to produce insignificant amount of sand which is not harmful to the surface facilities.

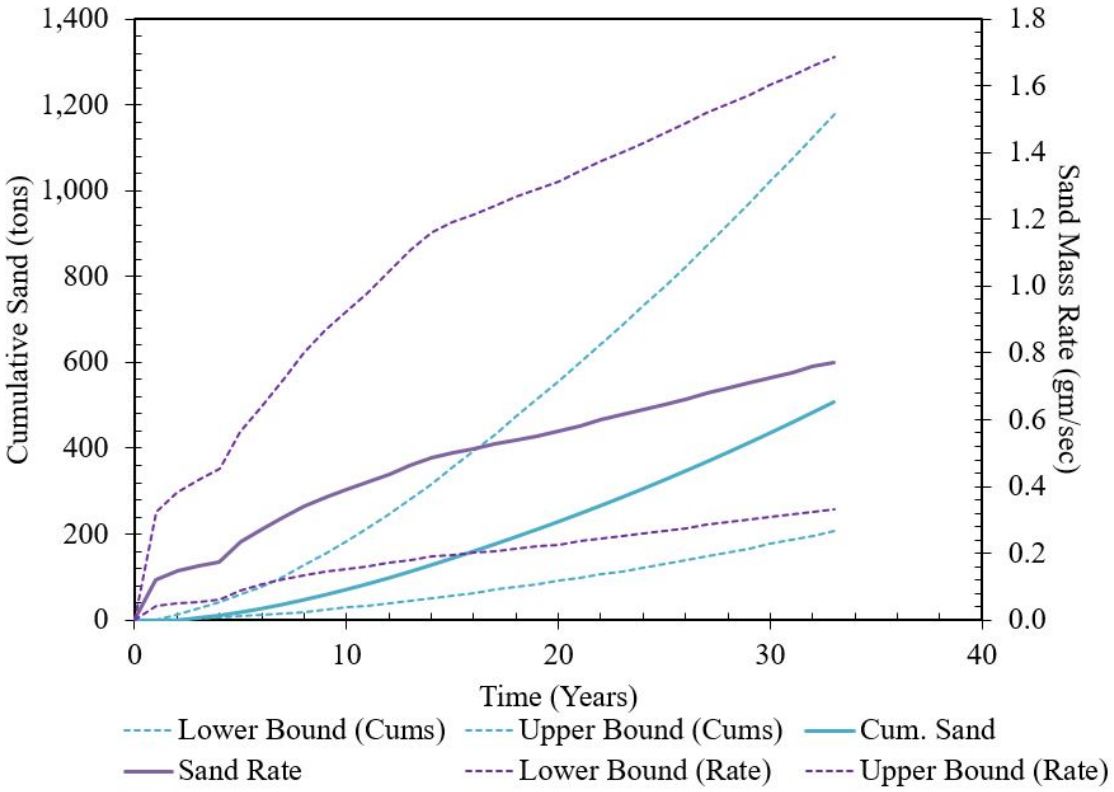

Figure 5.78: Total sand rate and cumulative prediction for B1 layer with 300 psi of drawdown.

6. SUMMARY AND CONCLUSIONS

In this research, we have developed a 3D coupled single phase poro-elasto-plastic finite element numerical model, and applied it to estimate onset of sanding and subsequent sand rate predictions. The numerical model is calibrated using state-of-the-art poly-axial volumetric sand production experiments and a loading factor is estimated. Finally, the model is used to evaluate sand rates and cumulative sand production from an offshore field.

This chapter summarizes and states conclusions for each aspect of the research.

6.1 Development of poro-elasto-plastic model

- A fully 3D sequentially coupled geomechanical and single phase fluid flow finite element model is developed to calculate dynamically fluid pressure, flow rates, rock deformation and stresses.

- The onset of plasticity is governed by Drucker-Prager yield criterion.

- After yielding, the relationship between stress and strain is given by strain hardening. The yield surface varies at each stage of plastic deformation, with subsequent yield surfaces being dependent on the plastic strains.

6.2 Development of sand rate model

- The model includes the mechanism of sand production involving coupling of the mechanical instability and degradation around the perforation and the hydromechanical instability due to flow-induced pressure gradient on the decemented material around the cavity.

- The geomechanical model is used to calculate displacements in the domain due to application of various loads. There are four types of loading considered:

  - In-situ stresses with drilling overbalance are applied first;

  - Release overbalance due to cementing the borehole to a rigid casing;

  - Effective stresses are increased due to depletion and;
  - Total drawdown loads are applied in the end.

- A transient single phase fluid flow model is used to calculate pore pressures and flow rate in the domain taking into account the non-Darcy effect.

- Sand production is a phenomena which happens during oil and gas production and thus fixed strain method is used for coupling of fluid flow and mechanical behavior of rock and reservoir fluids.

- A mathematical constitutive relation describing the deformation of rock material as a response to the stress applied is used as an input.

- Due to excessive plastic deformations during sand production, critical plastic strain criterion is used to judge failures.

- Many volumetric sand production experiments have been observed to show a change in material properties after decementation of sandstones. Hence, material property of the failed material is changed to mimic unconsolidated sand.

- Even after failure, post-failure zone tends to form stable arches halting sand production. A critical flow rate is estimated to destabilize these arches and produce sand. This is termed as an erosion criterion and is incorporated into the model.

- A novel sand rate calculation approach is used which is dependent on the failed surface area, extent of post-failure zone, flow velocity and mobility ratio of fluids. It also includes a loading factor which needs to be calibrated using experiments and results.

- Simulation of sand production is a moving boundary problem and thus a new computational geometric algorithm is developed to remesh the failed perforations. The advantage of this method is that it save considerable computational time and effort.

- Two types of remeshing algorithms are developed, one for experiments and the other for field problems.

- Due to deformations, the fabric of rock structure alters. The void spaces leading to porosity and the connected pores leading to permeability also change their shapes and sizes. Thus, with each increment of loading, altered porosity and permeabilities are also calculated.

6.3 Sand rate prediction for single-hole poly-axial experiments

- The experimental setup for isotropic and poly-axial volumetric sand production is explained.

- Isotropic simulation results seem to qualitatively mimic the behavior of experimental sand production.

- Six poly-axial volumetric sand production results are compared to simulations.

  - K_z = 1, K_r = 1/3
  - K_z = 1, K_r = 2/3
  - K_z = 2/3, K_r = 2/3
  - K_z = 4/3, K_r = 2/3
  - K_z = 2, K_r = 2/3
  - K_z = 1, K_r = 1

- The numerical model is calibrated using these poly-axial sand rate results and a loading factor is determined to be dependent on the ratio of change in maximum principal effective stress (after the onset of sand production) and the thick-walled cylinder strength.

- The average ratio of produced sand from experiment and calibrated model is calculated to be 0.72.

- The lower and upper bound of this ratio are 0.25 and 3 respectively.

- With increase in lateral stress anisotropy, sand production potential increases and early sanding occurs.
- In another detailed study, increase in axial stress anisotropy showed sand production potential increase and early sanding.
- With increasing axial/lateral anisotropy, sand rates are lower for the a normalized σ_R.

6.4 Sand Rate Prediction for an Offshore Field

- Offshore field is considered one of the major oil fields in the Middle East region.
- This extensive field with dimensions of about 20 km by 8 km has two sandstone layers B1 and B2 which are the subject of this study.
- Rock mechanical properties were measured using triaxial tests on cores during a previous study.
- Constitutive relations were derived from the triaxial data and is used as an input in the geomechanical simulation.
- Preliminary study shows that no sand is produced from rocks with UCS above 1,725 psi.
- Artificial rock properties are derived by extrapolating the triaxial data.
- Sand rate and cumulative sand rates are estimated using sand rate model for these artificial rocks in the B1 layer.
- It is found that the cumulative sand produced from a well is 0.001% and 0.002% (by weight) of total production for 300 psi and 500 psi drawdown respectively.
- 3.5 lb and 5 lb per 1,000 bbl of crude oil are estimated for 300 psi and 500 psi drawdown respectively.

- Although the simulation results match field observations reasonably well, produced sand is still higher than expected. It may be attributed to errors in rock strength estimation as the triaxial test results data were limited.

REFERENCES

Nouri Alireza, Vaziri Hans, Belhaj Hadi, and Islam Rafiqul. Effect of volumetric failure on sand production in oil-wellbores, 2003/1/1/ 2003. URL https://doi.org/10.2118/80448-MS.

D. Antheunis, P. B. Vriezen, B. A. Schipper, and A. C. van der Vlis. Perforation collapse: Failure of perforated friable sandstones, 1976/1/1/ 1976. URL https://doi.org/10.2118/5750-MS.

Saman Azadbakht, Mahshid Jafarpour, Hossein Rahmati, Alireza Nouri, Hans Vaziri, and Dave Chan. A numerical model for predicting the rate of sand production in injector wells, 2012/1/1/ 2012. URL https://doi.org/10.2118/156394-MS.

L. C. B. Bianco and P. M. Halleck. Mechanisms of arch instability and sand production in two-phase saturated poorly consolidated sandstones, 2001/1/1/ 2001. URL https://doi.org/10.2118/68932-MS.

M. A. Biot. Nonlinear and semilinear rheology of porous solids. *Journal of Geophysical Research (1896-1977)*, 78(23):4924–4937, 1973. ISSN 0148-0227. doi: 10.1029/JB078i023p04924. URL https://doi.org/10.1029/JB078i023p04924.

Maurice A. Biot. General theory of three-dimensional consolidation. *Journal of Applied Physics*, 12(2):155–164, 1941. ISSN 0021-8979. doi: 10.1063/1.1712886. URL https://doi.org/10.1063/1.1712886.

Rolf K. Bratli and Rasmus Risnes. Stability and failure of sand arches. *Society of Petroleum Engineers Journal*, 21(02):236–248, 1981. ISSN 0197-7520. doi: 10.2118/8427-PA. URL https://doi.org/10.2118/8427-PA.

R. C. Burton, E. R. Davis, and N. Morita. Application of reservoir strength characterization and formation failure modeling to analyze sand production potential and formulate sand control strategies for a series of north sea gas reservoirs, 1998/1/1/ 1998. URL https://doi.org/10.2118/48979-MS.

L. Y. Chin and G. G. Ramos. Predicting volumetric sand production in weak reservoirs, 2002/1/1/ 2002. URL https://doi.org/10.2118/78169-MS.

Michael P. Clearly, Joseph J. Melvan, and Charles A. Kohlhaas. The effect of confining stress and fluid properties on arch stability in unconsolidated sands, 1979/1/1/ 1979. URL https://doi.org/10.2118/8426-MS.

Japan Oil Engineering Co. Accuracy improvement of onset of sand production for existing reservoirs, Internal Report, December 2000.

George R. Coates and S. A. Denoo. Mechanical properties program using borehole analysis and mohr's circle, 1981/1/1/ 1981. URL https://doi.org/.

Christine Detournay. Numerical modeling of the slit mode of cavity evolution associated with sand production. *SPE Journal*, 14(04):797–804, 2009. ISSN 1086-055X. doi: 10.2118/116168-PA. URL https://doi.org/10.2118/116168-PA.

D. C. Drucker and W. Prager. Soil mechanics and plastic analysis or limit design. *Quart. Appl. Math. 10 (1952), 157-165*, 1952. doi: https://doi.org/10.1090/qam/48291.

F. A. L. Dullien. *Porous media : fluid transport and pore structure*. Academic Press, New York, 1979. ISBN 0122236505 9780122236501. URL http://www.ulb.tu-darmstadt.de/tocs/84979062.pdf.

Y.; Charron A. Edwards, D. P.; Sharma. Zones of sand production identified by log-derived mechanical properties: a case study. In *Proceedings of the 8th European Formation Evaluation*

Symposium, 1983.

Vahidoddin Fattahpour, Mahdi Moosavi, and Mahdi Mehranpour. An experimental investigation on the effect of rock strength and perforation size on sand production. *Journal of Petroleum Science and Engineering*, 86-87:172–189, 2012. ISSN 0920-4105. doi: https://doi.org/10.1016/j.petrol.2012.03.023. URL http://www.sciencedirect.com/science/article/pii/S0920410512000769.

Erling Fjaer, R.M. Holt, P. Horsrud, A.M. Raaen, and R. Risnes. *Petroleum related rock mechanics. 2nd ed. E. Fjær [and others]*. Developments in petroleum science: 53. Elsevier, 2nd ed. edition, 2008. ISBN 0444502602 9780444502605.

B. Haimson. Micromechanisms of borehole failure in reservoir rocks, 2007/1/1/ 2007. URL https://doi.org/.

Bezalel Haimson and Joseph Kovacich. Borehole instability in high-porosity berea sandstone and factors affecting dimensions and shape of fracture-like breakouts. *Engineering Geology*, 69(3):219–231, 2003. ISSN 0013-7952. doi: https://doi.org/10.1016/S0013-7952(02)00283-1. URL http://www.sciencedirect.com/science/article/pii/S0013795202002831.

Jr. Hall, C. D. and W. H. Harrisberger. Stability of sand arches: A key to sand control. *Journal of Petroleum Technology*, 22(07):821–829, 1970. ISSN 0149-2136. doi: 10.2118/2399-PA. URL https://doi.org/10.2118/2399-PA.

Abbas Khaksar, Philip Geoffrey Taylor, Zhi Fang, Toby John Kayes, Abraham Salazar, and Khalil Rahman. Rock strength from core and logs, where we stand and ways to go, 2009/1/1/ 2009. URL https://doi.org/10.2118/121972-MS.

Abbas Khaksar, Sadegh Asadi, Ahmadreza Younessi, Feng Gui, and Yan Zheng. Thick wall cylinder strength and critical strain limit from core tests and well logs, implications for sand control

decisions, 2018/1/1/ 2018. URL https://doi.org/.

Sung Hyun Kim, Mukul Mani Sharma, and Harvey J. Fitzpatrick. A predictive model for sand production in poorly consolidated sands, 2011/1/1/ 2011. URL https://doi.org/10.2523/IPTC-15087-MS.

A. P. Kooijman, P. M. Halleck, Philippus de Bree, C. A. M. Veeken, and C. J. Kenter. Large-scale laboratory sand production test, 1992/1/1/ 1992. URL https://doi.org/10.2118/24798-MS.

N. Morita, D. L. Whitfill, O. P. Fedde, and T. H. Levik. Parametric study of sand-production prediction: Analytical approach. *SPE Production Engineering*, 4(01):25–33, 1989a. ISSN 0885-9221. doi: 10.2118/16990-PA. URL https://doi.org/10.2118/16990-PA.

N. Morita, D. L. Whitfill, I. Massie, and T. W. Knudsen. Realistic sand-production prediction: Numerical approach. *SPE Production Engineering*, 4(01):15–24, 1989b. ISSN 0885-9221. doi: 10.2118/16989-PA. URL https://doi.org/10.2118/16989-PA.

Nobuo Morita. Field and laboratory verification of sand-production prediction models. *SPE Drilling & Completion*, 9(04):227–235, 1994. ISSN 1064-6671. doi: 10.2118/27341-PA. URL https://doi.org/10.2118/27341-PA.

Nobuo Morita and K. E. Gray. A constitutive equation for nonlinear stress-strain curves in rocks and its application to stress analysis around a borehole during drilling, 1980/1/1/ 1980. URL https://doi.org/10.2118/9328-MS.

Nobuo Morita, R. C. Burton, and Eric Davis. Fracturing, frac packing, and formation failure control: Can screenless completions prevent sand production? *SPE Drilling & Completion*, 13 (03):157–162, 1998. ISSN 1064-6671. doi: 10.2118/51187-PA. URL https://doi.org/10.2118/51187-PA.

Nobuo Morita, Giin-Fa Fuh, and Robert C. Burton. Field and laboratory observations of post-failure stabilizations during sand production, 2006/1/1/ 2006. URL https://doi.org/10.2118/102802-MS.

V. Murti, Y. Wang, and S. Valliappan. Numerical inverse isoparametric mapping in 3d fem. *Computers & Structures*, 29(4):611–622, 1988. ISSN 0045-7949. doi: https://doi.org/10.1016/0045-7949(88)90371-9. URL http://www.sciencedirect.com/science/article/pii/0045794988903719.

R. P. Nordgren. Strength of well completions, 1977/1/1/ 1977. URL https://doi.org/.

A. Nouri, E. Kuru, and H. Vaziri. Elastoplastic modelling of sand production using fracture energy regularization method. *Journal of Canadian Petroleum Technology*, 48(04):64–71, 2009. ISSN 0021-9487. doi: 10.2118/09-04-64. URL https://doi.org/10.2118/09-04-64.

Alireza Nouri, Hans H. Vaziri, Hadi A. Belhaj, and M. Rafiqul Islam. Sand-production prediction: A new set of criteria for modeling based on large-scale transient experiments and numerical investigation. *SPE Journal*, 11(02):227–237, 2006. ISSN 1086-055X. doi: 10.2118/90273-PA. URL https://doi.org/10.2118/90273-PA.

Alireza Nouri, Hans H. Vaziri, Hadi Arbi Belhaj, and M. Rafiqul Islam. Comprehensive transient modeling of sand production in horizontal wellbores. *SPE Journal*, 12(04):468–474, 2007. ISSN 1086-055X. doi: 10.2118/84500-PA. URL https://doi.org/10.2118/84500-PA.

D. R. J. Owen and E. Hinton. *Finite elements in plasticity : theory and practice. D.R.J. Owen, E. Hinton*. Pineridge Press, 1980.

E. Papamichos. Sand production in isotropic and anisotropic stress tests, 2018/8/21/ 2018. URL https://doi.org/.

E. Papamichos and M. Stavropoulou. An erosion-mechanical model for sand production rate

prediction. *International Journal of Rock Mechanics and Mining Sciences*, 35(4):531–532, 1998. ISSN 1365-1609. doi: https://doi.org/10.1016/S0148-9062(98)00106-5. URL http://www.sciencedirect.com/science/article/pii/S0148906298001065.

E. Papamichos, A. Skjærstein, and J. Tronvoll. A volumetric sand production experiment, 2000/1/1/ 2000. URL https://doi.org/.

E. Papamichos, T. E. Unander, and P. M. T. M. Schutjens. Volumetric sand production - internal report. 2002.

E. Papamichos, J. Stenebraten, P. Cerasi, A. Lavrov, I. Vardoulakis, G. F. Fuh, M. Brignoli, Goncalves C. J. de Castro, and O. Havmoller. Rock type and hole failure pattern effects on sand production, 2008/1/1/ 2008. URL https://doi.org/.

E. Papamichos, P. Cerasi, J. F. Stenebraten, A. N. Berntsen, I. Ojala, I. Vardoulakis, M. Brignoli, G. F. Fuh, G. Han, A. Nadeem, P. Ray, and S. Wold. Sand production rate under multiphase flow and water breakthrough, 2010/1/1/ 2010. URL https://doi.org/.

Euripides Papamichos and Eva M. Malmanger. A sand-erosion model for volumetric sand predictions in a north sea reservoir. *SPE Reservoir Evaluation & Engineering*, 4(01):44–50, 2001. ISSN 1094-6470. doi: 10.2118/69841-PA. URL https://doi.org/10.2118/69841-PA.

J. M. Peden and A. A. M. Yassin. The determination of optimum completion and production conditions for sand-free oil production, 1986/1/1/ 1986. URL https://doi.org/10.2118/15406-MS.

W. L. Penberthy and C. M. Shaughnessy. *Sand control. W. L. Penberthy, C. M. Shaughnessy*. SPE series on special topics Henry L. Doherty series: v. 1. Richardson, TX : Henry L. Doherty Memorial Fund of AIME : Society of Petroleum Engineers, 1992., 1992. ISBN 1555630413 9781555630416.

T. K. Perkins and J. S. Weingarten. Stability and failure of spherical cavities in unconsolidated sand and weakly consolidated rock, 1988/1/1/ 1988. URL https://doi.org/10.2118/18244-MS.

Hossein Rahmati, Alireza Nouri, Hans Vaziri, and Dave Chan. Validation of predicted cumulative sand and sand rate against physical-model test. *Journal of Canadian Petroleum Technology*, 51 (05):403–410, 2012. ISSN 0021-9487. doi: 10.2118/157950-PA. URL https://doi.org/10.2118/157950-PA.

Hossein Rahmati, Mahshid Jafarpour, Saman Azadbakht, Alireza Nouri, Hans Vaziri, Dave Chan, and Yuxing Xiao. Review of sand production prediction models. *Journal of Petroleum Engineering*, 2013:16, 2013. doi: 10.1155/2013/864981. URL http://dx.doi.org/10.1155/2013/864981.

Rasmus Risnes, Rolf K. Bratli, and Per Horsrud. Sand stresses around a wellbore. *Society of Petroleum Engineers Journal*, 22(06):883–898, 1982. ISSN 0197-7520. doi: 10.2118/9650-PA. URL https://doi.org/10.2118/9650-PA.

Guillaume Servant, Philippe Marchina, Yannick Peysson, Elisabeth Bemer, and Jean-Francois Nauroy. Sand erosion in weakly consolidated reservoirs: Experiments and numerical modeling, 2006/1/1/ 2006. URL https://doi.org/10.2118/100023-MS.

Jean Sulem, Ioannis Vardoulakis, Euripides Papamichos, Ahmed Oulahna, and Johan Tronvoll. Elasto-plastic modelling of red wildmoor sandstone. *Mechanics of Cohesive-frictional Materials*, 4(3):215–245, 1999. ISSN 1082-5010. doi: 10.1002/(SICI)1099-1484(199905)4:3<215::AID-CFM61>3.0.CO;2-8. URL https://doi.org/10.1002/(SICI)1099-1484(199905)4:3<215::AID-CFM61>3.0.CO;2-8.

Karl V. Terzaghi. Stress distribution in dry and in saturated sand above a yielding trap door. *Proc., First Intl. Conf. on Soil Mechanics and Foundation Engineering*, pages 307–311, 1936.

Johan Tronvoll. Experimental investigation of perforation cavity stability, 1992/1/1/ 1992. URL https://doi.org/.

Johan Tronvoll, Nobuo Morita, and F. J. Santarelli. Perforation cavity stability: Comprehensive laboratory experiments and numerical analysis, 1992/1/1/ 1992. URL https://doi.org/10.2118/24799-MS.

Yuh Uchida, Masayoshi Goto, and Nobuo Morita. Comparative studies of compact triaxial perforation stability tests and thick wall cylinder tests, 2014/9/10/ 2014. URL https://doi.org/10.2118/170304-MS.

P. J. van den Hoek, G. M. M. Hertogh, A. P. Kooijman, Ph de Bree, C. J. Kenter, and E. Papamichos. A new concept of sand production prediction: Theory and laboratory experiments. *SPE Drilling & Completion*, 15(04):261–273, 2000. ISSN 1064-6671. doi: 10.2118/65756-PA. URL https://doi.org/10.2118/65756-PA.

I. Vardoulakis, M. Stavropoulou, and P. Papanastasiou. Hydro-mechanical aspects of the sand production problem. *Transport in Porous Media*, 22(2):225–244, 1996. ISSN 1573-1634. doi: 10.1007/BF01143517. URL https://doi.org/10.1007/BF01143517.

H. H. Vaziri, Y. Xiao, R. Islam, and A. Nouri. Numerical modeling of seepage-induced sand production in oil and gas reservoirs. *Journal of Petroleum Science and Engineering*, 36(1):71–86, 2002. ISSN 0920-4105. doi: https://doi.org/10.1016/S0920-4105(02)00264-4. URL http://www.sciencedirect.com/science/article/pii/S0920410502002644.

Hans H. Vaziri, Alireza Nouri, Knut Arne Hovem, and Xiuli Wang. Computation of sand production in water injectors. *SPE Production & Operations*, 23(04):518–524, 2008. ISSN 1930-1855. doi: 10.2118/107695-PA. URL https://doi.org/10.2118/107695-PA.

C. A. M. Veeken, D. R. Davies, C. J. Kenter, and A. P. Kooijman. Sand production prediction review: Developing an integrated approach, 1991/1/1/ 1991. URL https://doi.org/10.

2118/22792-MS.

R. G. Wan and J. Wang. Modelling of sand production and wormhole propagation in an oil saturated sand pack using stabilized finite element methods. *Journal of Canadian Petroleum Technology*, 43(04):8, 2004. ISSN 0021-9487. doi: 10.2118/04-04-04. URL https://doi.org/10.2118/04-04-04.

J. Wang, D. Walters, R. G. Wan, and A. Settari. Prediction of volumetric sand production and wellbore stability analysis of a well at different completion schemes, 2005/1/1/ 2005. URL https://doi.org/.

Jianlin Wang, David P. Yale, and Ganeswara Rao Dasari. Numerical modeling of massive sand production, 2011/1/1/ 2011. URL https://doi.org/10.2118/147110-MS.

Jin Wang, A. Tony Settari, Dale Walters, and Richard Wan. An integrated modular approach to modeling sand production and cavity growth with emphasis on the multiphase and 3d effects, 2006/1/1/ 2006. URL https://doi.org/.

J. S. Weingarten and T. K. Perkins. Prediction of sand production in gas wells: Methods and gulf of mexico case studies. *Journal of Petroleum Technology*, 47(07):596–600, 1995. ISSN 0149-2136. doi: 10.2118/24797-PA. URL https://doi.org/10.2118/24797-PA.

S. M. Willson, Z. A. Moschovidis, J. R. Cameron, and I. D. Palmer. New model for predicting the rate of sand production, 2002/1/1/ 2002. URL https://doi.org/10.2118/78168-MS.

K. Yim, M. B. Dusseault, and L. Zhang. Experimental study of sand production processes near an orifice, 1994/1/1/ 1994. URL https://doi.org/10.2118/28068-MS.

O. C. Zienkiewicz, Robert L. Taylor, and J. Z. Zhu. *The finite element method : its basis and fundamentals. Seventh edition. O.C. Zienkiewicz, R.L. Taylor, J.Z. Zhu*. Butterworth-Heinemann, seventh edition. edition, 2013. ISBN 9780080951355.

APPENDIX A

RESULT FIGURES FROM POLY-AXIAL EXPERIMENT SIMULATIONS

The figures in this appendix show the changes in ε^p, σ^e_{xx}, σ^e_{yy}, σ^e_{zz}, ε_{xx}, ε_{yy}, ε_{zz}, porosity and permeability between onset and end of simulation for all the poly-axial experiment simulations from chapter 4.

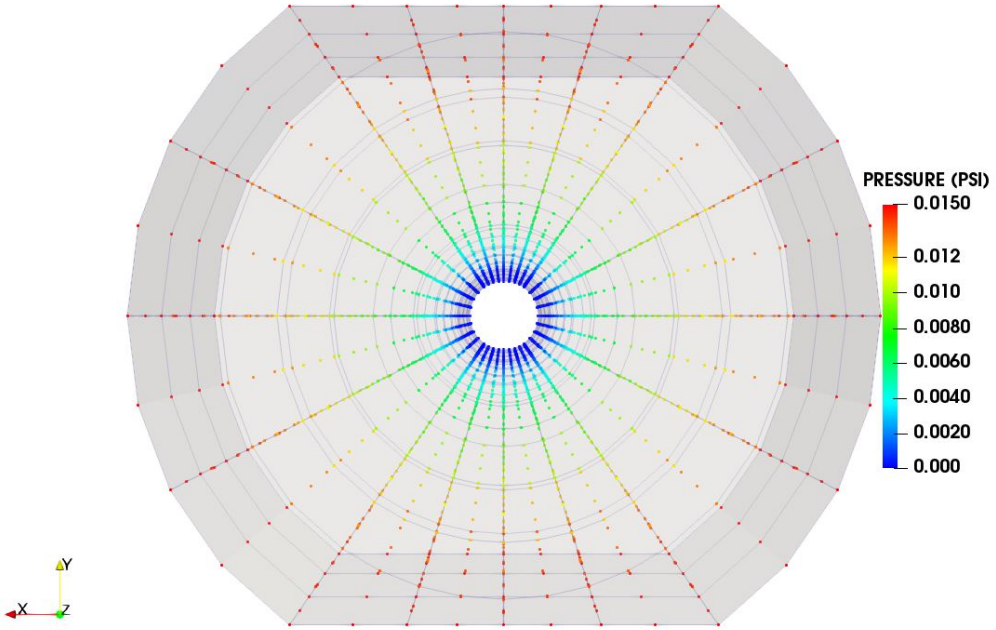

Figure A.1: Pressure profile during the simulation run for all the poly-axial cases.

A.1 Case 01 - K_z = 1, K_r = 1/3

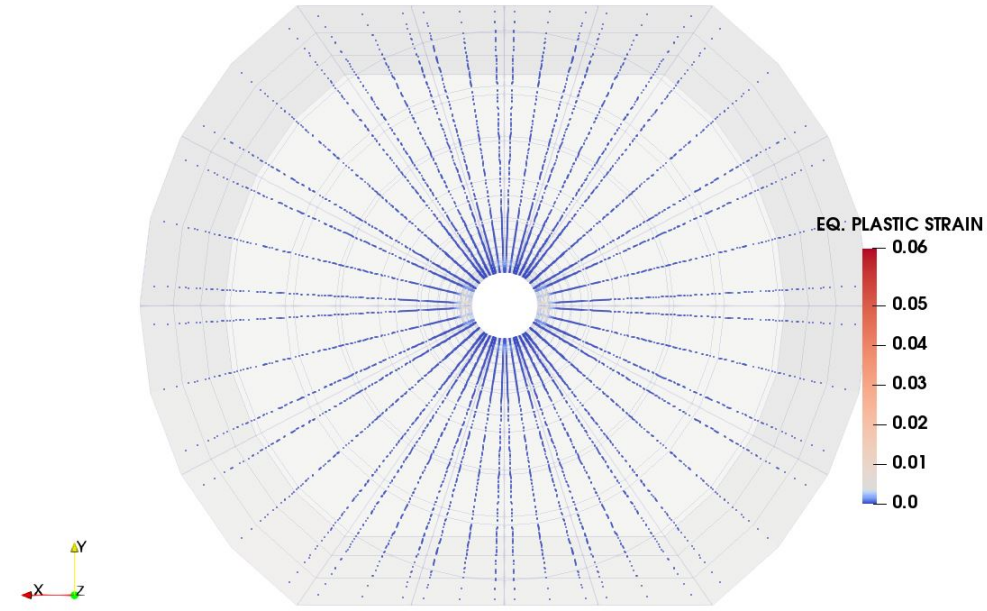

(a)

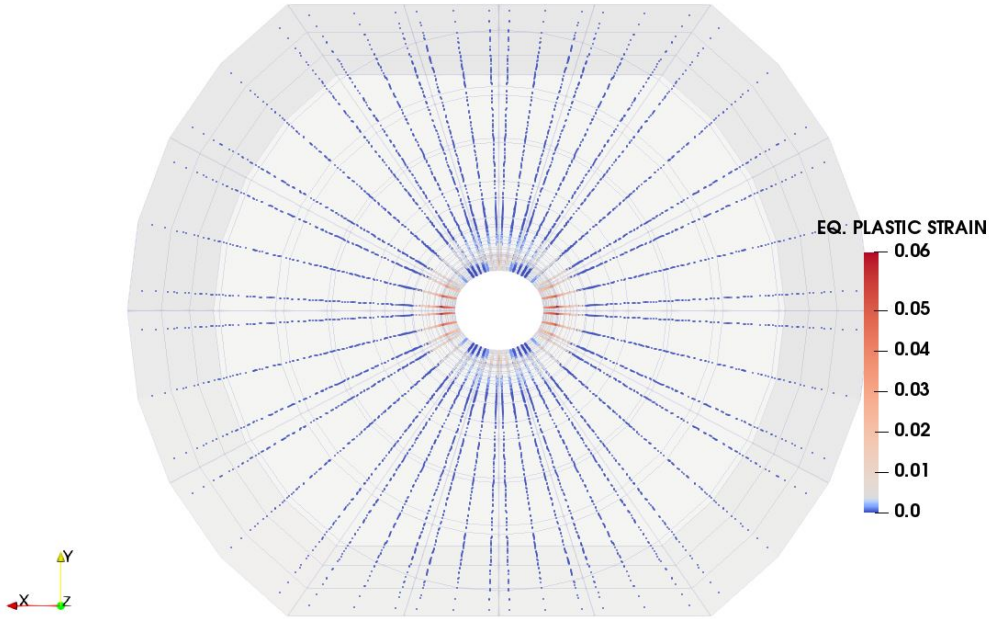

(b)

Figure A.2: ε^p at the onset of sand production (a) and end (b) of simulation for the poly-axial experiment simulation with K_z = 1 and K_r = 1/3.

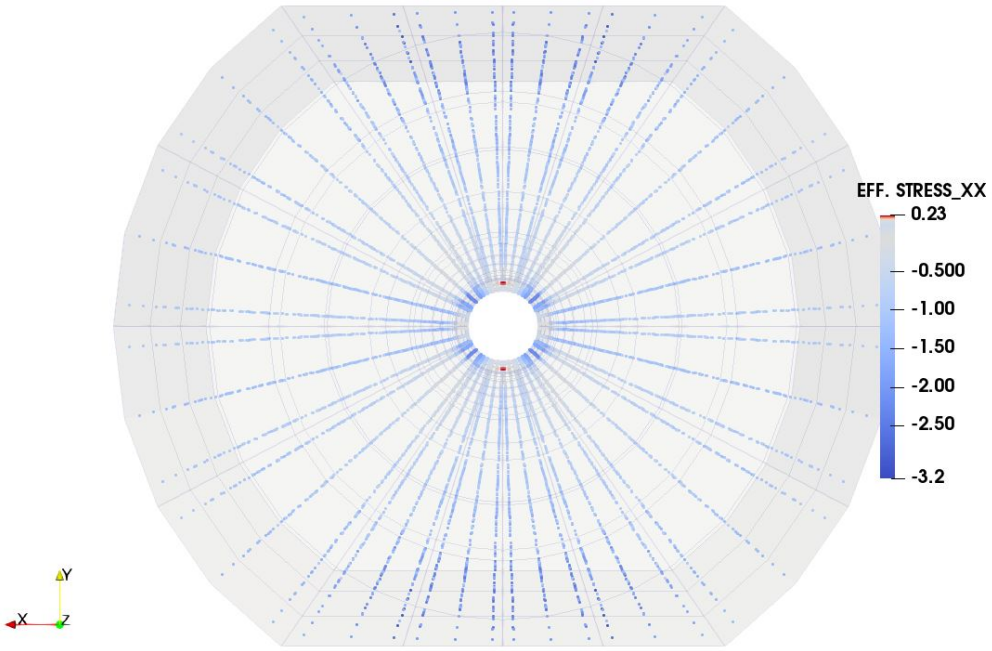

(a)

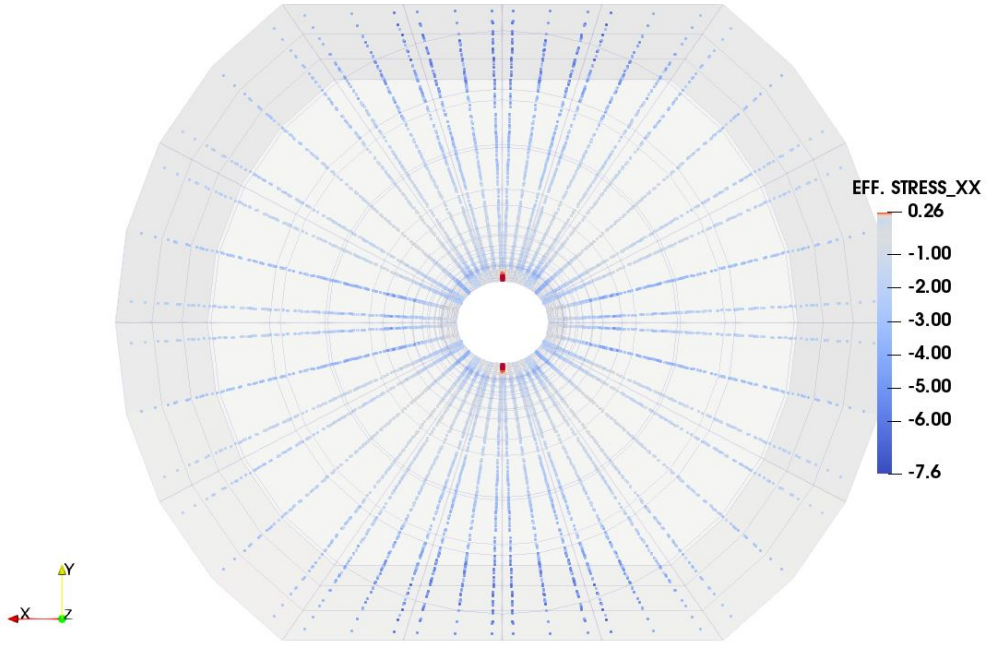

(b)

Figure A.3: σ^e_{xx} at the onset of sand production (a) and end (b) of simulation for the poly-axial experiment simulation with K_z = 1 and K_r = 1/3.

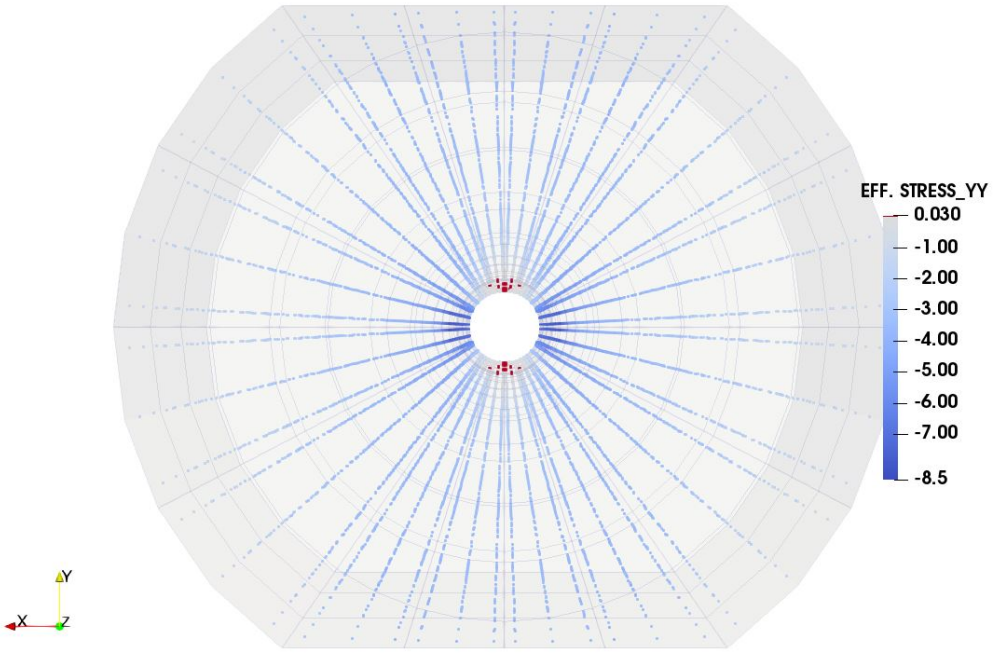

(a)

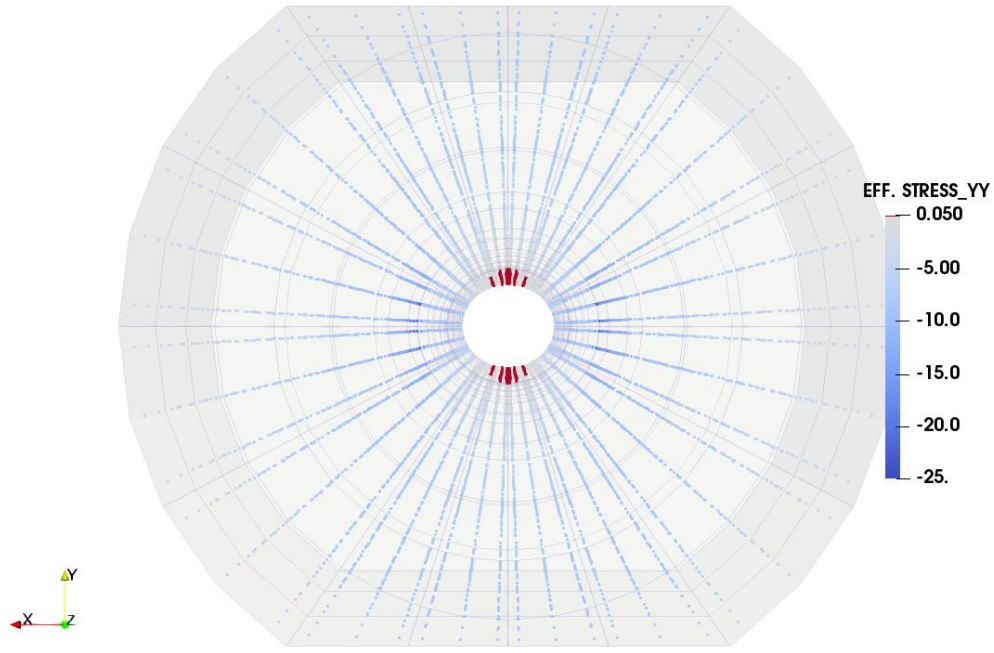

(b)

Figure A.4: σ^e_{yy} at the onset of sand production (a) and end (b) of simulation for the poly-axial experiment simulation with K_z = 1 and K_r = 1/3.

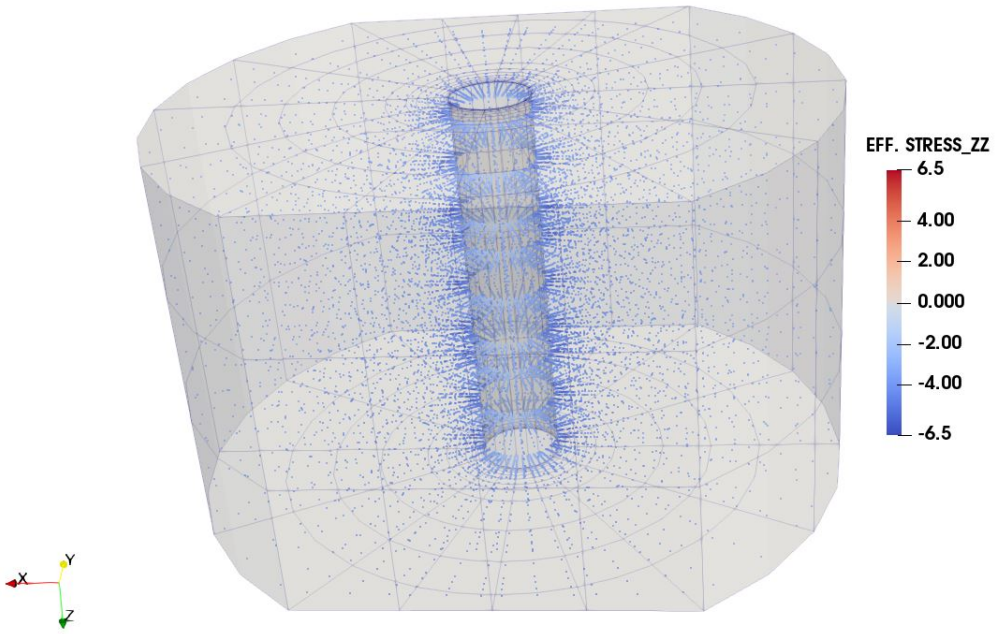

(a)

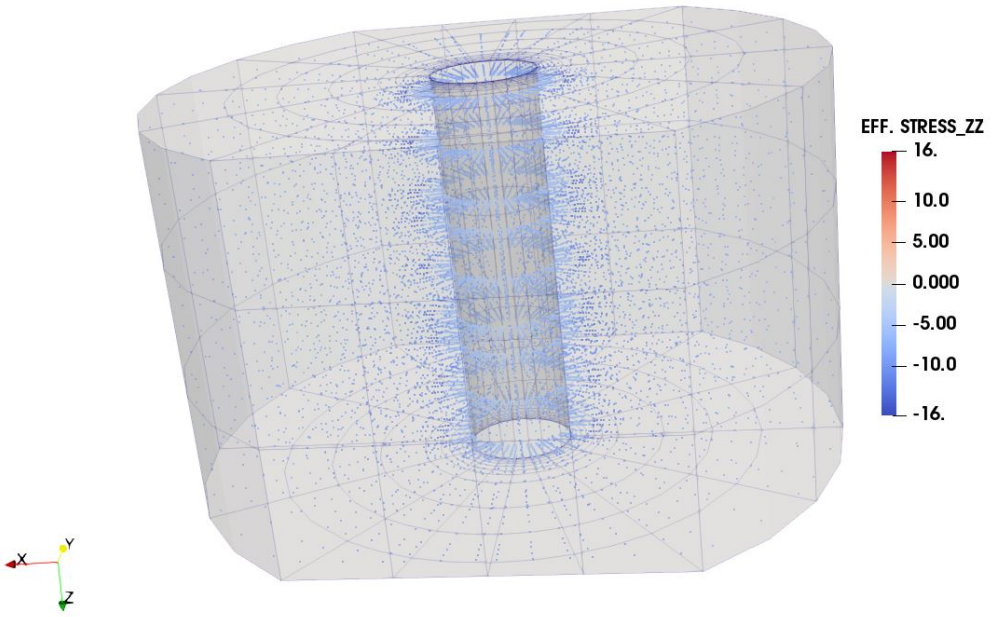

(b)

Figure A.5: σ^e_{zz} at the onset of sand production (a) and end (b) of simulation for the poly-axial experiment simulation with K_z = 1 and K_r = 1/3.

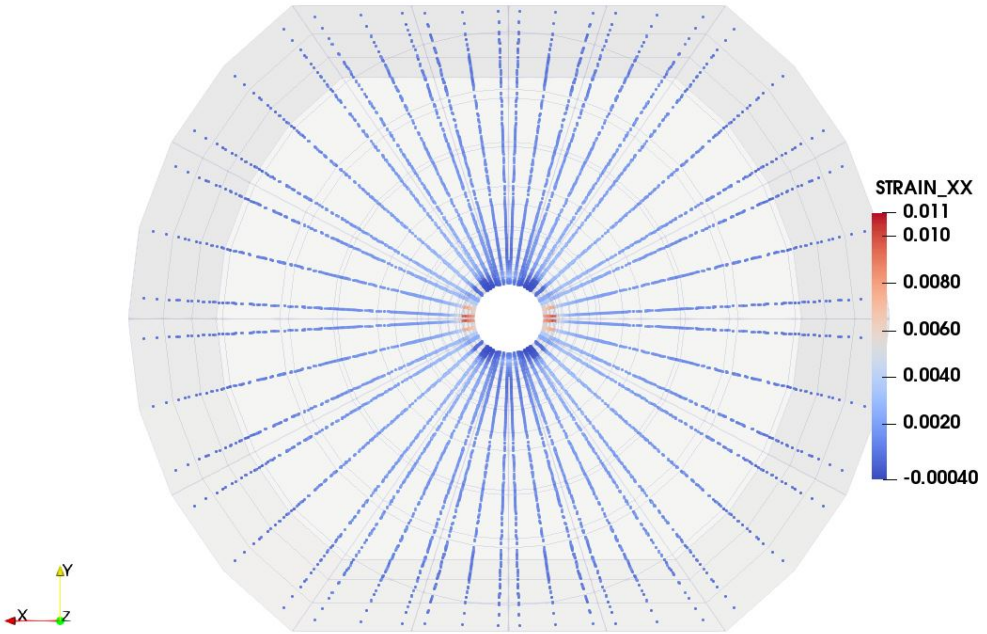

(a)

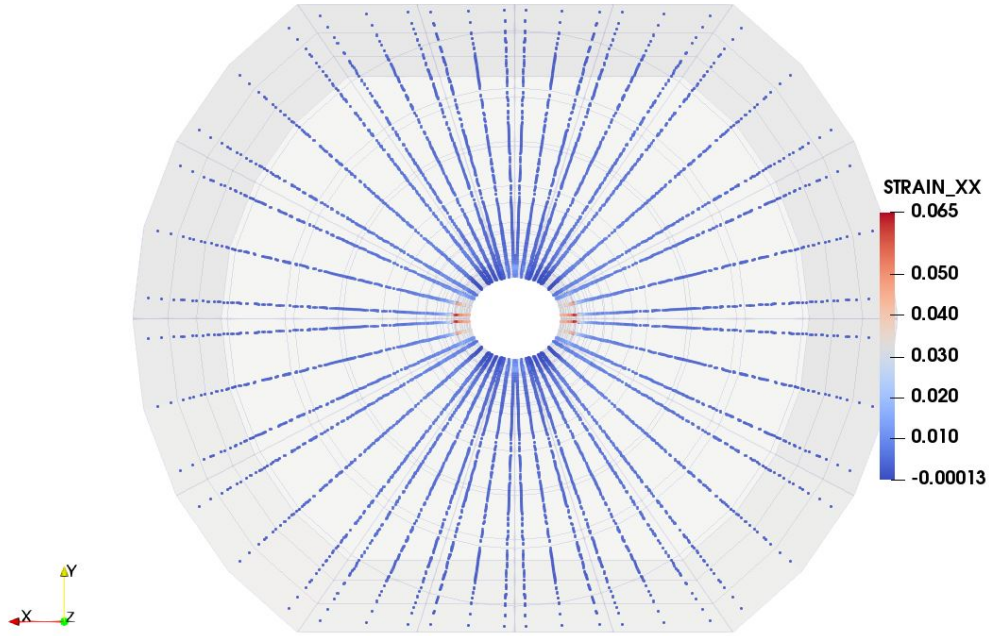

(b)

Figure A.6: ε_{xx} at the onset of sand production (a) and end (b) of simulation for the poly-axial experiment simulation with K_z = 1 and K_r = 1/3.

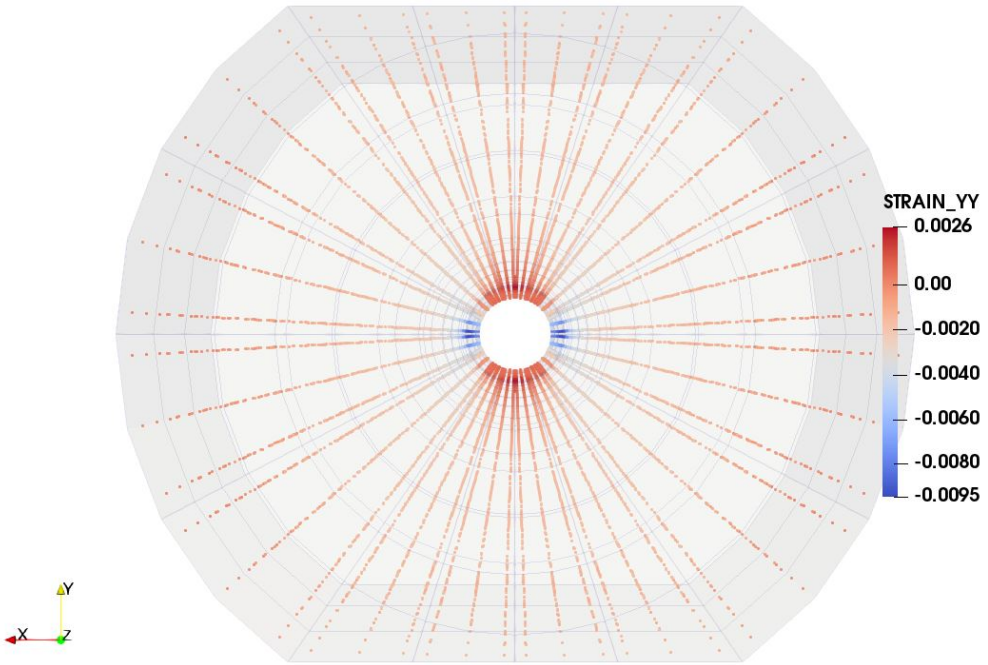

(a)

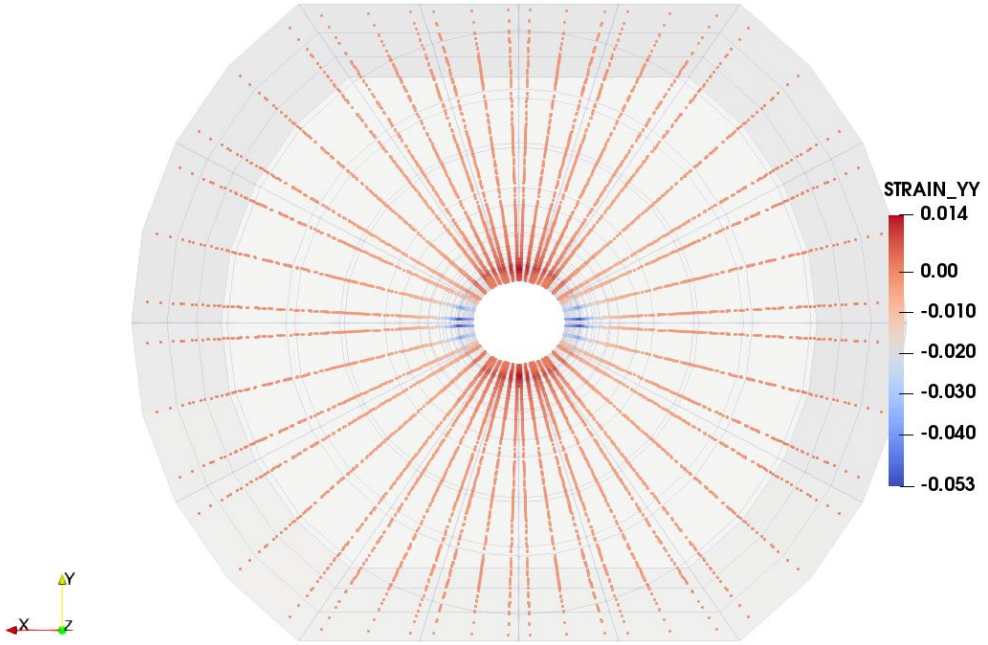

(b)

Figure A.7: ε_{yy} at the onset of sand production (a) and end (b) of simulation for the poly-axial experiment simulation with K_z = 1 and K_r = 1/3.

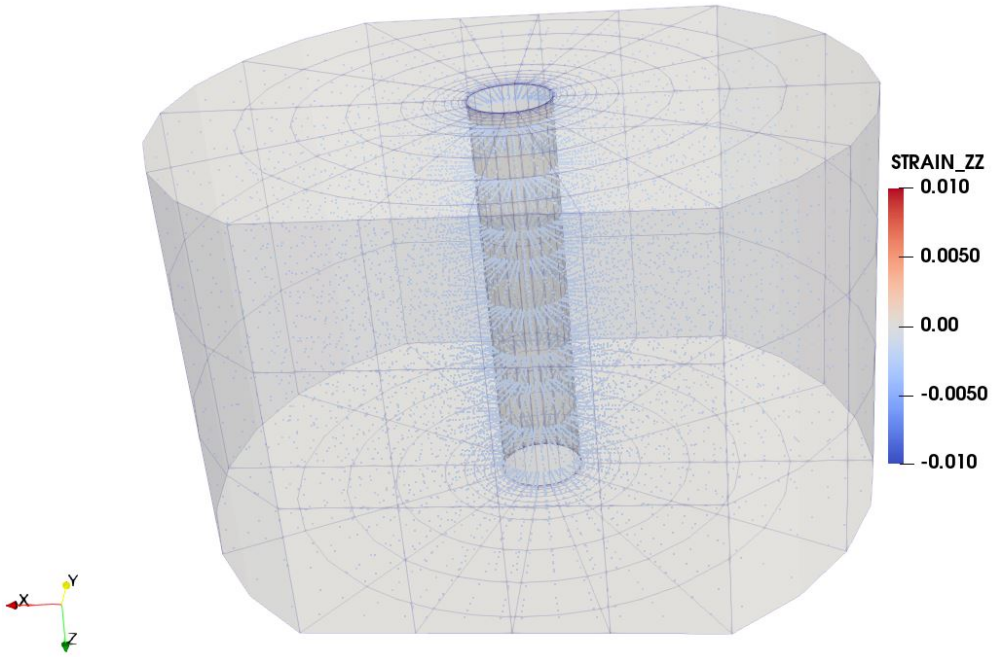

(a)

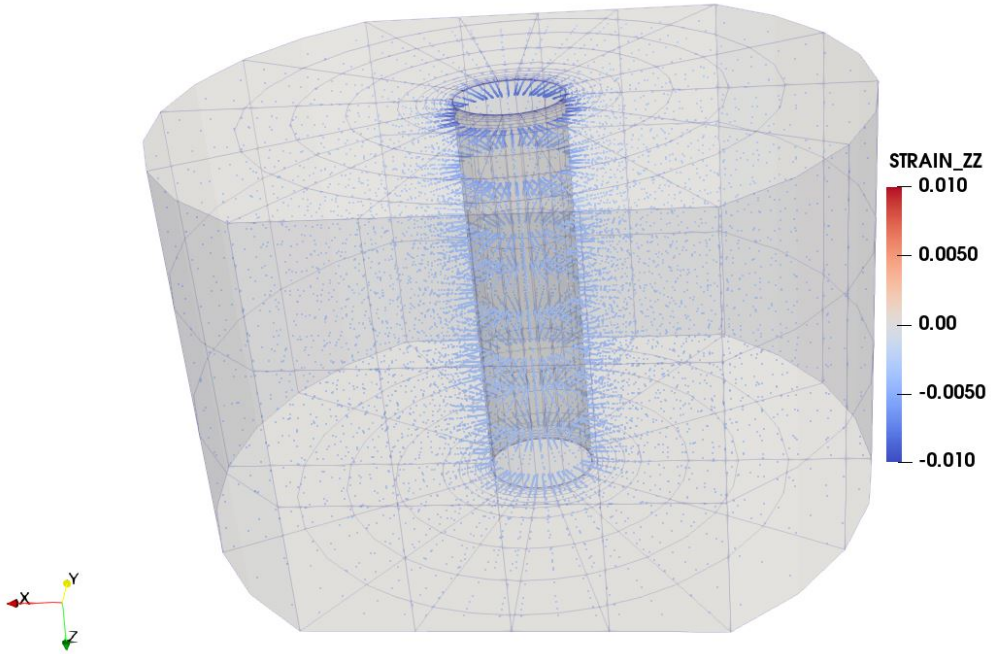

(b)

Figure A.8: ε_{zz} at the onset of sand production (a) and end (b) of simulation for the poly-axial experiment simulation with K_z = 1 and K_r = 1/3.

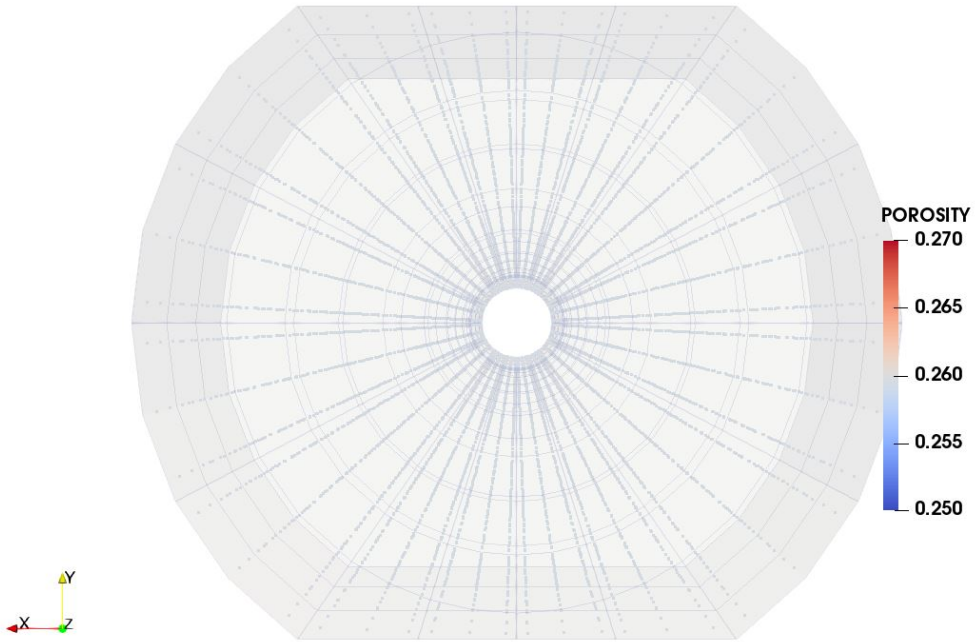

(a)

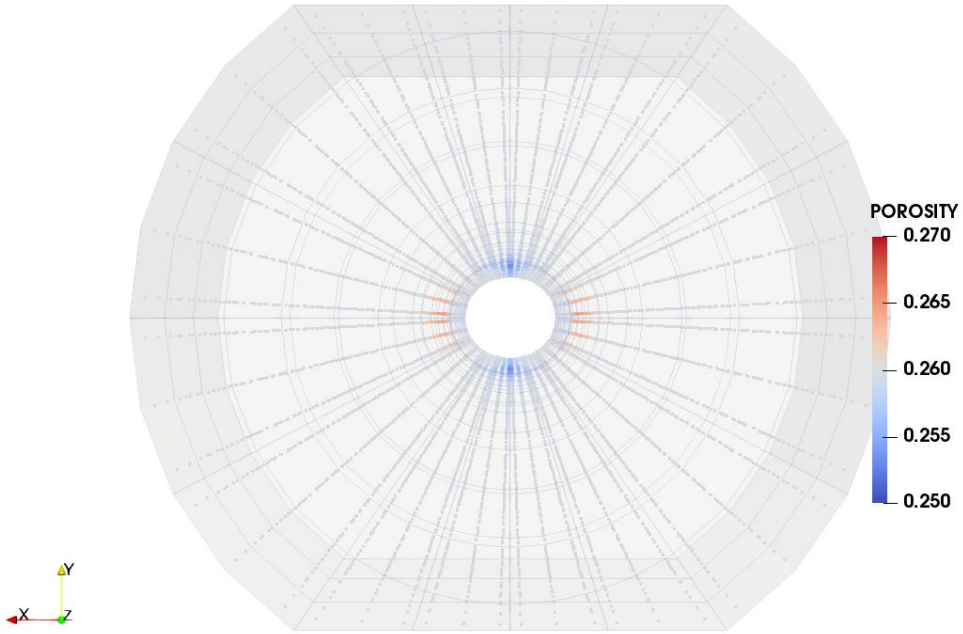

(b)

Figure A.9: Porosity at the onset of sand production (a) and end (b) of simulation for the poly-axial experiment simulation with K_z = 1 and K_r = 1/3.

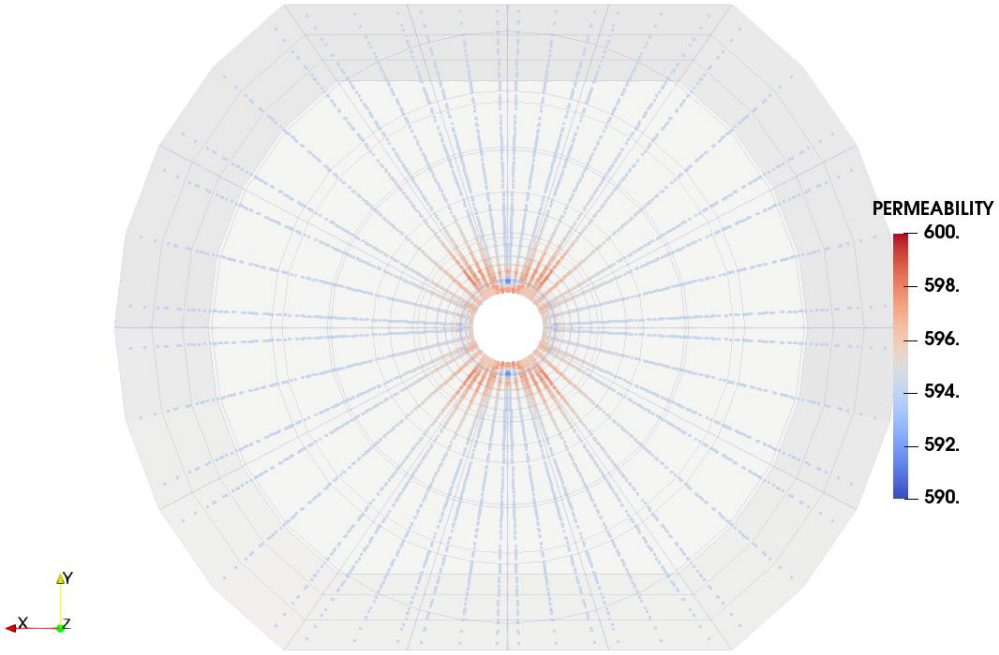

(a)

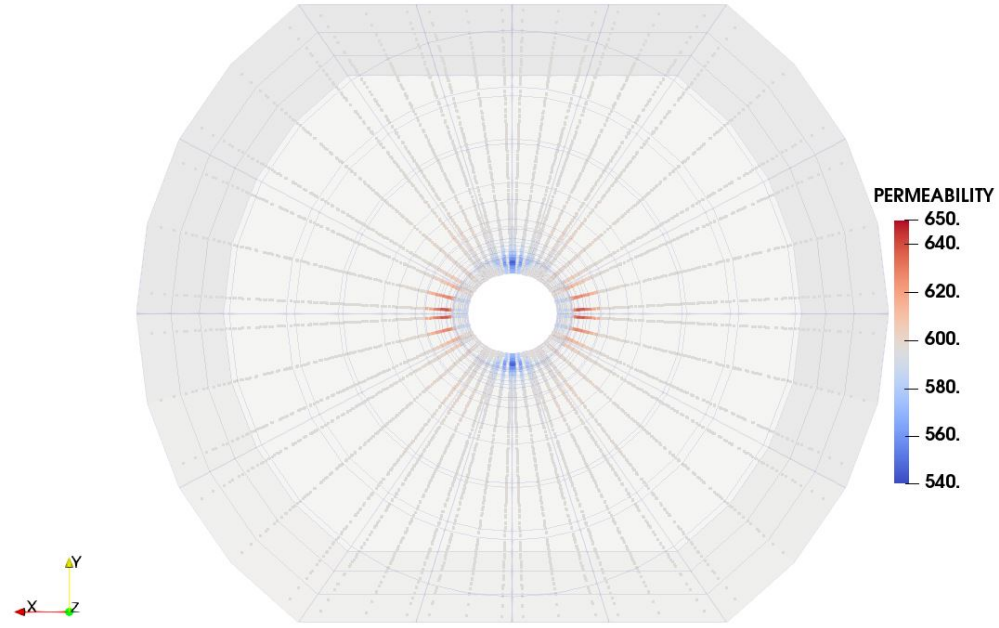

(b)

Figure A.10: Permeability (k_x, k_y and k_z) at the onset of sand production (a) and end (b) of simulation for the poly-axial experiment simulation with K_z = 1 and K_r = 1/3.

A.2 Case 02 - K_z = 1, K_r = 2/3

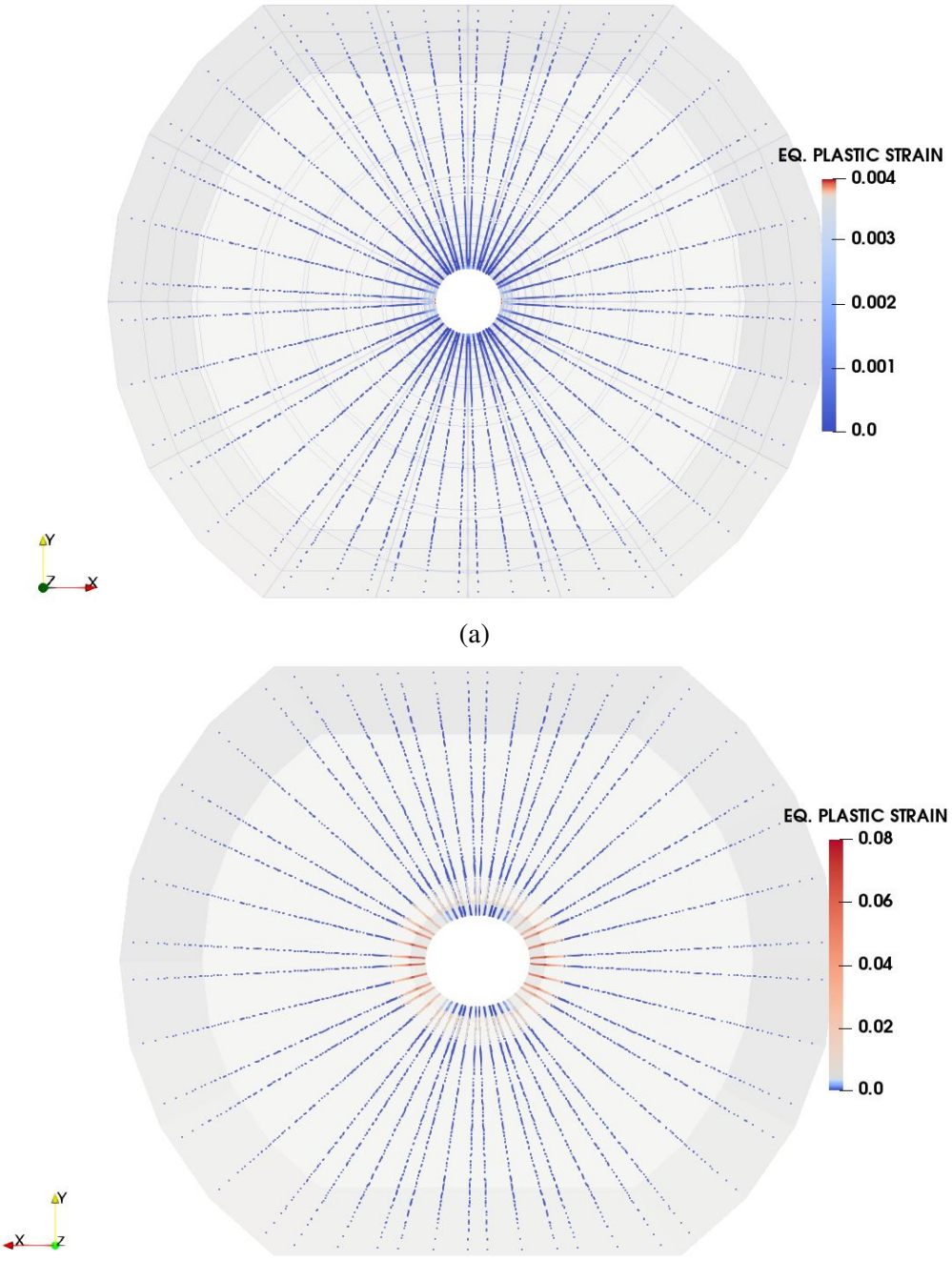

Figure A.11: ε^p at the onset of sand production (a) and end (b) of simulation for the poly-axial experiment simulation with K_z = 1 and K_r = 2/3.

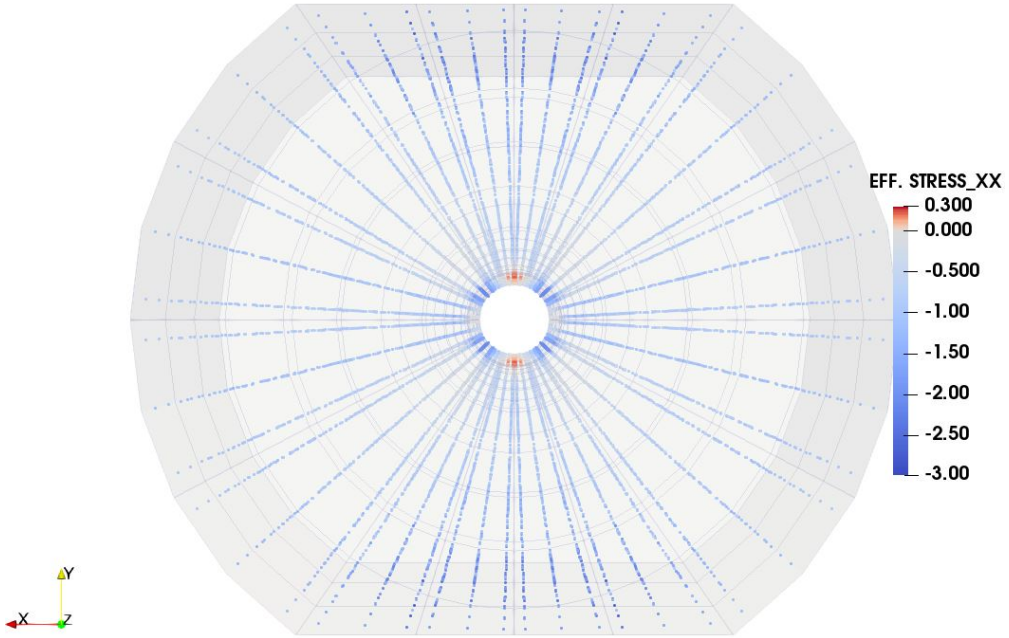

(a)

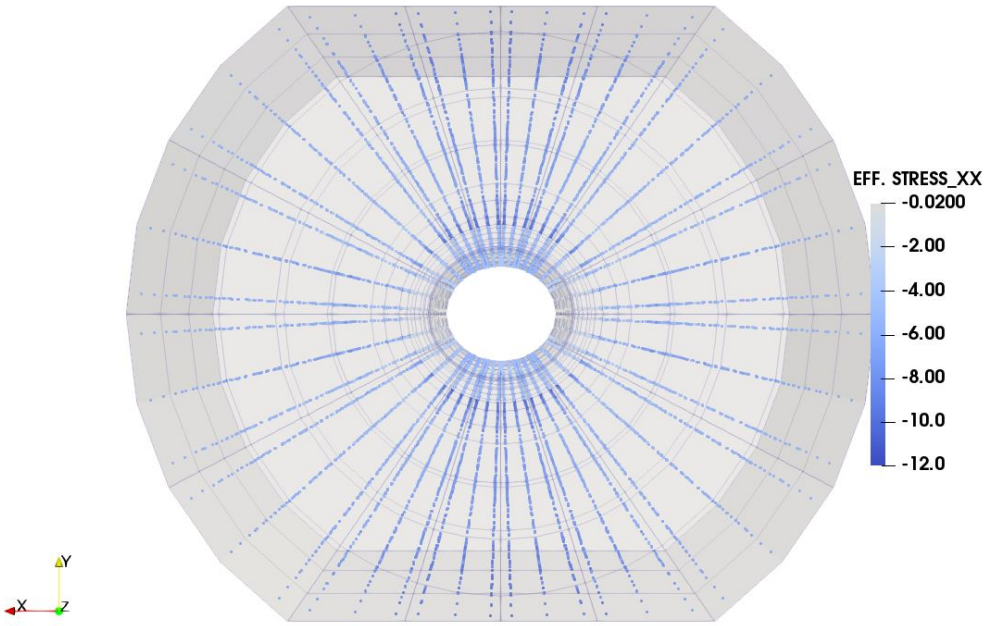

(b)

Figure A.12: σ^e_{xx} at the onset of sand production (a) and end (b) of simulation for the poly-axial experiment simulation with K_z = 1 and K_r = 2/3.

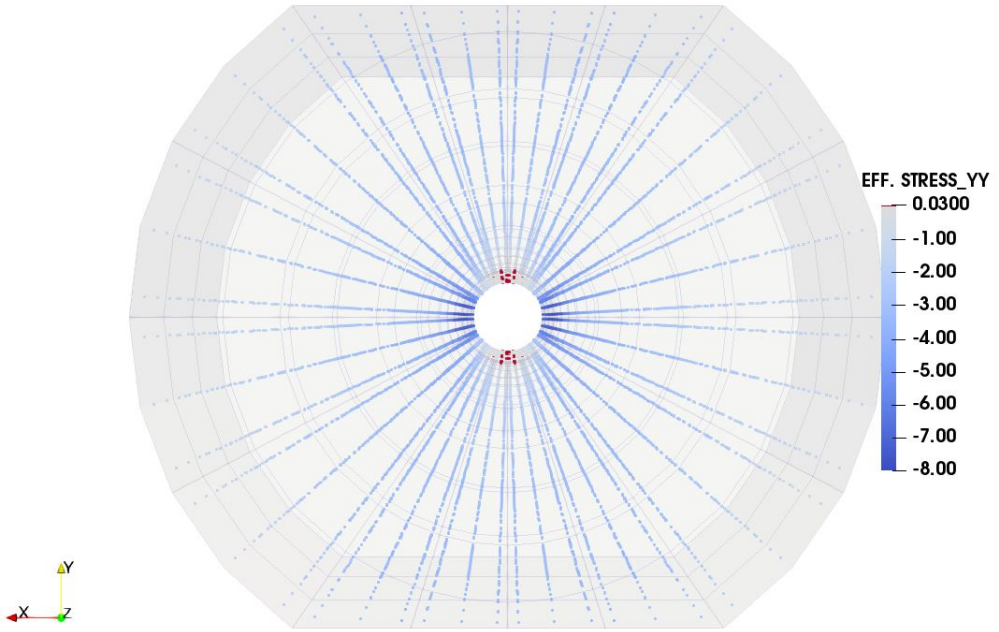

(a)

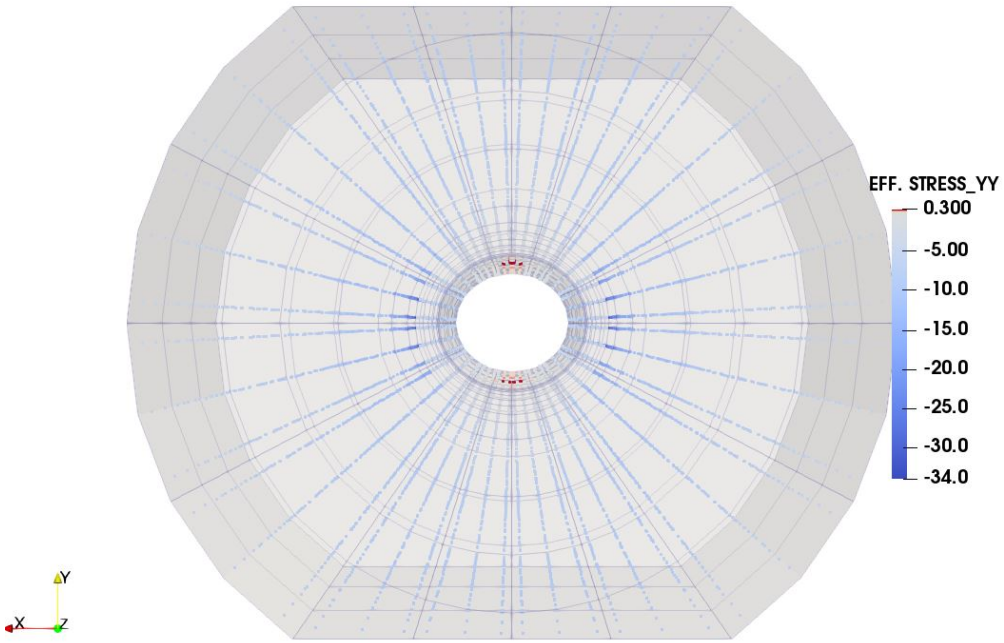

(b)

Figure A.13: σ^e_{yy} at the onset of sand production (a) and end (b) of simulation for the poly-axial experiment simulation with K_z = 1 and K_r = 2/3.

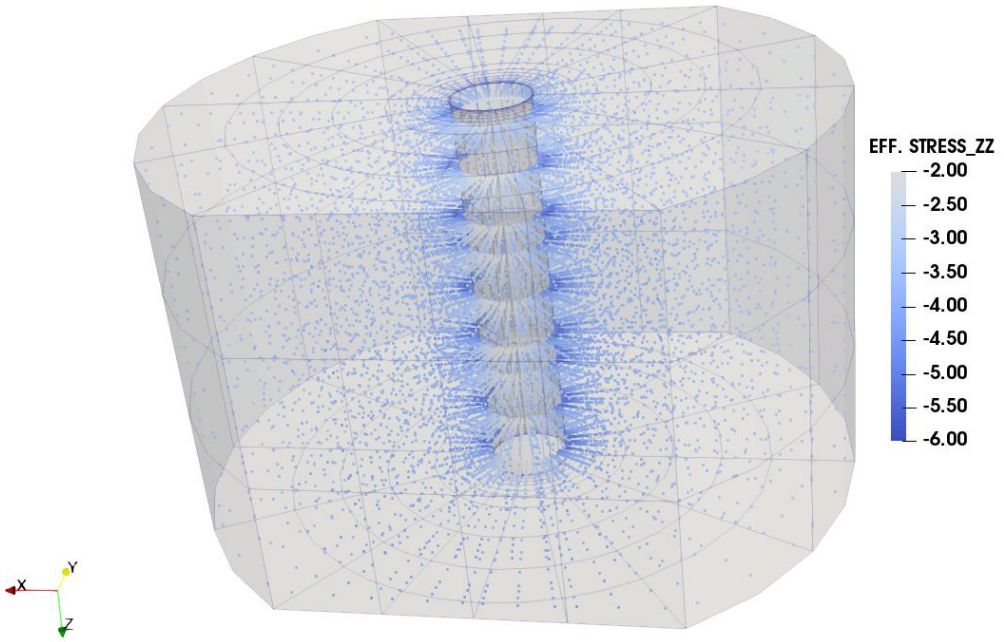

(a)

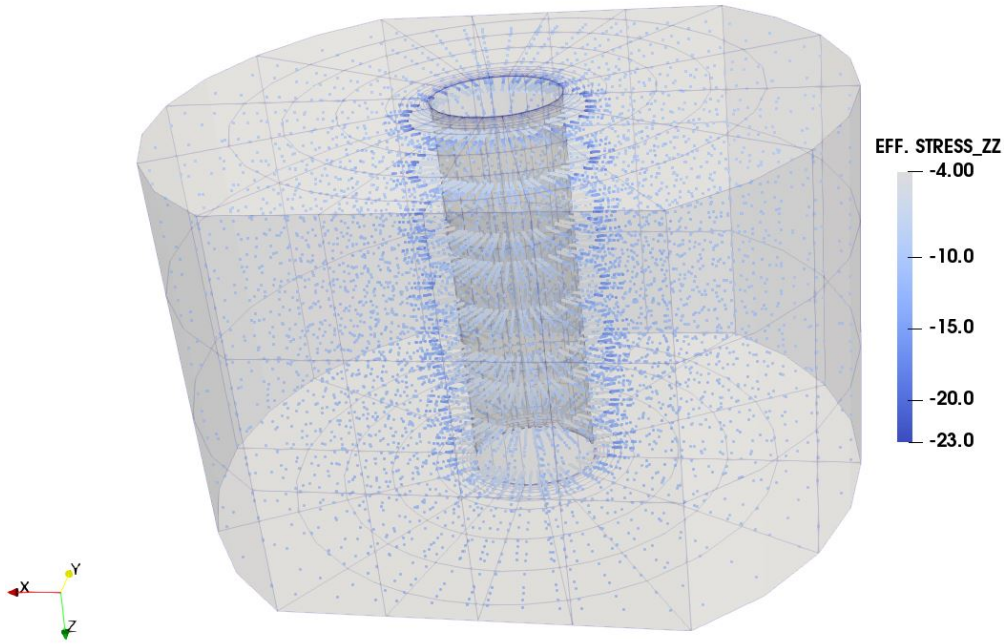

(b)

Figure A.14: σ^e_{zz} at the onset of sand production (a) and end (b) of simulation for the poly-axial experiment simulation with K_z = 1 and K_r = 2/3.

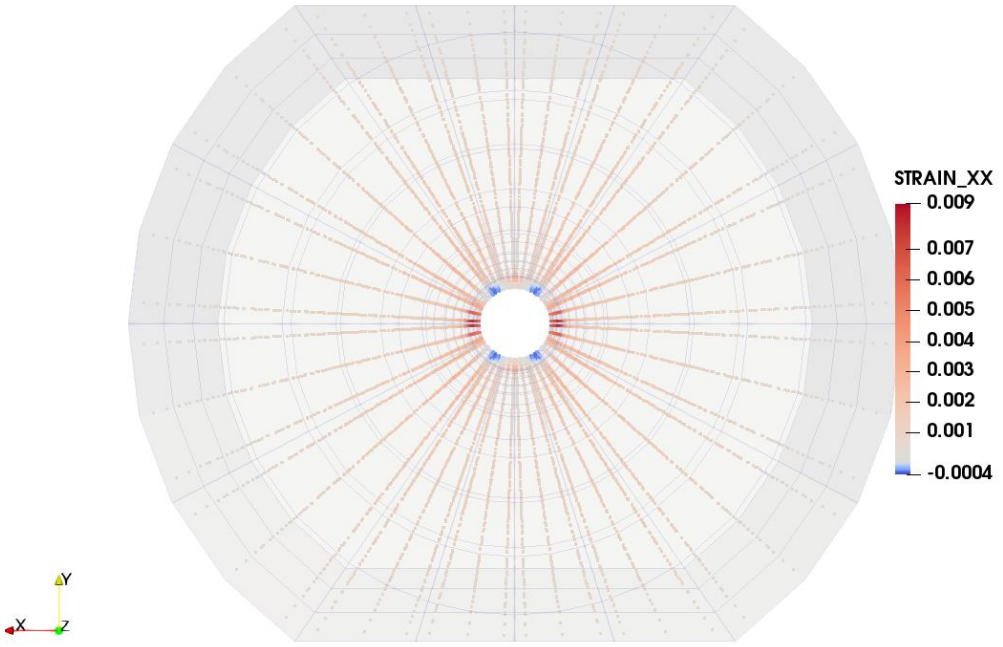

(a)

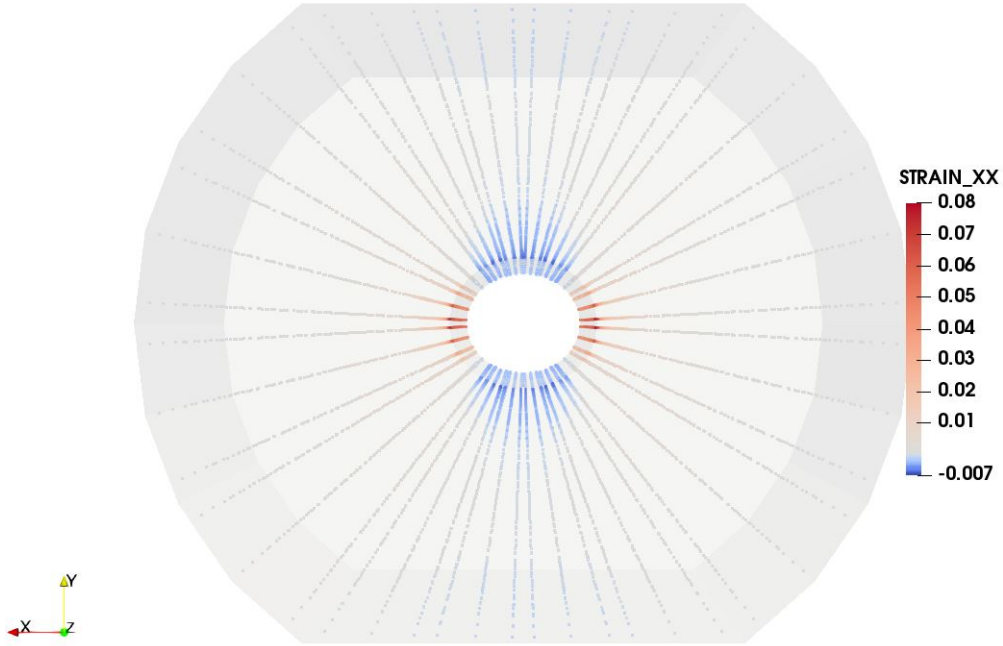

(b)

Figure A.15: ε_{xx} at the onset of sand production (a) and end (b) of simulation for the poly-axial experiment simulation with K_z = 1 and K_r = 2/3.

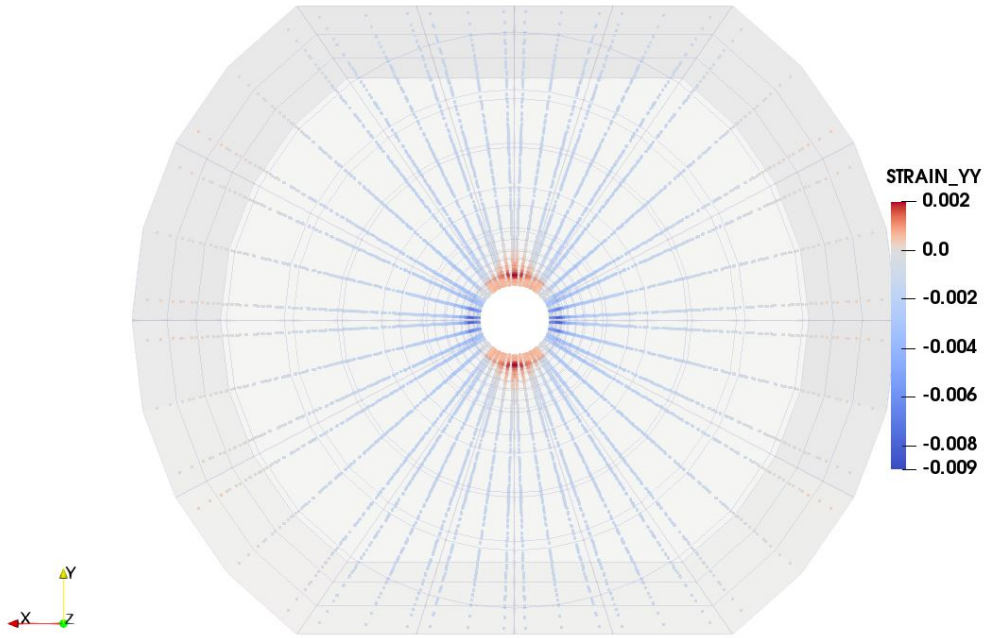

(a)

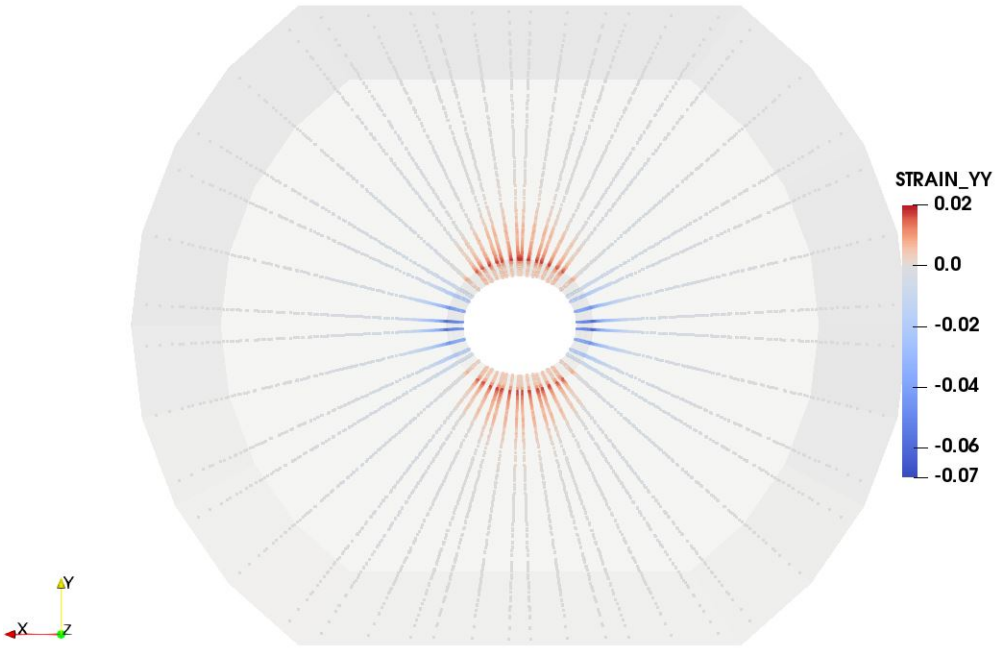

(b)

Figure A.16: ε_{yy} at the onset of sand production (a) and end (b) of simulation for the poly-axial experiment simulation with K_z = 1 and K_r = 2/3.

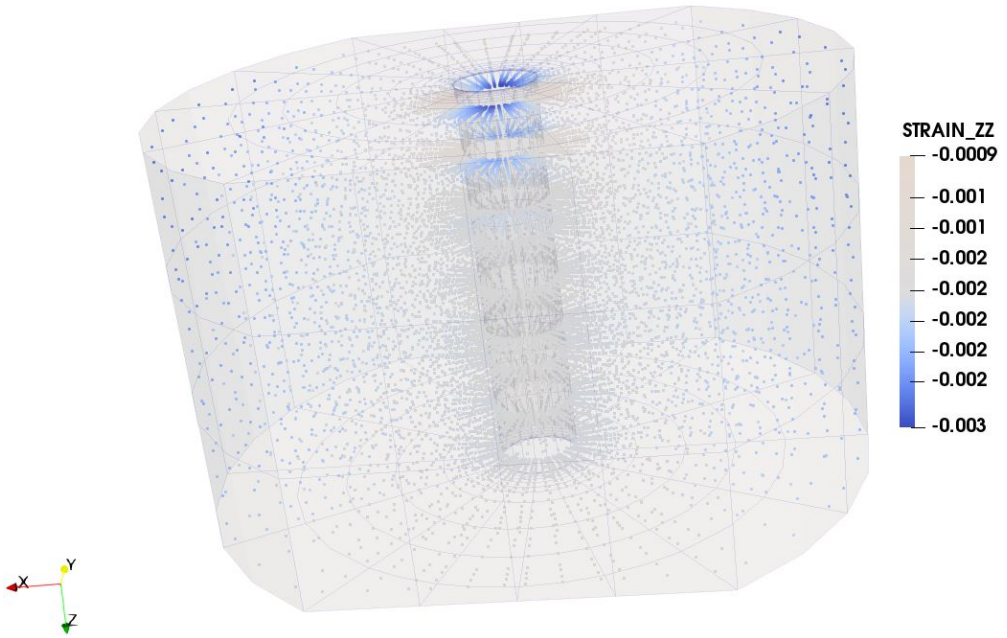

(a)

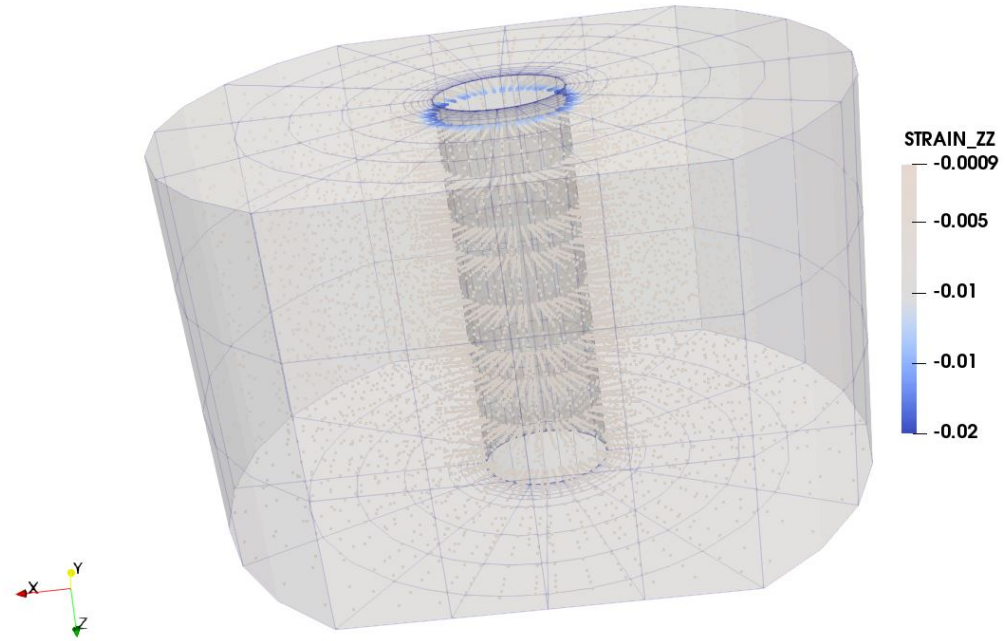

(b)

Figure A.17: ε_{zz} at the onset of sand production (a) and end (b) of simulation for the poly-axial experiment simulation with K_z = 1 and K_r = 2/3.

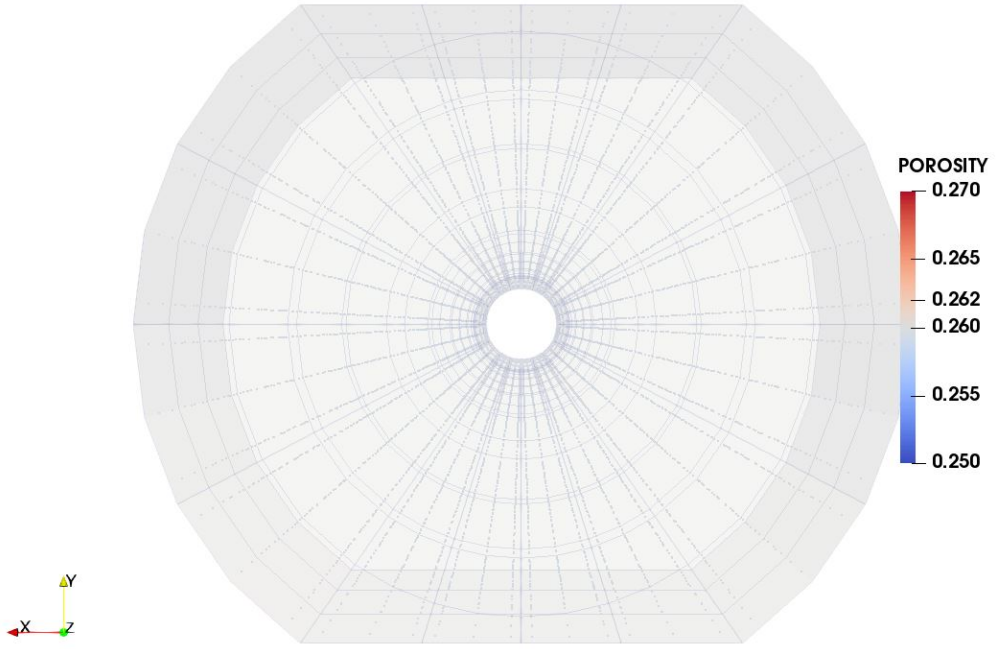

(a)

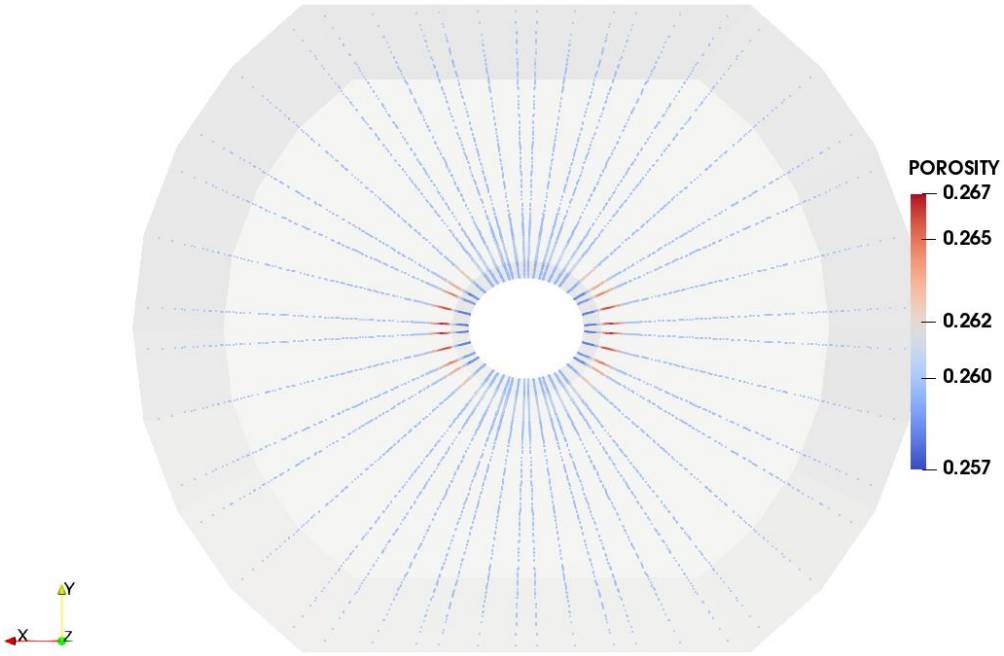

(b)

Figure A.18: Porosity at the onset of sand production (a) and end (b) of simulation for the poly-axial experiment simulation with K_z = 1 and K_r = 2/3.

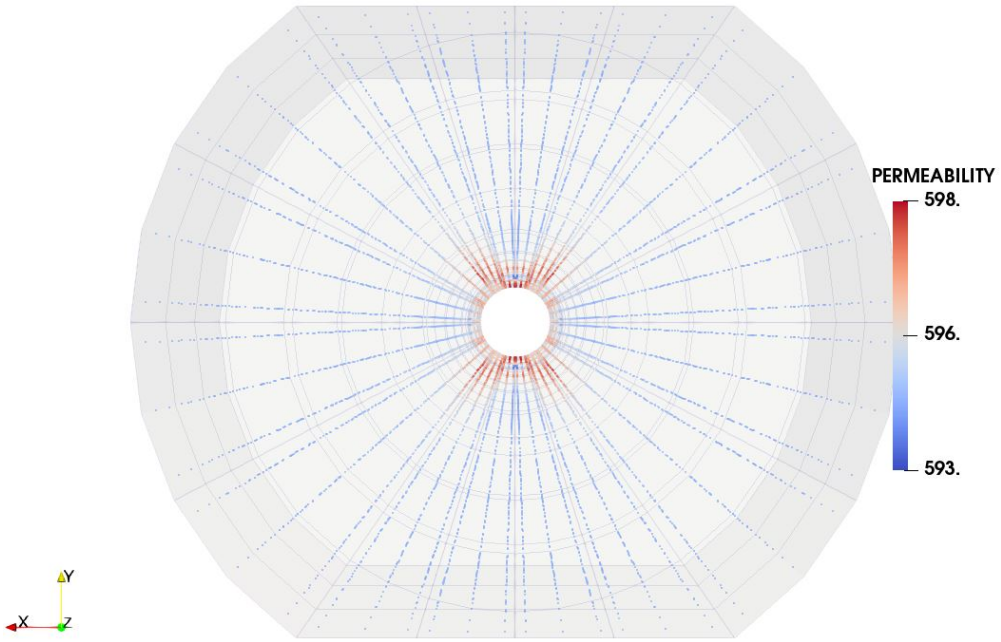

(a)

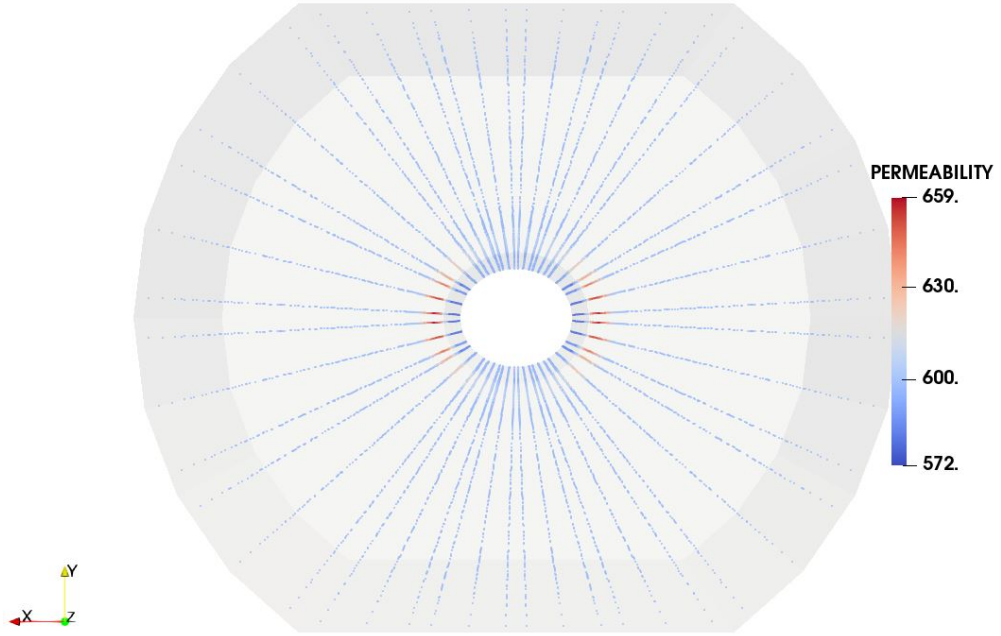

(b)

Figure A.19: Permeability (k_x, k_y and k_z) at the onset of sand production (a) and end (b) of simulation for the poly-axial experiment simulation with K_z = 1 and K_r = 2/3.

A.3 Case 03 - K_z = 2/3, K_r = 2/3

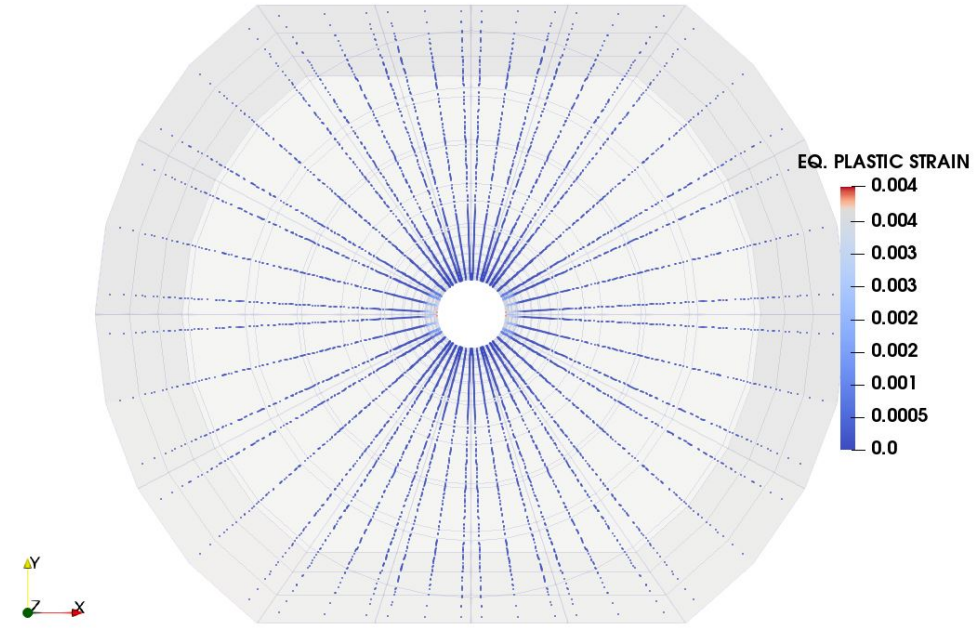

(a)

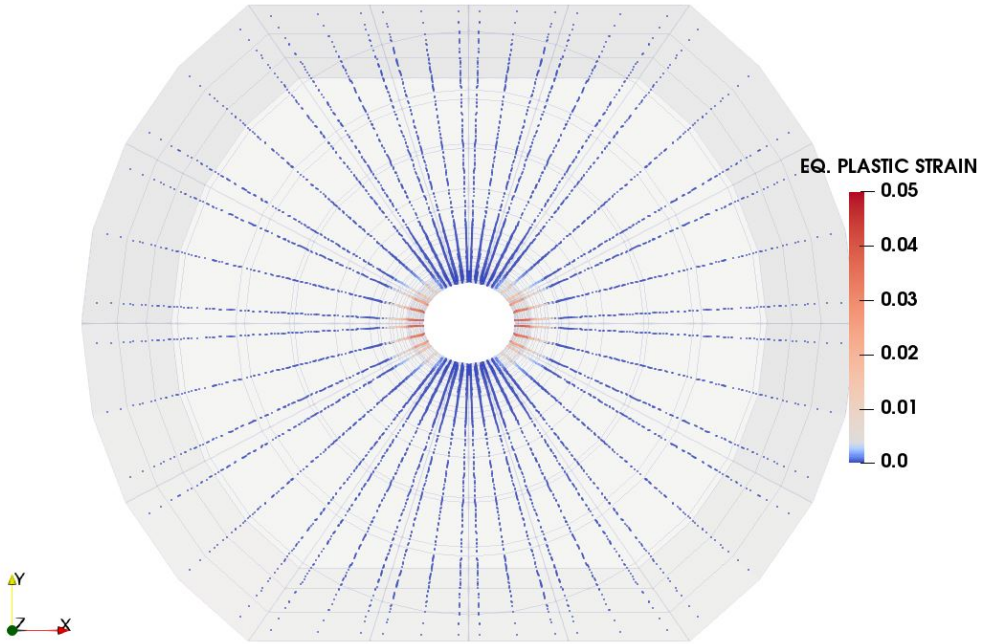

(b)

Figure A.20: ε^p at the onset of sand production (a) and end (b) of simulation for the poly-axial experiment simulation with K_z = 2/3 and K_r = 2/3.

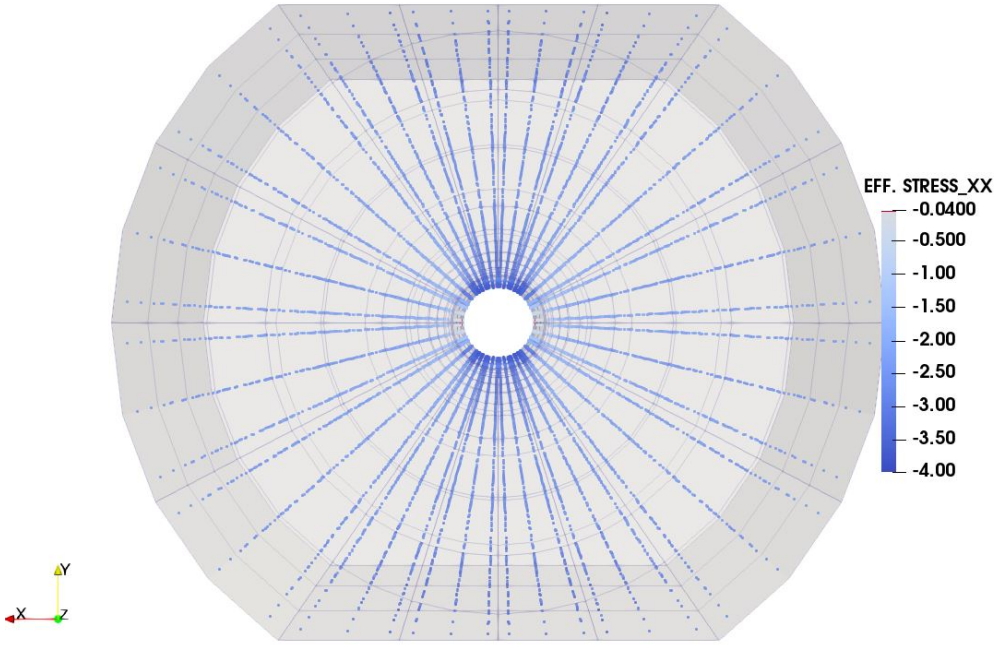

(a)

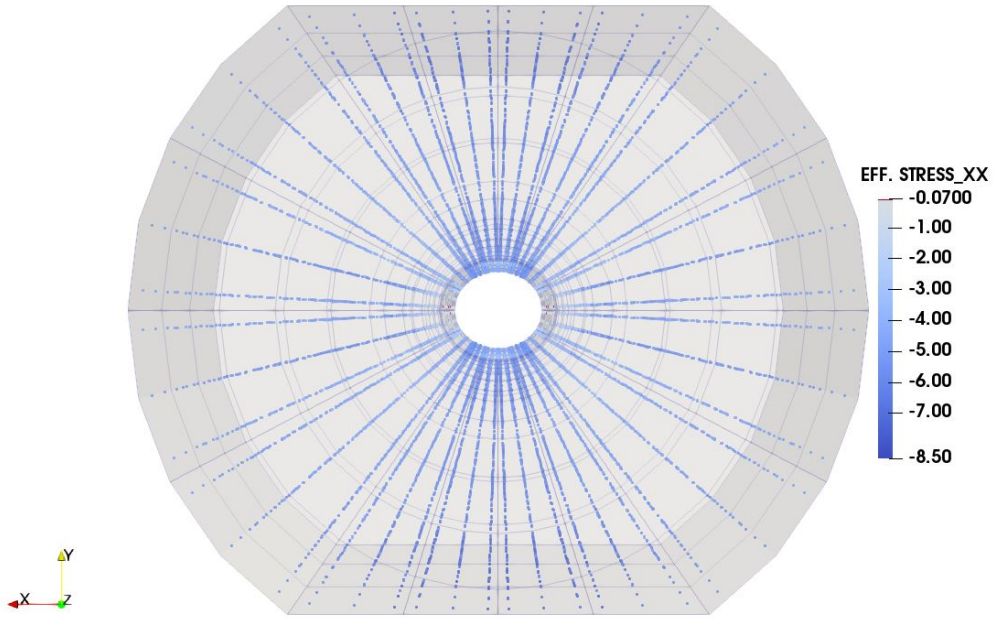

(b)

Figure A.21: σ^e_{xx} at the onset of sand production (a) and end (b) of simulation for the poly-axial experiment simulation with K_z = 2/3 and K_r = 2/3.

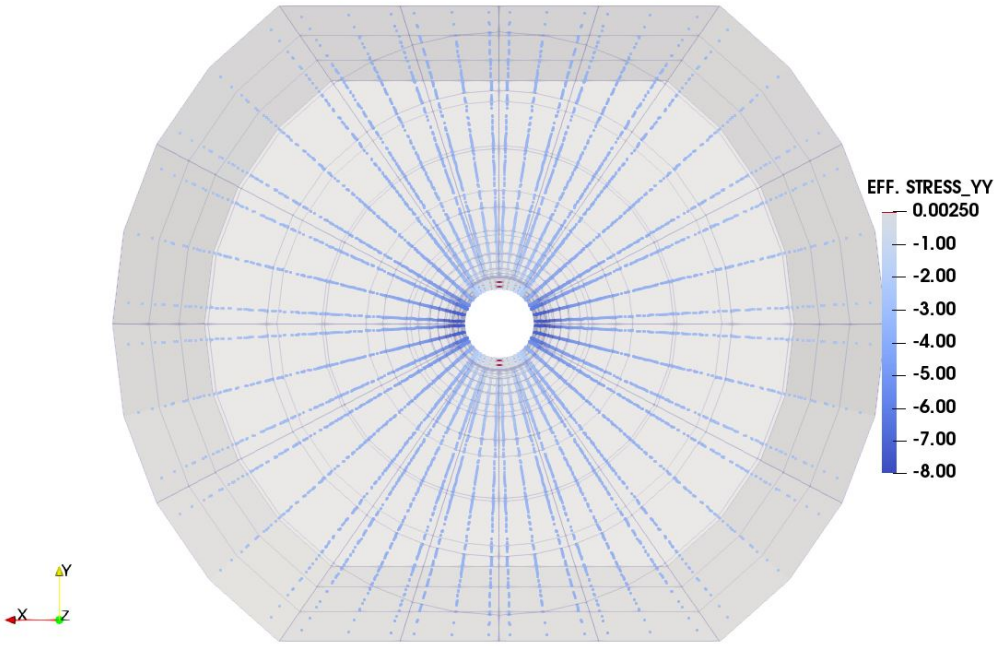

(a)

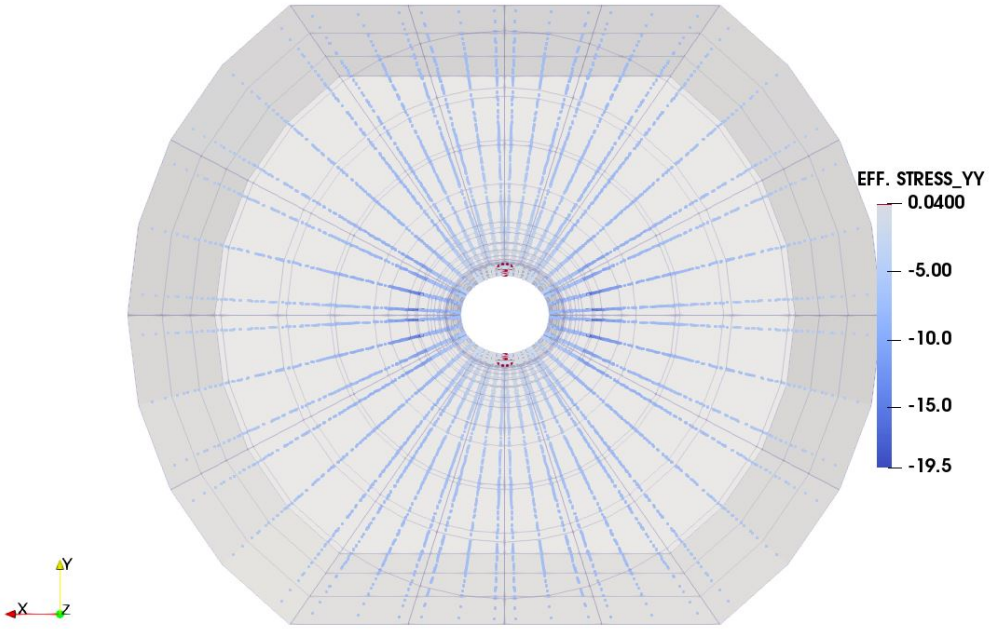

(b)

Figure A.22: σ^e_{yy} at the onset of sand production (a) and end (b) of simulation for the poly-axial experiment simulation with K_z = 2/3 and K_r = 2/3.

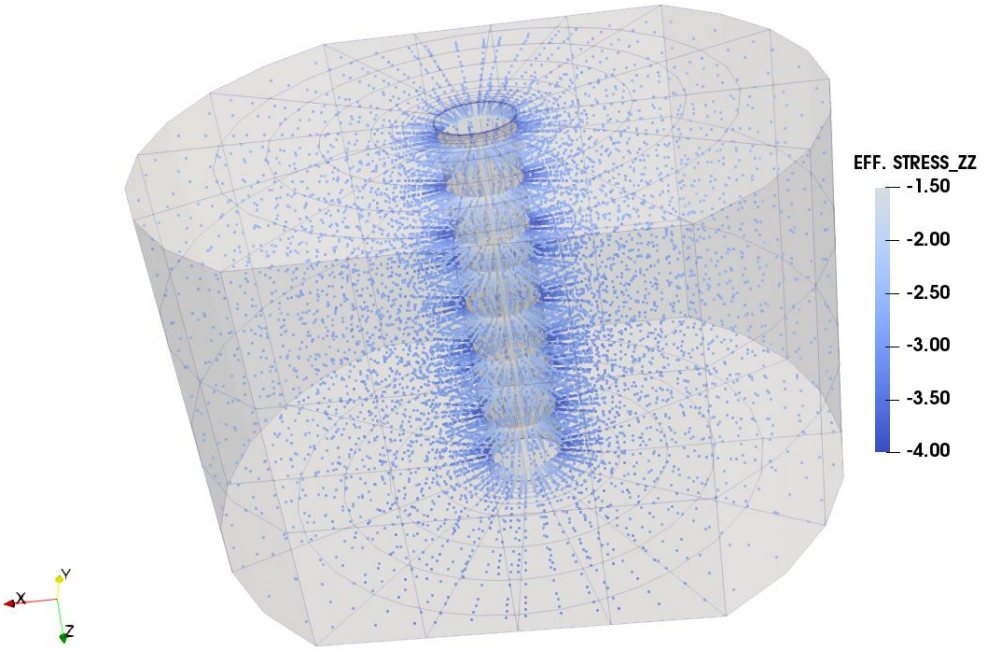

(a)

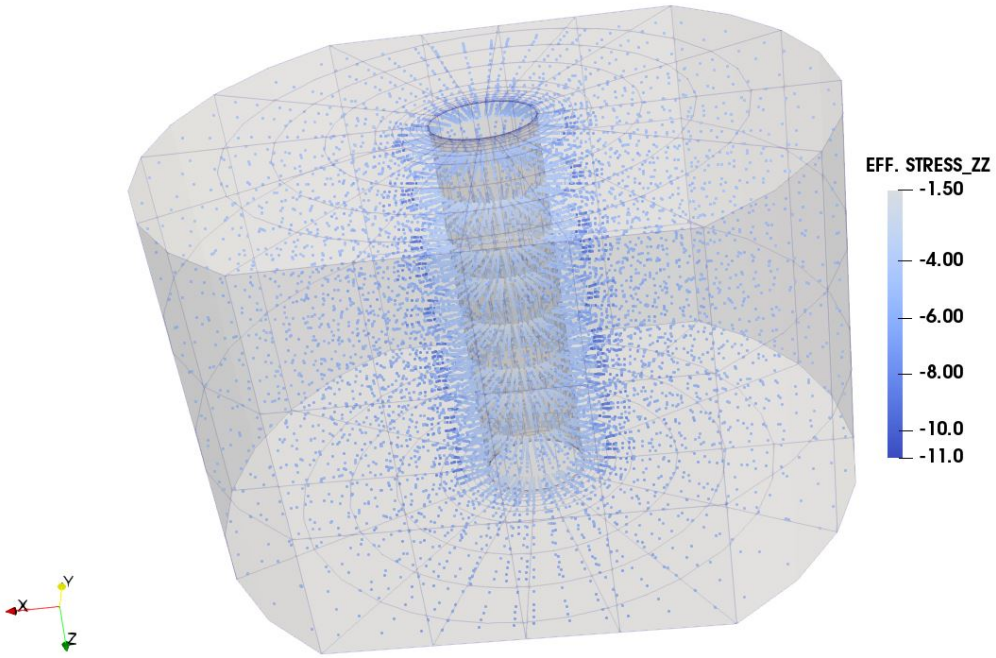

(b)

Figure A.23: σ^e_{zz} at the onset of sand production (a) and end (b) of simulation for the poly-axial experiment simulation with K_z = 2/3 and K_r = 2/3.

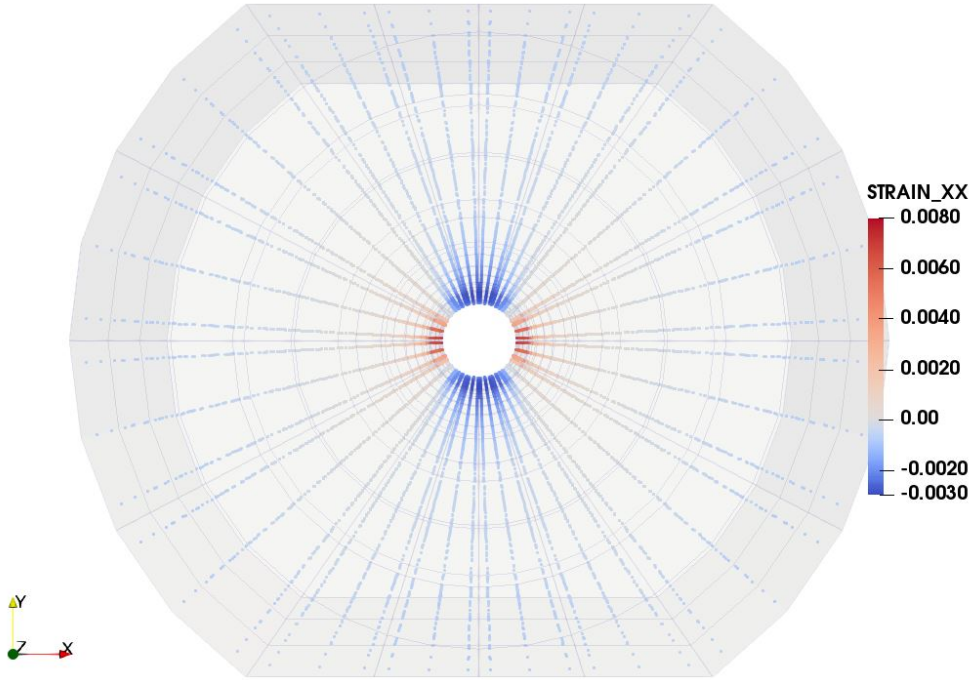

(a)

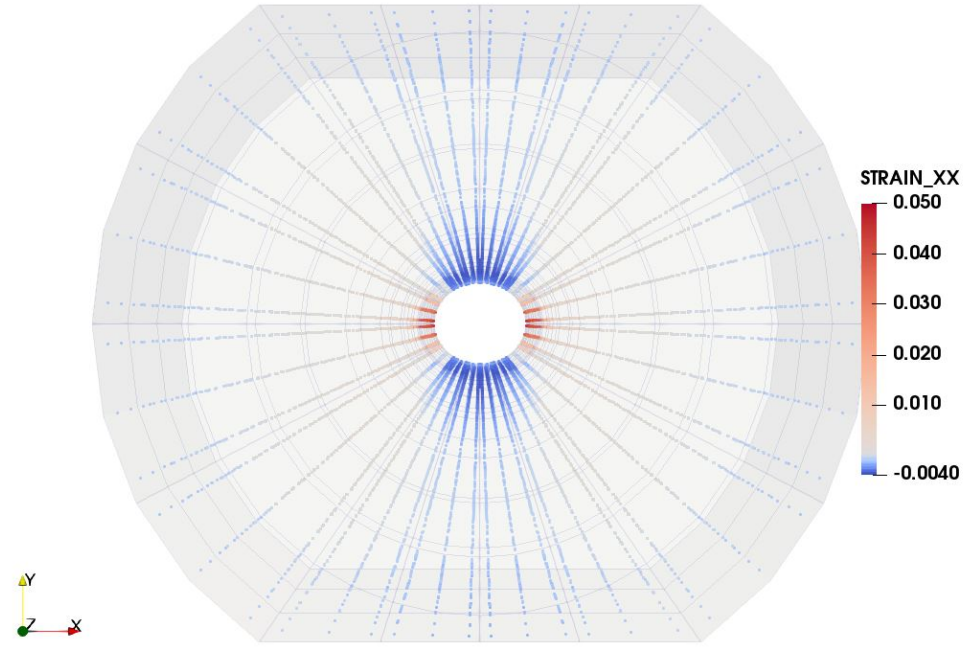

(b)

Figure A.24: ε_{xx} at the onset of sand production (a) and end (b) of simulation for the poly-axial experiment simulation with K_z = 2/3 and K_r = 2/3.

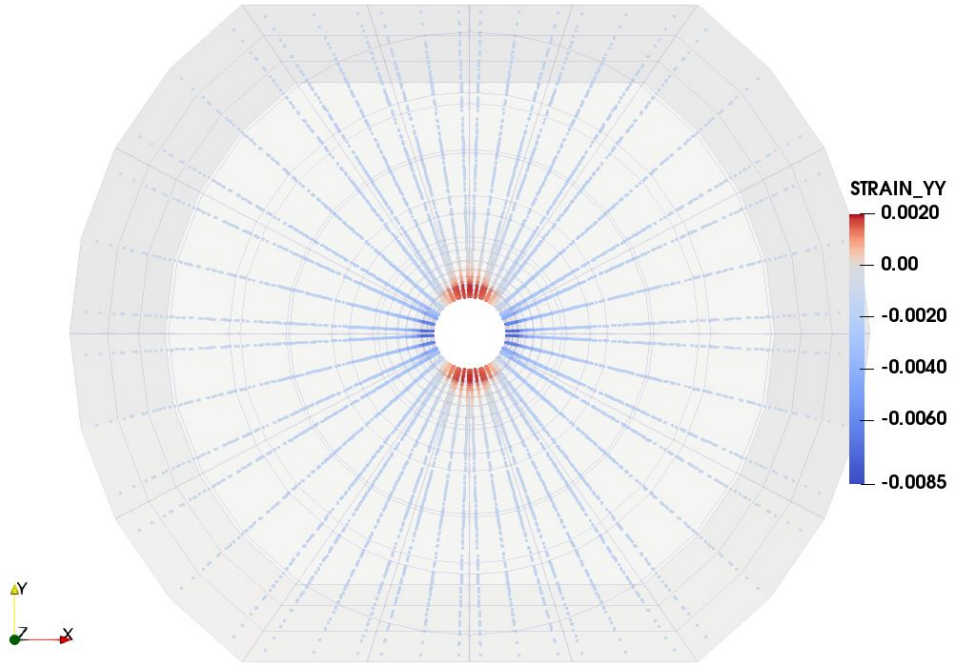

(a)

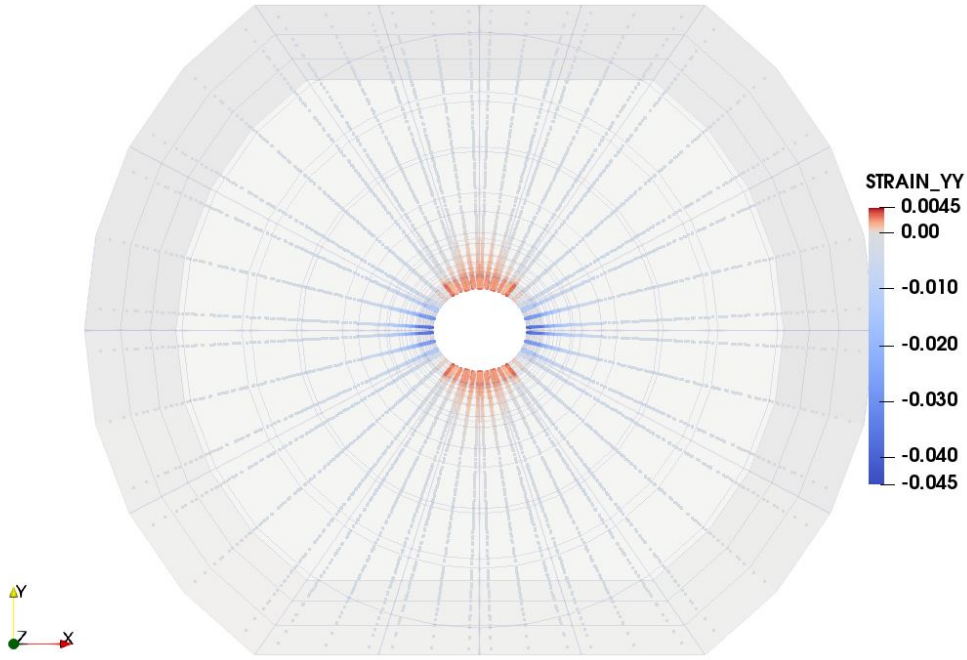

(b)

Figure A.25: ε_{yy} at the onset of sand production (a) and end (b) of simulation for the poly-axial experiment simulation with K_z = 2/3 and K_r = 2/3.

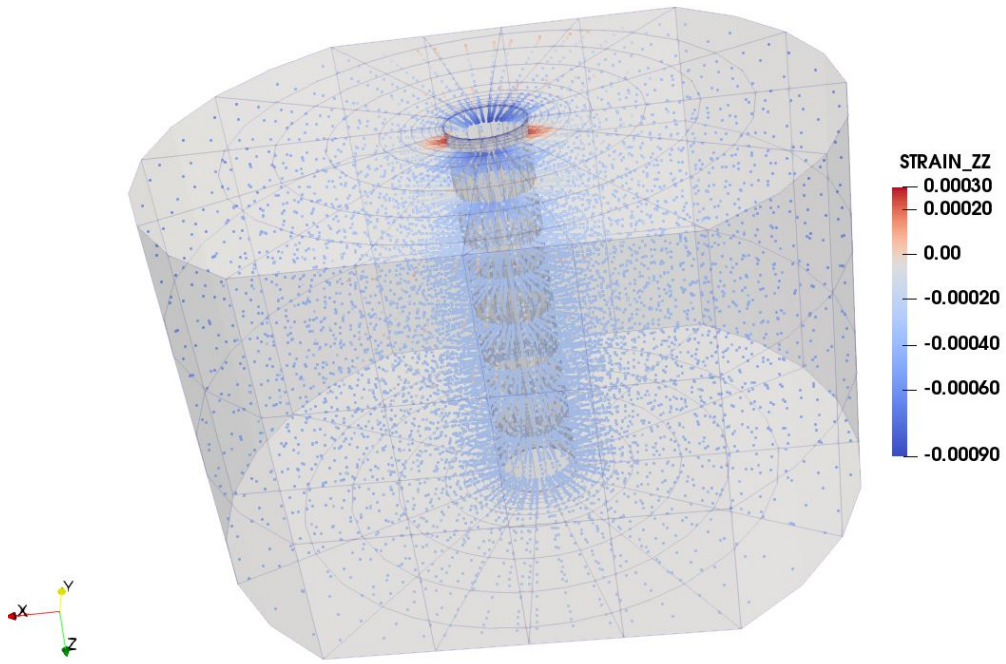

(a)

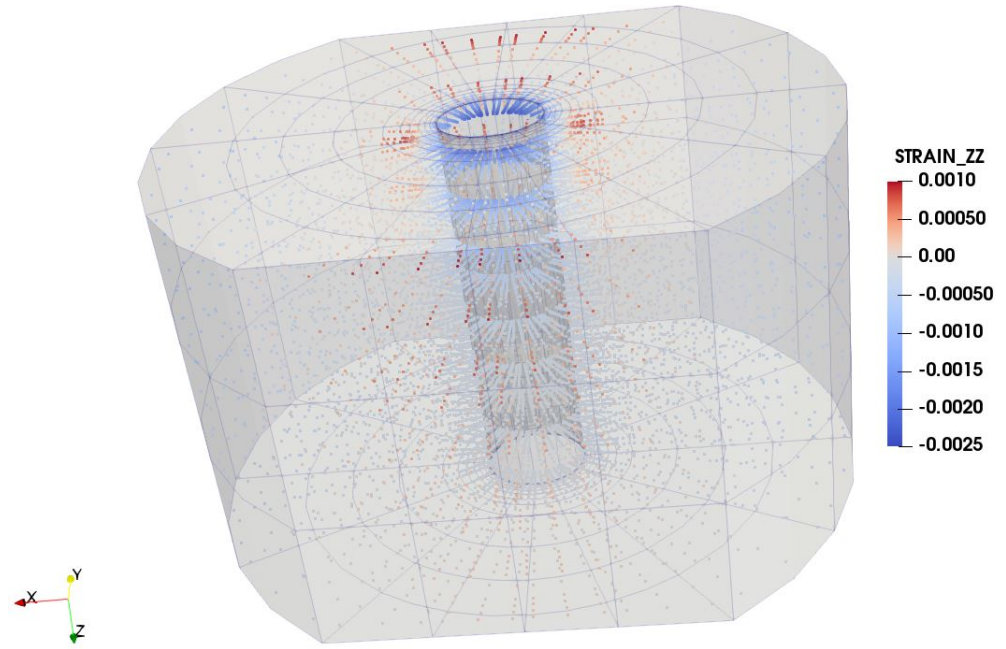

(b)

Figure A.26: ε_{zz} at the onset of sand production (a) and end (b) of simulation for the poly-axial experiment simulation with K_z = 2/3 and K_r = 2/3.

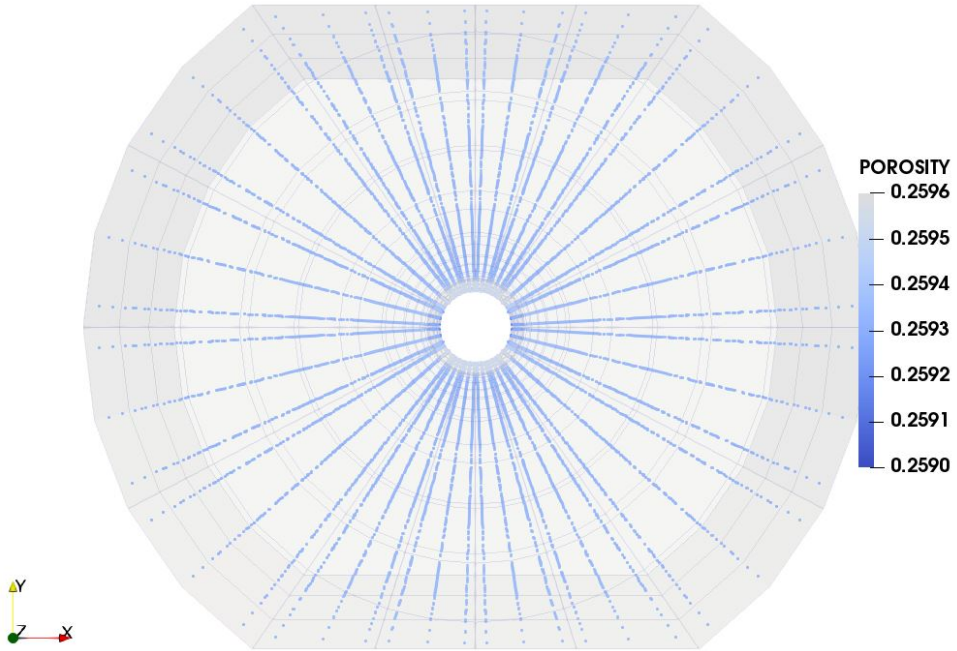

(a)

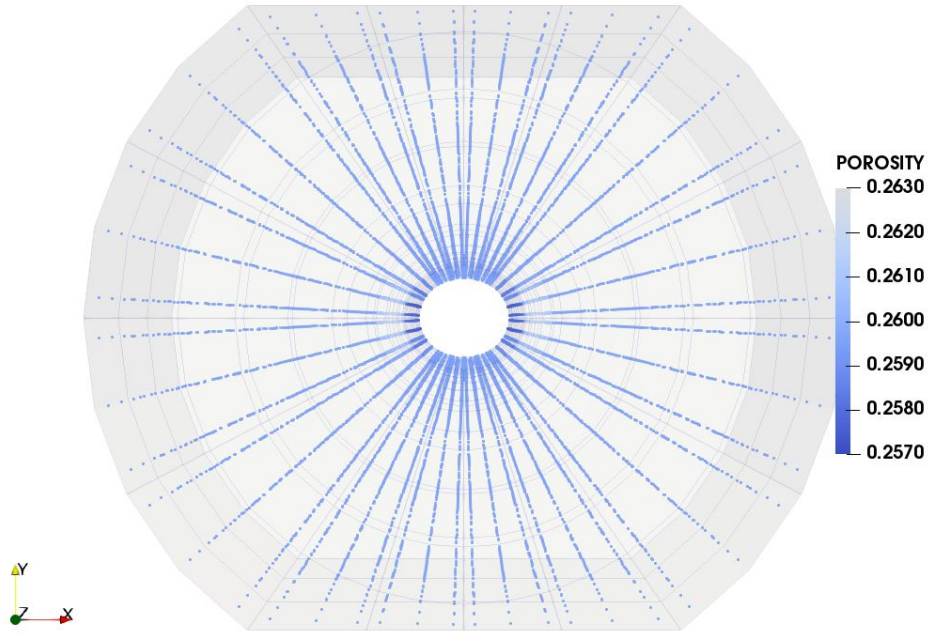

(b)

Figure A.27: Porosity at the onset of sand production (a) and end (b) of simulation for the poly-axial experiment simulation with K_z = 2/3 and K_r = 2/3.

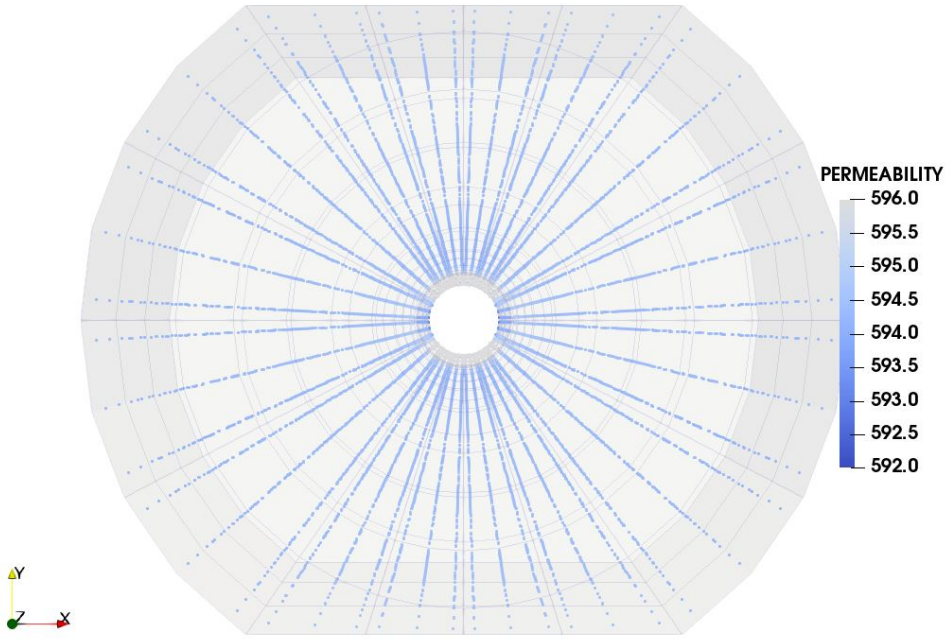

(a)

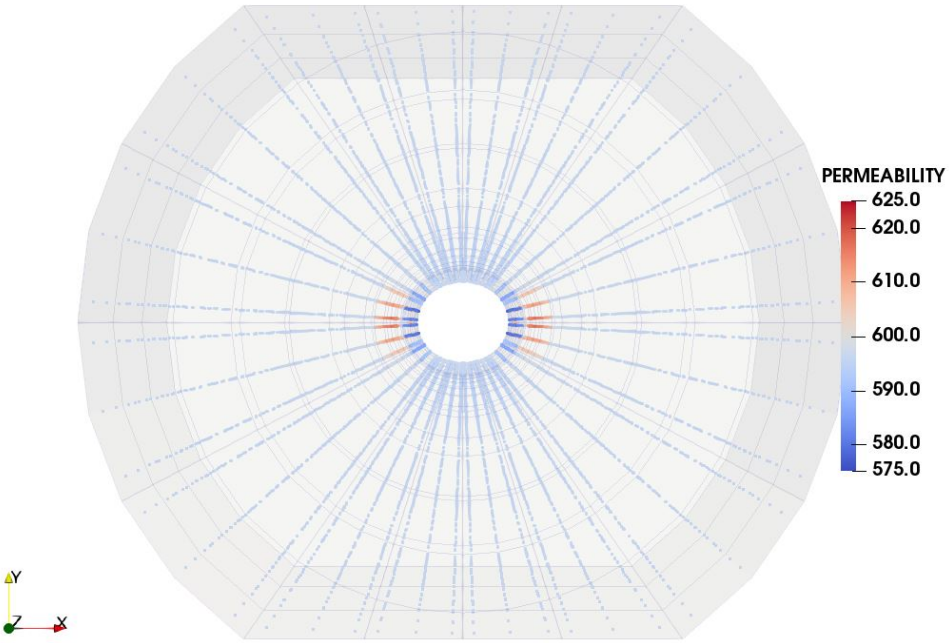

(b)

Figure A.28: Permeability (k_x, k_y and k_z) at the onset of sand production (a) and end (b) of simulation for the poly-axial experiment simulation with K_z = 2/3 and K_r = 2/3.

A.4 Case 04 - K_z = 4/3, K_r = 2/3

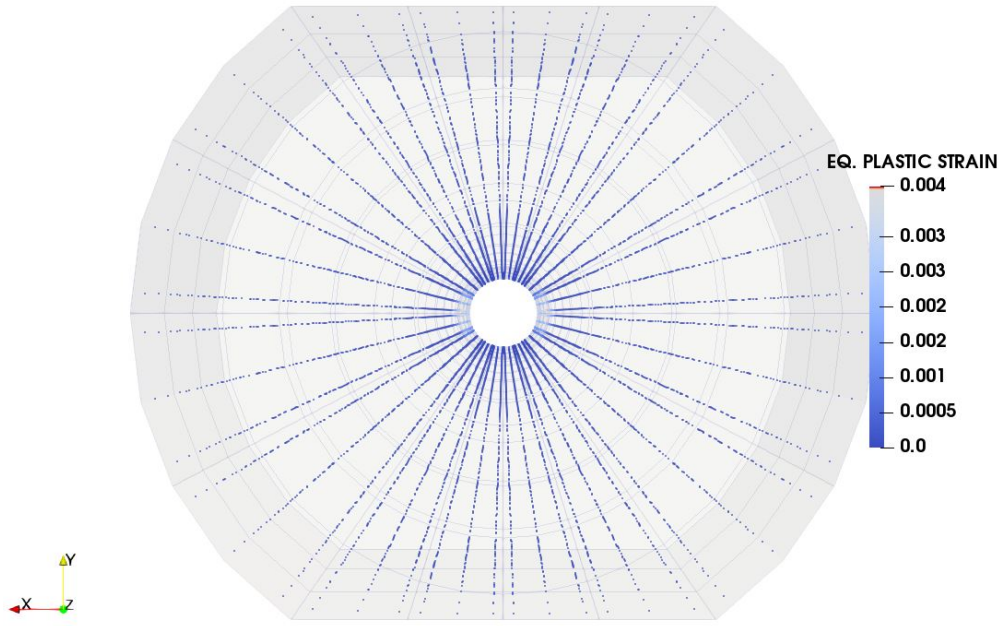

(a)

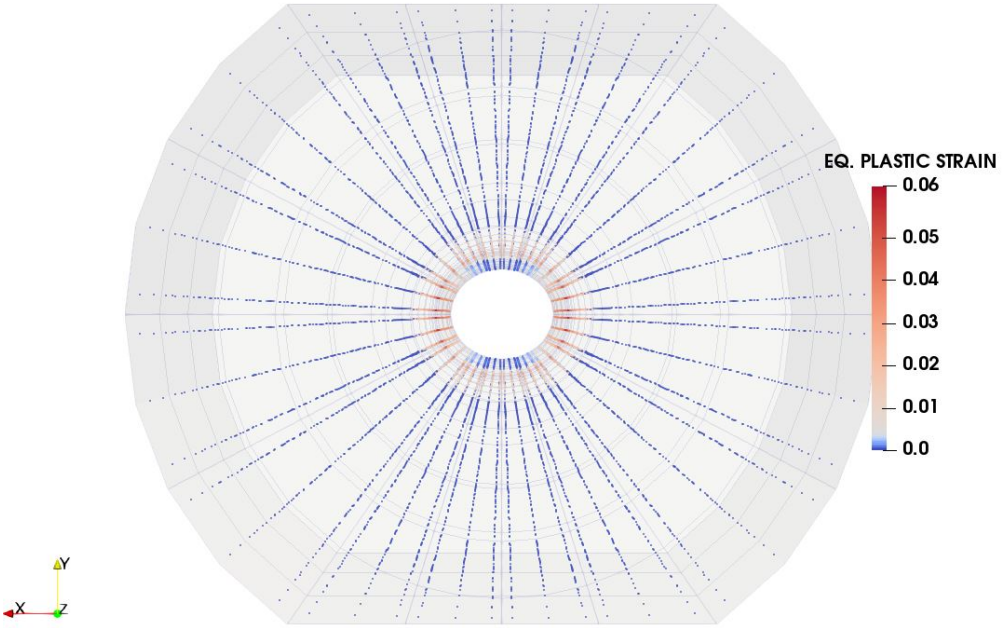

(b)

Figure A.29: ε^p at the onset of sand production (a) and end (b) of simulation for the poly-axial experiment simulation with K_z = 4/3 and K_r = 2/3.

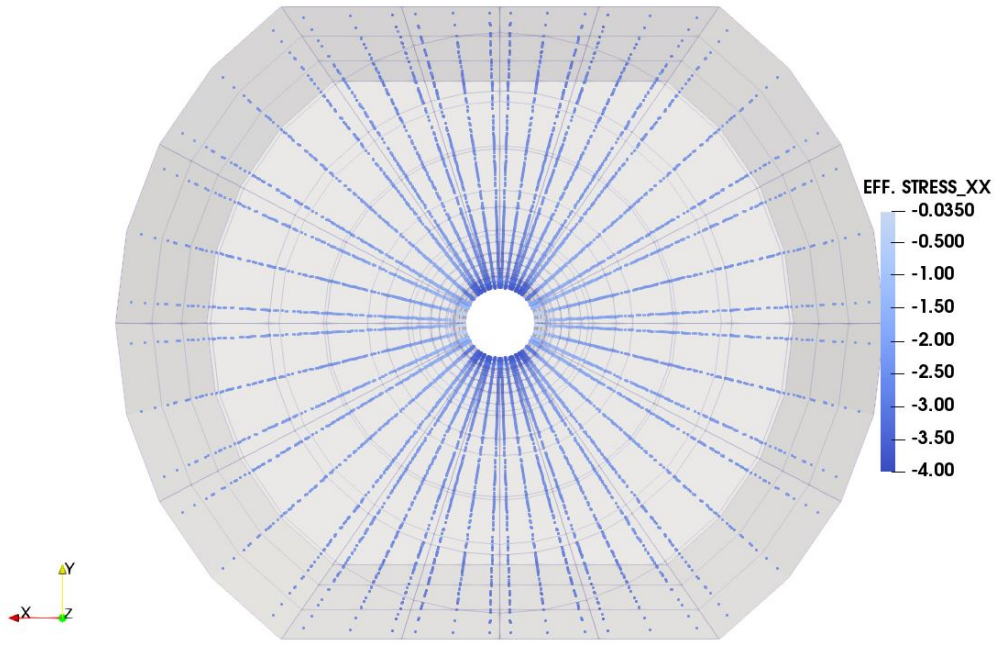

(a)

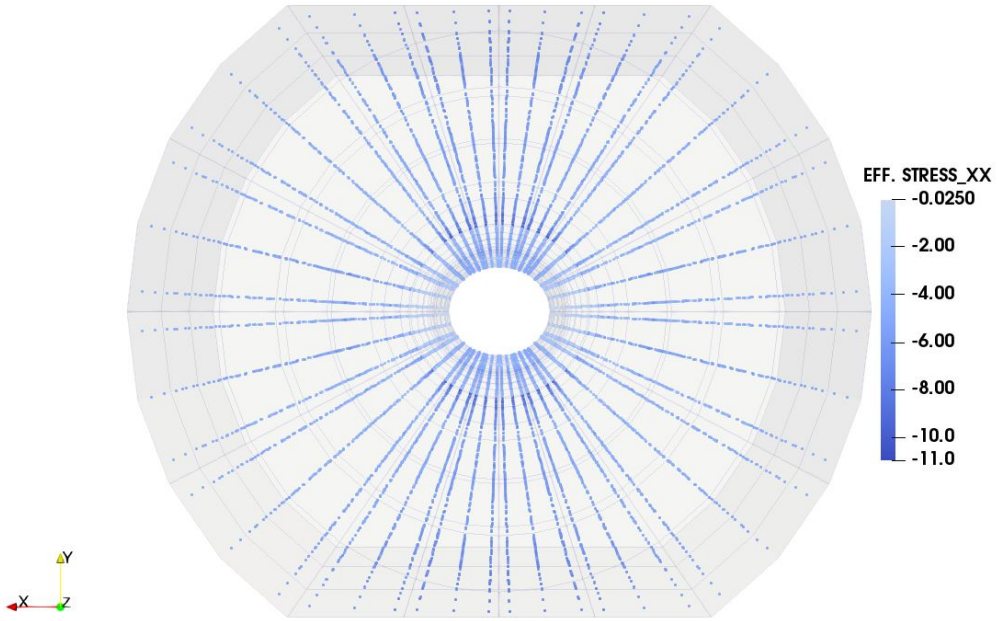

(b)

Figure A.30: σ^e_{xx} at the onset of sand production (a) and end (b) of simulation for the poly-axial experiment simulation with K_z = 4/3 and K_r = 2/3.

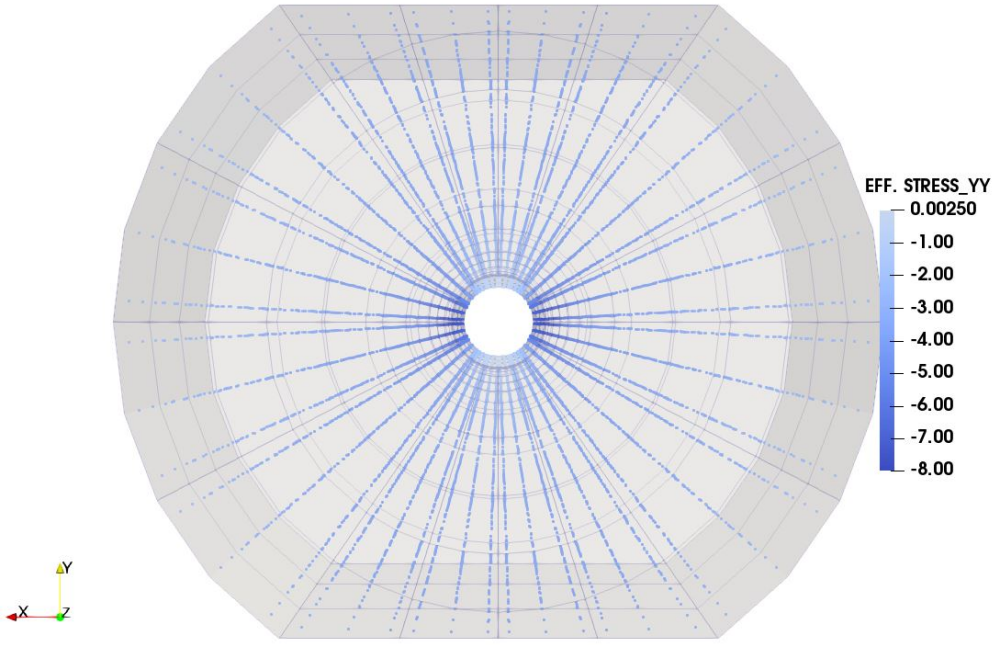

(a)

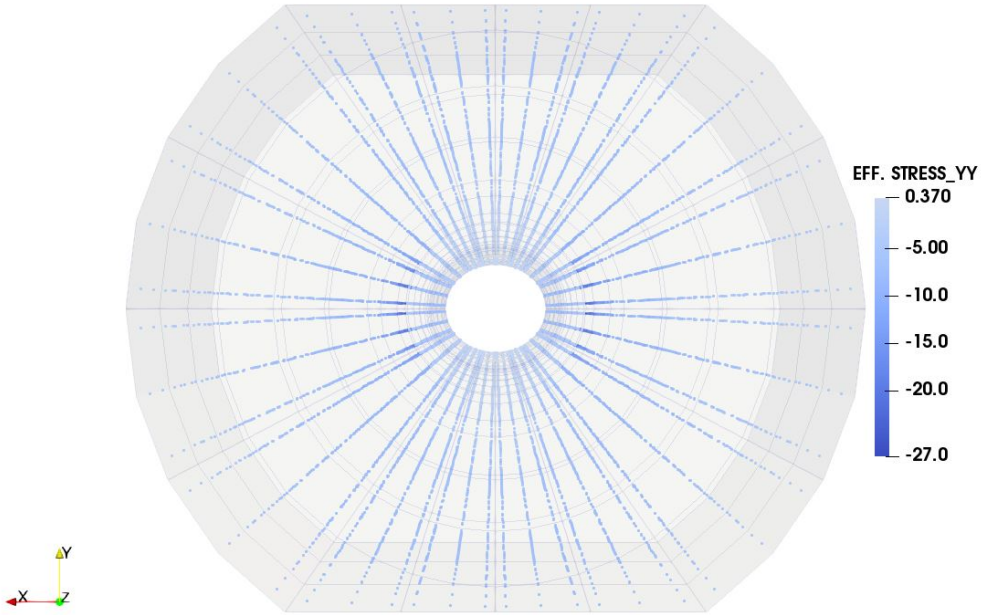

(b)

Figure A.31: σ^e_{yy} at the onset of sand production (a) and end (b) of simulation for the poly-axial experiment simulation with K_z = 4/3 and K_r = 2/3.

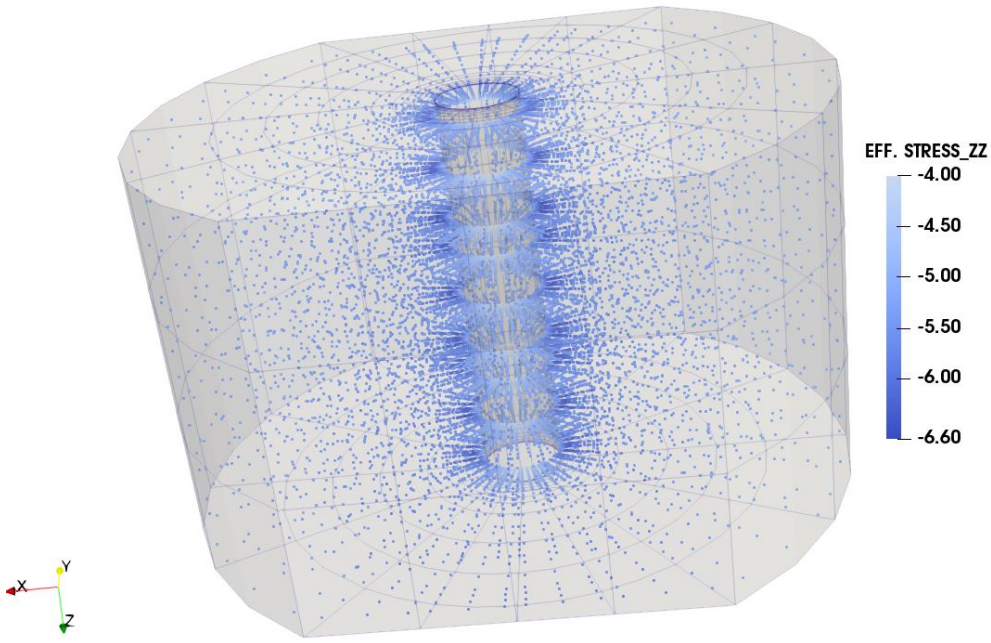

(a)

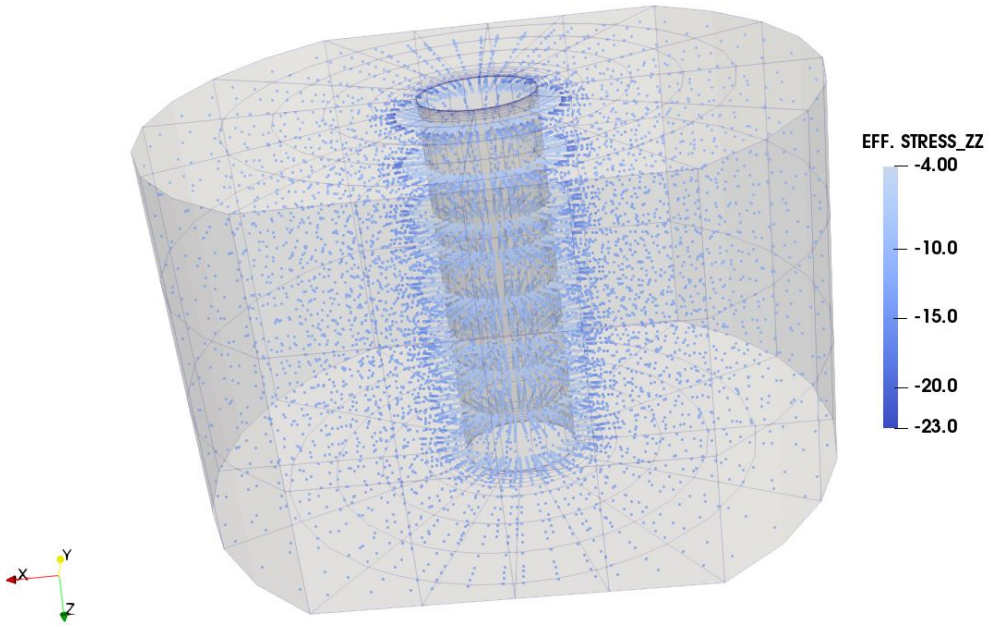

(b)

Figure A.32: σ^e_{zz} at the onset of sand production (a) and end (b) of simulation for the poly-axial experiment simulation with K_z = 4/3 and K_r = 2/3.

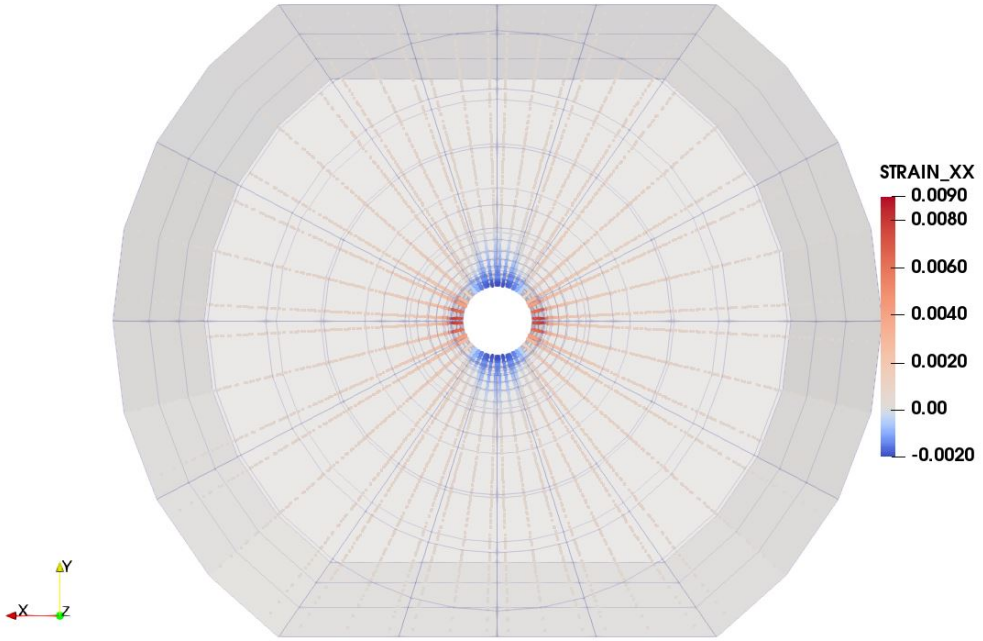

(a)

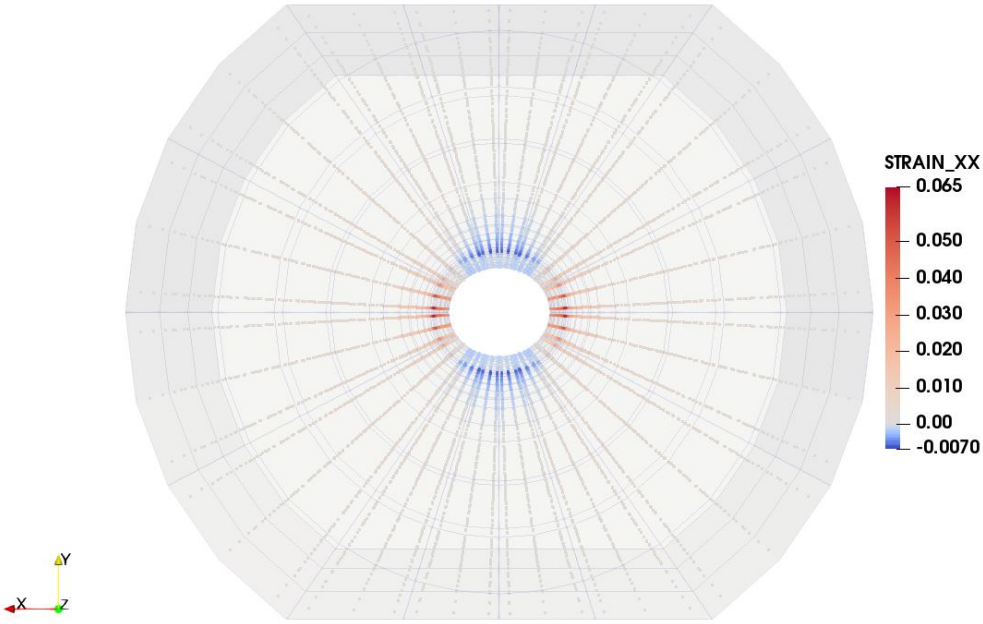

(b)

Figure A.33: ε_{xx} at the onset of sand production (a) and end (b) of simulation for the poly-axial experiment simulation with K_z = 4/3 and K_r = 2/3.

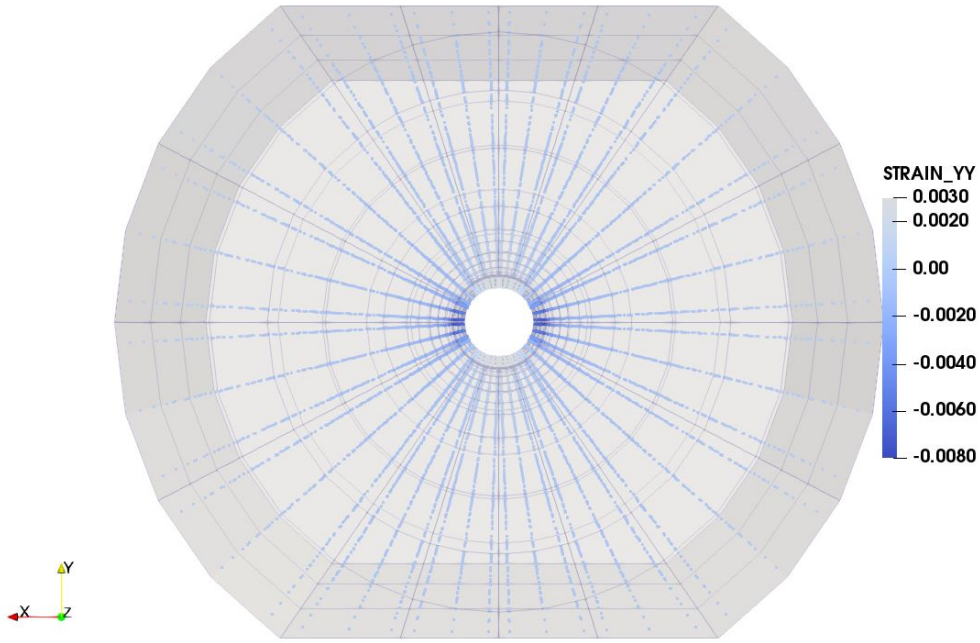

(a)

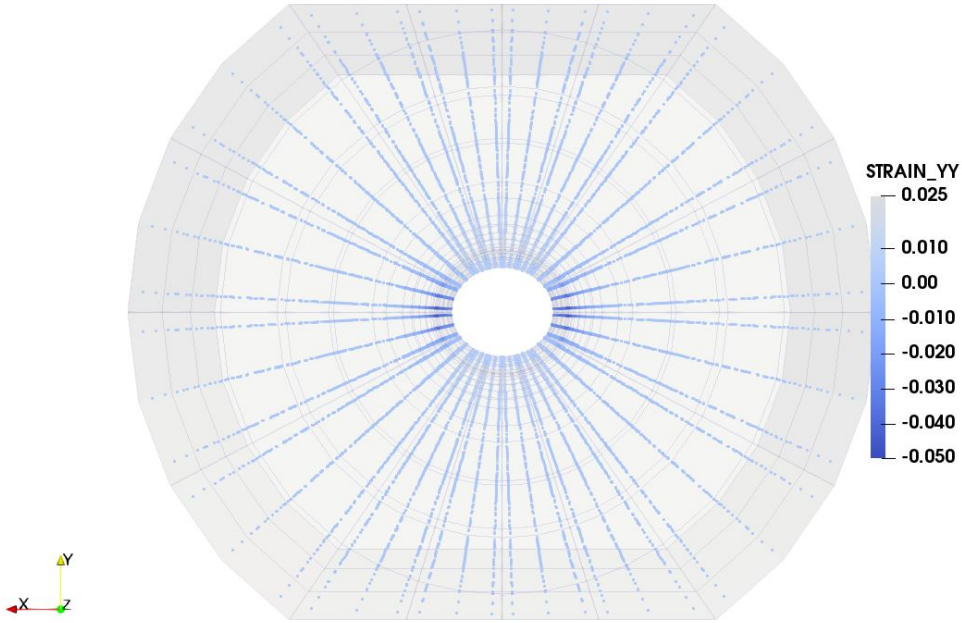

(b)

Figure A.34: ε_{yy} at the onset of sand production (a) and end (b) of simulation for the poly-axial experiment simulation with K_z = 4/3 and K_r = 2/3.

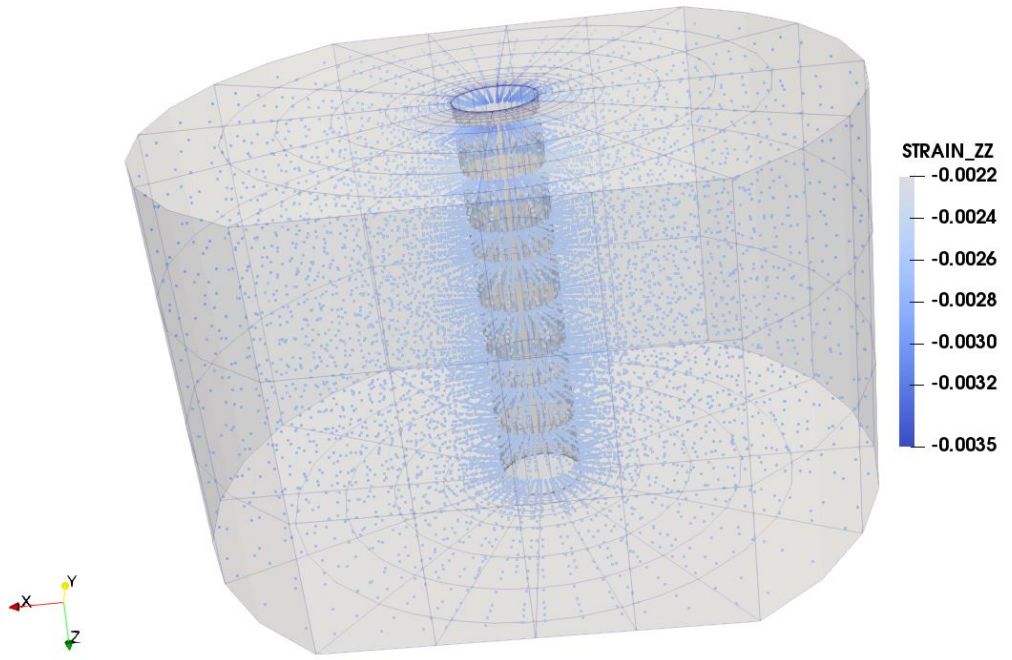

(a)

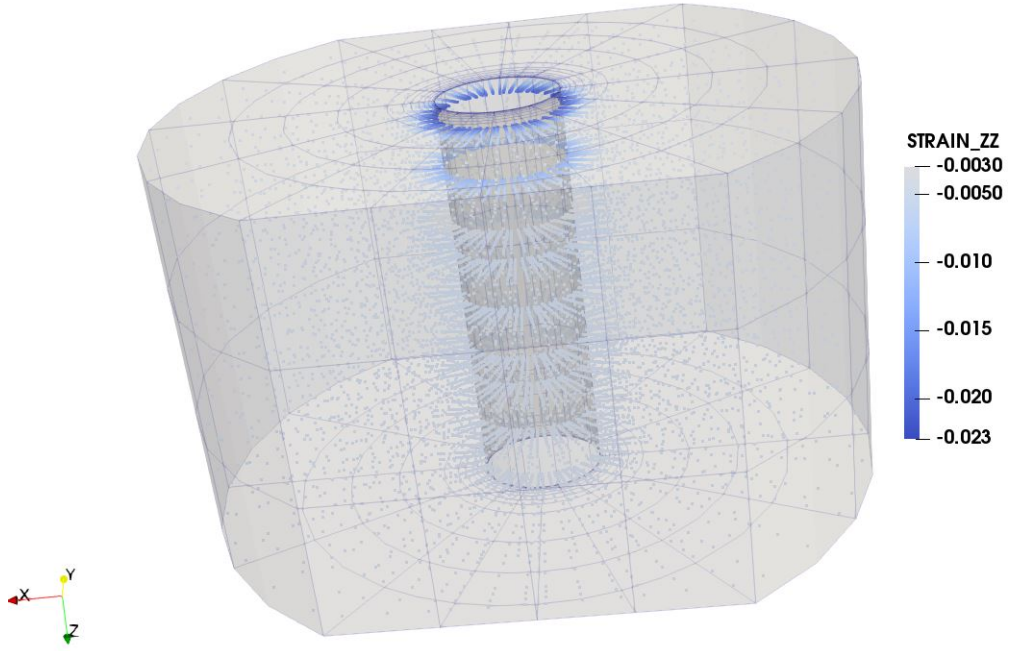

(b)

Figure A.35: ε_{zz} at the onset of sand production (a) and end (b) of simulation for the poly-axial experiment simulation with K_z = 4/3 and K_r = 2/3.

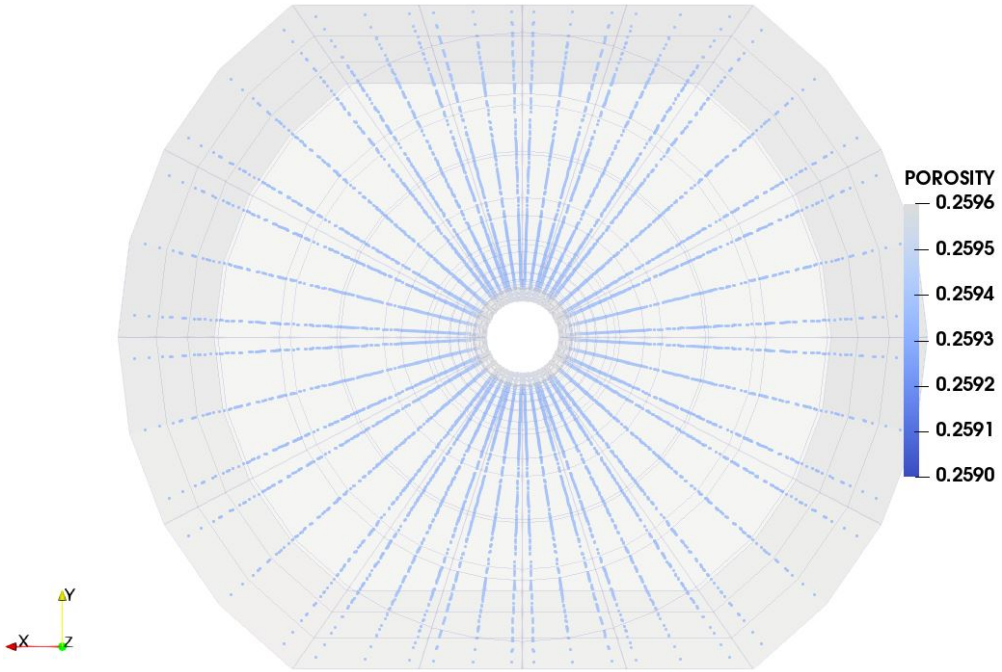

(a)

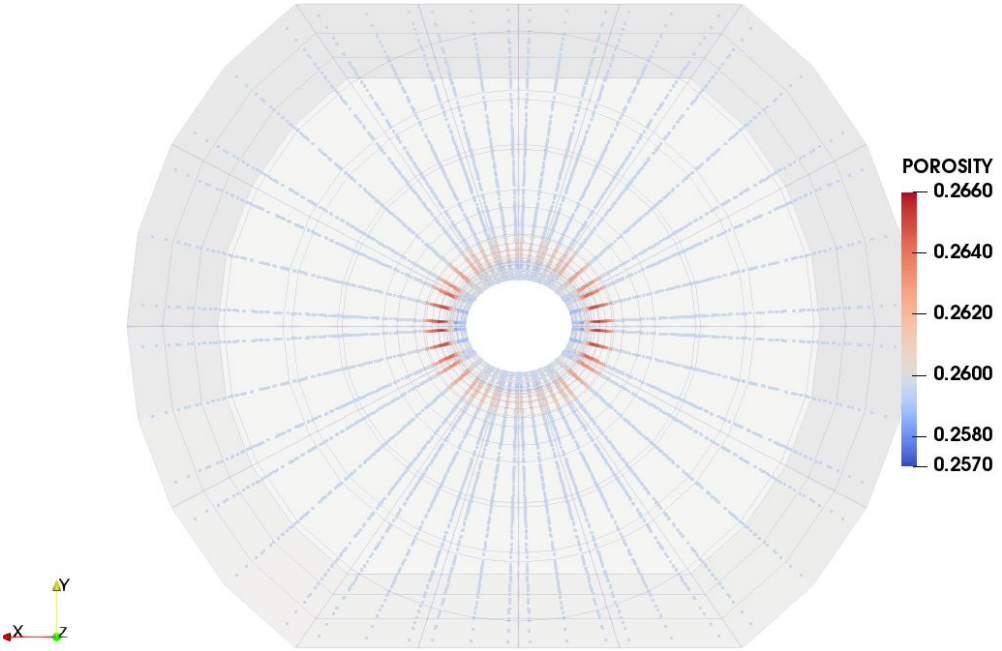

(b)

Figure A.36: Porosity at the onset of sand production (a) and end (b) of simulation for the poly-axial experiment simulation with K_z = 4/3 and K_r = 2/3.

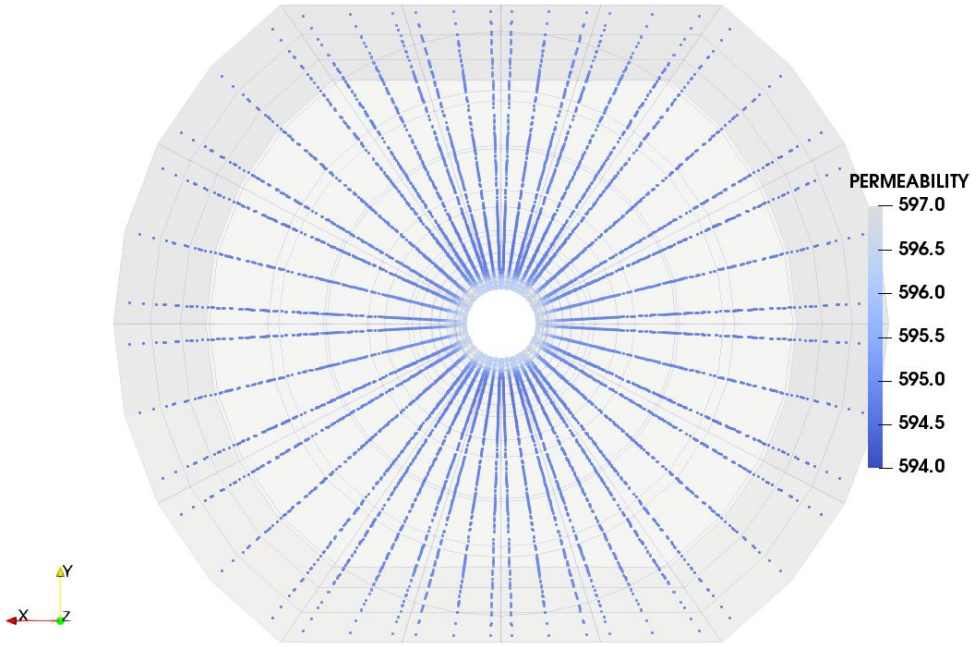

(a)

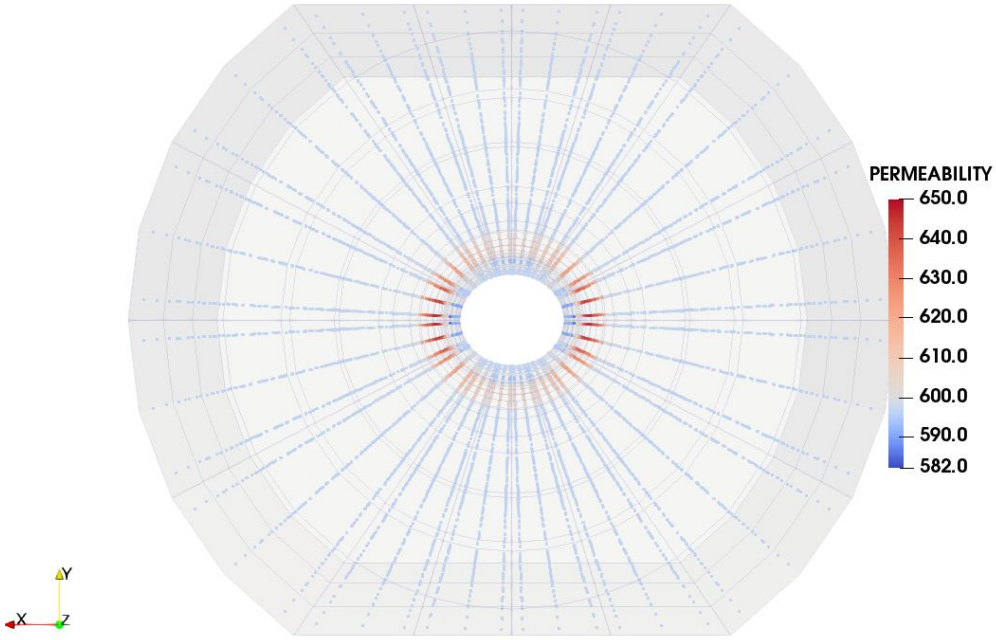

(b)

Figure A.37: Permeability (k_x, k_y and k_z) at the onset of sand production (a) and end (b) of simulation for the poly-axial experiment simulation with K_z = 4/3 and K_r = 2/3.

A.5 Case 05 - K_z = 2, K_r = 2/3

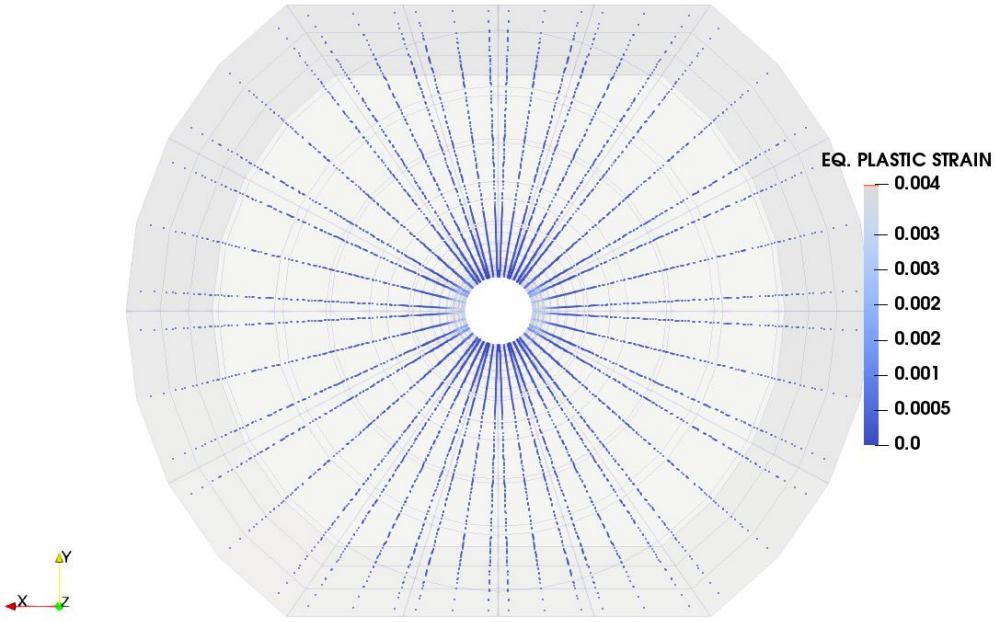

(a)

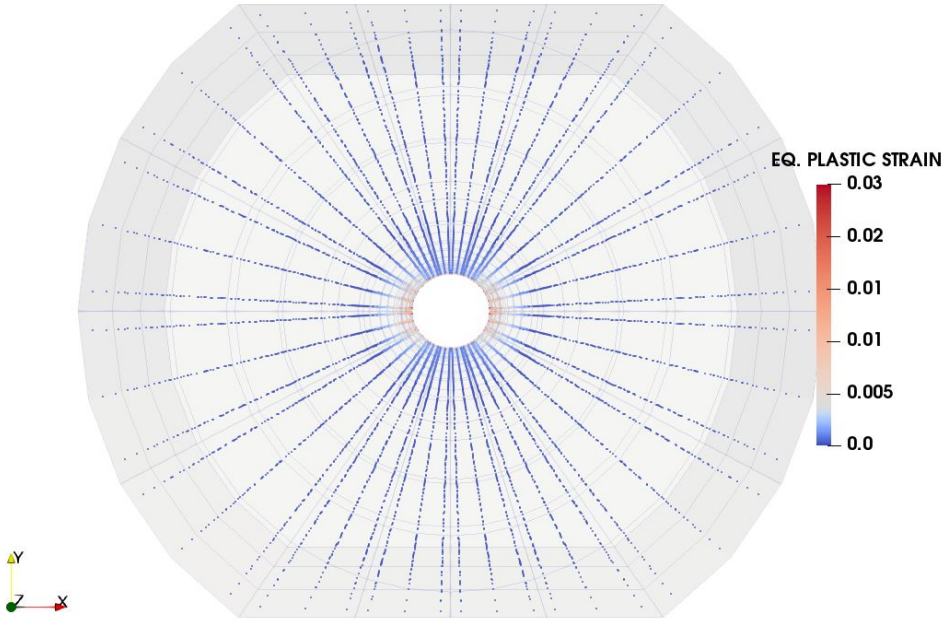

(b)

Figure A.38: ε^p at the onset of sand production (a) and end (b) of simulation for the poly-axial experiment simulation with K_z = 2 and K_r = 2/3.

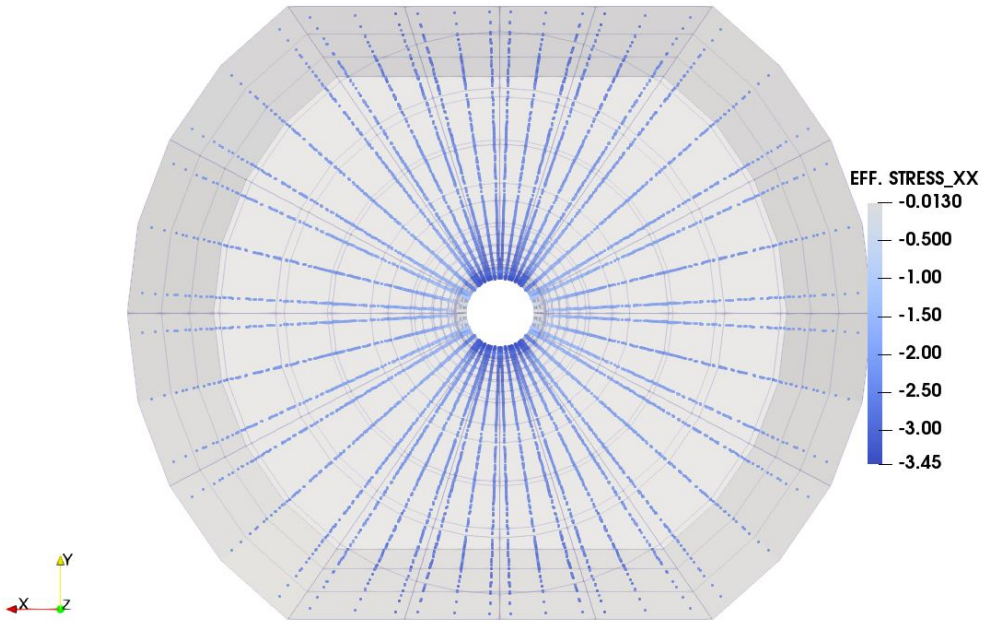

(a)

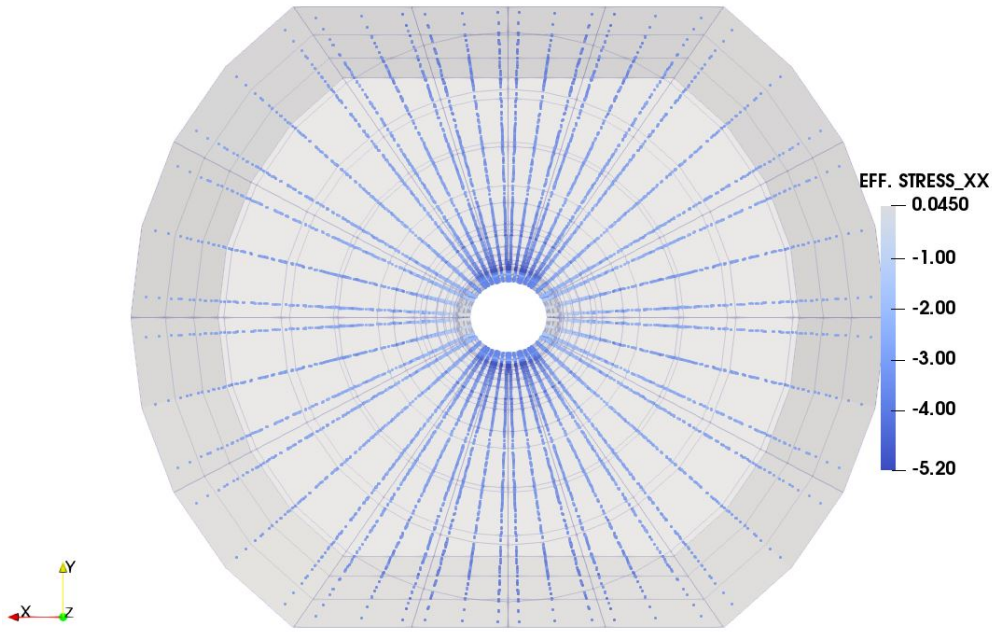

(b)

Figure A.39: σ^e_{xx} at the onset of sand production (a) and end (b) of simulation for the poly-axial experiment simulation with K_z = 2 and K_r = 2/3.

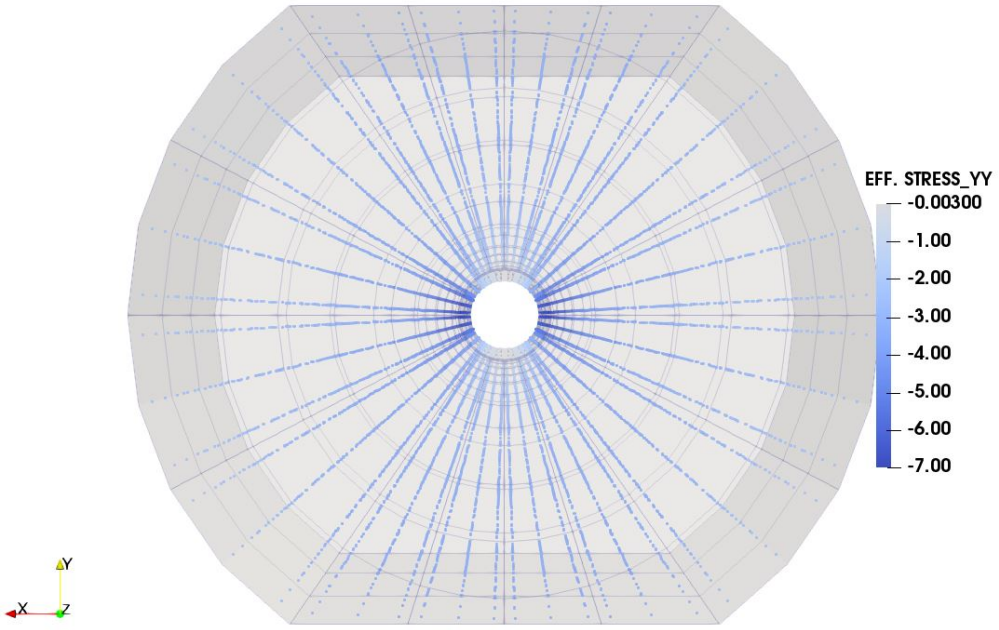

(a)

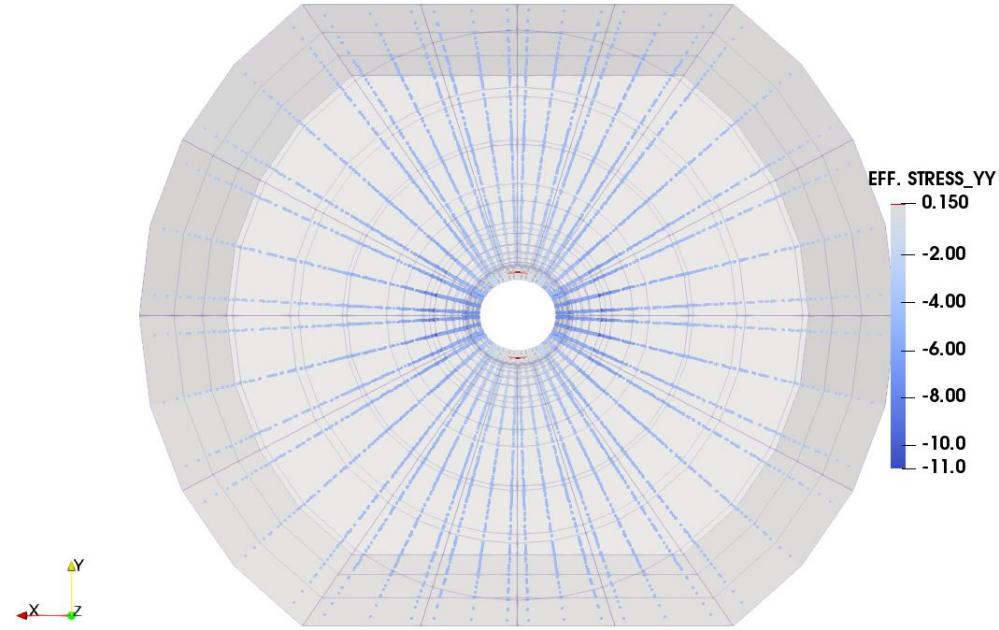

(b)

Figure A.40: σ^e_{yy} at the onset of sand production (a) and end (b) of simulation for the poly-axial experiment simulation with K_z = 2 and K_r = 2/3.

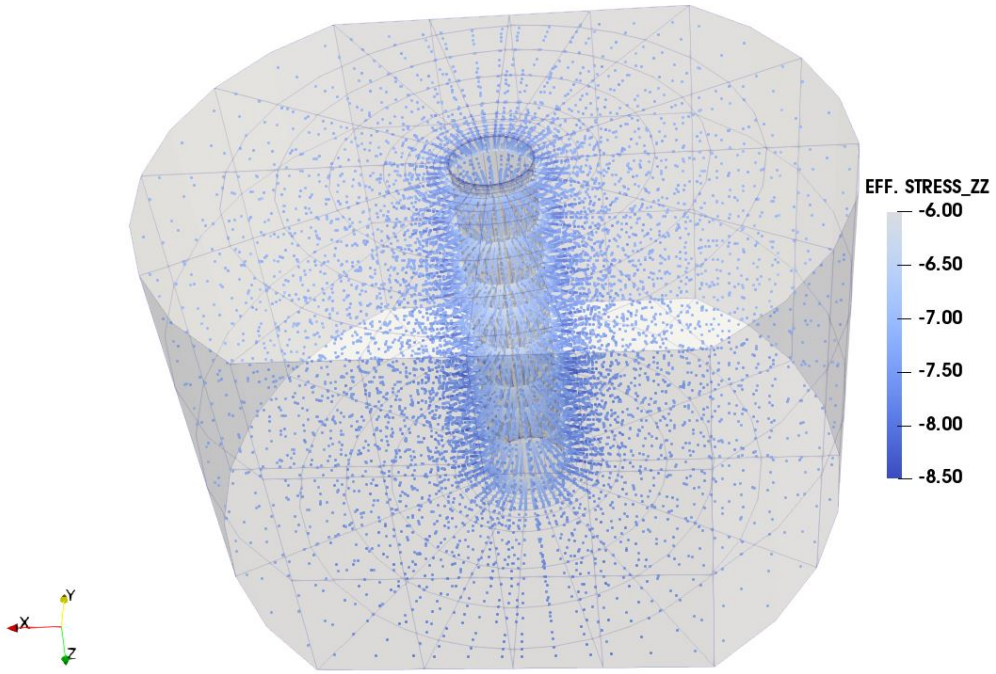

(a)

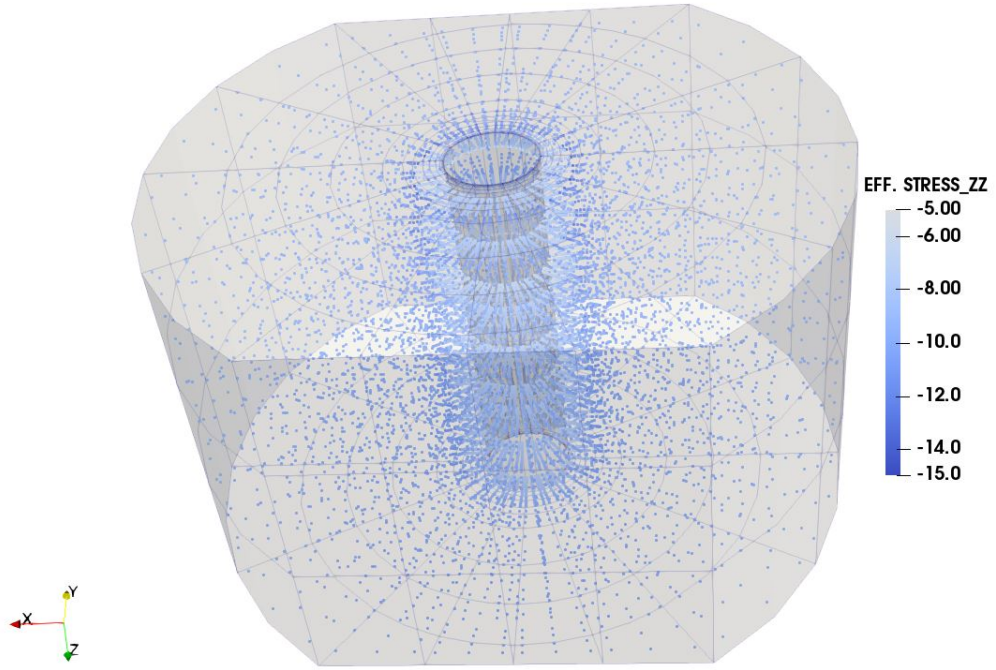

(b)

Figure A.41: σ^e_{zz} at the onset of sand production (a) and end (b) of simulation for the poly-axial experiment simulation with K_z = 2 and K_r = 2/3.

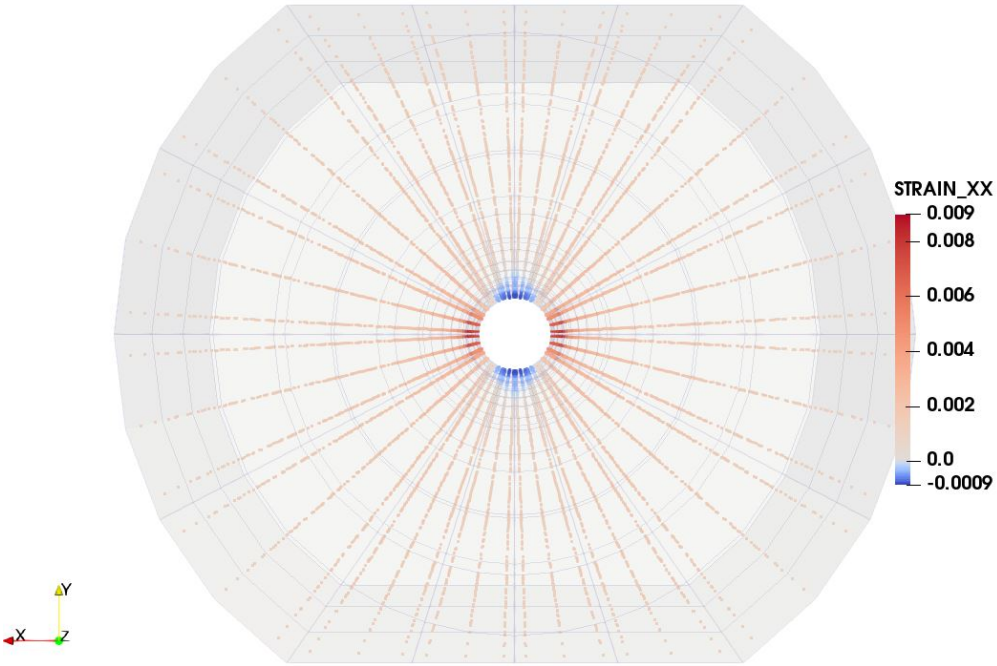

(a)

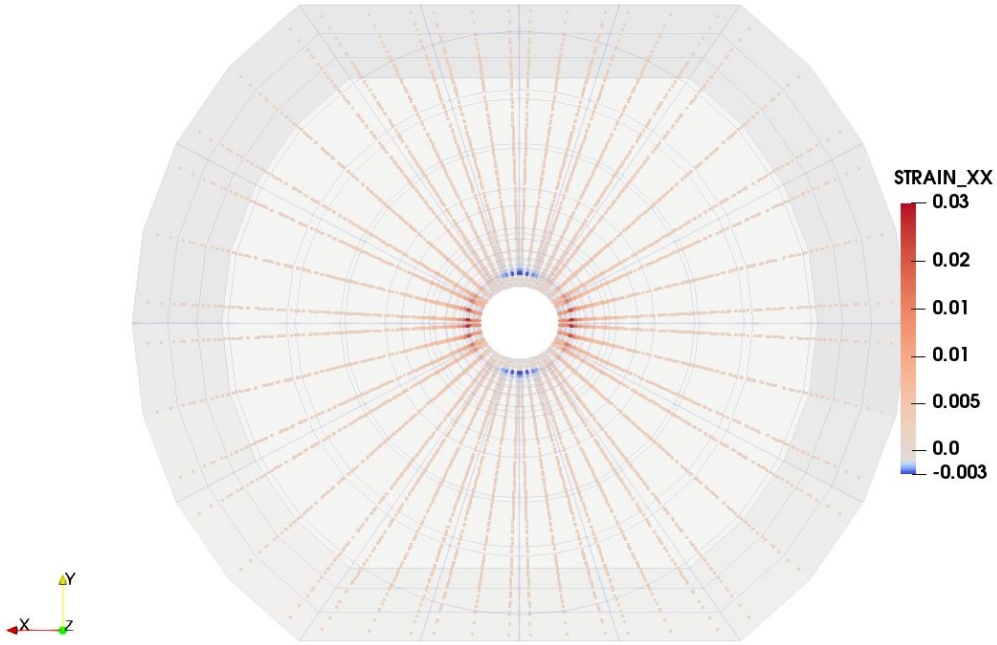

(b)

Figure A.42: ε_{xx} at the onset of sand production (a) and end (b) of simulation for the poly-axial experiment simulation with K_z = 2 and K_r = 2/3.

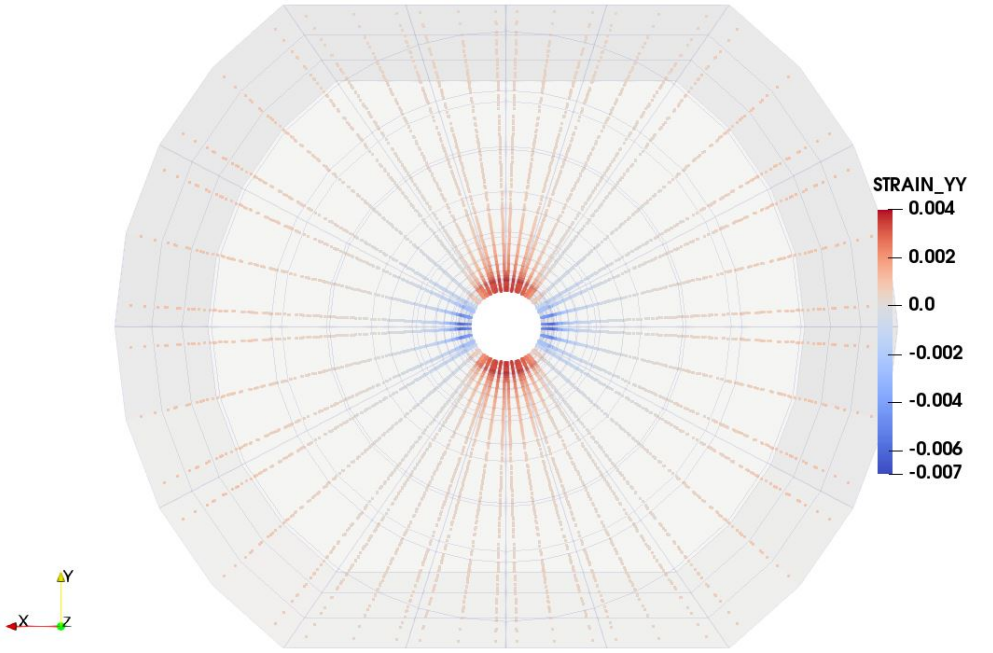

(a)

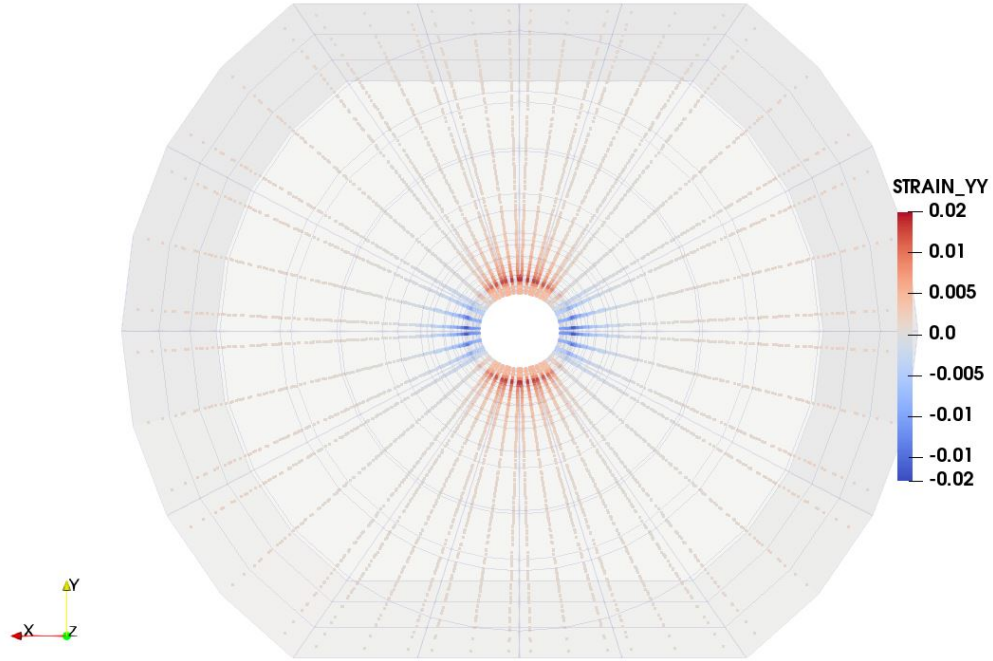

(b)

Figure A.43: ε_{yy} at the onset of sand production (a) and end (b) of simulation for the poly-axial experiment simulation with K_z = 2 and K_r = 2/3.

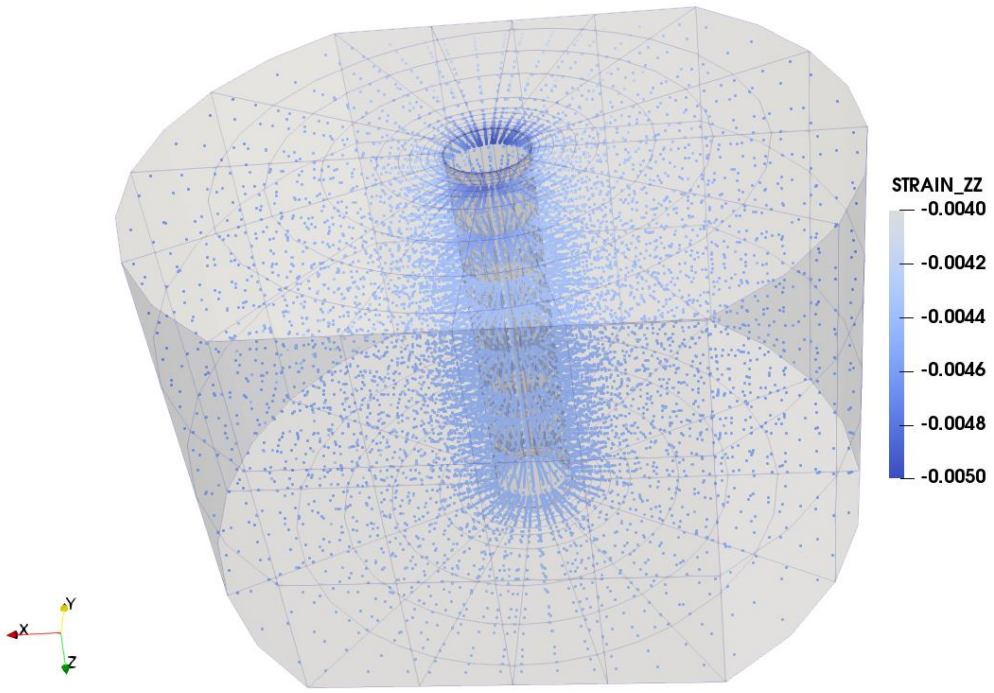

(a)

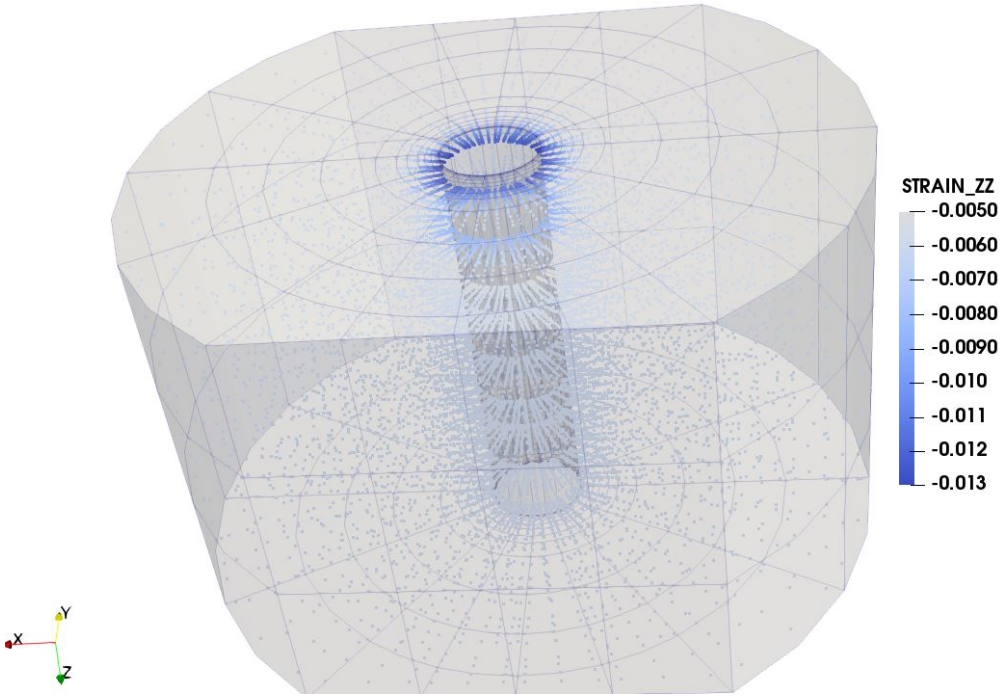

(b)

Figure A.44: ε_{zz} at the onset of sand production (a) and end (b) of simulation for the poly-axial experiment simulation with K_z = 2 and K_r = 2/3.

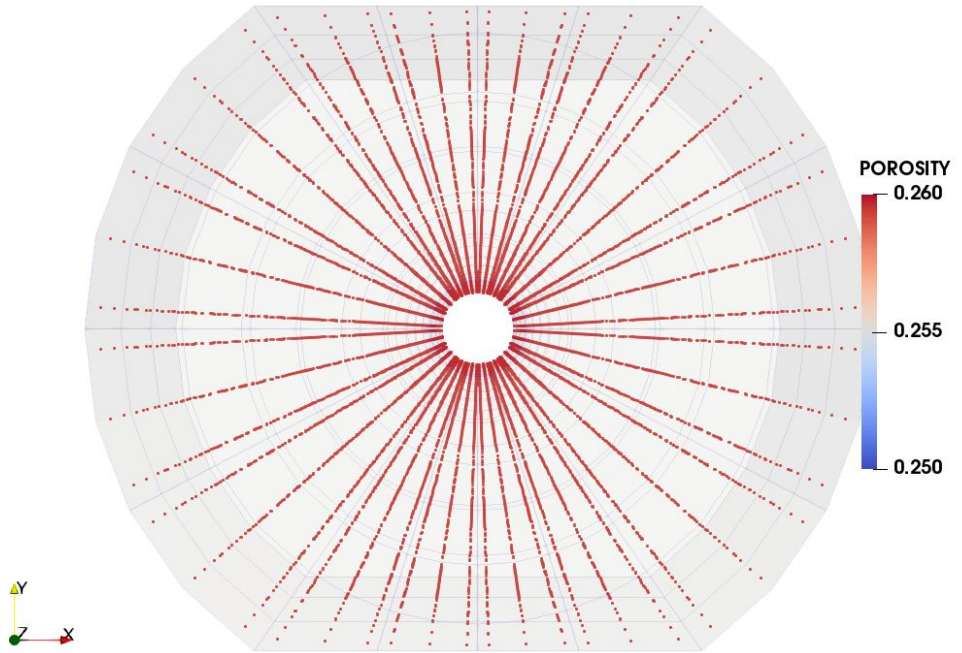

(a)

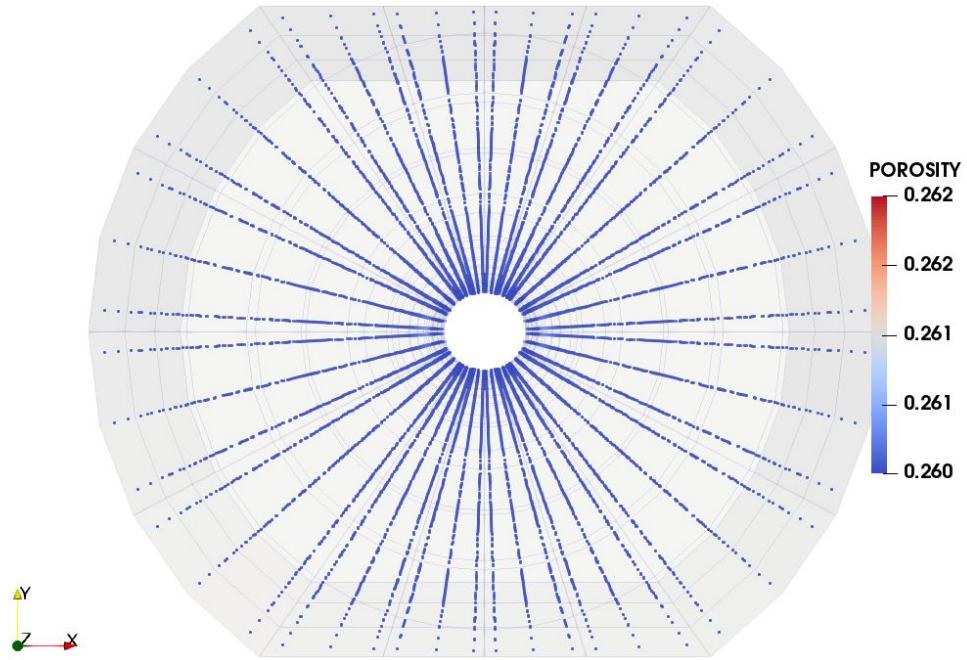

(b)

Figure A.45: Porosity at the onset of sand production (a) and end (b) of simulation for the poly-axial experiment simulation with $K_z = 2$ and $K_r = 2/3$.

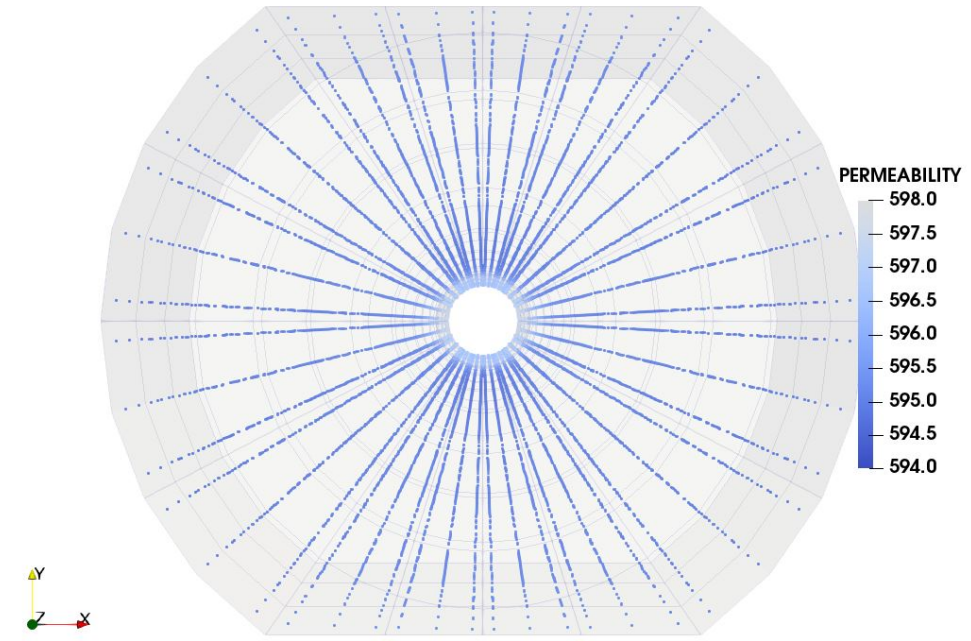

(a)

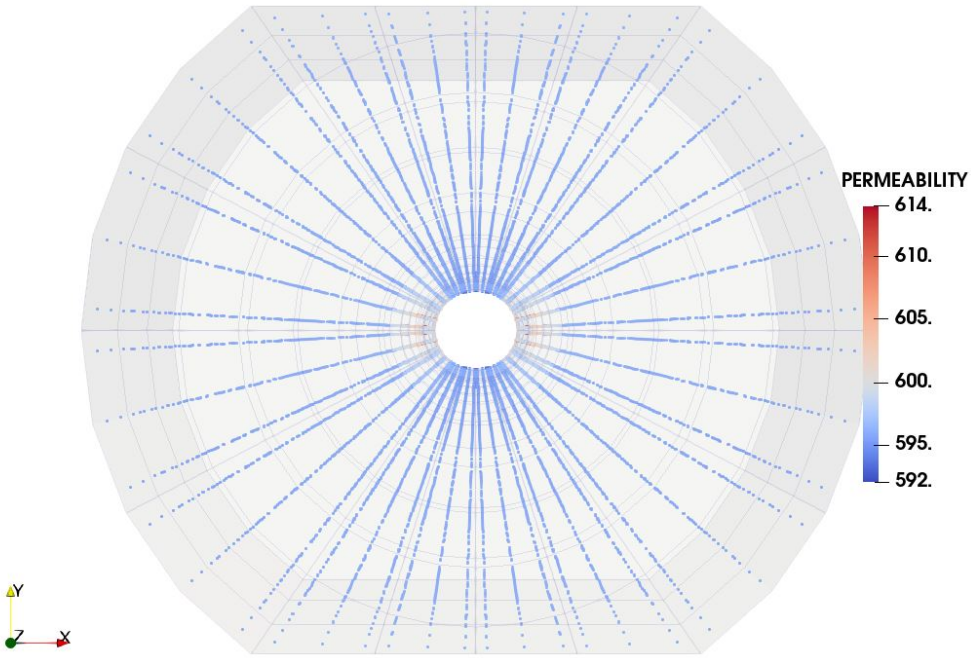

(b)

Figure A.46: Permeability (k_x, k_y and k_z) at the onset of sand production (a) and end (b) of simulation for the poly-axial experiment simulation with K_z = 2 and K_r = 2/3.

A.6 Case 06 - $K_z = 1$, $K_r = 1$

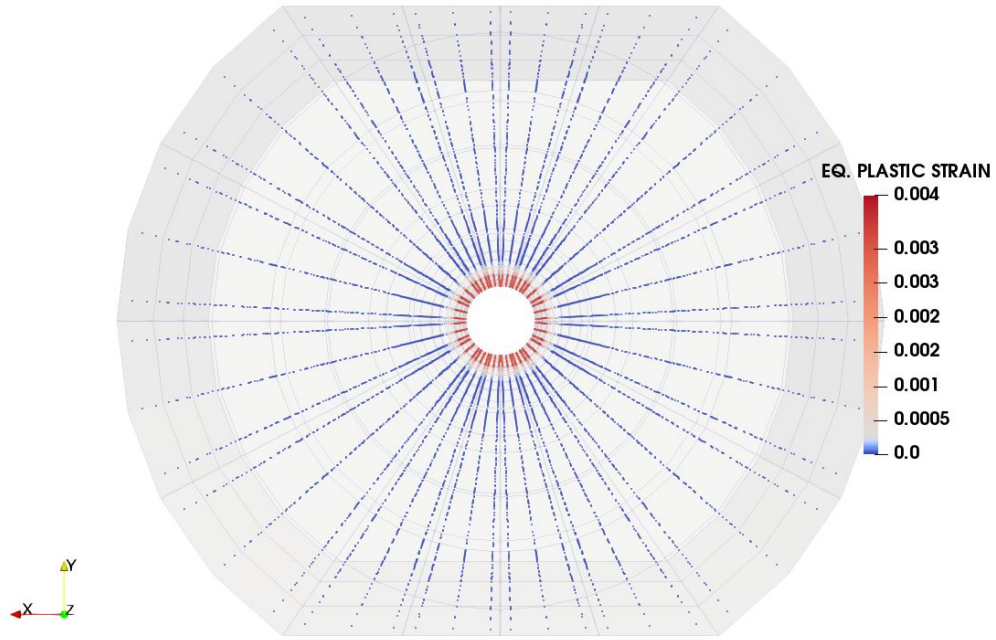

(a)

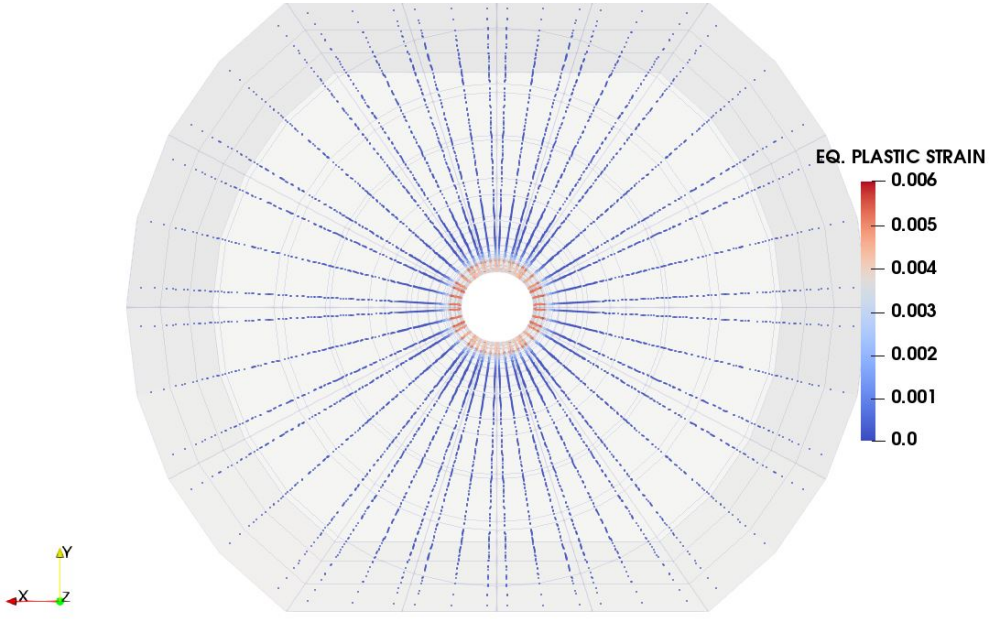

(b)

Figure A.47: ε^p at the onset of sand production (a) and end (b) of simulation for the poly-axial experiment simulation with $K_z = 1$ and $K_r = 1$.

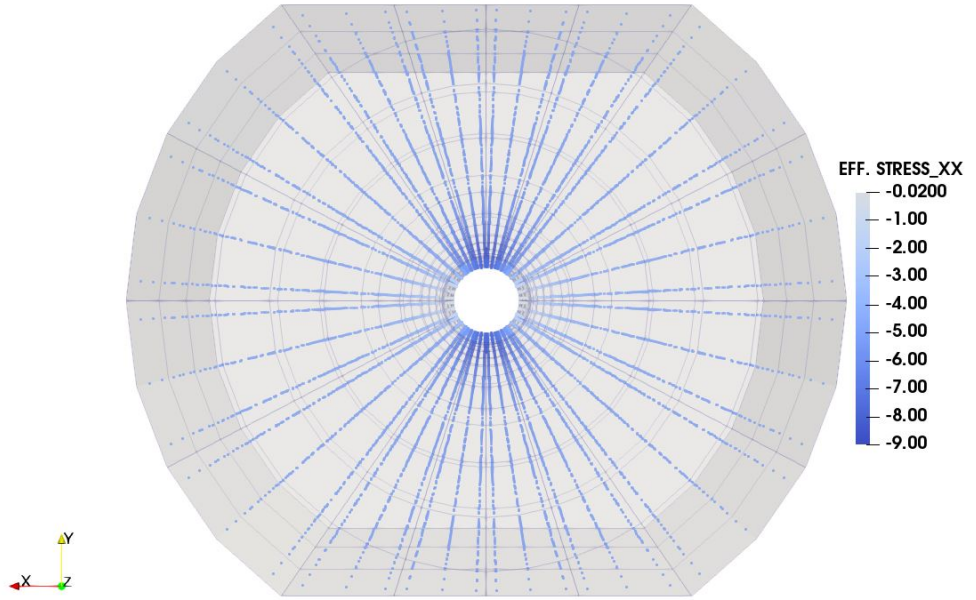

(a)

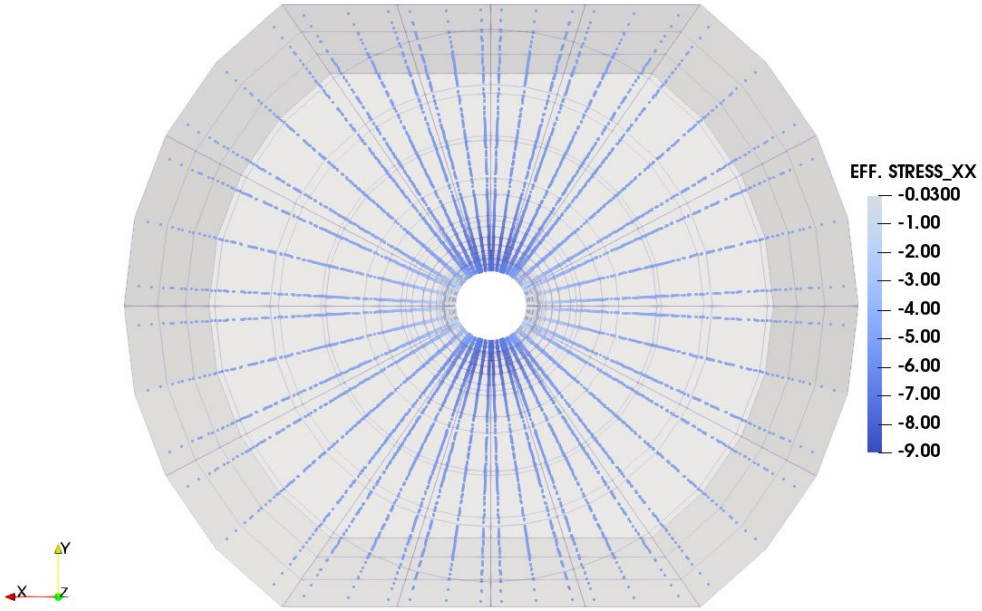

(b)

Figure A.48: σ^e_{xx} at the onset of sand production (a) and end (b) of simulation for the poly-axial experiment simulation with K_z = 1 and K_r = 1.

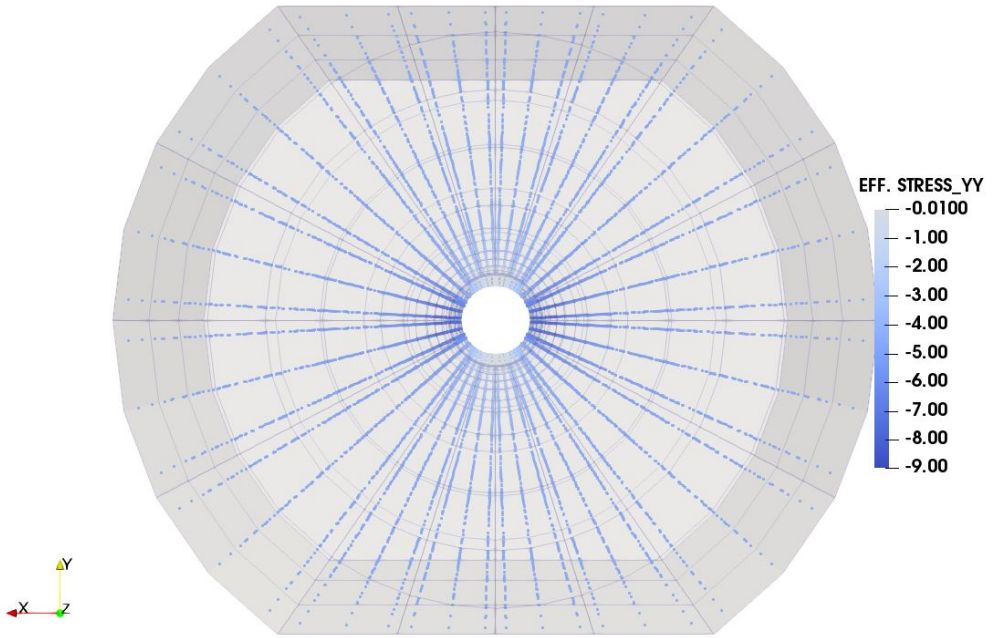

(a)

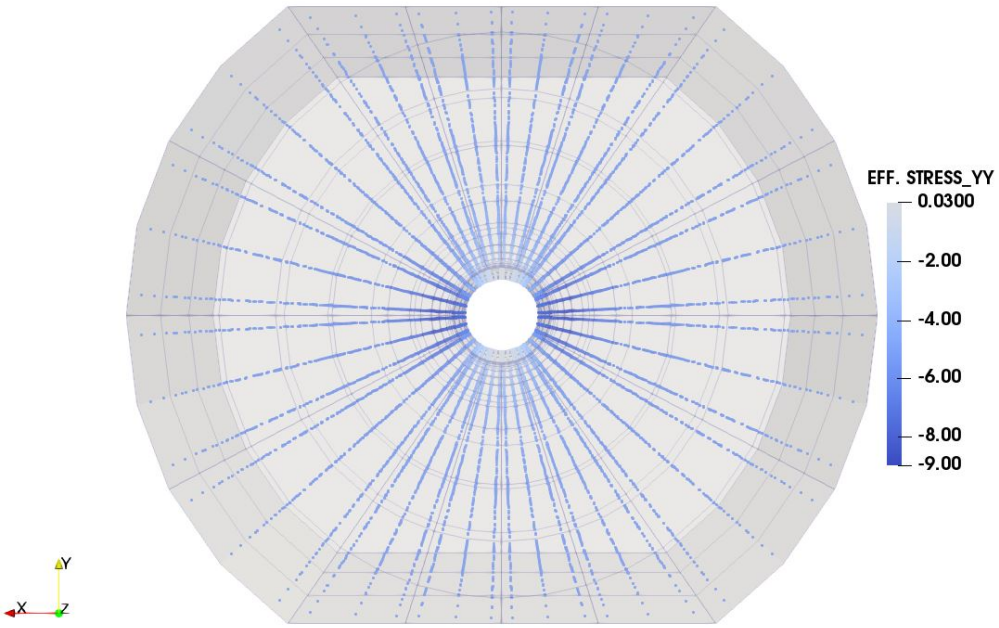

(b)

Figure A.49: σ^e_{yy} at the onset of sand production (a) and end (b) of simulation for the poly-axial experiment simulation with K_z = 1 and K_r = 1.

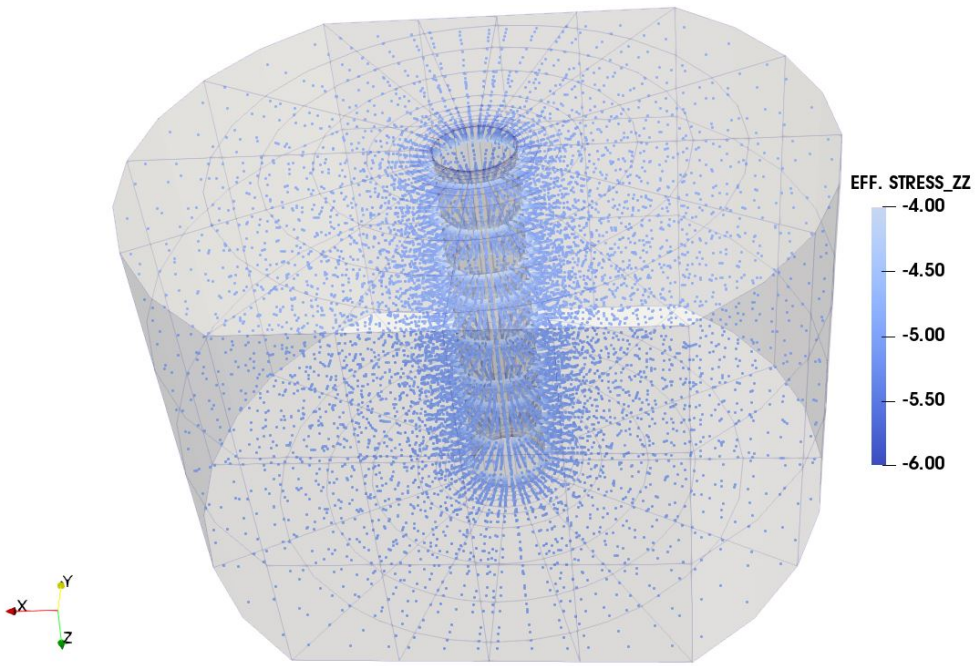

(a)

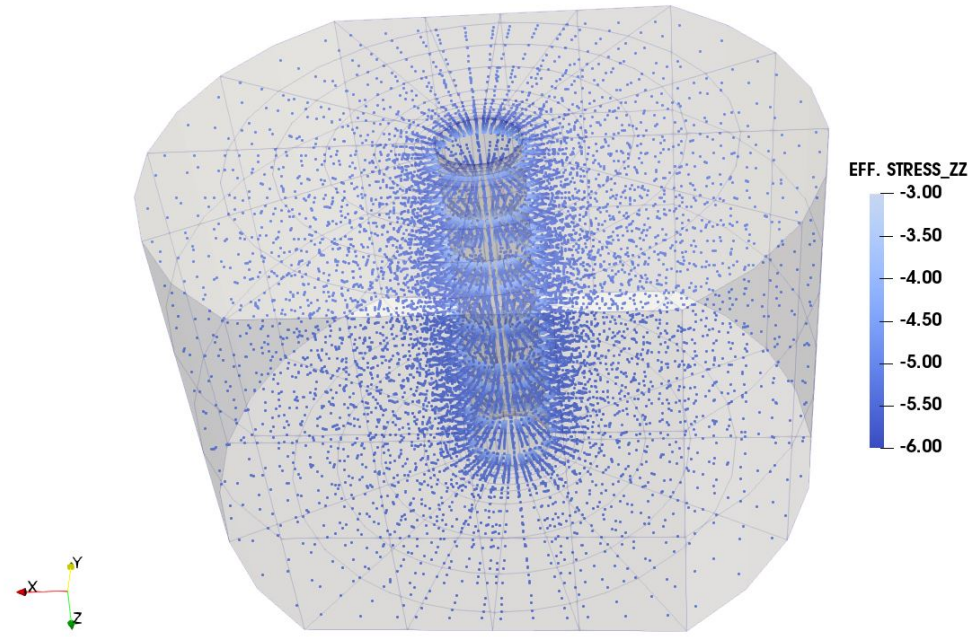

(b)

Figure A.50: σ^e_{zz} at the onset of sand production (a) and end (b) of simulation for the poly-axial experiment simulation with K_z = 1 and K_r = 1.

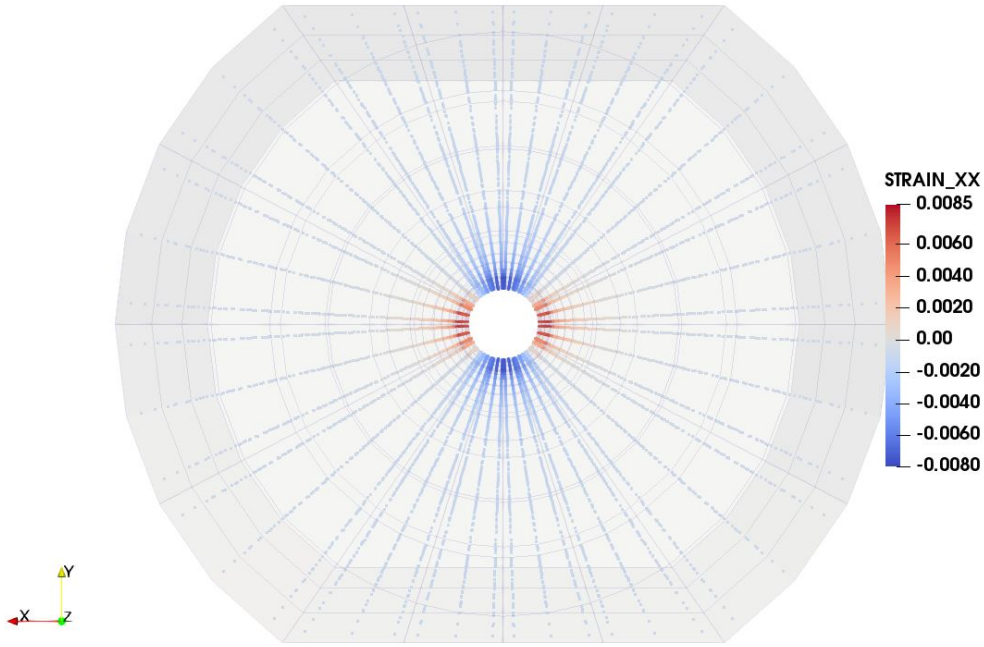

(a)

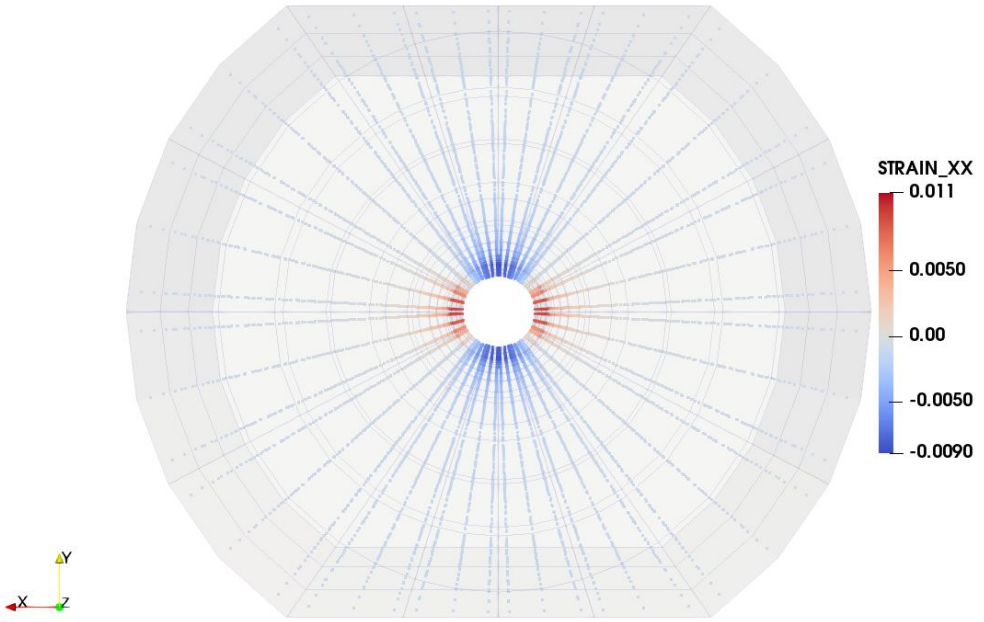

(b)

Figure A.51: ε_{xx} at the onset of sand production (a) and end (b) of simulation for the poly-axial experiment simulation with K_z = 1 and K_r = 1.

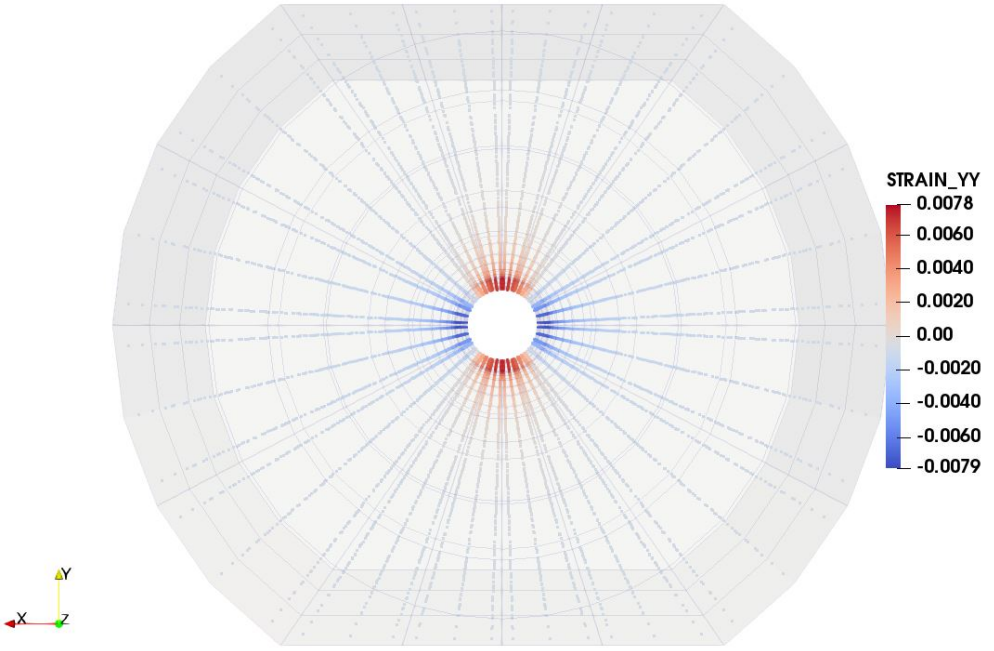

(a)

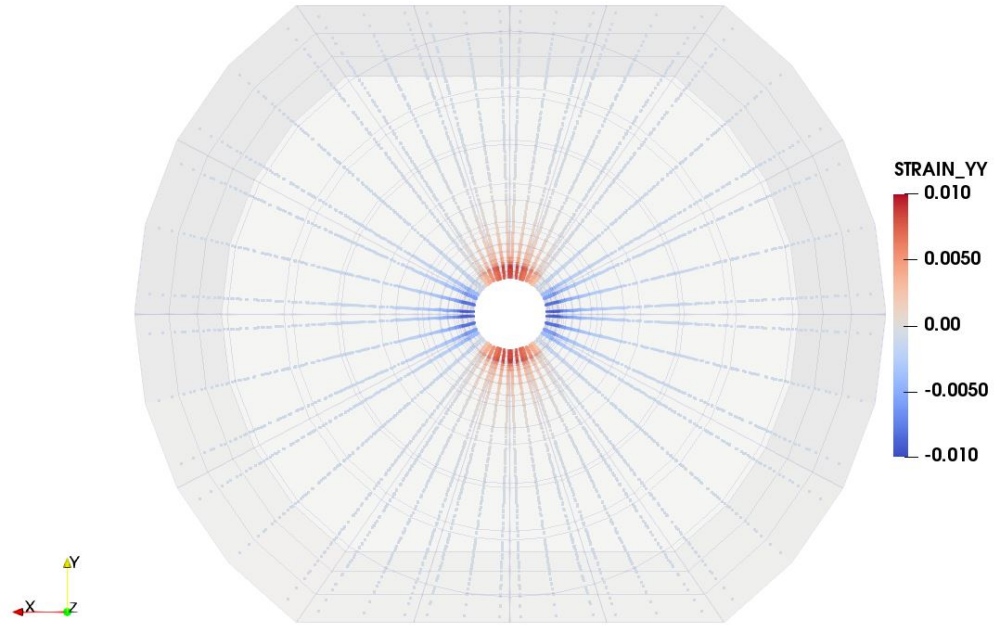

(b)

Figure A.52: ε_{yy} at the onset of sand production (a) and end (b) of simulation for the poly-axial experiment simulation with $K_z = 1$ and $K_r = 1$.

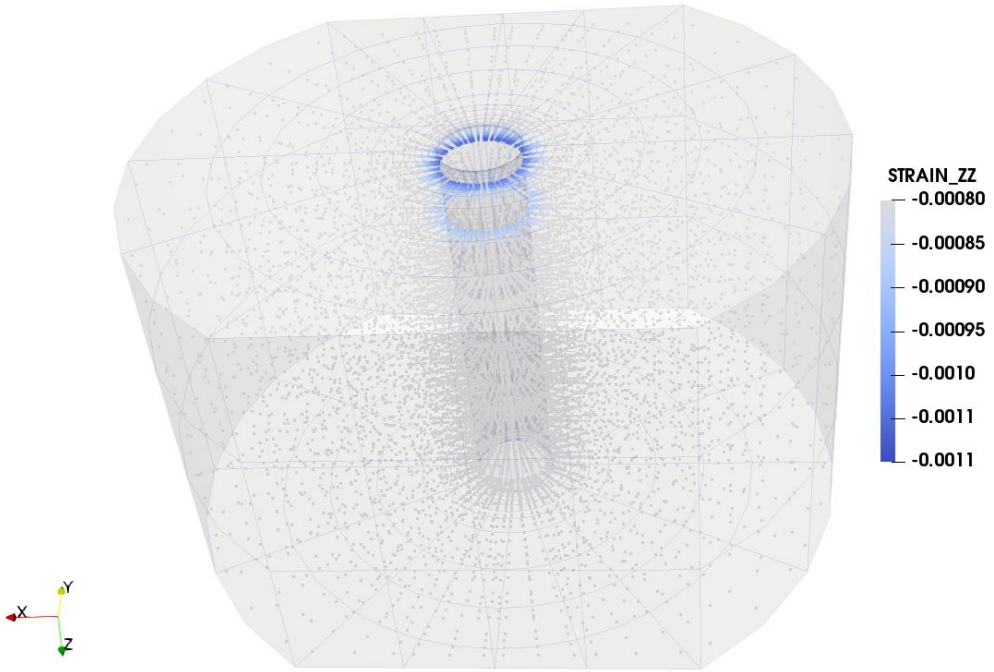

(a)

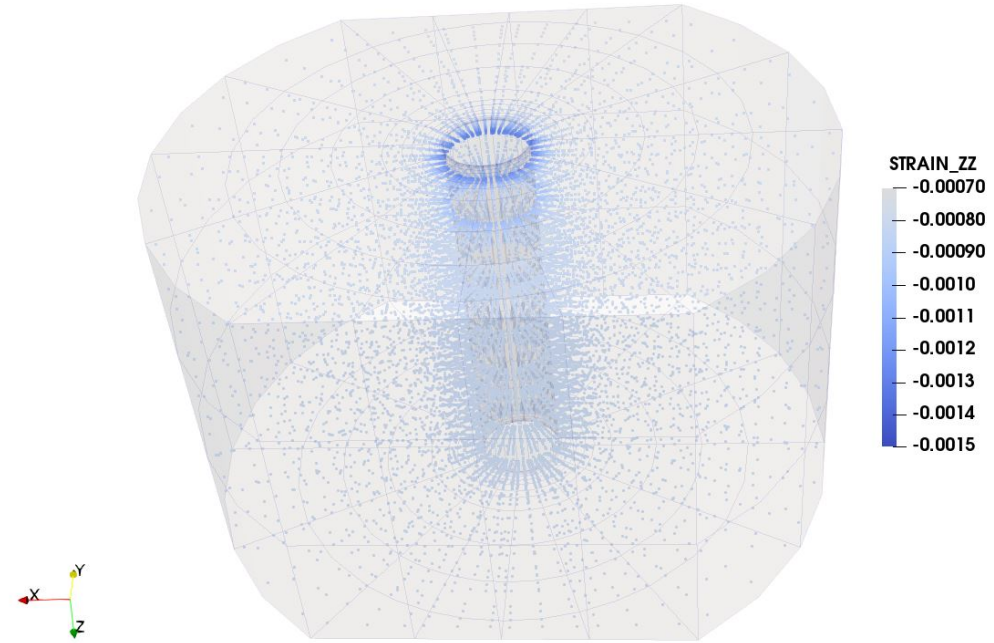

(b)

Figure A.53: ε_{zz} at the onset of sand production (a) and end (b) of simulation for the poly-axial experiment simulation with K_z = 1 and K_r = 1.

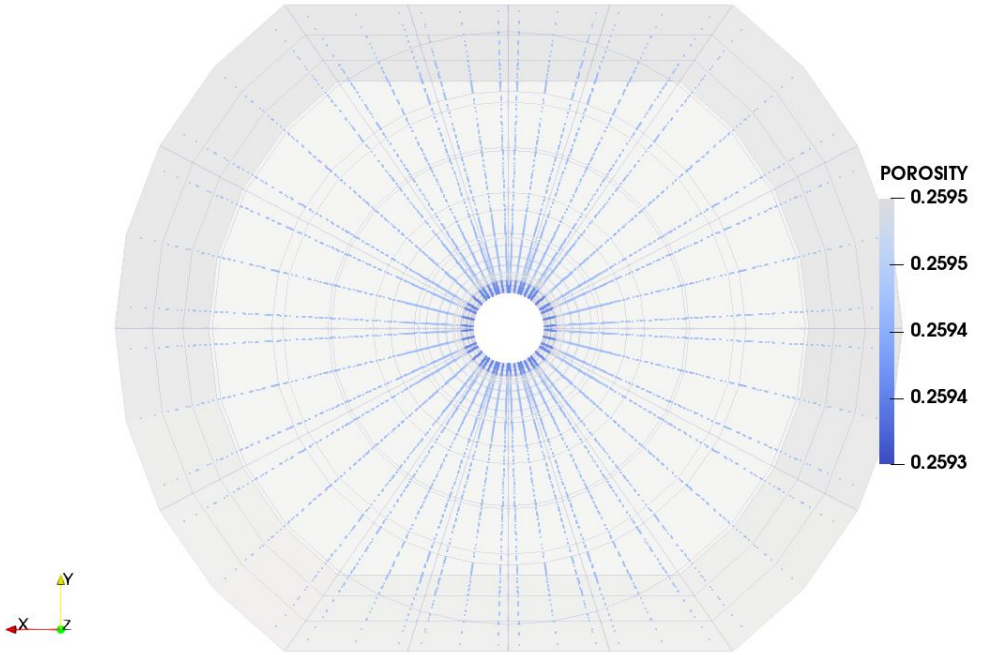

(a)

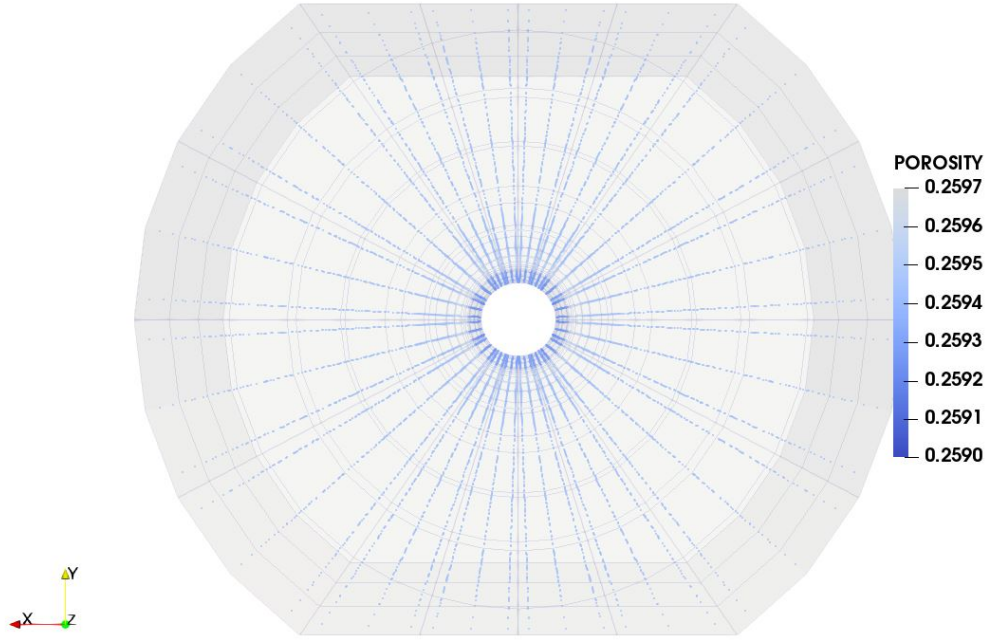

(b)

Figure A.54: Porosity at the onset of sand production (a) and end (b) of simulation for the poly-axial experiment simulation with $K_z = 1$ and $K_r = 1$.

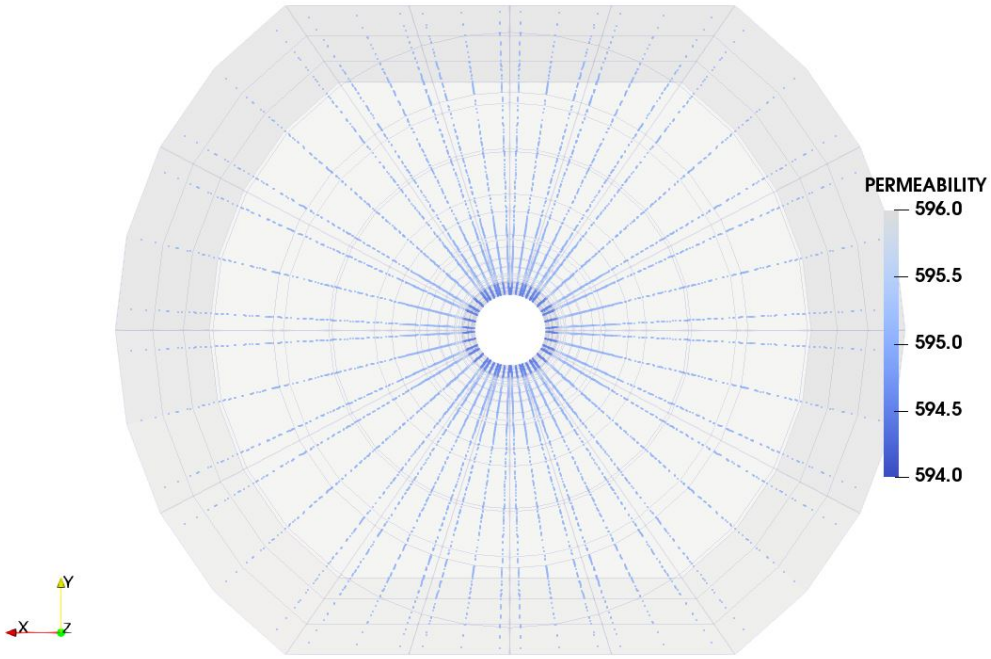

(a)

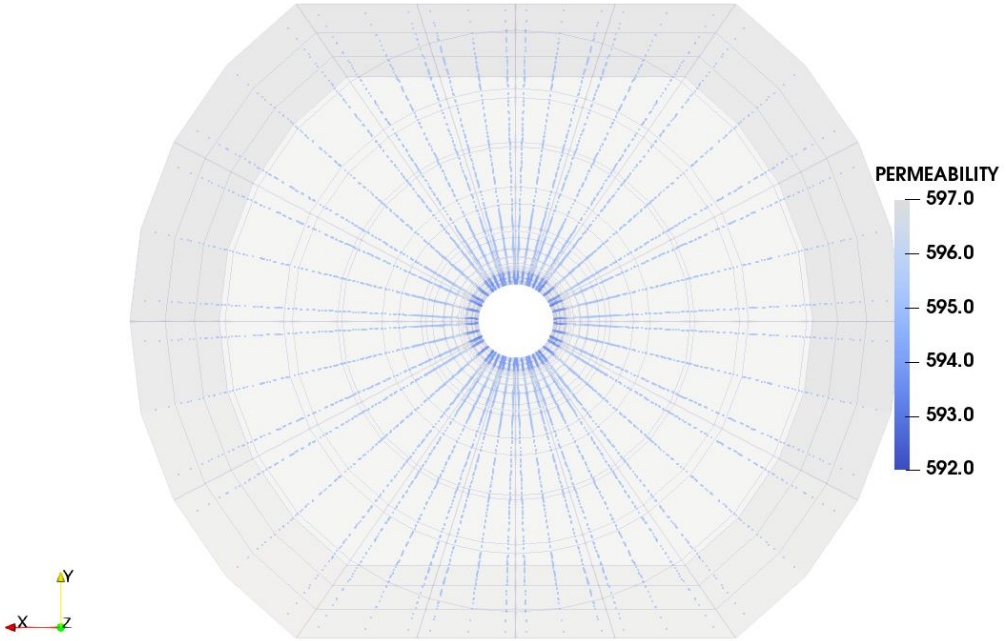

(b)

Figure A.55: Permeability (k_x, k_y and k_z) at the onset of sand production (a) and end (b) of simulation for the poly-axial experiment simulation with K_z = 1 and K_r = 1.